Development of Enabling Methodologies for Drug Metabolism Studies in Zebrafish Larvae

Dissertation
zur Erlangung des Grades
des Doktors der Naturwissenschaften
der Naturwissenschaftlich-Technischen Fakultät
der Universität des Saarlandes

von
Yu Mi Park
Saarbrücken
2022

Tag des Kolloquiums: 8. Dezember 2022

Dekan: Prof. Dr. Ludger Santen

Berichterstatter: Prof. Dr. Rolf Müller

Prof. Dr. Markus R. Meyer

Vorsitz: Prof. Dr. Christian Ducho

Akad. Mitarbeiter: Dr. Maria Lopatniuk

Die vorliegende Arbeit wurde von August 2017 bis Juni 2022 unter Anleitung von Herrn Prof. Dr. Rolf Müller am Helmholtz-Institut für Pharmazeutische Forschung Saarland (HIPS) in Kooperation mit KIST Europe Forschungsgesellschaft mbH angefertigt.

“What is important in life is life and not the result of life.”

- Johann Wolfgang von Goethe (1749-1832)

독일에서 5 년 동안의 박사과정 후 펼쳐질 내 미래를 열렬히 환영한다.

또 다른 도전을 위해 나아가자.

I welcome my future passionately post my five years of PhD in Germany.

Let me move forward with another challenge.

Acknowledgments

First, I would like to thank Prof. Dr. Rolf Müller for giving me the opportunity of a PhD position in his group and letting me study challenging and great scientific topics with excellent cooperation. I appreciate his supervision during all these times.

I would also like to thank Prof. Dr. Markus R. Meyer for being my second supervisor and for the outstanding support of all my projects.

Special big thanks go to Dr. Jennifer Herrmann, a great supervisor, and she always gave me entirely qualified support, including professional discussions and innovative suggestions for all works. I am so lucky to have you, and I could work through all my missions for PhD with you.

I appreciate everyone in our group and our team members sincerely for their friendly cooperation, scientific inspiration, and unlimited support during our time together. I would like to memorize all names of you in my heart; Anastasia Andreas, Felix Deschner, Franziska Fries, Janetta Coetzee, Katarina Cirnski, Philip Schippers, Sari Rasheed, Susanne Helene Kirsch-Dahmen, Timo Risch, Alexandra Amann, Besnik Qallaku, Stefanie Neuber, Verena Qallaku, Viktoria George, Jeenu Joy, and Jiaqi Liu. Frankly, I would like to thank my sincere best friends, Asfandyar Sikandar, Janetta Coetzee, and Dr. Jayoung Park. You have encouraged me to keep going through this long journey under my mental and professional fluctuations. I could finish the last page of my PhD book due to you gratefully.

Finally, I would like to express my sincere thanks to my family for their continued support in all situations, especially during my studying time abroad. My parents always trust my decision anytime and support me heartily. In particular, my father, as the best life mentor of my life, has given me excellent and wise advice whenever needed in a challenging situation and reminded me of what I will be looking forward to now and in the future. Moreover, my younger sister always cheers me on in difficult circumstances and puts positive power on my shoulder. I could get back to basics and resume all my work again with these encouragements.

Again, thank you, all of you, and your support made all of this possible.

독일에서의 5 년은 저에게 잊을 수 없는 소중한 경험이 되었습니다. 저의 박사과정을 끝마칠 수 있도록 여러 방면에서 도와주신 모든 분들에게 감사를 드립니다.

Summary

Drug metabolism studies are an integral part of the drug discovery and development process and preclinical testing. Likewise, drug metabolism is broadly investigated in clinical toxicology, particularly for screening purposes, since new emerging illicit drugs and drug-induced deaths are steadily increasing. More recently, zebrafish larvae became particularly popular as a non-animal *in vivo* model for predicting human metabolism. This work was dedicated to further refining zebrafish larvae models by applying and optimizing state-of-the-art technologies using three tool drugs. The direct administration of drugs using microinjection was found to be beneficial compared to conventional waterborne exposure since the fast circulation of the drug inside the larval bodies, and in turn, indicated a high concordance with human metabolism. With morpholino oligonucleotides as an antisense gene-knockdown tool, the onset of drug metabolism related to liver function and cannabinoid receptor function was investigated to understand complex biological processes contributing to drug metabolism. Having established protocols, the *in vivo* distribution of drugs and their metabolites inside zebrafish larvae was visualized using mass spectrometry imaging (MSI). In conclusion, by establishing novel approaches and new methods in zebrafish larvae, the potential of the model for predicting human drug metabolism was consolidated, and this will contribute to its expansion into conventional ADMET studies.

Zusammenfassung

Studien zum Arzneimittelstoffwechsel sind ein wesentlicher Bestandteil in der Entwicklung sowie in der präklinischen Testung neuer Arzneimittel. Da die Zahl neuer besorgniserregender illegaler Drogen und drogeninduzierte Todesfälle stetig zunehmen, wird der Arzneimittelmetabolismus ebenfalls in der klinischen Toxikologie, im Rahmen von Drogen-Screenings, umfassend untersucht. In jüngster Zeit haben sich Zebrafischlarven als ein beliebtes *in vivo* Testsystem für die Vorhersage des menschlichen Stoffwechsels erwiesen. Diese Arbeit widmet sich der weiteren Verfeinerung von Zebrafischlarvenmodellen durch Anwendung und Optimierung modernster Technologien. Die entwickelten Protokolle wurden mit Hilfe von drei Molekülen etabliert. Die direkte Verabreichung von Arzneistoffen mittels Mikroinjektion erwies sich als vorteilhaft im Vergleich zur herkömmlichen Verabreichung über das Wasser, da es eine schnelle Zirkulation des Arzneistoffs in den Larvenkörpern und damit einen effizienten Stoffwechsel ermöglicht, der eine hohe Übereinstimmung mit dem menschlichen Stoffwechsel aufweist. Mit Hilfe von Morpholino-Oligonukleotiden als Antisense-Gen-Knockdown-Tool wurde der Arzneimittelstoffwechsel im Zusammenhang mit der Leberfunktion und der Cannabinoidrezeptorfunktion untersucht, um die komplexen biologische Prozesse zu verstehen, die zum Metabolismus beitragen. Nach der Etablierung geeigneter Protokolle wurde die *in vivo* Verteilung von Arzneistoffen und ihren Metaboliten in Zebrafischlarven mithilfe von bildgebender Massenspektrometrie (MSI) visualisiert. Zusammenfassend lässt sich sagen, dass durch die erfolgreiche Etablierung neuer Ansätze und neuer Methoden in Zebrafischlarven das Potenzial des Modells zur Vorhersage des menschlichen Arzneimittelstoffwechsels konsolidiert wurde, was zu seiner Ausweitung auf konventionelle ADMET-Studien beitragen wird.

Graphical Abstract

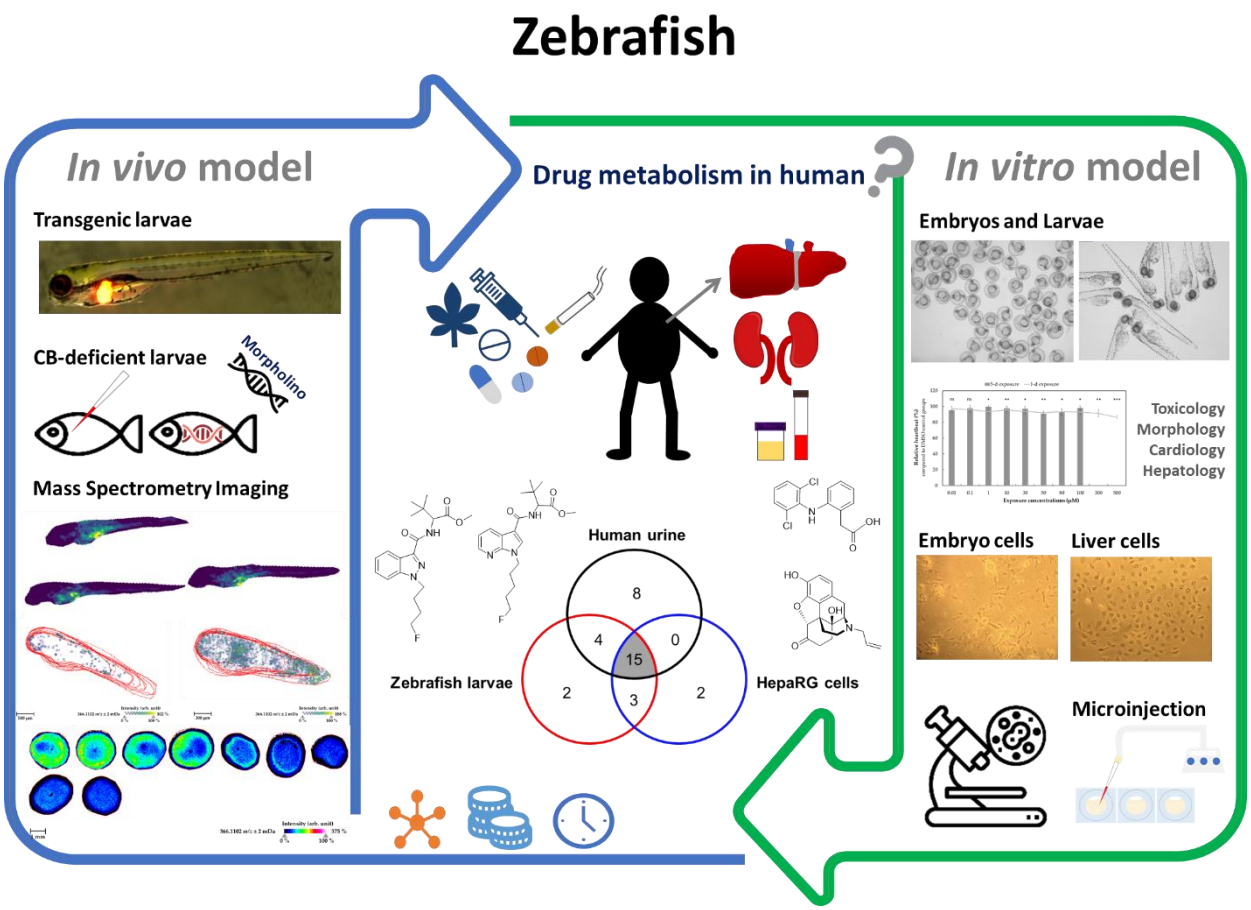

Vorveröffentlichungen aus dieser Dissertation

Teile dieser Arbeit wurden vorab mit Genehmigung der Naturwissenschaftlich-Technischen Fakultäten, vertreten durch den Mentor der Arbeit, in folgenden Beiträgen veröffentlicht oder sind derzeit in Vorbereitung der Veröffentlichung.

Publications

Bereits veröffentlichte Publikationen (mit offenem Zugang):

Yu Mi Park, Markus R. Meyer, Rolf Müller, and Jennifer Herrmann: Drug Administration Route Impact the Metabolism of a Synthetic Cannabinoid in the Zebrafish Larvae Model, *Molecules* **2020** Sep 29;25(19):4474, doi: 10.3390/molecules25194474.

Yu Mi Park, Charlotte Dahlem, Markus R. Meyer, Alexandra K. Kiemer, Rolf Müller, and Jennifer Herrmann: Induction of Liver Size Reduction in Zebrafish Larvae by the Emerging Synthetic Cannabinoid 4F-MDMB-BINACA and Its Impact on Drug Metabolism, *Molecules* **2022** Feb 15;27(4):1290, doi: 10.3390/molecules27041290.

Publikationen in Vorbereitung der Veröffentlichung:

Yu Mi Park, Markus R. Meyer, Rolf Müller, and Jennifer Herrmann: Optimization of mass spectrometry imaging for drug metabolism and distribution studies in the zebrafish larvae model: A case study with the opioid antagonist naloxone.

Weitere Publikationen, die nicht Teil dieser Arbeit sind:

Lilian H J Richter, Jennifer Herrmann, Anastasia Andreas, **Yu Mi Park**, Lea Wagmann, Veit Flockerzi, Rolf Müller, and Markus R. Meyer: Tools for studying the metabolism of new psychoactive substances for toxicological screening purposes - A comparative study using pooled human liver S9, HepaRG cells, and zebrafish larvae, *Toxicol Lett.*, **2019** May 1;305:73-80, doi: 10.1016/j.toxlet.2019.01.010.

Tanja M Gampfer, Lea Wagmann, **Yu Mi Park**, Annelies Cannaert, Jennifer Herrmann, Svenja Fischmann, Folker Westphal, Rolf Müller, Christophe P Stove, Markus R. Meyer: Toxicokinetics and toxicodynamics of the fentanyl homologs cyclopropanoyl-1-benzyl-4′-fluoro-4-anilinopiperidine and furanoyl-1-benzyl-4-anilinopiperidine, *Arch Toxicol.* **2020** Jun;94(6):2009-2025, doi: 10.1007/s00204-020-02726-1.

Lea Wagmann, Fabian Frankenfeld, **Yu Mi Park**, Jennifer Herrmann, Svenja Fischmann, Folker Westphal, Rolf Müller, Veit Flockerzi, and Markus R. Meyer: How to Study the Metabolism of New Psychoactive Substances for the Purpose of Toxicological Screenings-A Follow-Up Study Comparing Pooled Human Liver S9, HepaRG Cells, and Zebrafish Larvae, *Front Chem.* **2020** Jul 17;8:539, doi: 10.3389/fchem.2020.00539.

Conference Contributions (Posters and Oral Presentations)

Anastasia Andreas, **Yu Mi Park**, Jennifer Herrmann, Markus R. Meyer, Rolf Müller (2018), Zebrafish models for early in vivo evaluation of novel drug candidates and their metabolites. Poster presentation, 7th Summer School on Infection Research, 27–31 May 2018: Wernigerode, Germany.

Sari S. Rasheed, **Yu Mi Park**, Anastasia Andreas, Jennifer Herrmann, Rolf Müller (2019), Zebrafish as a model in anti-infective drug discovery at HIPS. Poster presentation, HIPS Symposium 2019 June 27-28, 2019: Saarbrücken, Germany

Yu Mi Park (2020), Drug metabolism and pharmacokinetics. Oral presentation, Bruker Anwendertreffen Massenspektrometrie 2020, February 17-18, 2020; Mainz, Germany.

Lukas Junk, **Yu Mi Park**, Sari Rasheed, Laura Stief, Alexander Kiefer, Jennifer Herrmann, Rolf Müller, Uli Kazmaier (2020), Synthesis of simplified Cyclomarin Derivatives and Pharmakokinetic Studies in Zebrafish. Poster presentation, 32nd Irseer Naturstofftage, February 19-21, 2020: Kloster Irsee, Germany.

Yu Mi Park, Jennifer Herrmann, Daniel Krug, Aiko Barsch, Nikolas Kessler, Alice Ly, Jan H. Kobarg, Rolf Müller (2020), A study of drug metabolism in zebrafish larvae using MALDI-MS imaging. Poster presentation, 68th Conference on Mass Spectrometry and Allied Topics, June 1–12, 2020: Online virtual, USA.

Yu Mi Park (2020), Drug metabolism studies in zebrafish larvae. Oral presentation, HIPS paper, September 15, Saarbrücken, Germany.

Table of Contents

Acknowledgments ..... **V**

Summary ..... **VI**

Zusammenfassung ..... **VII**

Graphical Abstract ..... **VIII**

Vorveröffentlichungen aus dieser Dissertation ..... **IX**

Chapter 1. Introduction

1.1 Drug Discovery and Development 16

1.2 Drug Metabolism and Pharmacokinetics 21

1.3 Zebrafish Model 28

1.4 Drug of Abuse 34

1.5 Enabling Methodologies for Drug Metabolism Studies 41

1.6 Outline of This Work 47

1.7 Bibliography 48

Chapter 2. 7′*N*-5F-ADB

Drug Administration Routes Impact the Metabolism of a Synthetic Cannabinoid in the Zebrafish Larvae Model

Contributions 64

2.1 Abstract 65

2.2 Graphical Abstract 66

2.3 Introduction 67

2.4 Results and Discussion 69

2.5 Materials and Methods 82

2.6 Summary and Conclusions 87

2.7 Acknowledgments 89

2.8 Bibliography 90

2.9 Supporting Information 94

Chapter 3. 4F-MDMB-BINACA

Induction of Liver Size Reduction in Zebrafish Larvae by the Emerging Synthetic Cannabinoid 4F-MDMB-BINACA and its Impact on Drug Metabolism

Contributions 112
[Additional Paper] 113
[Additional Paper] Contributions 114
3.1 Abstract 115
3.2 Graphical Abstract 116
3.3 Introduction 117
3.4 Results and Discussion 119
3.5 Materials and Methods 134
3.6 Summary and Conclusions 139
3.7 Bibliography 141
3.8 Supporting Information 147

Chapter 4. Naloxone

Optimization of Mass Spectrometry Imaging for Drug Metabolism and Distribution Studies in the Zebrafish Larvae Model: A Case Study with the Opioid Antagonist Naloxone

Contributions 162
4.1 Abstract 163
4.2 Graphical Abstract 164
4.3 Introduction 165
4.4 Results and Discussion 167
4.5. Materials and Methods 183
4.6 Summary and Conclusions 187
4.7 Bibliography 189
4.8 Supporting Information 195

Chapter 5. Discussion

5.1 Summary 218
5.2 Challenges in the Use of Zebrafish Larvae for Drug Metabolism Studies 221
5.3 Conclusion 236
5.4 Bibliography 237

Chapter 1.

Introduction

1.1 Drug Discovery and Development

Since the last century, humans have been in a continuous tug-of-war with diseases, and efforts to contain plagues and treat diseases have been mostly successful. The steady success of the drug discovery process can be partly attributed to a significant jump in the scientific disciplines of biology and organic chemistry [1–3]. Furthermore, unanticipated drug discovery also had a profound impact on society, as exemplified by the discovery of penicillin in 1928, which led to the introduction of antibiotics that greatly reduced the number of deaths associated with bacterial infections [3,4]. In the example at the top, the so-called golden era of antibiotics began in the 1940s, which led to the discovery of streptomycin in 1943, the first antibiotic used to treat tuberculosis [5,6]. Since then, several other classes of antibiotics have been discovered with investments from the pharmaceutical industry for antibiotic drug discovery continuously increased [7]. However, despite years of success, the current development of new drugs is suffering from some difficulties, such as the low success rate of drug candidates in the preclinical stage and in clinical trials and various regulatory requirements during preclinical testing [7]. Crucially, drug development costs have risen sharply, combined with increasing pressure on drug prices since the 1950s [8]. Although Research and Development (R&D) costs per newly approved drug have been inclined over time, its efficiency has declined [9]. These circumstances put some challenges in the current business model of the pharmaceutical industry [8,9]. On the basis of all these efforts in the past, the second golden era may have just begun in the twenty-first century due to the recent coronavirus disease, COVID-19 pandemic declared in 2020. The pandemic brought much needed attention to the importance and need for novel drug discovery and development.

Drug discovery and development is multifaceted and complicated because it involves the identification and validation of drug candidates, their synthesis and further modification, characterization, screening, and assays for therapeutic efficacy in early phases [3,10–14]. Later stages include regulatory affairs, pharmaceutical management, and clinical studies, as shown in Figure 1. The average expenditure on drug discovery and development is high since it needs a large budget for drug research and development (R&D), clinical trials, and the cost of numerous failures [12,15]. Also, in addition to the high cost of drug discovery and development, the timeline is another difficult hurdle to overcome. A single novel drug molecule takes around 10-15 years from the time it is discovered to when it is available on the market for treating patients [10,12]. However, recent improvements of technologies such as analytics, screening platforms, genome mining, genome engineering, modeling, and artificial intelligence aid in accelerating drug discovery and development [3,12,16,17].

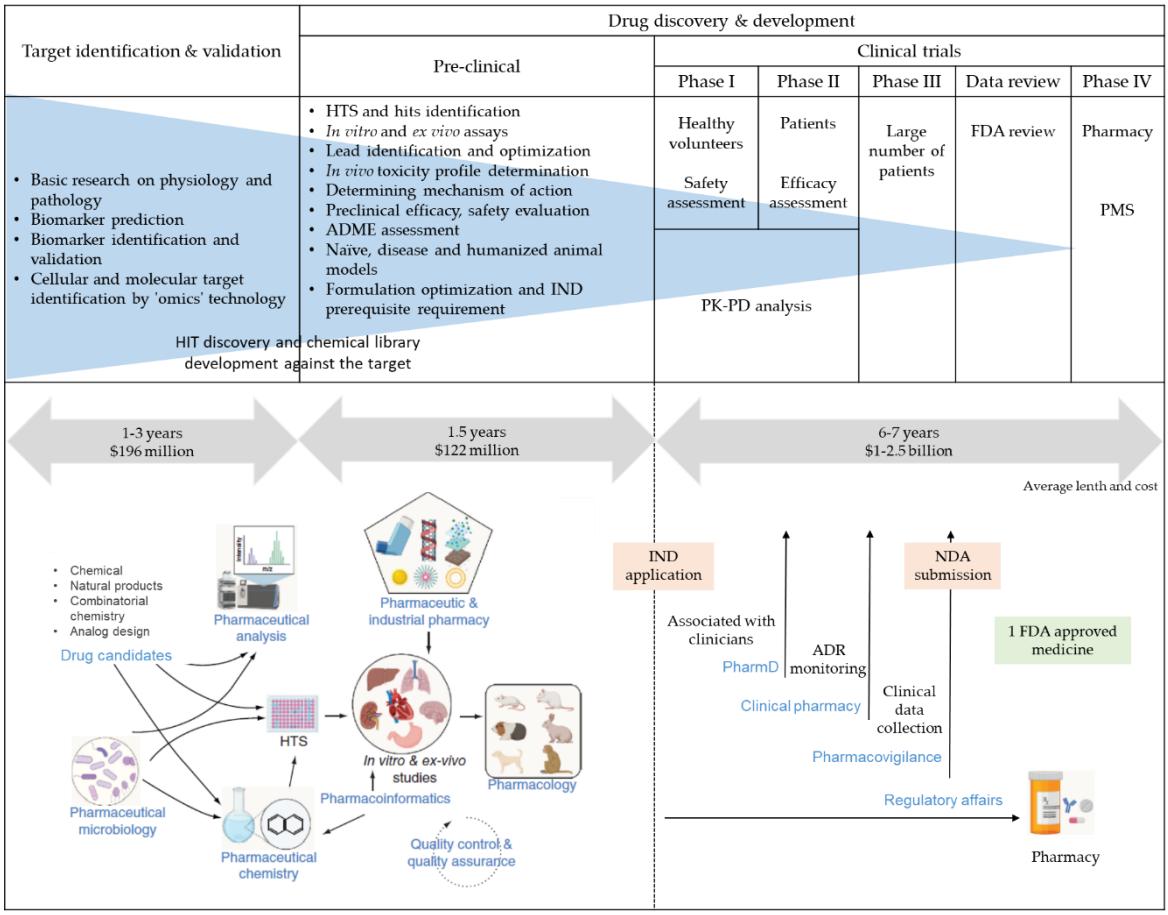

Figure 1. Drug discovery and development process. *ADME: Absorption, distribution, metabolism, and excretion; ADR: Adverse drug reaction; HTS: High-throughput screening; IND: Investigational new drug; PK-PD: Pharmacokinetics and pharmacodynamics; NDA: New drug application; PMS: Post-marketing surveillance [13,18].

Despite globale challenges due to the COVID-19 pandemic that affected research in most areas, the United States Food and Drug Administration (FDA) approved 53 and 44 novel therapeutics in 2020 and 2021, respectively [19,20]. The rich harvest of new drugs approved raises the 5-year average to 50 approvals per year, which is twice the approvals from the period 2007 to 2011 (Figure 2). The number of drug approvals was exceptionally low in 2016. In addition to the lower number of drug submissions and higher number of rejections and delays from the FDA, some delayed drugs won approval in 2017, such as Roche's ocrelizumab (Ocrevus) and Sanofi and Regeneron's biologic drug sarilumab. Five drugs expecting the approval in 2016 received early approval in 2015, which both lowered 2016's approvals and increased 2015's [21,22].

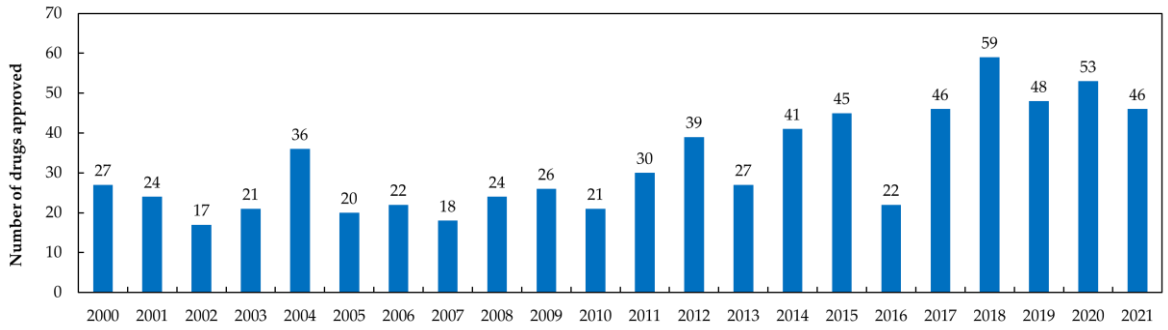

Figure 2. The status of novel FDA approvals from 2000 to November 2021. *Source: The United States Food and Drug Administration (FDA) [20].

Recent data from the Center for Medical Research (CMR) International consortium indicates that success rates in the late-stage development from phase III through to launch have increased from around a one in two chance of successfully getting to the market to almost two in three in 2015–2017 (Figure 3) [23]. Meanwhile, phase I and phase II success rates for launching have remained statically at relatively low rates of probability of success, and only approximately a quarter of projects transitioned successfully from phase II to phase III trials (Figure 3). These data could be interpreted that the full support of progressing candidates should start from increasing success rate inclination in early-stage development. Also, the first promising outcomes at the initial steps will hopefully induce the success rates from the following step until the late stage.

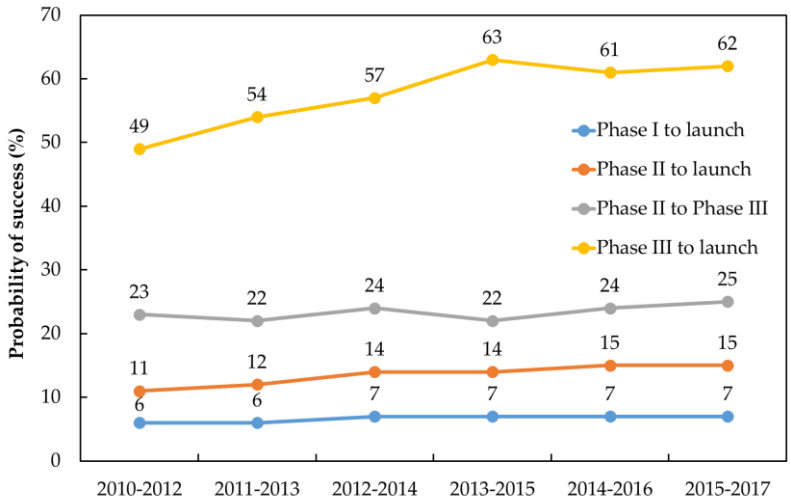

Figure 3. Trends in the probability of launch from the start of phase I, phase II, and phase III for new drug approvals by the FDA at intervals of three years from 2010. *Source: The Center for Medical Research (CMR) R&D Performance Metrics [23].

Swinney *et al*. [24] analyzed the distribution of new medicines in terms of the discovery strategy in the 10-year period between 1999 and 2008, which included a total of 232 agents approved by the FDA, and classified them into four approaches, such as phenotypic and

target-based screening, modified natural substances, and biologics (Figure 4). In this period, most small molecule first-in-class drugs comprising new molecular entities (NMEs) were discovered using phenotypic assays. With sorting out all the drugs found in this study by discovery approach, 100 NMEs were found using target-based screening approaches and 58 NMEs by phenotypic screening approaches [24]. Interestingly, 48% (28 new medicines) of the total 58 NMEs from phenotypic screening approaches were developed into first-in-class drugs, compared to only 17 new drugs out of 100 NMEs from target-based screening approaches. On the contrary, in the case of follower drugs, 53% of the total follower drugs were revealed by target-based screening approaches (Figure 4) [24–26]. Concerning the discovery of follower drugs, that trend reversal could be caused by a detailed understanding of previously identified molecular mechanism of action (MMOA) making the use of target-based tools very efficient. The appropriate timing of the usage of these tools may also be crucial for drug discovery [24,25]. Also, the report by DiMasi *et al.* [25] indicates that research on a big percentage of follower drugs was launched before first-in-class approval.

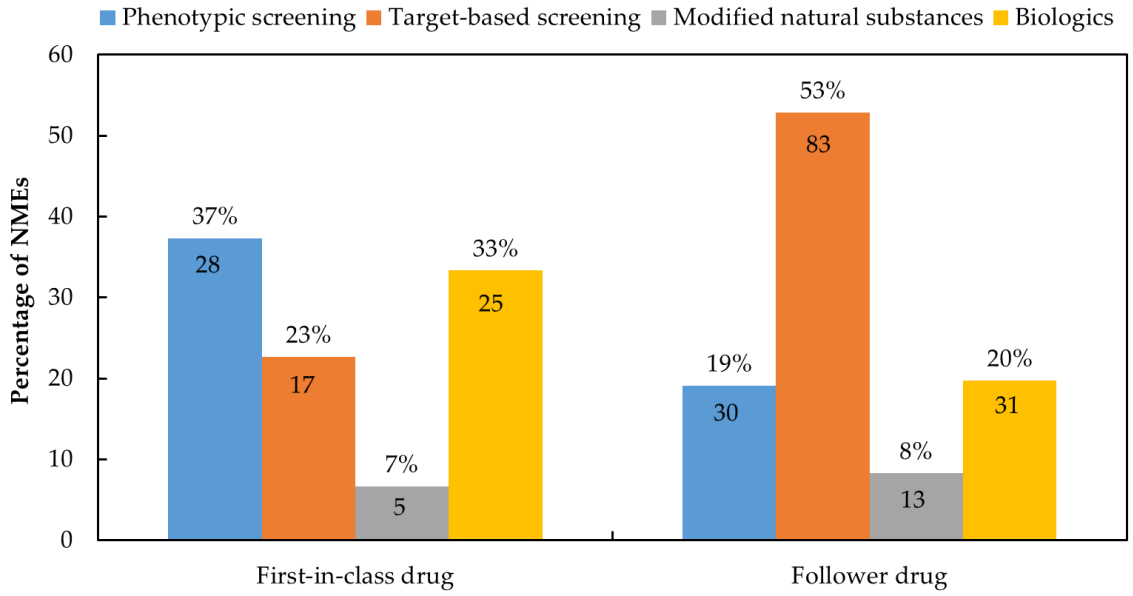

Figure 4. The distribution of 232 new drugs discovered between 1999 and 2008 according to the discovery strategy: 75 drug candidates for first-in-class drug status and 157 drug candidates for follower drugs. The number inside an individual bar graph represents the number of new molecular entities (NMEs) revealed by the individual screening approach, and its composition rate within the respective drug discovery strategy is displayed above the bar graph [24].

The end product(s) of these distinct screening approaches is regarded as one candidate drug, which then goes into pre-clinical studies. This stage of drug development focuses on efficacy, safety, dosing, and tolerability of the drug candidate before it can be tested on humans [27]. For the period of 2013-2015, the most common reasons for failure at this stage were either poor efficacy (52%), or lack of safety (24%) (Figure 5) [3,28,29]. These major reasons for clinical failure remain mostly unchanged over the following 3-year time period

(2016-2018) [23]. Thus, various strategic approaches from the target identification and validation process to the pre-clinical stage should be implemented before reaching the clinical stage to improve success rates.

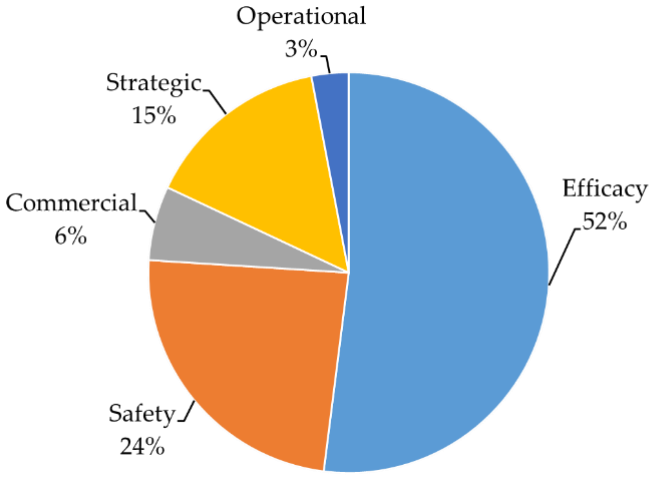

Figure 5. The analysis of the reasons for the failures of 174 drug candidates in clinical trials reported from 2013 to 2015 [28].

1.2 Drug Metabolism and Pharmacokinetics

In general, pharmacology is the study of drugs and their interaction with the body, representing biochemical and physiological effects of drugs [30,31]. Pharmacology comprises two main branches, pharmacodynamics (PD) and pharmacokinetics (PK) [30–32]. In particular, PD is a drug's effect on the human body or organism; whereas, PK focuses on understanding how a drug is delivered all over the body, i.e. absorption, distribution, metabolism, and excretion (ADME). Initial PK studies are, in general, conducted to determine the plasma concentration-time curve (Figure 6a). Subsequently, PD studies are accomplished by measuring the effect of a drug according to concentration, which is based on the drug's ADME properties and other components of the pharmacokinetic profile (Figure 6b).

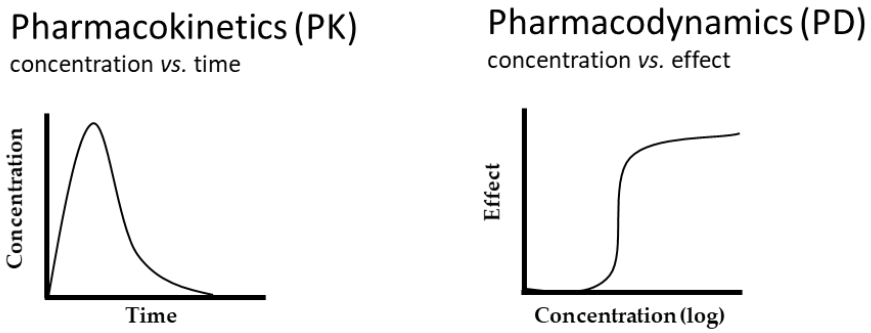

(a) (b)

Figure 6. The concept of (a) pharmacokinetics (PK) and (b) pharmacodynamics (PD) [31].

In drug discovery and development, drug metabolism and pharmacokinetics (DMPK) is a fundamental discipline that considers the biotransformation of drug candidates and assessment of their safety, thereby helping to confirm which drug candidates warrant further investigation and development [32–35].

DMPK typically comprises the following studies; protein binding (including blood-plasma partitioning and plasma stability), hepatocyte stability, metabolic enzyme phenotyping, human CYP inhibition, mechanism-based inactivation, ADME studies in animals (as well as oral and *i.v.* PK studies), mass balance, drug distribution (by quantitative whole-body autoradiography), drug elimination pathways (bile duct cannulated animals), *ex vivo* induction, metabolite identification, transporter substrate (using Caco-2 and other cell lines) and/or inhibitor evaluation, drug-drug interaction evaluation, and DMPK modeling (including scaling up from *in vitro* to *in vivo* and from preclinical animals to humans), and humans dosing projection [30,32,33].

For the basic understanding of DMPK, its schematic process in human blood, including variously possible absorption routes, is shown in Figure 7 [11]. Moreover, the practical roles of DMPK at each stage of drug discovery are summarized in Table 1 [30], and the major model systems used for ADME studies are listed in Table 2 [33].

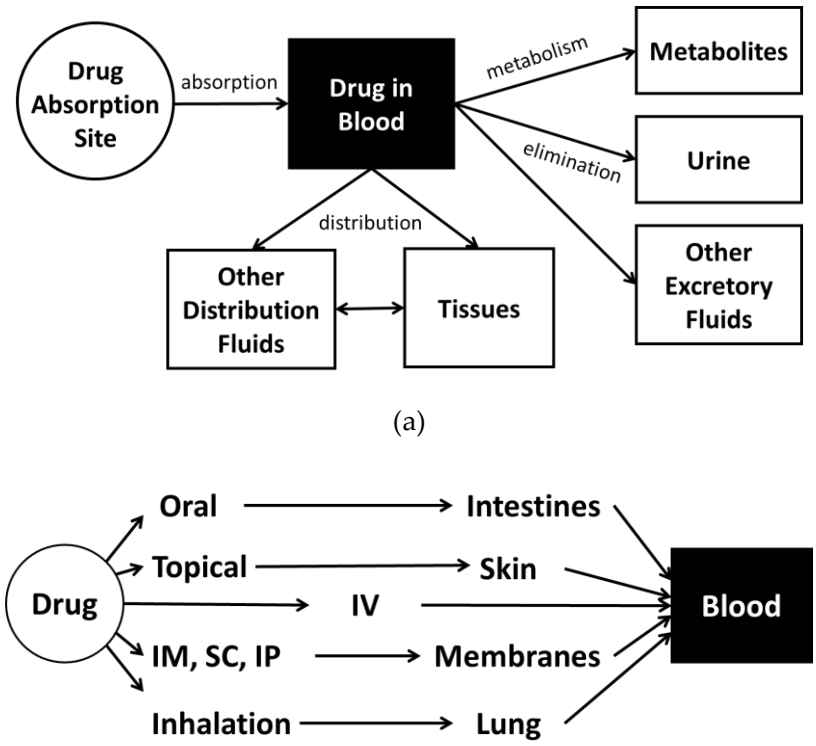

Figure 7. (a) Schematic representations of DMPK of a drug via blood and (b) Absorption routes of a drug after administration. *Parenteral administration routes; IV: intravenous; IM: intramuscular; SC: subcutaneous; IP: intraperitoneal [11].

Table 1. The significant role of drug metabolism and pharmacokinetics (DMPK) models at the various stages of drug discovery [30].

Discovery phase	Role of DMPK models
Target Identification	○ Selection and characterization of tool compounds ○ Partner with *in vivo* pharmacology and toxicology in target validation and safety assessment activities
Hit Identification	○ *In silico* and *in vitro* DMPK profiling to help prioritize hit series
Lead Identification	○ Identify DMPK liabilities of lead series ○ Determine whether DMPK properties in lead series are optimizable (DMPK liabilities not linked to pharmacophore) ○ Develop structure property relationship (SPR) ○ Develop '*in vitro in vivo*' correlation (IVIVC) ○ Guide selection of lead series ○ Contribute to the development of PD assays and develop early PK/PD understanding
Lead Optimization	○ Guide optimization of DMPK properties toward target profile ○ Comprehensive DMPK characterization of candidate compounds

	○ Develop biomarker-based and/or efficacy/disease-related PK/PD models ○ Prediction of human PK ○ Prediction of efficacious human dose ○ Integration of predicted profile to calculate critical margins against side effects

Table 2. Experimental ADME model systems primarily used in drug discovery and development [33].

Category	Models
In vitro metabolic models	○ Expressed enzymes ○ Sub-cellular fractions ○ Whole cell system
In vitro transporter models	○ Immortalized cell lines ○ Transfected cell lines ○ Hepatocytes ○ Membrane vesicles
In situ and *ex vivo* models	○ *In situ* models (perfusion) ○ *Ex vivo* models for induction and toxicity studies
In vivo model	○ Pharmacokinetic studies ○ Preclinical ADME models
Engineered mouse models	○ Mouse models ○ Utility of engineered mouse models

With comprehensive DMPK studies at hand, the intrinsic properties of a drug candidate and how it will be cleared from the body when administrated to humans can be understand at a high level of confidence. Extended DMPK studies evaluate the drug's metabolites, toxicity, and adverse side effects. DMPK *in vivo* and *in vitro* studies have been utilized primarily to facilitate target validation and safety assessment and to convert early screening hits and leads into drug candidates throughout the whole discovery process [30,32]. Notably, the potential risk of a drug candidate assessed in DMPK studies can predict the potential for drug-drug interactions (DDIs), causing side effects in a patient taking multiple medications. The proper investigation of DDI with metabolizing enzymes and drug transporters *in vitro* enables us to identify the risks before starting clinical trials.

To compare the reasons for the failure of drug discovery related to DMPK and PD studies between the past and the present, a more comprehensive analysis of the failures of drug candidates from 1997 to 2004 [36–38] was shown in Figure 8. Overall, half of all failure cases in these references were due to lack of sufficient human ADME and unexpected toxicity. In particular, Kennedy T. [38] reported in 1997 that 39% of 198 new chemical compounds in clinical development failed due to poor PK/ADME, 30% by lack of efficacy, and 11% by the deficiency of animal toxicity. Although it passed 18 years with the advanced technologies for DMPK studies, such as various alternative animal models and recently developed analytical instruments and modeling systems, the primary reasons for the failure of drug discovery and development have remained in poor DMPK and PD studies with ca. 70% (Figure

5 and 8). These data underpin the importance of DMPK studies in the drug design process, and therefore, the continuing trend in drug discovery has been to access ADME information early on in drug discovery and development process [39]. Strategies for well-organized ADME assessment of drug candidates in pre-clinical development during the drug discovery process have been crucial, and the dependence on such information has been rising [39]. Along the same lines, the global ADMET testing market is expected to increase by 5-fold from 2020 to 2027 [40].

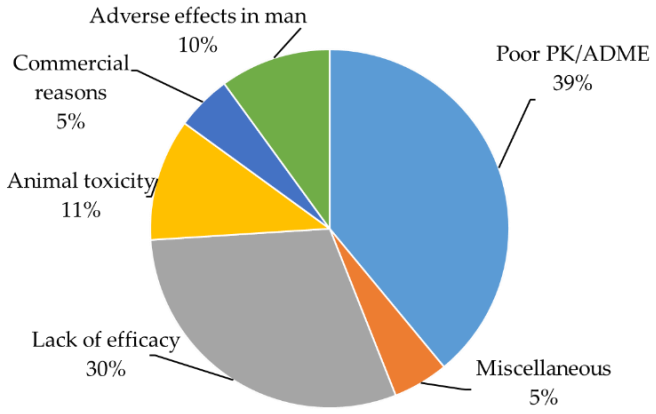

Figure 8. Detailed practical analysis of the failure of 198 new drug candidates, focusing on DMPK and PD, in clinical development from 1997 to 2004 [36–38].

In DMPK, establishing an *in vitro-in vivo* correlation for an ADME parameter in multi-parametric models, pre-clinical studies are the most common step in finding models that correlate to humans. In other words, selecting an appropriate model, followed by applying the specific model(s), and correct data interpretation, are critical [33,41]. The results from *in vivo* models reflect the combinational effect of multi-factorial mechanisms associated with an organism's biological systems, and, based on these results; we can generate PK parameters and toxicological endpoints similar to humans. However, *in vitro* assays have unique advantages, although *in vitro* models generally return one specific parameter of the global DMPK properties of a drug. They can provide a fast and convenient way to test the potency and drug-like properties of chemical entities with small amounts of test compound, and such assays can serve as a predictor for human pharmacology. In conclusion, animal studies like mammalian models are required for PK/PD studies in the pre-clinical stages. Rodent models (i.p. mouse) are the most popular and widely used for testing e.g. drug exposure and efficacy. For these models, anatomical and physiological aspects as well as genetic (dis-)similarity to humans have been studied extensively [42]. Besides mouse, rat, guinea pig, dog, miniature pig (also called minipig), monkey, and rabbit are also commonly used models for drug testing.

For the year 2020, the Federal Institue for Risk Assessment (BfR) reported on the usage of animals experiments in Germany, and the main species used in 2020 were mice (73%), fish (11%), rats (8%), and rabbits (3%) (Figure 9a) in comparison to mice (69%), fish (14%), rats (9%), and rabbits (3%) in 2019 [43–45]. However, mandatory tests with non-human primates conducted by law, such as toxicology or other safety tests, took up to 90%, and only 10% of the models were used for science and basic research (Figure 9b). On taking a closer look at the actual number of animal experiments by research field, the rodent model is by far the most widely applied model (96%). (Figure 9c).

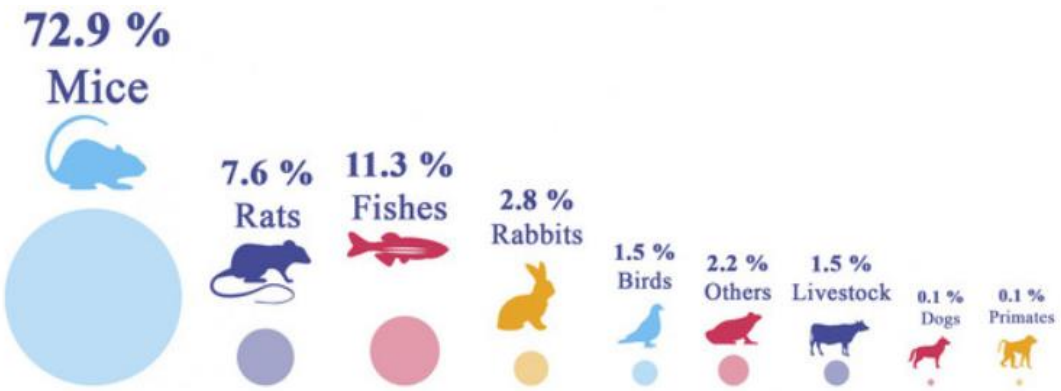

(a)

Figure 9. *Continued.*

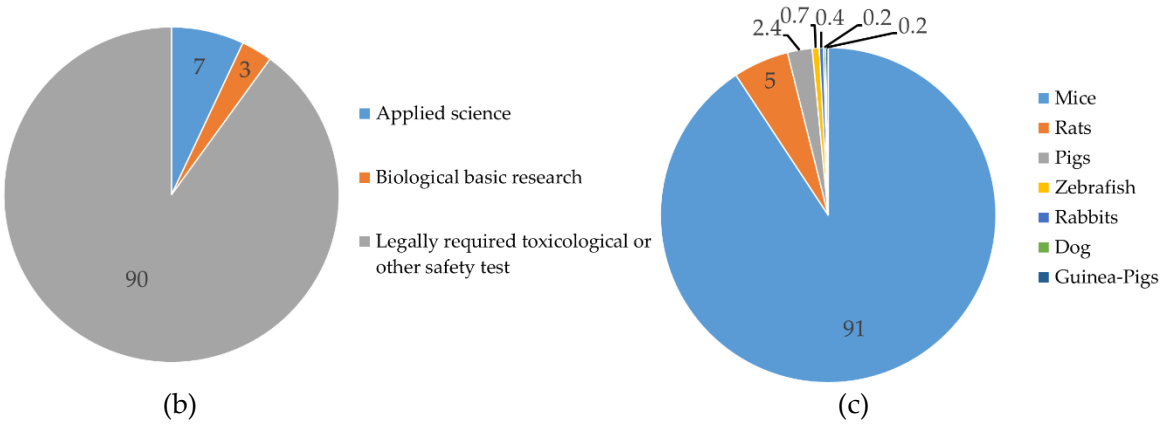

Figure 9. (a) Comparison to the portion of experimental animals used in Germany in 2020, (b) animal research with non-human primates divided by intended purpose, and (c) the percentage distribution of animal numbers for science or research. *Source: The Federal Ministry of Food and Agriculture in Germany [44,45].

Once again, drug discovery involves complicated biochemical and cellular assays, followed by validation (proof-of-concept) in animal models and eventually in humans. In the late pre-clinical stage, mammalian models for DMPK are expensive, laborious, and require large quantities of the valuable compound. There is also a high pressure to minimize the use of animals in research and development in line with the 3Rs (Replacement, Reduction, Refinement) philosophy [46–49].

The 3Rs principle was first introduced in the book 'The principles of humane experimental technique' written by W.M.S. Russell and R.L. Burch in 1959 [50]. This book first used the term 'inhumanity' to explain the negative mental states of animals caused by experimental procedures [48,50–52]. They emphasized eliminating inhumanity towards animals, and their goals were to prohibit the use of animals wherever possible and enhance significantly the treatment of the animals still considered inevitable to improve the quality of scientific and medical research or testing [48,50–54]. Despite their remarkable principles of humane experimental techniques, the 3Rs principle did not receive attention until the early 1980s. However, in the 1980s, some progress was made by regulators, industry, and scientists in finding alternatives to regulatory toxicology tests as legislative changes took place in Switzerland and the Federal Republic of Germany demanding consideration of alternatives [53,55]. Eventually, the movement was stimulated in the 2000s, and for instance, the European consensus platform ECOPA for 3Rs alternatives to animal experimentation was established in December 2000. Also, the first government-funded national center in the United Kingdom (UK) to focus on the 3Rs, the National Centre for the Replacement Refinement & Reduction of Animals in Research (NC3Rs), was set up in 2004 which inspired foundation of the Danish 3R-center in 2013 [53]. By now, legislation controlling the use of animals in research has adopted the 3Rs. In 2010, as a radical change, the 1986 European Directive was updated and replaced by European Directive 2010/63/EU. In order to protect the animal

welfare used for scientific purposes, it came into effect in 2013, thereby requiring all European union (EU) member states to fully implement the 3Rs [48,52,56]. Until now, most of the scientific fields using animal models have accepted 3Rs activities. However, the 3Rs implementation still varies worldwide, even though its perception has changed significantly over the last ten years.

In future, there will be unprecedented challenges to advance 3Rs with many cross-sector and cross-discipline collaborations supported by new technology, scientific discovery, and many commercial opportunities [57]. Thus, more desirable experimental design, development of alternative animal models, and statistical approaches to minimize animal use in research are required to comply with the 3Rs. Some platforms have been considered alternatives to the use of animals in line with the 3Rs philosophy, such as studies with human induced pluripotent stem cells [58], 3D tissue models [59–61], organs on chips [62], *in silico* prediction or computer modeling [63,64], machine learning [65], and humanized chimeric mouse models for more translatable data [66], as well as non-mammalian animal testing in animals like *Caenorhabditis elegans* [67] and teleost fish *Danio rerio* (Zebrafish) [47,68–70]. However, there are still many challenges, such as developing sophisticated human-relevant models and integrated approaches using the aboved mentioned models complying with the 3Rs principle.

1.3 Zebrafish Model

Many animal models are applied to improve consistency and validity of research results with the aim to predict drug effects on humans, and these are typically done prior to extensive *in vitro* profiling. However, even though cell-based assay systems using monolayer cultures or 3D cultures have been widely used in drug discovery, there are still some difficulties in mimicking complex mechanisms as found in whole organisms having multiple organs and various types of tissues. This lack of reproducibility causes a large gap between human pharmacological effect and the results from *in vitro* assays, despite obvious advantages of *in vitro* studies, such as reduced cost, higher throughput, and reduced animal use. Consequently, many efforts to develop and implement alternative assays have beenm undertaken since the paradigm shift of the ethics for animal welfare in research in terms of the 3Rs principle, starting in earnest in the early 2000s. The primary focus is on improving preclinical testing with high predictivity for clinical safety issues and therapeutic outcomes [68]. Therefore, developing simple, whole organism based assay systems is required in particular in the early stages of drug discovery [69].

In particular, fish models were utilized by scientists for more than 200 years due to high reproduction rates, fast maturation, and more recently the possibility to apply genetic manipulations [71]. The most common fish model species in different research areas are zebrafish (*Danio rerio*), medaka (*Oryzias aculeatus*), roach (*Rutilus rutilus*), three-spined stickleback (*Gasterosteus aculeatus*), pufferfish (*Takifugu rubripes*), and swordtail (*Xiphophorus hellerii*), with each fish species having unique advantages and disadvantages [72].

For instance, medaka fish were the most popular species used for the studies of genetics, reproduction, and development, the goldfish for growth, stress, immunology, and reproduction [71,73], and recently, the zebrafish has gained popularity and it is utilized to study human diseases [70,71,74–76]. In fact, the number of publications of studies using zebrafish dramatically increased from 1998 to 2020 by a factor of ca. 13-fold (460 → 6213), followed by an increased use of medaka (ca. 7-fold higher: 106 → 741), pufferfish (ca. 5-fold higher: 40 → 202), and stickleback (ca. 5-fold higher: 33 →142) (Figure 10). Interestingly, the turning point of the number of scientific publications applying the zebrafish model is in the period 2000-2004, and it seems to be affected by the increasing application of the 3Rs in animal welfare. Furthermore, the current high demand for the zebrafish model is expected to continue for a while given the continuous increase of usage, in particular in the period 2018 to 2020 [72].

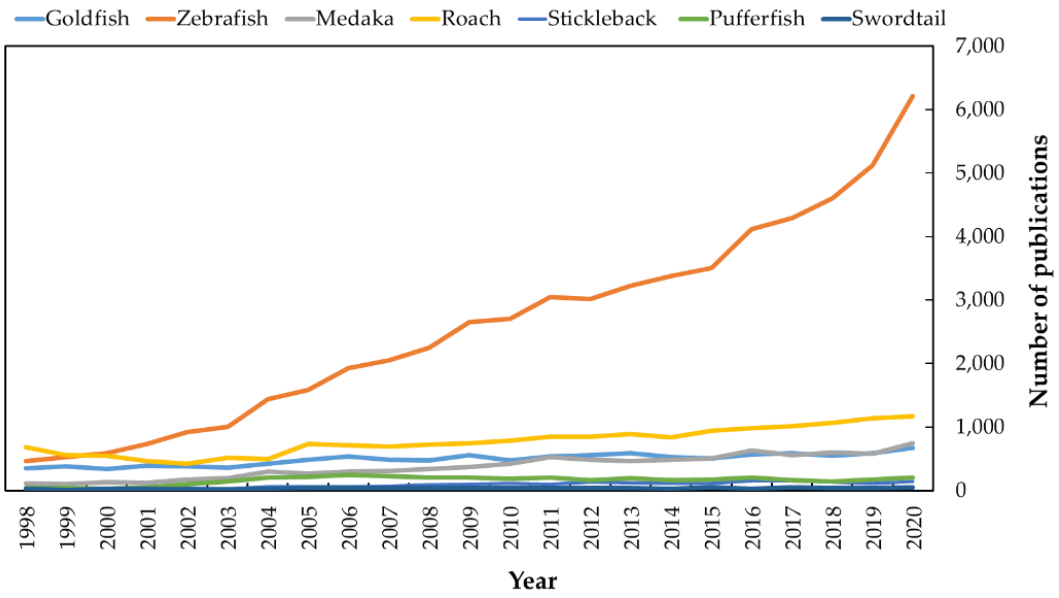

Figure 10. Publication trends of fish models from 1998 to 2020. The cumulative number of studies using the zebrafish model has represented a three-fold increase in ca. eight years (between March 2013 and May 2021). These analyses were carried out by the bibliographic search for fish models as a keyword on the ScienceDirect website, displaying in chronological order.

The zebrafish (*Danio rerio*) is a small vertebrate tropical fish (3-5 cm in length and 0.5-0.9 g in body weight, and an average lifespan of three years; Figure 11) originating from the Ganges River and its tributaries in northern India [69,70,72,73]. It was first discovered in the northern Himalayan rivers of India, and George Streisinger pioneered work on zebrafish and first introduced it as a potential biological model organism in 1972 [70,77]. The zebrafish model has a high reproduction rate, in which one pair of adult fish is able to lay several hundred eggs per mating, reaching ten thousand eggs per year. Moreover, it is also possible to mate again already after ten days, thereby further increasing the number of eggs available for research. Due to these advantages, zebrafish housing facilities can be maintained at low costs and in less space than facilities for other popular animal models such as mice and dogs [78–80].

Furthermore, early embryonic and larval stages of zebrafish are optically transparent with rapid development. This characteristic enables non-invasive *in vivo* optical experiments for monitoring their development and morphological changes throughout the entire developmental stages in multi-well plates [47,69,80,81]. The modification of zebrafish embryos and larvae for studying gene mutation is incredibly straightforward because external fertilization allows simple injections into the single-cell zygote [49,69,80,82,83].

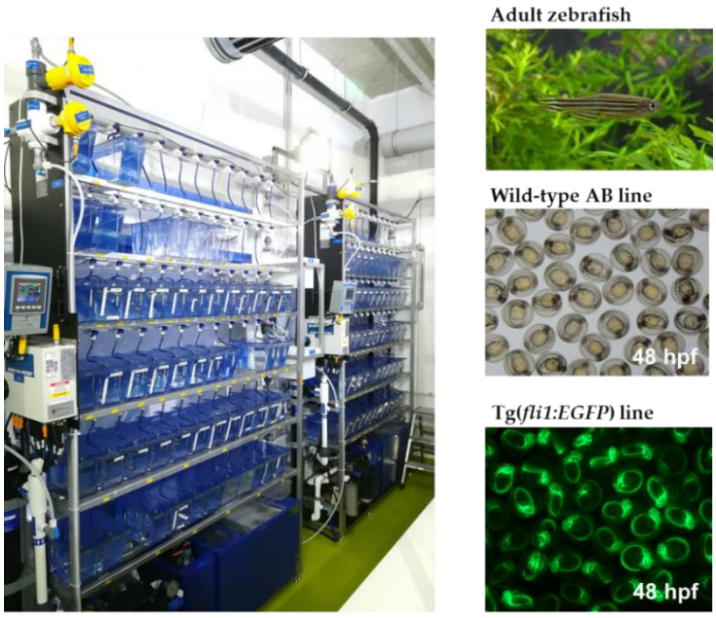

(a) (b)

Figure 11. (a) Zebrafish facility at HIPs operating for reproducing zebrafish embryos and larvae and (b) The pictures of adult zebrafish and embryos of two different fish lines. Tg (*fli1*:EGFP) represents a transgenic line with a green fluorescent protein under the control of the promotor of the *Fli*1 gene. *hpf; hour post-fertilization.

One of the major advantages of the zebrafish model are its high genomic similarity to human genes (≥ 70%), which is even higher when looking at human disease-related genes (82%) (Figure 12a) [47,69,81,84]. The high-quality genome of zebrafish has shown that orthologous proteins are similar to human counterparts, particularly within functional domains. For instance, the protein targets of the ten most-prescribed drugs have zebrafish orthologues with sequence identity; 54% for glucocorticoid receptor and 91% for thyroid receptor [47]. Howe *et al*. [84] generated a high-quality sequence assembly of the zebrafish genome and performed a four-way comparison between the proteome of two mammals (human and mouse), a bird (chicken), and zebrafish. The fraction of shared and species-specific genes is quantified in each genome and then represented in a Venn diagram (Figure 12b). Given the sequence divergence between zebrafish and human proteins, zebrafish model conservatively has the high possibility of anticipating close to the pharmacological effect in humans. In practice, several compounds discovered in zebrafish (adult fish, embryos, and larvae) screens rapidly went through to *in vivo* mammalian models with minimal optimization of pharmacological properties required because similar effects were found in rodent models and humans [47,84,85].

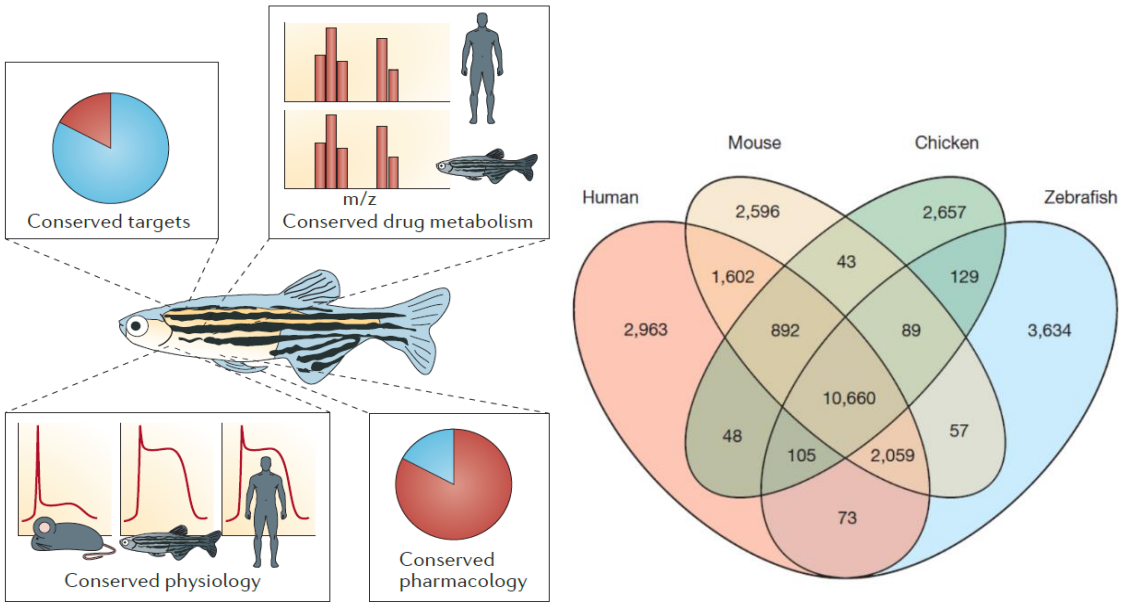

(a) (b)

Figure 12. (a) The descriptive image to explain how relevant zebrafish are for discovering humans drugs [47] (Reprinted from Ref. [47] with permission from Springer Nature) and (b) Orthologous gene comparisons among zebrafish, human, mouse, and chicken genomes using orthology relationships from Ensembl Compara 63 [84]. Zebrafish share 82% of disease-associated targets and a large number of drug metabolism pathways, and zebrafish physiology is well conserved and exhibits similar effects discovered in rodent models and humans to several compounds.

A survey performed by Zhang *et al*. in 2020 revealed 114 studies using the zebrafish model comprising eleven major research fields (Figure 13a) [82]. In particular, 56 tissue-specific studies have commonly used specific tissues of zebrafish to study modulators of organogenesis or rescuers of tissue-specific pathologies being focused on heart, angiogenesis, and hair cells/lateral line of zebrafish (Figure 13b). Moreover, twelve metabolism studies were designed to investigate the role of pancreatic β-cells, metal homeostasis, and glucose metabolism (Figure 13c), and in ten signaling pathway studies were published (Figure 13d). Remarkably, 55 studies, out of 114 studies, rely on wild-type fish, compared to 50 and nine studies using transgenic lines and mutant models, respectively. In detail, five out of the six inflammation screens use neutrophil-specific reporter lines with *lyz*- or *mpx*-driven fluorescence (Figure 13a) [79,82]. Most transgenic zebrafish encode fluorescent proteins, e.g. green fluorescent protein (GFP) and its variants, as the most common technique for cell type-specific visualization. For example, all of the nine angiogenesis screens only use a *fli*1- or *flik*1 reporter line for fluorescence imaging of the entire vasculature (Figure 13b), and all of these mutant zebrafish lines used in screening were identified from forward genetic screens. Also, forward genetics in these studies contributed significantly to the availability of zebrafish mutants for chemical screening, whereas recent advancements in genome editing technologies, such as transcription activator-like effector nucleases (TALENS) and clustered regularly interspaced short palindromic repeats-CRISPR associated protein 9 (CRISPR-Cas9),

moved toward a growing tendency in a targeted model generation. Such genetic tools also accelerated the generation of various zebrafish mutant lines for diverse applications [86–88]. Interestingly, most studies employed zebrafish larvae at life stages earlier than eight days-post fertilization (dpf), and only four studies used adult zebrafish.

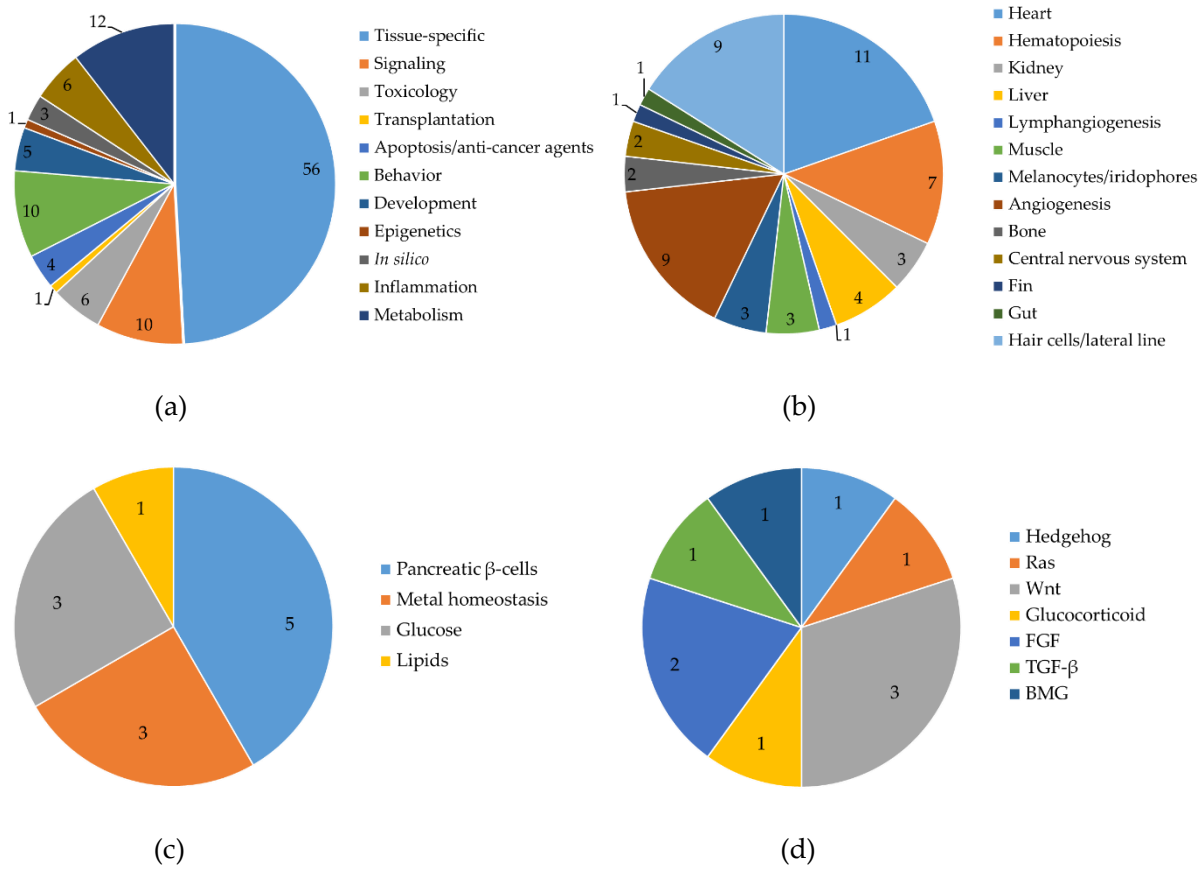

Figure 13. (a) A total of 114 studies were found and categorized into 11 research fields based on the survey result for the availability of zebrafish model in literature from 2000 to 2017. In addition, based on the values in panel a, three main research fields were detailed in (b) 56 tissue-specific studies, (c) 12 metabolism studies, and (c) 10 signaling pathways [82].

Notably, the European legislation categorizes the self-feeding zebrafish embryos and larvae younger than 120 h post-fertilization (hpf) as a non-animal model (EU directive 2010/63/EU). Thus, experiments with zebrafish larvae at ≤ 120 hpf is in compliance with the 3Rs principle (see Section 1.2) as it contributes to the reduction of animal experiments. Taken together, zebrafish models are very useful and attractive tools for scientists and researchers bridging the gap between *in vitro* screening and animal models (Figure 10 and 13). Eight small molecules initially discovered in zebrafish model have proceeded into clinical trials during the past decade [89–95], demonstrating that the use of the zebrafish model can indeed contribute to successful translation [68,96]. Moreover, zebrafish assays have been accepted by the United States Food and Drug Administration (FDA) for toxicity and safety

assessments of investigative new drugs [97]. Over the past few years, the zebrafish model has been increasingly used in functional and safety studies, and drug metabolism studies, wherby its reproducibility and high coverage of human metabolites have been demonstrated [66,98–101].

However, despite many advantages of the zebrafish model in various research fields, there are some biological limitations: some missing organs (i.e., lungs, prostate, and mammary glands), the embryological difference [i.e., kidney (single nephron in larvae, free of Henle loops), heart (one atrium/ventricle)], and its fast regeneration unlikely to those of mammals (i.e., retinas, spinal cord, kidney, heart, and liver). In addition, it is impossible to proceed with multi-endpoint assays in a single animal for PK and PD in the zebrafish model. Furthermore, due to its small body size and consequently the limited amount of tissue/organ, technical skills for experimental operations such as administration and blood/tissue sampling are required to handle it [59]. Above all, understanding the capabilities and limitations of each animal model as an alternative for humans is most crucial. Thus, despite many efforts to improve and replace some of the traditional animal models, these models have reliably predicted drug efficacy and toxicity in humans. However, zebrafish can contribute to mimicking human effects in studies on human disease and toxicity [47,49,81,102].

1.4 Drug of Abuse

1.4.1 Origin and Characterization of Psychoactive Substances

Throughout history, the usage of drugs was primarily focused on medicinal applications and religious aspects (e.g. fermented fruits and substances from nature such as opium, hemp, ergot, blue lotus, mad honey, henbane, deadly nightshade, and dreamfish), and an international drug trade occurred as early as 1000 BC [103]. However, it is unclear at what point psychobiological factors took over, and drug abuse or dependence occurred [104]. Moreover, the definition of abuse and misuse vary, and both terms generally include the use of illegal substances such as cocaine and heroin, the misuse of legal substances such as solvents, over-the-counter drugs, and prescription drugs, the abuse of tobacco and alcohol, and also, containing the case of underage children [104,105]. Generally speaken, most of these substances are misused to produce psychoactive effects without the supervision of medical professionals.

The United Nations Office for Drugs and Crime (UNODC) has defined new psychoactive substances (NPSs) as 'substances of abuse, either in a pure form or a preparation, that are not controlled by the 1961 Single Convention on Narcotic Drugs or the 1971 Convention on Psychotropic Substances, but which may pose a public health threat'. The term 'new' indicates that these substances have recently become available on the black market. These substances have been prominent in illicit drug market under labels such as 'legal highs', 'herbal highs', 'research chemicals', or 'spice'.

NPSs are a complex and inhomogeneous group of substances known as either designer or synthetic drugs [106–110] and are generally categorized into four classes, synthetic opioids, synthetic cannabinoids, synthetic cathinones, and stimulants [107]. Importantly, as these substances pose severe health risks, their use cannot be prevented without an in-depth understanding of their PK and PD properties [107]. The rapid growth at which new NPSs have emerged on the global market is unparalleled, as shown in Figure 14a, and UNODC estimated that at the peak in 2015, new NPSs appeared at a rate of at least one new substance per week [110,111]. Moreover, of all the NPSs detected up to December 2021 by UNODC, stimulants and synthetic cannabinoids can account for the most commonly abused NPSs (63%) (Figure 14b).

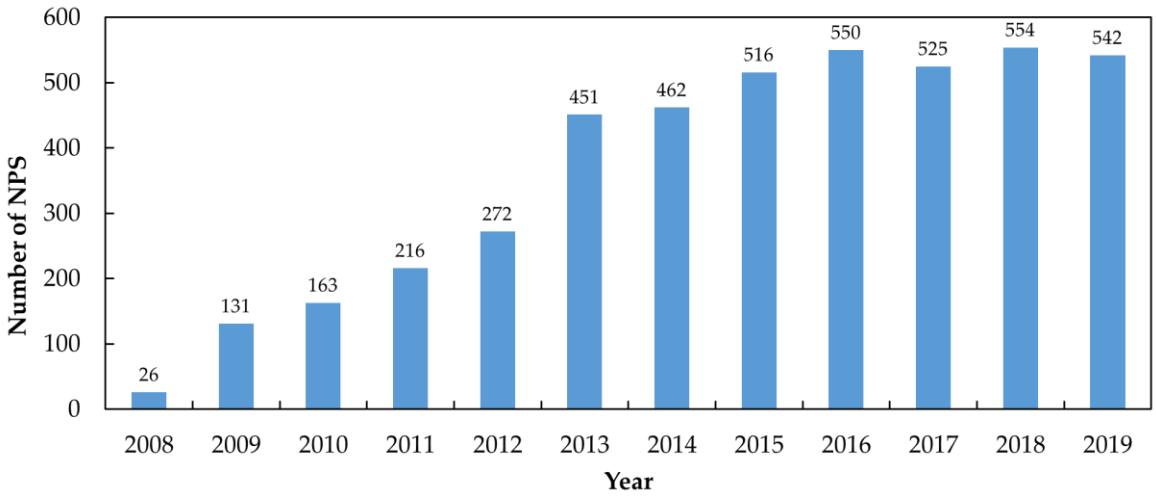

(a)

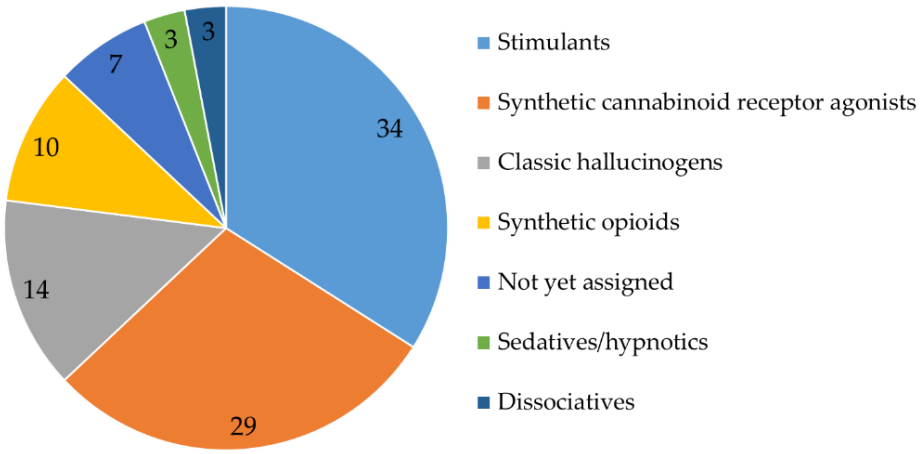

(b)

Figure 14. (a) The number of new psychoactive substances (NPSs) reported by the United Nations Office on Drugs and Crime (UNODC) from 2008 to 2019 and (b) The portion of synthetic NPSs categorized by seven effect groups. For data analysis in panel b, a total of 1,124 substances has been used, which were reported to the UNODC Early warning advisory (EWA) on NPSs by governments, laboratories, and partner organization up to December 2021. *Source: UNODC EWA on NPSs, 2020.

The number of seizures in the EU has been increasing since 2009, and approximately 1.1 million seizures were reported in 2019 alone, with misuse of cannabis products being the most common cause (Figure 15). [112]. Also, the European Drug Emergencies Network (Euro-DEN Plus network) in 2019 reported that cannabis presented in 26 % of all acute drug toxicity cases, usually with other psychoactive substances, in the network's 23 hospitals in 17 countries [112].

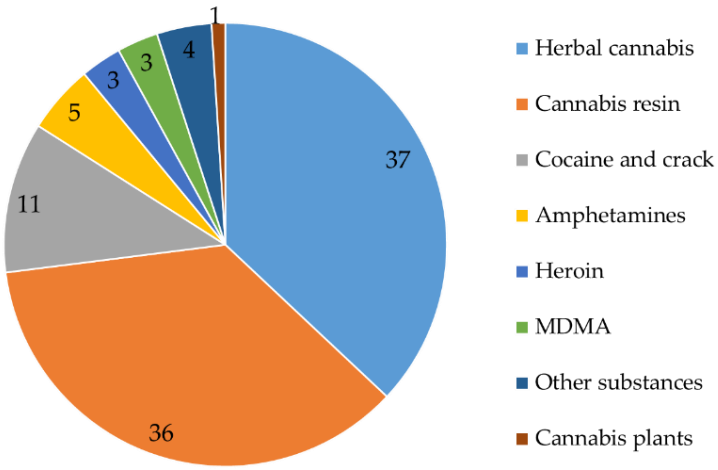

Figure 15. Percentage of drugs of abuse related to drug seizures and breakdowns (around 1.1 million cases) reported by the European Union (EU) in 2019 [112].

Furthermore, cannabis resin is, in general, more potent than before with a tetrahydrocannabinol content [THC; (-)-*trans*-Δ^9-THC as principal psychoactive constituent among multiple isomers of THC], almost twice as high as that of herbal cannabis (20–28%). Hence, the new forms of cannabis, including cannabis resin, should be carefully monitored to detect changes in cannabis problems and understand the influence of shits in their drug markets because the cases of first-time cannabis treatment entrants [112] .

With the increase in NPSs emergence and consumption, associated health risks liekwise increased. Most deaths directly linked to drug abuse involve intake of opioids, mainly heroin in conjunction with other drugs. However, stimulants like cocaine and amphetamines and, more recently, synthetic cannabinoids are now also becoming a major concern [110,112]. Based on data surveyed in the EU between 2015 and 2018 by the European Monitoring Centre for Drugs and Drug Addiction (EMCDDA), last year's prevalence of NPSs use among adults (aged 15–64) was ranged from 0.1% to 1.4%, with an average of 0.6% across the 15 countries monitored [112]. Furthermore, around 83 million (28.9%) of adults have used illicit drugs at least once in their lifetime. Importantly, the EMCDDA reported the latest data on European's drug situation that drug abuse occurred mainly among young adults since it was calculated that around 17.4 million young adults (aged 15-34) used drugs in the last year (16.9%) with about twice as many males (21.6%) as females (12.1%) [112,113].

The COVID-19 pandemic has been considered the worst global economic and social crisis since its first confirmation in early 2020. The world has experienced an unprecedented public health emergency affecting all aspects of daily life due to the introduction of mobility restrictions and social distancing measures [114]. Inevitably, COVID-19 related measures also affected the illegal drug markets from production, trafficking, and marketing to availability and demand [114,115]. However, drug markets have been resilient to the changes due to COVID-19 as crime groups quickly adopted to initial disruptions early in the pandemic. By early 2021, drug trafficking continuously showed the same pace as before the

pandemic or even at a higher pace [112,114]. Nonetheless, the global demand for synthetic drugs used in recreational settings appears to have decreased due to the closure of bars and nightclubs and the cancellation of music festivals, leading to a drop in wholesale prices of more than 20 percent [113,116]. On the other hand, COVID-19 has accelerated some drug trafficking patterns, such as larger shipment sizes and increasing use of private aircraft and waterway routes as a new contactless method for delivering drugs to end consumers, and it is of deep concern that these routes are likely to contribute to rising accessibility of NPSs in future [114].

1.4.2 Drug Control for Emerging Drugs of Concern

For the international classification and control of illegal drugs, all aspects of illegal drug classification and control are governed by three international drug control conventions: the Single Convention on Narcotic Drugs 1961, focusing on the control of cannabis, cocaine, and opioids; the Convention on Psychotropic Substances 1971 for the control of synthetic drugs such as 3,4-methylenedioxymethamphetamine (MDMA, ecstasy) and lysergic acid diethylamide (LSD); the Convention against Illicit Traffic in Narcotic Drugs and Psychotropic Substances 1988, targeting police suppression of illicit markets and control of drug precursor chemicals [108].

As an intimate connecting process of these three conventions, in a controlled substance under the 1961 and 1971 Conventions, its abuse potential and risks need to be reviewed by the World Health Organization (WHO) Experts Committee on Drug Dependence (ECDD). In genenral, if the Committee recommends control, the report is referred via the WHO Director-General to the UN Secretary-General and then to the Commission on Narcotic Drugs (CND). In the CND annual meeting, its voting member states determine whether a substance should be scheduled. Although the decision of the ECDD is determinative of scientific matters, the CND can take economic and other matters into consideration. Finally, once a substance is scheduled on the annex, each member state must regulate the substance at a minimum or higher level. Recommendations on control of precursor chemicals under the 1988 Convention are prepared by the International Narcotics Control Board and decided by a vote in the CND [108].

The Psychoactive Substances Act 2013 (NZ PSA 2013) in New Zealand is the most cited example of the establishment of a legal and regulated market. It proposed a pre-market approval regulatory regime in which product sponsors could legally manufacture and sell their products if they provided evidence that their products were low risk. However, a later amendment to the PSA finally forbade the approval of any new products, with some members arguing that the amended regulatory regime has become corresponding to a blanket ban [117,118].

Although some previous NPSs have been subordinate to international control under the UN Conventions (e.g., mephedrone in 2015; the synthetic cannabinoid ADB-FUBINACA in 2019), different access methods have been embraced by legal authority to control at the national level [110,119]. As an additional control channel, the national and regional drug

control have also adopted to be more flexible and immediate legislative after scheduling of specific substances. For instance, in the EU, a three-step legal framework of early warning, risk assessment, and fast track control measures have a tendancy to quickly detect, assess, and respond to public health threats caused by NPSs. The EMCDDA is in charge of the first two steps in the European-wide control measures [108], and at the end of 2020, it announced that it monitored around 830 NPSs with the Early warning system (EWS), 46 of which were first reported in 2020 [113].

1.4.3 Monitoring and Surveillance of Psychoactive Substances

Implementation of international and national regulations for drugs of abuse (DOA) control as described in Section 1.4.2 should be fulfilled by monitoring the scheduled substances and screening NPSs simultaneously in different matrices, which include blood, urine, hair, saliva, bile, and the products (powder, pill, or weed types) used in drug dealings. For drug identification aimed to control drug usage, a blood sample is mostly of choice to quantify and interpret the parent drug and its metabolites. In the analytical toxicology field, urine has been the preferred matrix as it is collected noninvasively in large volumes, normally has greater drug concentrations, and a longer detection window without any ethical and practical problems compared to the collection of a blood sample. Also, hair samples present particularities and some specific advantages in different judicial investigations, such as a more remarkable temporal window of drug detection, where the abuse that happened in previous months or even years can be detected [120]. Overall, the continually increasing number of NPSs with diversely effective forms has created many challenges for forensic and clinical toxicology research and its related fields, such as doping control [121,122].

In general, psychoactive substances lead to a high volume of distribution due to extensive accumulation in tissues, whose primary characteristic could be determined by the physicochemical properties of a drug (log *P* and pK_a), the type of tissue associated with the distribution (phospholipid pattern and lysosomal density), and the presence of functional groups in the molecular structure of a drug. Therefore, these factors are of critical importance in understanding drug mechanisms [123,124]. Accordingly, NPSs have lipophilic and highly protein-bound properties, which can help improve their efficacy and toxicity with accumulation and varying blood levels of a drug. In other words, their impact on humans could be exacerbated by their passage across cellular barriers, increasing with lipophilicity and following a high absorption rate through the stomach and intestines after the dosage.

Metabolism studies with the parent drug are compulsory since a drug is often metabolized. However, PK data for NPSs are mostly insufficient due to their fast circulation and rapid disappearance in illegal drug trafficking [122,125,126]. Ideally, a drug and its metabolites should be analyzed in various biosamples together so that the metabolic profile can be identified in human biosamples obtained from authentic cases. However, this case hardly occurrs and faces some ethical concerns. Instead, *in vitro* or non-human *in vivo* models have

been widely used to gain this information, but still, many projects aim at finding an appropriate model to precisely predict human drug metabolism [101,122].

A main concern in the analytical screening is the rapid, sensitive, and specific identification of NPSs in diverse biological samples without any previous knowledge and the need for these studies to be conducted as fast as possible. However, the chemical variety of NPSs, ranging from synthetic analogs of known illicit drugs or newly synthesized molecules to natural products with psychotropic activity, makes their identification extremely difficult in routine toxicological screening setups. As an alternative, immunoassays applicable to NPS detection were developed and provided an indication of the presence of a limited set of drugs [125,127]. Favretto *et al*. reported that only one manufacturer of immunoassays had developed commercial kit for NPSs, namely synthetic cannabinoids and bath salts (synthetic cathinones) [128]. In particular, newly developed NPSs are either difficult to detect via existing immunoassay methods or evade detection completely [121]. In addition, for post-mortem and human drug testing, broad selectivity is required, further limiting the utility of these assays [127].

Hyphenated mass spectrometry techniques have been utilized widely, particularly gas chromatography-mass spectrometry (GC-MS) and liquid chromatography-mass spectrometry (LC-MS). High-resolution and high-accuracy mass spectrometry (HRMS), a more recent MS technology, offers multi-target screening enabling the precise mass determination of a drug and its metabolites without references and with an accuracy of at least four decimal digits [128]. With HRMS, the accurate mass and structural details of an unknown drug can be studied, allowing determining the elemental composition of the molecule and then confirming the base of the specific fragmentation pathway through MS/MS [121,128]. Up to now, different types of technological solutions are available for HRMS namely, Sector mass spectrometer (mostly coupled to GC), Time-of-flight (TOF), Fourier transform ion cyclotron resonance (FT-ICR), Fourier transform orbitrap (FT Orbitrap), and Electrostatic traps. Recently, TOF and FT Orbitrap mass analyzers are the most widely used, especially for multi-screening of NPSs. Studies applying HRMS are frequently reported in various fields, including doping [129–132], metabolism studies [133,134], veterinary drug residues in food and wastewater [135], hair drug test [120,136], non-target analysis in groundwater [137], and organochlorine pesticides in multi-environmental matrices [138].

Alternatively, with the conventional approaches mentioned above, wastewater-based epidemiology (WBE), based on these precise analytical techniques, has been demonstrated as an additional tool for monitoring illicit drug use [139,140]. In 2022, the EMCDDA published the wastewater analysis of drugs – a European multi-city study that provided the mass loads of tfive stimulant drugs in wastewater samples at the population level (mg/1,000 head of population/day; daily, weekday, or weekend mean unit) [139]. Indeed, 37 cities in the EU have participated in at least five of the annual wastewater monitoring campaigns since 2011, and currently (2021), 75 cities in 17 countries participated. This project proceeds with the analysis of municipal wastewaters for drugs and their metabolic byproducts for

estimating the current local consumption, and the findings reveal geographical and temporal profiles of illicit drug use across European cities. In addition, some research investigated various substances more specified in the local or national perspective, such as cannabis in Canada and Washington State, USA [141], synthetic cathinones in different EU countries [142], and antibiotics [143] as well as COVID-19 [144] based on the concept of WBE. This information contributed to a better understanding of illicit drugs and their consumers. With these multi-purged approaches to control drugs of abuse, the actual spectrum of these illegal drugs consumed can be identified under hidden and complex circumstances.

1.5 Enabling Methodologies for Drug Metabolism Studies

This chapter describes some of the key technologies applied in this work.

1.5.1 Mass Spectrometry Imaging

Mass spectrometry imaging (MSI, also referred to as imaging mass spectrometry; IMS) has its origin in laser desorption/ionization approaches (laser microprobe), which provided the ability to focus a laser at a specific location and acquire a mass spectrum from the ions in the resulting plume [145]. In 1973, Franz Hillenkamp developed a high-performance laser microprobe mass spectrometer with 0.5 μm resolution [146], which was commercialized as one of the first laser desorption mass spectrometer, the LAMMA 500 being the initial model for the LAMMA 1000 in 1985 [147]. Based on this, matrix-assisted laser desorption (MALDI) was introduced as an ionization method for large molecules in 1988 by Franz Hillenkamp and Michael Karas using nicotinic acid as matrix agent and a frequency-quadrupled Neodymium-doped Yttrium aluminum garnet laser (Nd^{3+}:YAG) in their original work. Since then, it has become a popular analytical instrument for peptide and protein analysis [148]. Caprioli *et al*. [149] performed the first successful demonstration of MADLI imaging in 1997, and both, the pituitary gland and pancreas of rats were imagined using MALDI-MS [150,151]. Up to date, MSI technologies can be distinguished by the ionization methods [e.g. secondary ion mass spectrometry (SIMS), desorption electrospray ionization (DESI), MALDI, laser ablation electrospray ionization (LAESI); Figure 16] and HRMS detectors (e.g., FT-ICR, FT Orbitrap, TOF MS, tandem MS; described in Section 1.4.3) [145,152,153].

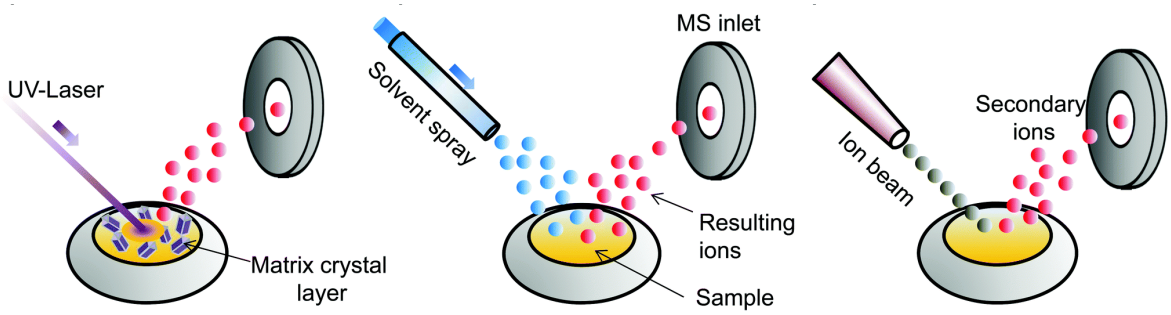

Figure 16. Three ionization techniques for mass spectrometry imaging (MSI); (a) matrix-assisted laser desorption ionization (MALDI), (b) desorption electrospray ionization (DESI), and (c) secondary ion mass spectrometry [152] (Reprinted from Ref. [152] with permission from CCC, inc. on behalf of the rightsholder Royal Society of Chemistry).

MSI has been proven to be a remarkable technique to visualize the distribution of diverse molecular species in a variety of sample matrices (e.g. human biological organs such as liver, brain, pancreas, and bones, zebrafish, and plant species with tissues such as leaves, stems, roots, flowers, or fruits, et cetera) [154–160]. It can simultaneously visualize various

molecule images such as metabolites, lipids, peptides, proteins, and glycans in a single experiment with no need for labeling and identify the analyte accurately based on its molecular mass and MS^2 fragmentation pattern without other measuring steps [161–163]. Therefore, MSI has received much attention from research related to drug discovery and development and PK studies since it can provide spatial information about a drug's localization via penetration or absorption inside the target organ. In particular, this distributional information is crucial in organs such as the brain or tumors where the plasma level does not precisely reflect the tissue concentration [162,164]. Furthermore, the MSI information of a drug plays a critical role in linking the metabolites to potential functionality [158]. As a possible example, considering the convincing analytical perspectives of MSI (e.g., high spatial resolution (20-100 µm) and high-resolution and accurate mass (< 5 ppm)), its application could discover novel metabolites and reveal a new metabolite identification, its localizations, and metabolic compartmentalization in human tissues at a glance [158,162].

One of the most important steps for analytical success is to develop optimal procedures of sample preparation, and especially for mass spectrometry, even subtle differences in sample integrity or molecular density can induce significant effects on the signal intensity and types of molecules being ionized, detected, and localized [163]. One of the most critical challenges is ensuring that the spatial distribution of molecules in measured MSI datasets is consistent with the actual distribution in *in vivo* conditions. For this, MSI is closely bound up with proper sample preparation strategies [163], and its exemplary workflow for the zebrafish larvae model is depicted in Figure 17.

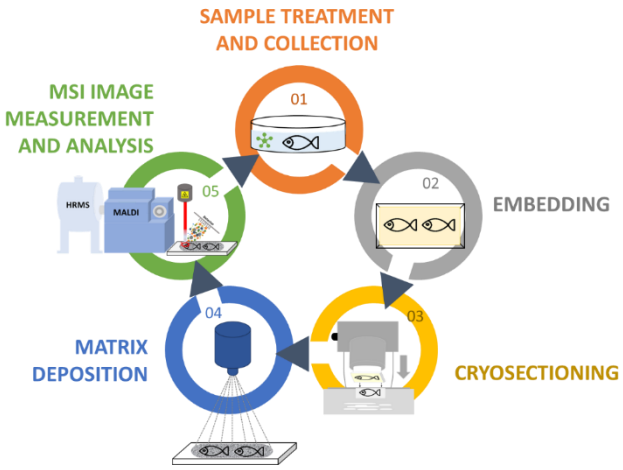

Figure 17. General workflow of sample preparation of zebrafish larvae for MSI applications.

With further advancements of crucial challenges such as ion suppression, sample throughput, homogeneity of matrix application, spatial resolution, analyte delocalization, and the availability of validated and standardized protocols [165], MSI has attained high-throughput capability, flexibility, and streamlined data analysis for the molecular species of interest and can be used even for a single cell as a matrix [163,166]. Furthermore, 3-dimensional visualization of MS images (3D-MSI) depicts the biological variability in entire tissue

samples beyond conventional 2D-MSI, and it can provide rich molecular contextual information about the investigated biological tissues [166–170]. Despite these improvments, MSI still has some unique challenges that need to be solved, e.g. improving the accuracy and precision of MSI quantification equivalent to LC-HRMSMS, an extension of MSI to other models/organisms, and overcoming the so-called 'batch effects' (occurring due todifferent experiment times, handlers, reagents, and instruments) [165,171,172].

1.5.2 Microinjection

In molecular biology and drug discovery, molecular screening at the single-cell level is crucial, which requires introducing target molecules into single cells, enabling cellular-function-targeted molecules to directly regulate cell development and their functions. For this, several technologies were developed, e.g., electroporation, viral vectors, gene gun, ultrasound, and micro-electromechanical system (MEMS)-based injection, as summarized in Table 3 [173–177]. Biological methods have been mostly used to transfer living carriers, usually viruses, which often cause side effects on cells without controling the number of substances transported. Also, the chemical method, especially when applied to large molecules, suffers from a penetration issue through cell membranes. Until now, physical methods have been commonly used, including microinjection, electroporation, ultrasound, and gene gun [173–177].

Table 3. The three principal approaches used for introducing chemical and biological agents into cells [173–177].

Type	Methods
Biological	○ Viral vector ○ Non-viral vector
Chemical	○ Diethylaminoethyl (DEAE)-dextran ○ Artificial lipids ○ Proteins ○ Other compounds (natural and synthetic)
Physical	○ Microinjection ○ Electroporation ○ Ultrasound ○ Gene gun ○ Other physical methods

Notably, microinjection is the most widely used physical method as it is most efficient in causing the least cell damage, and it is effective in delivering molecules freely from concerns about cell damage and cell viability in biomedicine, gene therapy, reproductive research, and other fields (Figure 18) [173,174]. In general, microinjection is described as the direct introduction of material with a micro/nano-volume into a cell using a small glass needle or micropipette [178]. It has been carried out for over 100 years since it was developed in conjunction with microscopy of microorganisms, embryos, plants, and animal cells at the beginning of the twentieth century [178–180].

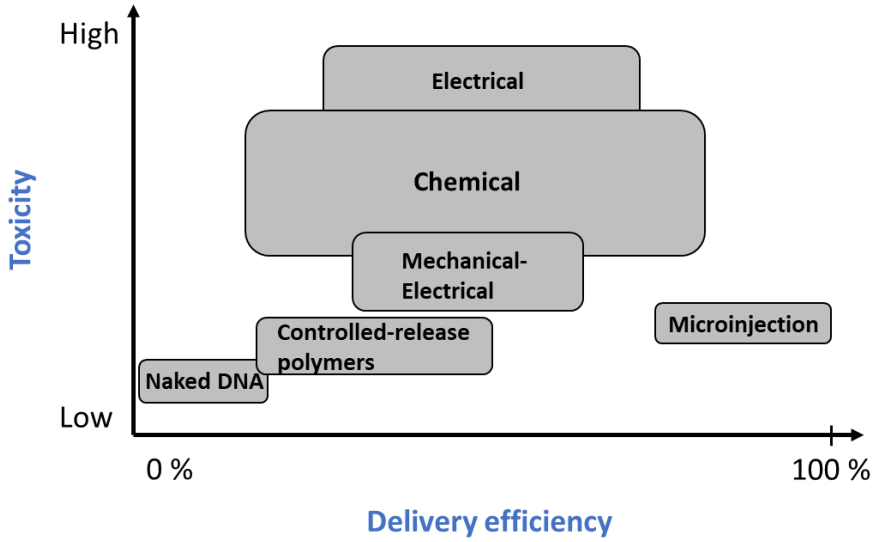

Figure 18. Comparison of the delivery efficiency and toxicity of leading technologies commonly used for delivering substances into cells [174].

Furthermore, microinjection has been intensively applied in the production of transgenic animals and for *in vitro* fertilization to engineer their genomes. In the most common application for these animal experiments, exogenous DNA or chemical/biological agent (e.g., sperm, protein, drug compounds, and viruses) is directly injected into the pronucleus of a fertilized egg using a microinjector system, and they are transmitted by its integration into the host cell genome [174,178,181]. Among various biological models, zebrafish has emerged as a promising model organism for developmental genetic studies as well as drug discovery, as mentioned in Section 1.3. In particular, molecular and genetic analysis of zebrafish embryogenesis mainly depend on the injection of xenobiotics into early zebrafish embryos [173,182] because microinjection technique could eliminate the problems of administration routes and natural barriers (i.e., chorion and embryonic envelope), which were caused by its physicochemical properties, such as solubility, volatility, and hydrophilic/lipophilic property [181]. Remarkably, a high-throughput robotic cell injection system has been developed in 2007 greatly enhancing the throughput of manipulation of zebrafish embryos [173,183,184]. Most recently, Chi *et al*. reviewed the recent advances in automated cell microinjection technologies, including the advantages and disadvantages of currently seven popular actuators [174,185].

1.5.3 Morpholino Oligonucleotide

Due to the lack of diverse tools for efficient and targeted mutagenesis in the early 2000s, morpholino antisense oligonucleotides (MOs) became the most popular tool for gene knockdown in various models, including frog, zebrafish, sea urchin, and chick [186–189]. Phillips *et al*. analyzed that the number of published studies using zebrafish for modelling genetic disease has been steadily growing (9% → 19%) at three-yearly intervals between September

2017 to April 2019, based on the data samples provided by the Zebrafish Information Network (ZFIN) [190]. Outstandingly, MOs for reverse genetic approaches were mainly employed in this survey, and the utilization of TALENS and targeting induced local lesions in genomes (TILLINGs) have been significantly arising likewise. Significantly, the number of published reverse genetic approaches used for zebrafish genetic disease models grew 4-fold higher than forward metagenesis screen approaches from 2017 to 2019 in total zebrafish genetic disease models [190].

MOs are synthesized short oligonucleotides (generally oligomers of around 25 morpholine bases) that are typically injected into embryos at the 1-cell stage, bind complementary target mRNAs, and prevent their translation or splicing. In principle, antisense MOs inhibit the interactions of macromolecules with mRNA by base-pairing with the targeted mRNA in a complementary fashion, thus preventing initiation of complex read-through or modifying splicing in cells ranging from bacterial species to human, as described in Figure 19 [189,191–193]. The most significant advantage of this technique is that it can be used easily and rapidly to assess the function of a specific gene during the early Jenni [68]development of both *in vitro* and *in vivo* models [189].

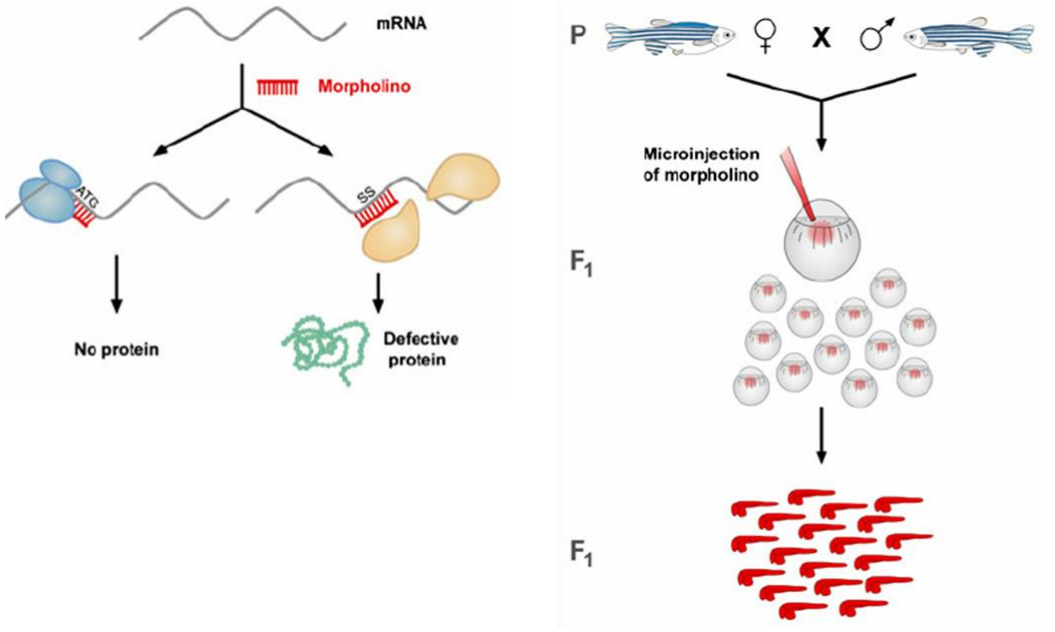

(a) (b)

Figure 19. (a) Two mechanisms of gene knockdown by Morpholino antisense nucleotides (MOs) injection and (b) A general overview of the generation of knockdown phenotypes in zebrafish by MO injection. *Translation blocking is designed for mRNA or in the coding region close to anti-thymocyte globulin (ATG); Splice blocking is designed to splice site (SS) junction [189] (Reprinted from [189] with permission from Springer Nature).

With their ability to phenocopy well-characterized mutants, MOs have become a standard and efficient tool for developmental biologists to manipulate gene expression in embryos like zebrafish and *Xenopus* sp. [186,188,191,194]. However, as concerns arose about the off-target effects of MOs, Eisen *et al*. first published guidelines in 2008 in order to assist scientists in designing and interpreting MOs-related experiments. These guidelines cover the design of controls, the effectiveness of gene knockdown, off-target effects of MOs, and appropriate controls [195]. The guidelines were improved in 2017 by Stainier *et al*. [186,195].

For studying human disease, many studies with gene-targeting tools have been accomplished for screening potential therapies for common genetic diseases such as cancer, cardiovascular disorders, kidney disorders, and cystic fibrosis in zebrafish models [190,196–198]. The ease with which zebrafish can be subject to enhancing an underlying genetic condition is directly reflected in the fundamental research performed indispensably before clinical trials [190].

1.6 Outline of This Work

In this work, the zebrafish larvae model is used to study the metabolism of three different drugs. The applications of the three crucial methodologies are performed for drug metabolism studies in the zebrafish larvae model. These applied methodologies include microinjection, morpholino oligonucleotides, and mass spectrometry imaging. To date, these applications pose still a challenge in the zebrafish larvae model despite many practical uses. Therefore, these techniques were intensively optimized in the zebrafish larvae model for predicting human drug metabolism. Two emerging new synthetic cannabinoids (SCs), 7′*N*-5F-ADB and 4F-MDMB-BINACA, and the opioid antagonist naloxone being widely used to reverse the effects of an opoid overdose, were studied as tools to obtain a first proof-of-concept for the applicability of zebrafish larvae in such studies being part of DMPK.

The first part investigates a new approach employing various administration routes for drug exposure to zebrafish larvae to enhance metabolite identification, which can be performed through direct microinjection of the studied drug into three individual vital organs, such as the caudal vein, heart ventricle, and hindbrain. In particular, the distribution of the parent drug 7′*N*-5F-ADB and its metabolites are visualized inside the zebrafish larval body using matrix-assisted laser desorption/ionization (MALDI)-MSI as a state-of-the-art technology allowing us to localize the spatial distributions of untargeted multiple molecules in biological tissues with a labeling free procedure. For the metabolic comparison to human and zebrafish larvae, the *in vitro* HepaRG model is also explored due to its characteristic activities of cytochrome P450 biotransformation enzymes, phase II enzymes, and several transporters similarly to human.

The second part focuses on the metabolism of 4F-MDMB-BINACA in zebrafish larvae and spatial distribution inside the larval body relying on the protocol optimized in the first part. Notably, for understanding the role of two endocannabinoid receptors (type 1 and type 2; CB1 and CB2) on the metabolism of two SCs (7′*N*-5F-ADB and 4F-MDMB-BINACA), the genetic modification of these receptors via morpholino oligonucleotides as an antisense gene-knockdown is introduced. The metabolic profiles of these two drugs using microinjected wild-type zebrafish larvae and each receptor-deficient mutant larvae are explored, and these findings are compared to data from human biosamples and previous metabolic study results of the larvae treated by direct microinjections studied in the first part.

The final part is devoted to investigating the optimization of mass spectrometry imaging for zebrafish larvae to characterize the distribution of the opioid antagonist naloxone and its metabolites. Moreover, with this improved methodology, quantification of naloxone using a calibration curve of naloxone-spikedin zebrafish larvae homogenates is undertaken. The generated spatial distributional images are examined to evaluate the consistency with data from liquid chromatography-high resolution tandem mass spectrometry as a well-established analytical system for the quantification and qualification of molecules.

1.7 Bibliography

1. Drews, J. Drug Discovery: A Historical Perspective **2000**, *287*, 1960–1964, doi:10.1126/science.287.5460.1960.
2. Rotella, D.P. The Critical Role of Organic Chemistry in Drug Discovery. *ACS Chem. Neurosci.* **2016**, *7*, 1315–1316, doi:10.1021/acschemneuro.6b00280.
3. Kiriiri, G.K.; Njogu, P.M.; Mwangi, A.N. Exploring different approaches to improve the success of drug discovery and development projects: a review. *Futur J Pharm Sci* **2020**, *6*, 1960, doi:10.1186/s43094-020-00047-9.
4. Gaynes, R. The Discovery of Penicillin—New Insights After More Than 75 Years of Clinical Use. *Emerg. Infect. Dis.* **2017**, *23*, 849–853, doi:10.3201/eid2305.161556.
5. Lewis, K. Antibiotics: Recover the lost art of drug discovery. *Nature* **2012**, *485*, 439–440, doi:10.1038/485439a.
6. Shen, B. A New Golden Age of Natural Products Drug Discovery. *Cell* **2015**, *163*, 1297–1300, doi:10.1016/j.cell.2015.11.031.
7. Marx, U.; Andersson, T.B.; Bahinski, A.; Beilmann, M.; Beken, S.; Cassee, F.R.; Cirit, M.; Daneshian, M.; Fitzpatrick, S.; Frey, O.; et al. Biology-inspired microphysiological system approaches to solve the prediction dilemma of substance testing. *ALTEX* **2016**, *33*, 272–321, doi:10.14573/altex.1603161.
8. Yildirim, O.; Gottwald, M.; Schüler, P.; Michel, M.C. Opportunities and Challenges for Drug Development: Public-Private Partnerships, Adaptive Designs and Big Data. *Front. Pharmacol.* **2016**, *7*, 461, doi:10.3389/fphar.2016.00461.
9. Scannell, J.W.; Blanckley, A.; Boldon, H.; Warrington, B. Diagnosing the decline in pharmaceutical R&D efficiency. *Nat. Rev. Drug Discov.* **2012**, *11*, 191–200, doi:10.1038/nrd3681.
10. Deore, A.B.; Dhumane, J.R.; Wagh, R.; Sonawane, R. The Stages of Drug Discovery and Development Process. *Asian J Pharm Res Dev* **2019**, *7*, 62–67, doi:10.22270/ajprd.v7i6.616.
11. Chandrani Gunaratna. Gunaratna_drug metabolism and PK_Part_I **2000**, *19*, 17–23.
12. Smith, C.G.; O'Donnell, J. *The process of new drug discovery and development*, 2nd ed.; Informa Healthcare: New York, 2006, ISBN 9780849327797.
13. Bonam, S.R.; Sekar, M.; Guntuku, G.S.; Nerella, S.G.; Pawar A, K.M.; Challa, S.R.; Eswara, G.K.; Mettu, S. Role of pharmaceutical sciences in future drug discovery. *Future Drug Discovery* **2021**, *3*, 484, doi:10.4155/fdd-2021-0005.
14. Gad, S.C. *Drug discovery handbook;* Wiley-Interscience: Hoboken N.J., 2005, ISBN 0471213845.
15. DiMasi, J.A.; Hansen, R.W.; Grabowski, H.G. The price of innovation: new estimates of drug development costs. *Journal of Health Economics* **2003**, *22*, 151–185, doi:10.1016/S0167-6296(02)00126-1.
16. Gashaw, I.; Ellinghaus, P.; Sommer, A.; Asadullah, K. What makes a good drug target? *Drug Discov. Today* **2011**, *16*, 1037–1043, doi:10.1016/j.drudis.2011.09.007.

17. Atanasov, A.G.; Zotchev, S.B.; Dirsch, V.M.; Supuran, C.T. Natural products in drug discovery: advances and opportunities. *Nat. Rev. Drug Discov.* **2021**, *20*, 200–216, doi:10.1038/s41573-020-00114-z.
18. Caroline Horizny. The Drug Discovery Process. Available online: https://www.taconic.com/taconic-insights/quality/drug-development-process.html.
19. Urquhart, L. FDA new drug approvals in Q3 2021. *Nat. Rev. Drug Discov.* **2021**, *20*, 807, doi:10.1038/d41573-021-00175-8.
20. Mullard, A. 2020 FDA drug approvals. *Nat. Rev. Drug Discov.* **2021**, *20*, 85–90, doi:10.1038/d41573-021-00002-0.
21. Hirschler, B. New drug approvals fall to six-year low in 2016. *REUTERS [Online]*, 2017, January 2. Available online: https://www.reuters.com/article/us-pharmaceuticals-approvals-idUSKBN14M08R.
22. Toich, L. FDA Drug Approvals Drop in 2016. *Pharmacy Times [Online]*, 2017, January 6. Available online: https://www.pharmacytimes.com/view/fda-drug-approvals-drop-in-2016.
23. Dowden, H.; Munro, J. Trends in clinical success rates and therapeutic focus. *Nat. Rev. Drug Discov.* **2019**, *18*, 495–496, doi:10.1038/d41573-019-00074-z.
24. Swinney, D.C.; Anthony, J. How were new medicines discovered? *Nat. Rev. Drug Discov.* **2011**, *10*, 507–519, doi:10.1038/nrd3480.
25. DiMasi, J.A.; Faden, L.B. Competitiveness in follow-on drug R&D: a race or imitation? *Nat. Rev. Drug Discov.* **2011**, *10*, 23–27, doi:10.1038/nrd3296.
26. Moffat, J.G.; Vincent, F.; Lee, J.A.; Eder, J.; Prunotto, M. Opportunities and challenges in phenotypic drug discovery: an industry perspective. *Nat. Rev. Drug Discov.* **2017**, *16*, 531–543, doi:10.1038/nrd.2017.111.
27. Hughes, J.P.; Rees, S.; Kalindjian, S.B.; Philpott, K.L. Principles of early drug discovery. *Br. J. Pharmacol.* **2011**, *162*, 1239–1249, doi:10.1111/j.1476-5381.2010.01127.x.
28. Harrison, R.K. Phase II and phase III failures: 2013-2015. *Nat. Rev. Drug Discov.* **2016**, *15*, 817–818, doi:10.1038/nrd.2016.184.
29. van Norman, G.A. Phase II Trials in Drug Development and Adaptive Trial Design. *JACC Basic Transl. Sci.* **2019**, *4*, 428–437, doi:10.1016/j.jacbts.2019.02.005.
30. Ballard, P.; Brassil, P.; Bui, K.H.; Dolgos, H.; Petersson, C.; Tunek, A.; Webborn, P.J.H. Metabolism and pharmacokinetic optimization strategies in drug discovery. *Drug Discovery and Development*; Elsevier, 2013; pp 135–155, ISBN 9780702042997.
31. Müller, M.; Müller-Zellenberg, U.; Hochhaus, G.; Derendorf, H. Current concepts in pharmacokinetics and their implications for clinical medicine **2001**, *15/16*, 566–572.
32. Sinha, S.; Vohora, D. Drug Discovery and Development. *Pharmaceutical Medicine and Translational Clinical Research*; Elsevier, 2018; pp 19–32, ISBN 9780128021033.
33. Zhang, D.; Luo, G.; Ding, X.; Lu, C. Preclinical experimental models of drug metabolism and disposition in drug discovery and development. *Acta Pharmaceutica Sinica B* **2012**, *2*, 549–561, doi:10.1016/j.apsb.2012.10.004.

34. Baillie, T.A. Metabolism and toxicity of drugs. Two decades of progress in industrial drug metabolism. *Chem. Res. Toxicol.* **2008**, *21*, 129–137, doi:10.1021/tx7002273.
35. Wan, H. What ADME tests should be conducted for preclinical studies? *ADMET DMPK* **2013**, *1*, doi:10.5599/admet.1.3.9.
36. Kola, I.; Landis, J. Can the pharmaceutical industry reduce attrition rates? *Nat. Rev. Drug Discov.* **2004**, *3*, 711–715, doi:10.1038/nrd1470.
37. Hodgson, J. ADMET—turning chemicals into drugs: Rapidly resolving the pharmacokinetic and toxicological properties of drug candidates remains a key challenge for drug developers. **2001**, *19*, 722–726.
38. Kennedy, T. Managing the drug discovery/development interface **1997**, *2*, 436–444.
39. Kassel, D.B. Applications of high-throughput ADME in drug discovery. *Curr. Opin. Chem. Biol.* **2004**, *8*, 339–345, doi:10.1016/j.cbpa.2004.04.015.
40. Data Bridge Market Research Private Ltd. *Global ADME Toxicology Testing Market – Industry Trends and Forecast to 2027;* Data Bridge Market Research Private Ltd.
41. Bhusnure, O.G.; Mane, J.M.; Gholve, S.B. Drug Target Screening and its Validation by Zebrafish as a Novel Tool. *Pharm Anal Acta* **2015**, *6*, doi:10.4172/2153-2435.1000426.
42. Balcombe, J. Laboratory rodent welfare: thinking outside the cage. *J. Appl. Anim. Welf. Sci.* **2010**, *13*, 77–88, doi:10.1080/10888700903372168.
43. European Commission. REPORT FROM THE COMMISSION TO THE EUROPEAN PARLIAMENT AND THE COUNCIL: 2019 report on the statistics on the use of animals for scientific purposes in the Member States of the European Union in 2015-2017 **2020**.
44. Bundesinstitut für Risikobewertung. *Verwendung von Versuchstieren im Jahr 2020 (Use of experimental animals in 2020)*, 2021.
45. Deutsches Primatenzentrum GmbH, Leibniz-Institut für Primatenforschung. *Figures of animals used for scientific purposes in Germany*.
46. Hornberg, J.J.; Laursen, M.; Brenden, N.; Persson, M.; Thougaard, A.V.; Toft, D.B.; Mow, T. Exploratory toxicology as an integrated part of drug discovery. Part I: Why and how. *Drug Discov. Today* **2014**, *19*, 1131–1136, doi:10.1016/j.drudis.2013.12.008.
47. Macrae, C.A.; Peterson, R.T. Zebrafish as tools for drug discovery. *Nat. Rev. Drug Discov.* **2015**, *14*, 721–731, doi:10.1038/nrd4627.
48. Tannenbaum, J.; Bennett, B.T. Russell and Burch_3Rs_then and now_Tannenbaum_2015 **2015**, *54*, 120–132.
49. Zon, L.I.; Peterson, R.T. In vivo drug discovery in the zebrafish. *Nat. Rev. Drug Discov.* **2005**, *4*, 35–44, doi:10.1038/nrd1606.
50. W.M.S. Russell; R.L. Burch. The Principles of Humane Experimental Technique. *Medical Journal of Australia* **1960**, *1*, 500, doi:10.5694/j.1326-5377.1960.tb73127.x.
51. Zurlo, J.; Rudacille, D.; Goldberg, A.M. The three Rs: the way forward. **1996**, *104*, 878–880.
52. *Animal experimentation*: *Working towards a paradigm change;* Herrmann, K., Ed.; Brill: Leiden, Boston, 2019, ISBN 9789004391192.

53. Hubrecht, R.C.; Carter, E. The 3Rs and Humane Experimental Technique: Implementing Change. *Animals (Basel)* **2019**, *9*, doi:10.3390/ani9100754.
54. Guhad, F. Introduction to the 3Rs (Refinement, Reduction and Replacement) **2005**, *44*, 58–59.
55. Stephens, M.L.; Goldberg, A.M.; Rowan, A.N. The First Forty Years of the Alternatives Approach: Refining, Reducing, and Replacing the Use of Laboratory Animals **2001**, *The State of the Animals*, 121–135.
56. Scholz, S.; Sela, E.; Blaha, L.; Braunbeck, T.; Galay-Burgos, M.; García-Franco, M.; Guinea, J.; Klüver, N.; Schirmer, K.; Tanneberger, K.; et al. A European perspective on alternatives to animal testing for environmental hazard identification and risk assessment. *Regul. Toxicol. Pharmacol.* **2013**, *67*, 506–530, doi:10.1016/j.yrtph.2013.10.003.
57. Natalie Burden; Kathryn Chapman; Fiona Sewell; Vicky Robinson. Pioneering Better Science through the 3Rs: An Introduction to the National Centre for the Replacement, Refinement, and Reduction of Animals in Research (NC3Rs) **2015**, *54*, 198–208.
58. Kim, T.-W.; Che, J.-H.; Yun, J.-W. Use of stem cells as alternative methods to animal experimentation in predictive toxicology. *Regul. Toxicol. Pharmacol.* **2019**, *105*, 15–29, doi:10.1016/j.yrtph.2019.03.016.
59. Langhans, S.A. Three-Dimensional in Vitro Cell Culture Models in Drug Discovery and Drug Repositioning. *Front. Pharmacol.* **2018**, *9*, 6, doi:10.3389/fphar.2018.00006.
60. Kuna, L.; Bozic, I.; Kizivat, T.; Bojanic, K.; Mrso, M.; Kralj, E.; Smolic, R.; Wu, G.Y.; Smolic, M. Models of Drug Induced Liver Injury (DILI) - Current Issues and Future Perspectives. *Curr. Drug Metab.* **2018**, *19*, 830–838, doi:10.2174/1389200219666180523095355.
61. Zscheppang, K.; Berg, J.; Hedtrich, S.; Verheyen, L.; Wagner, D.E.; Suttorp, N.; Hippenstiel, S.; Hocke, A.C. Human Pulmonary 3D Models For Translational Research. *Biotechnol. J.* **2018**, *13*, doi:10.1002/biot.201700341.
62. Weinhart, M.; Hocke, A.; Hippenstiel, S.; Kurreck, J.; Hedtrich, S. 3D organ models-Revolution in pharmacological research? *Pharmacol. Res.* **2019**, *139*, 446–451, doi:10.1016/j.phrs.2018.11.002.
63. Brogi, S.; Ramalho, T.C.; Kuca, K.; Medina-Franco, J.L.; Valko, M. Editorial: In silico Methods for Drug Design and Discovery. *Front. Chem.* **2020**, *8*, 612, doi:10.3389/fchem.2020.00612.
64. Kar, S.; Leszczynski, J. Exploration of Computational Approaches to Predict the Toxicity of Chemical Mixtures. *Toxics* **2019**, *7*, doi:10.3390/toxics7010015.
65. Wu, Y.; Wang, G. Machine Learning Based Toxicity Prediction: From Chemical Structural Description to Transcriptome Analysis. *Int. J. Mol. Sci.* **2018**, *19*, doi:10.3390/ijms19082358.
66. Bissig, K.-D.; Han, W.; Barzi, M.; Kovalchuk, N.; Ding, L.; Fan, X.; Pankowicz, F.P.; Zhang, Q.-Y.; Ding, X. P450-Humanized and Human Liver Chimeric Mouse Models for Studying Xenobiotic Metabolism and Toxicity. *Drug Metab. Dispos.* **2018**, *46*, 1734–1744, doi:10.1124/dmd.118.083303.

67. O'Reilly, L.P.; Luke, C.J.; Perlmutter, D.H.; Silverman, G.A.; Pak, S.C. C. elegans in high-throughput drug discovery. *Adv. Drug Deliv. Rev.* **2014**, *69-70*, 247–253, doi:10.1016/j.addr.2013.12.001.
68. Cassar, S.; Adatto, I.; Freeman, J.L.; Gamse, J.T.; Iturria, I.; Lawrence, C.; Muriana, A.; Peterson, R.T.; van Cruchten, S.; Zon, L.I. Use of Zebrafish in Drug Discovery Toxicology. *Chem. Res. Toxicol.* **2020**, *33*, 95–118, doi:10.1021/acs.chemrestox.9b00335.
69. Miyawaki, I. Application of zebrafish to safety evaluation in drug discovery **2020**, *33*, 197–210.
70. Katoch, S.; Patial, V. Zebrafish: An emerging model system to study liver diseases and related drug discovery. *J. Appl. Toxicol.* **2021**, *41*, 33–51, doi:10.1002/jat.4031.
71. Lin, C.-Y.; Chiang, C.-Y.; Tsai, H.-J. Zebrafish and Medaka: new model organisms for modern biomedical research. *J. Biomed. Sci.* **2016**, *23*, 19, doi:10.1186/s12929-016-0236-5.
72. Ribas, L.; Piferrer, F. The zebrafish (Danio rerio) as a model organism, with emphasis on applications for finfish aquaculture research. *Rev Aquacult* **2014**, *6*, 209–240, doi:10.1111/raq.12041.
73. Teame, T.; Zhang, Z.; Ran, C.; Zhang, H.; Yang, Y.; Ding, Q.; Xie, M.; Gao, C.; Ye, Y.; Duan, M.; et al. The use of zebrafish (Danio rerio) as biomedical models. *Anim. Front.* **2019**, *9*, 68–77, doi:10.1093/af/vfz020.
74. Letrado, P.; Miguel, I. de; Lamberto, I.; Díez-Martínez, R.; Oyarzabal, J. Zebrafish: Speeding Up the Cancer Drug Discovery Process. *Cancer Res.* **2018**, *78*, 6048–6058, doi:10.1158/0008-5472.CAN-18-1029.
75. Bootorabi, F.; Manouchehri, H.; Changizi, R.; Barker, H.; Palazzo, E.; Saltari, A.; Parikka, M.; Pincelli, C.; Aspatwar, A. Zebrafish as a Model Organism for the Development of Drugs for Skin Cancer. *Int. J. Mol. Sci.* **2017**, *18*, doi:10.3390/ijms18071550.
76. Villacrez, M.; Hellman, K.; Ono, T.; Sugihara, Y.; Rezeli, M.; Ek, F.; Marko-Varga, G.; Olsson, R. Evaluation of Drug Exposure and Metabolism in Locust and Zebrafish Brains Using Mass Spectrometry Imaging. *ACS Chem. Neurosci.* **2018**, *9*, 1994–2000, doi:10.1021/acschemneuro.7b00459.
77. Pitchai, A.; Rajaretinam, R.K.; Freeman, J.L. Zebrafish as an Emerging Model for Bioassay-Guided Natural Product Drug Discovery for Neurological Disorders. *Medicines (Basel)* **2019**, *6*, doi:10.3390/medicines6020061.
78. Lawrence, C.; Eisen, J.S.; Varga, Z.M. Husbandry and Health Program Survey Synopsis. *Zebrafish* **2016**, *13 Suppl 1*, S5-7, doi:10.1089/zeb.2016.1309.
79. Rennekamp, A.J.; Peterson, R.T. 15 years of zebrafish chemical screening. *Curr. Opin. Chem. Biol.* **2015**, *24*, 58–70, doi:10.1016/j.cbpa.2014.10.025.
80. van Wijk, R.C.; Krekels, E.H.J.; Hankemeier, T.; Spaink, H.P.; van der Graaf, P.H. Systems pharmacology of hepatic metabolism in zebrafish larvae. *Drug Discovery Today: Disease Models* **2016**, *22*, 27–34, doi:10.1016/j.ddmod.2017.04.003.
81. Tal, T.; Yaghoobi, B.; Lein, P.J. Translational Toxicology in Zebrafish. *Curr. Opin. Toxicol.* **2020**, *23-24*, 56–66, doi:10.1016/j.cotox.2020.05.004.

82. Zhang, T.; Peterson, R.T. Zebrafish as a Platform for Drug Screening. *The Zebrafish in Biomedical Research*; Elsevier, 2020; pp 659–675, ISBN 9780128124314.
83. Zhang, X.; Li, C.; Gong, Z. Development of a convenient in vivo hepatotoxin assay using a transgenic zebrafish line with liver-specific DsRed expression. *PLoS One* **2014**, *9*, e91874, doi:10.1371/journal.pone.0091874.
84. Howe, K.; Clark, M.D.; Torroja, C.F.; Torrance, J.; Berthelot, C.; Muffato, M.; Collins, J.E.; Humphray, S.; McLaren, K.; Matthews, L.; et al. The zebrafish reference genome sequence and its relationship to the human genome. *Nature* **2013**, *496*, 498–503, doi:10.1038/nature12111.
85. Peterson, R.T.; Macrae, C.A. Systematic approaches to toxicology in the zebrafish. *Annu. Rev. Pharmacol. Toxicol.* **2012**, *52*, 433–453, doi:10.1146/annurev-pharmtox-010611-134751.
86. Goessling, W.; North, T.E.; Lord, A.M.; Ceol, C.; Lee, S.; Weidinger, G.; Bourque, C.; Strijbosch, R.; Haramis, A.-P.; Puder, M.; et al. APC mutant zebrafish uncover a changing temporal requirement for wnt signaling in liver development. *Dev. Biol.* **2008**, *320*, 161–174, doi:10.1016/j.ydbio.2008.05.526.
87. Grech, A.; Tebby, C.; Brochot, C.; Bois, F.Y.; Bado-Nilles, A.; Dorne, J.-L.; Quignot, N.; Beaudouin, R. Generic physiologically-based toxicokinetic modelling for fish: Integration of environmental factors and species variability. *Sci. Total Environ.* **2019**, *651*, 516–531, doi:10.1016/j.scitotenv.2018.09.163.
88. Choi, T.-Y.; Choi, T.-I.; Lee, Y.-R.; Choe, S.-K.; Kim, C.-H. Zebrafish as an animal model for biomedical research. *Exp. Mol. Med.* **2021**, *53*, 310–317, doi:10.1038/s12276-021-00571-5.
89. Cutler, C.; Multani, P.; Robbins, D.; Kim, H.T.; Le, T.; Hoggatt, J.; Pelus, L.M.; Desponts, C.; Chen, Y.-B.; Rezner, B.; et al. Prostaglandin-modulated umbilical cord blood hematopoietic stem cell transplantation. *Blood* **2013**, *122*, 3074–3081, doi:10.1182/blood-2013-05-503177.
90. Li, D.; March, M.E.; Gutierrez-Uzquiza, A.; Kao, C.; Seiler, C.; Pinto, E.; Matsuoka, L.S.; Battig, M.R.; Bhoj, E.J.; Wenger, T.L.; et al. ARAF recurrent mutation causes central conducting lymphatic anomaly treatable with a MEK inhibitor. *Nat. Med.* **2019**, *25*, 1116–1122, doi:10.1038/s41591-019-0479-2.
91. Mandelbaum, J.; Shestopalov, I.A.; Henderson, R.E.; Chau, N.G.; Knoechel, B.; Wick, M.J.; Zon, L.I. Zebrafish blastomere screen identifies retinoic acid suppression of MYB in adenoid cystic carcinoma. *J. Exp. Med.* **2018**, *215*, 2673–2685, doi:10.1084/jem.20180939.
92. North, T.E.; Goessling, W.; Walkley, C.R.; Lengerke, C.; Kopani, K.R.; Lord, A.M.; Weber, G.J.; Bowman, T.V.; Jang, I.-H.; Grosser, T.; et al. Prostaglandin E2 regulates vertebrate haematopoietic stem cell homeostasis. *Nature* **2007**, *447*, 1007–1011, doi:10.1038/nature05883.
93. Ryals, M.; Morell, R.J.; Martin, D.; Boger, E.T.; Wu, P.; Raible, D.W.; Cunningham, L.L. The Inner Ear Heat Shock Transcriptional Signature Identifies Compounds That Protect

Against Aminoglycoside Ototoxicity. *Front. Cell. Neurosci.* **2018**, *12*, 445, doi:10.3389/fncel.2018.00445.

94. White, R.M.; Cech, J.; Ratanasirintrawoot, S.; Lin, C.Y.; Rahl, P.B.; Burke, C.J.; Langdon, E.; Tomlinson, M.L.; Mosher, J.; Kaufman, C.; et al. DHODH modulates transcriptional elongation in the neural crest and melanoma. *Nature* **2011**, *471*, 518–522, doi:10.1038/nature09882.
95. Yu, P.B.; Hong, C.C.; Sachidanandan, C.; Babitt, J.L.; Deng, D.Y.; Hoyng, S.A.; Lin, H.Y.; Bloch, K.D.; Peterson, R.T. Dorsomorphin inhibits BMP signals required for embryogenesis and iron metabolism. *Nat. Chem. Biol.* **2008**, *4*, 33–41, doi:10.1038/nchembio.2007.54.
96. Poon, K.L.; Wang, X.; Ng, A.S.; Goh, W.H.; McGinnis, C.; Fowler, S.; Carney, T.J.; Wang, H.; Ingham, P.W. Humanizing the zebrafish liver shifts drug metabolic profiles and improves pharmacokinetics of CYP3A4 substrates. *Arch. Toxicol.* **2017**, *91*, 1187–1197, doi:10.1007/s00204-016-1789-5.
97. He, J.-H.; Gao, J.-M.; Huang, C.-J.; Li, C.-Q. Zebrafish models for assessing developmental and reproductive toxicity. *Neurotoxicol. Teratol.* **2014**, *42*, 35–42, doi:10.1016/j.ntt.2014.01.006.
98. Diao, X.; Huestis, M.A. New Synthetic Cannabinoids Metabolism and Strategies to Best Identify Optimal Marker Metabolites. *Front. Chem.* **2019**, *7*, 109, doi:10.3389/fchem.2019.00109.
99. Richter, L.H.J.; Herrmann, J.; Andreas, A.; Park, Y.M.; Wagmann, L.; Flockerzi, V.; Müller, R.; Meyer, M.R. Tools for studying the metabolism of new psychoactive substances for toxicological screening purposes - A comparative study using pooled human liver S9, HepaRG cells, and zebrafish larvae. *Toxicol. Lett.* **2019**, *305*, 73–80, doi:10.1016/j.toxlet.2019.01.010.
100. Gampfer, T.M.; Wagmann, L.; Park, Y.M.; Cannaert, A.; Herrmann, J.; Fischmann, S.; Westphal, F.; Müller, R.; Stove, C.P.; Meyer, M.R. Toxicokinetics and toxicodynamics of the fentanyl homologs cyclopropanoyl-1-benzyl-4′-fluoro-4-anilinopiperidine and furanoyl-1-benzyl-4-anilinopiperidine. *Arch. Toxicol.* **2020**, *94*, 2009–2025, doi:10.1007/s00204-020-02726-1.
101. Wagmann, L.; Frankenfeld, F.; Park, Y.M.; Herrmann, J.; Fischmann, S.; Westphal, F.; Müller, R.; Flockerzi, V.; Meyer, M.R. How to Study the Metabolism of New Psychoactive Substances for the Purpose of Toxicological Screenings-A Follow-Up Study Comparing Pooled Human Liver S9, HepaRG Cells, and Zebrafish Larvae. *Front. Chem.* **2020**, *8*, 539, doi:10.3389/fchem.2020.00539.
102. Guarin, M.; Ny, A.; Croze, N. de; Maes, J.; Léonard, M.; Annaert, P.; Witte, P.A.M. de. Pharmacokinetics in Zebrafish Embryos (ZFE) Following Immersion and Intrayolk Administration: A Fluorescence-Based Analysis. *Pharmaceuticals (Basel)* **2021**, *14*, doi:10.3390/ph14060576.
103. Philip Matyszak. Happy plants and laughing weeds: how people of the ancient world used – and abused – drugs. *HistoryExtra_The official website for BBC History Magazine and*

BBC History Revealed [Online], August 1, 2019. Available online: https://www.historyextra.com/period/ancient-history/ancient-drug-use-history-how-what-for-opium-hemp/.

104. *Epidemiology of drug abuse;* Sloboda, Z., Ed.; Springer: New York, London, 2005, ISBN 0-387-24415-8.
105. Myers, M.G.; Kelly, J.F. Cigarette Smoking Among Adolescents With Alcohol and Other Drug Use Problems. *Alcohol Research & Health* **2006**, *29*, 221–227.
106. Luethi, D.; Liechti, M.E. Designer drugs: mechanism of action and adverse effects. *Arch. Toxicol.* **2020**, *94*, 1085–1133, doi:10.1007/s00204-020-02693-7.
107. Giorgetti, A.; Pascali, J.P.; Fais, P.; Pelletti, G.; Gabbin, A.; Franchetti, G.; Cecchetto, G.; Viel, G. Molecular Mechanisms of Action of Novel Psychoactive Substances (NPS). A New Threat for Young Drug Users with Forensic-Toxicological Implications. *Life (Basel)* **2021**, *11*, doi:10.3390/life11050440.
108. Peacock, A.; Bruno, R.; Gisev, N.; Degenhardt, L.; Hall, W.; Sedefov, R.; White, J.; Thomas, K.V.; Farrell, M.; Griffiths, P. New psychoactive substances: challenges for drug surveillance, control, and public health responses. *The Lancet* **2019**, *394*, 1668–1684, doi:10.1016/S0140-6736(19)32231-7.
109. Specka, M.; Kuhlmann, T.; Sawazki, J.; Bonnet, U.; Steinert, R.; Cybulska-Rycicki, M.; Eich, H.; Zeiske, B.; Niedersteberg, A.; Schaaf, L.; et al. Prevalence of Novel Psychoactive Substance (NPS) Use in Patients Admitted to Drug Detoxification Treatment. *Front. Psychiatry* **2020**, *11*, 569, doi:10.3389/fpsyt.2020.00569.
110. Shafi, A.; Berry, A.J.; Sumnall, H.; Wood, D.M.; and Tracy, D.K. New psychoactive substances: a review and updates.
111. UNODC. Global Smart Update: Understanding the synthetic drug market: the NPS factor **2018**, *19*, 1–12.
112. European Monitoring Centre for Drugs and Drug Addiction. European drug report 2021: trends and developments.
113. EMCDDA-Europol. *EU drug markets*: *Impact of COVID-19;* Publications Office of the European Union: Luxembourg, 2020, ISBN 9789294974938.
114. UNODC. World Drug Report 2021: Booklet 5 - COVID-19 AND DRUGS: IMPACT AND OUTLOOK **2021**.
115. Catalani, V.; Arillotta, D.; Corkery, J.M.; Guirguis, A.; Vento, A.; Schifano, F. Identifying New/Emerging Psychoactive Substances at the Time of COVID-19; A Web-Based Approach. *Front. Psychiatry* **2020**, *11*, 632405, doi:10.3389/fpsyt.2020.632405.
116. UNODC. Global Synthetic Drugs Assessment 2020 **2020**.
117. Rychert, M.; Wilkins, C. Understanding the development of a regulated market approach to new psychoactive substances (NPS) in New Zealand using Punctuated Equilibrium Theory. *Addiction* **2018**, *113*, 2132–2139, doi:10.1111/add.14260.
118. Wilkins, C.; Rychert, M. Recent developments with the New Zealand regulated market approach to 'low-risk' psychoactive products. *Addiction* **2016**, *112*, 32–39, doi:10.1002/dta.1943.

119. UNODC. GLOBAL SMART UPDATE: Post-UNGASS 2016: NPS trends, challenges and recommendations **2016**, *16*, 1–12.
120. Matey, J.M.; Montalvo, G.; García-Ruiz, C.; Zapata, F.; López-Fernández, A.; Martínez, M.A. Prevalence study of drugs and new psychoactive substances in hair of ketamine consumers using a methanolic direct extraction prior to high-resolution mass spectrometry. *Forensic Sci. Int.* **2021**, *329*, 111080, doi:10.1016/j.forsciint.2021.111080.
121. Adamowicz, P.; Tokarczyk, B. Simple and rapid screening procedure for 143 new psychoactive substances by liquid chromatography-tandem mass spectrometry. *Drug Test. Anal.* **2016**, *8*, 652–667, doi:10.1002/dta.1815.
122. Wagmann, L.; Gampfer, T.M.; Meyer, M.R. Recent trends in drugs of abuse metabolism studies for mass spectrometry-based analytical screening procedures. *Anal. Bioanal. Chem.* **2021**, *413*, 5551–5559, doi:10.1007/s00216-021-03311-w.
123. Daniel, W.A. Mechanisms of cellular distribution of psychotropic drugs. Significance for drug action and interactions. *Progress in Neuro-Psychopharmacology and Biological Psychiatry* **2003**, *27*, 65–73, doi:10.1016/S0278-5846(02)00317-2.
124. Bickel, M.H. Factors affecting the storage of drugs and other xenobiotics in adipose tissue. *Advances in drug research* **1994**, *25*, 55–86.
125. Wagmann, L.; Maurer, H.H. Bioanalytical Methods for New Psychoactive Substances. *Handb. Exp. Pharmacol.* **2018**, *252*, 413–439, doi:10.1007/164_2017_83.
126. Meyer, M.R. New psychoactive substances: an overview on recent publications on their toxicodynamics and toxicokinetics. *Arch. Toxicol.* **2016**, *90*, 2421–2444, doi:10.1007/s00204-016-1812-x.
127. Swortwood, M.J.; Hearn, W.L.; DeCaprio, A.P. Cross-reactivity of designer drugs, including cathinone derivatives, in commercial enzyme-linked immunosorbent assays. *Drug Test. Anal.* **2014**, *6*, 716–727, doi:10.1002/dta.1489.
128. Favretto, D.; Pascali, J.P.; Tagliaro, F. New challenges and innovation in forensic toxicology: focus on the "New Psychoactive Substances". *J. Chromatogr. A* **2013**, *1287*, 84–95, doi:10.1016/j.chroma.2012.12.049.
129. Girón, A.J.; Deventer, K.; Roels, K.; van Eenoo, P. Development and validation of an open screening method for diuretics, stimulants and selected compounds in human urine by UHPLC-HRMS for doping control. *Anal. Chim. Acta* **2012**, *721*, 137–146, doi:10.1016/j.aca.2012.02.002.
130. Virus, E.D.; Sobolevsky, T.G.; Rodchenkov, G.M. 'Wrong-way-round ionization' and screening for doping substances in human urine by high-performance liquid chromatography/orbitrap mass spectrometry. *J. Mass Spectrom.* **2012**, *47*, 381–391, doi:10.1002/jms.2055.
131. Haschimi, B.; Mogler, L.; Halter, S.; Giorgetti, A.; Schwarze, B.; Westphal, F.; Fischmann, S.; Auwärter, V. Detection of the recently emerged synthetic cannabinoid 4F-MDMB-BINACA in "legal high" products and human urine specimens. *Drug Test. Anal.* **2019**, *11*, 1377–1386, doi:10.1002/dta.2666.

132. Vincenti, F.; Montesano, C.; Di Ottavio, F.; Gregori, A.; Compagnone, D.; Sergi, M.; Dorrestein, P. Molecular Networking: A Useful Tool for the Identification of New Psychoactive Substances in Seizures by LC-HRMS. *Front. Chem.* **2020**, *8*, 572952, doi:10.3389/fchem.2020.572952.
133. Zhu, M.; Zhang, H.; Humphreys, W.G. Drug metabolite profiling and identification by high-resolution mass spectrometry. *J. Biol. Chem.* **2011**, *286*, 25419–25425, doi:10.1074/jbc.R110.200055.
134. Negreira, N.; Kinyua, J.; Brabanter, N. de; Maudens, K.; van Nuijs, A.L.N. Identification of in vitro and in vivo human metabolites of the new psychoactive substance nitracaine by liquid chromatography coupled to quadrupole time-of-flight mass spectrometry. *Anal. Bioanal. Chem.* **2016**, *408*, 5221–5229, doi:10.1007/s00216-016-9616-7.
135. Strittmatter, N.; Düring, R.-A.; Takáts, Z. Analysis of wastewater samples by direct combination of thin-film microextraction and desorption electrospray ionization mass spectrometry. *Analyst* **2012**, *137*, 4037–4044, doi:10.1039/c2an35411j.
136. Fabresse, N.; Larabi, I.A.; Stratton, T.; Mistrik, R.; Pfau, G.; La Lorin de Grandmaison, G.; Etting, I.; Grassin Delyle, S.; Alvarez, J.-C. Development of a sensitive untargeted liquid chromatography-high resolution mass spectrometry screening devoted to hair analysis through a shared MS2 spectra database: A step toward early detection of new psychoactive substances. *Drug Test. Anal.* **2019**, *11*, 697–708, doi:10.1002/dta.2535.
137. Kiefer, K.; Du, L.; Singer, H.; Hollender, J. Identification of LC-HRMS nontarget signals in groundwater after source related prioritization. *Water Res.* **2021**, *196*, 116994, doi:10.1016/j.watres.2021.116994.
138. Ashesh, A.; Singh, S.; Linthoingambi Devi, N.; Chandra Yadav, I. Organochlorine pesticides in multi-environmental matrices of India: A comprehensive review on characteristics, occurrence, and analytical methods. *Microchemical Journal* **2022**, *177*, 107306, doi:10.1016/j.microc.2022.107306.
139. European Monitoring Centre for Drugs and Drug Addiction. *Wastewater analysis and drugs — a European multi-city study*, 2022.
140. Castiglioni, S. *Assessing illicit drugs in wastewater*: *Advances in wastewater-based drug epidemiology*; EMCDDA insights TD-XD-16-022-EN-C, Luxembourg, 2016.
141. Bijlsma, L.; Burgard, D.A.; Been, F.; Ort, C.; Matias, J.; Yargeau, V. The estimation of cannabis consumption through wastewater analysis. *Analysis of Cannabis*; Elsevier, 2020; pp 453–482, ISBN 9780444643414.
142. González-Mariño, I.; Gracia-Lor, E.; Rousis, N.I.; Castrignanò, E.; Thomas, K.V.; Quintana, J.B.; Kasprzyk-Hordern, B.; Zuccato, E.; Castiglioni, S. Wastewater-Based Epidemiology To Monitor Synthetic Cathinones Use in Different European Countries. *Environ. Sci. Technol.* **2016**, *50*, 10089–10096, doi:10.1021/acs.est.6b02644.
143. Gao, J.; Li, L.; Duan, L.; Yang, M.; Zhou, X.; Zheng, Q.; Ou, Y.; Li, Z.; Lai, F.Y. Exploring antibiotic consumption between urban and sub-urban catchments using both parent drugs and related metabolites in wastewater-based epidemiology. *Science of The Total Environment* **2022**, *827*, 154171, doi:10.1016/j.scitotenv.2022.154171.

144. Bivins, A.; North, D.; Ahmad, A.; Ahmed, W.; Alm, E.; Been, F.; Bhattacharya, P.; Bijlsma, L.; Boehm, A.B.; Brown, J.; et al. Wastewater-Based Epidemiology: Global Collaborative to Maximize Contributions in the Fight Against COVID-19. *Environ. Sci. Technol.* **2020**, *54*, 7754–7757, doi:10.1021/acs.est.0c02388.
145. McDonnell, L.A.; Heeren, R.M.A. Imaging mass spectrometry. *Mass Spectrom. Rev.* **2007**, *26*, 606–643, doi:10.1002/mas.20124.
146. Hillenkamp, F.; Unsöld, E.; Kaufmann, R.; Nitsche, R. Laser microprobe mass analysis of organic materials. *Nature* **1975**, *256*, 119–120, doi:10.1038/256119a0.
147. Feigl, P.; Schueler, B.; Hillenkamp, F. LAMMA 1000, a new instrument for bulk microprobe mass analysis by pulsed laser irradiation. *International Journal of Mass Spectrometry and Ion Physics* **1983**, *47*, 15–18, doi:10.1016/0020-7381(83)87125-3.
148. Vorm, O.; Roepstorff, P.; Mann, M. Improved Resolution and Very High Sensitivity in MALDI TOF of Matrix Surfaces Made by Fast Evaporation. *Anal. Chem.* **1994**, *66*, 3281–3287, doi:10.1021/ac00091a044.
149. Caprioli, R.M.; Farmer, T.B.; Gile, J. Molecular imaging of biological samples: localization of peptides and proteins using MALDI-TOF MS. *Anal. Chem.* **1997**, *69*, 4751–4760, doi:10.1021/ac970888i.
150. Weaver, E.M.; Hummon, A.B. Imaging mass spectrometry: from tissue sections to cell cultures. *Adv. Drug Deliv. Rev.* **2013**, *65*, 1039–1055, doi:10.1016/j.addr.2013.03.006.
151. Swales, J.G.; Hamm, G.; Clench, M.R.; Goodwin, R.J.A. Mass spectrometry imaging and its application in pharmaceutical research and development: A concise review. *International Journal of Mass Spectrometry* **2019**, *437*, 99–112, doi:10.1016/j.ijms.2018.02.007.
152. Vaysse, P.-M.; Heeren, R.M.A.; Porta, T.; Balluff, B. Mass spectrometry imaging for clinical research - latest developments, applications, and current limitations. *Analyst* **2017**, *142*, 2690–2712, doi:10.1039/c7an00565b.
153. Heeren, R.M.A. MALDI Techniques in Mass Spectrometry Imaging. In *Encyclopedia of spectroscopy and spectrometry*, Third edition; Lindon, J.C., Tranter, G.E., Koppenaal, D.W., Eds.; Elsevier/AP Academic Press is an imprint of Elsevier: Amsterdam, Boston, 2017; pp 711–718, ISBN 9780128032244.
154. Taylor, A.J.; Dexter, A.; Bunch, J. Exploring Ion Suppression in Mass Spectrometry Imaging of a Heterogeneous Tissue. *Anal. Chem.* **2018**, *90*, 5637–5645, doi:10.1021/acs.analchem.7b05005.
155. Johnson, J.; Sharick, J.T.; Skala, M.C.; Li, L. Sample preparation strategies for high-throughput mass spectrometry imaging of primary tumor organoids. *J. Mass Spectrom.* **2020**, *55*, e4452, doi:10.1002/jms.4452.
156. Pessotti, R.d.C.; Hansen, B.L.; Zacharia, V.M.; Polyakov, D.; Traxler, M.F. High Spatial Resolution Imaging Mass Spectrometry Reveals Chemical Heterogeneity Across Bacterial Microcolonies. *Anal. Chem.* **2019**, *91*, 14818–14823, doi:10.1021/acs.analchem.9b03909.

157. Garrard, K.P.; Ekelöf, M.; Khodjaniyazova, S.; Bagley, M.C.; Muddiman, D.C. A Versatile Platform for Mass Spectrometry Imaging of Arbitrary Spatial Patterns. *J. Am. Soc. Mass Spectrom.* **2020**, *31*, 2547–2552, doi:10.1021/jasms.0c00128.
158. Gorzolka, K.; Kölling, J.; Nattkemper, T.W.; Niehaus, K. Spatio-Temporal Metabolite Profiling of the Barley Germination Process by MALDI MS Imaging. *PLoS One* **2016**, *11*, e0150208, doi:10.1371/journal.pone.0150208.
159. Liu, B.; Meng, X.; Li, K.; Guo, J.; Cai, Z. Visualization of lipids in cottonseeds by matrix-assisted laser desorption/ionization mass spectrometry imaging. *Talanta* **2021**, *221*, 121614, doi:10.1016/j.talanta.2020.121614.
160. Hu, W.; Han, Y.; Sheng, Y.; Wang, Y.; Pan, Q.; Nie, H. Mass spectrometry imaging for direct visualization of components in plants tissues. *J. Sep. Sci.* **2021**, *44*, 3462–3476, doi:10.1002/jssc.202100138.
161. Lamont, L.; Hadavi, D.; Viehmann, B.; Flinders, B.; Heeren, R.M.A.; Vreeken, R.J.; Porta Siegel, T. Quantitative mass spectrometry imaging of drugs and metabolites: a multi-platform comparison. *Anal. Bioanal. Chem.* **2021**, *413*, 2779–2791, doi:10.1007/s00216-021-03210-0.
162. Davoli, E.; Zucchetti, M.; Matteo, C.; Ubezio, P.; D'Incalci, M.; Morosi, L. THE SPACE DIMENSION AT THE MICRO LEVEL: MASS SPECTROMETRY IMAGING OF DRUGS IN TISSUES. *Mass Spectrom. Rev.* **2021**, *40*, 201–214, doi:10.1002/mas.21633.
163. Buchberger, A.R.; DeLaney, K.; Johnson, J.; Li, L. Mass Spectrometry Imaging: A Review of Emerging Advancements and Future Insights. *Anal. Chem.* **2018**, *90*, 240–265, doi:10.1021/acs.analchem.7b04733.
164. Jove, M.; Spencer, J.; Clench, M.; Loadman, P.M.; Twelves, C. Precision pharmacology: Mass spectrometry imaging and pharmacokinetic drug resistance. *Crit. Rev. Oncol. Hematol.* **2019**, *141*, 153–162, doi:10.1016/j.critrevonc.2019.06.008.
165. Balluff, B.; Hopf, C.; Porta Siegel, T.; Grabsch, H.I.; Heeren, R.M.A. Batch Effects in MALDI Mass Spectrometry Imaging. *J. Am. Soc. Mass Spectrom.* **2021**, *32*, 628–635, doi:10.1021/jasms.0c00393.
166. Dueñas, M.E.; Essner, J.J.; Lee, Y.J. 3D MALDI Mass Spectrometry Imaging of a Single Cell: Spatial Mapping of Lipids in the Embryonic Development of Zebrafish. *Sci. Rep.* **2017**, *7*, 14946, doi:10.1038/s41598-017-14949-x.
167. Abdelmoula, W.M.; Pezzotti, N.; Hölt, T.; Dijkstra, J.; Vilanova, A.; McDonnell, L.A.; Lelieveldt, B.P.F. Interactive Visual Exploration of 3D Mass Spectrometry Imaging Data Using Hierarchical Stochastic Neighbor Embedding Reveals Spatiomolecular Structures at Full Data Resolution. *J. Proteome Res.* **2018**, *17*, 1054–1064, doi:10.1021/acs.jproteome.7b00725.
168. Vos, D.R.N.; Ellis, S.R.; Balluff, B.; Heeren, R.M.A. Experimental and Data Analysis Considerations for Three-Dimensional Mass Spectrometry Imaging in Biomedical Research. *Mol. Imaging Biol.* **2021**, *23*, 149–159, doi:10.1007/s11307-020-01541-5.

169. Mallah, K.; Quanico, J.; Trede, D.; Kobeissy, F.; Zibara, K.; Salzet, M.; Fournier, I. Lipid Changes Associated with Traumatic Brain Injury Revealed by 3D MALDI-MSI. *Anal. Chem.* **2018**, *90*, 10568–10576, doi:10.1021/acs.analchem.8b02682.
170. Paine, M.R.L.; Kooijman, P.C.; Fisher, G.L.; Heeren, R.M.A.; Fernández, F.M.; Ellis, S.R. Visualizing molecular distributions for biomaterials applications with mass spectrometry imaging: a review. *J. Mater. Chem. B* **2017**, *5*, 7444–7460, doi:10.1039/c7tb01100h.
171. Goh, W.W.B.; Wang, W.; Wong, L. Why Batch Effects Matter in Omics Data, and How to Avoid Them. *Trends Biotechnol.* **2017**, *35*, 498–507, doi:10.1016/j.tibtech.2017.02.012.
172. Barry, J.A.; Groseclose, M.R.; Castellino, S. Quantification and assessment of detection capability in imaging mass spectrometry using a revised mimetic tissue model. *Bioanalysis* **2019**, *11*, 1099–1116, doi:10.4155/bio-2019-0035.
173. Wang, W.; Liu, X.; Gelinas, D.; Ciruna, B.; Sun, Y. A fully automated robotic system for microinjection of zebrafish embryos. *PLoS One* **2007**, *2*, e862, doi:10.1371/journal.pone.0000862.
174. Chi, Z.; Xu, Q.; Zhu, L. A Review of Recent Advances in Robotic Cell Microinjection. *IEEE Access* **2020**, *8*, 8520–8532, doi:10.1109/ACCESS.2020.2964305.
175. Kotterman, M.A.; Chalberg, T.W.; Schaffer, D.V. Viral Vectors for Gene Therapy: Translational and Clinical Outlook. *Annu. Rev. Biomed. Eng.* **2015**, *17*, 63–89, doi:10.1146/annurev-bioeng-071813-104938.
176. Ramamoorth, M.; Narvekar, A. Non viral vectors in gene therapy- an overview. *J. Clin. Diagn. Res.* **2015**, *9*, GE01-6, doi:10.7860/JCDR/2015/10443.5394.
177. Gao, X.; Kim, K.-S.; Liu, D. Nonviral gene delivery: what we know and what is next. *AAPS J.* **2007**, *9*, E92-104, doi:10.1208/aapsj0901009.
178. Dean, D.A. Microinjection. *Brenner's Encyclopedia of Genetics*; Elsevier, 2013; pp 409–410, ISBN 9780080961569.
179. Metcalfe, C.D.; Sonstegard, R.A. Microinjection of Carcinogens Into Rainbow Trout Embryos: An In Vivo Carcinogenesis Assay. *JNCI: Journal of the National Cancer Institute* **1984**, *73*, 1125–1132, doi:10.1093/jnci/73.5.1125.
180. Komamine, A.; Nomura, K. Application of Microinjection to a High Frequency and Synchronous Somatic Embryogenesis System in Carrot Suspension Cultures. In *Ciba Foundation Symposium 137 - Applications of Plant Cell and Tissue Culture*; Bock, G., Marsh, J., Eds.; John Wiley & Sons, Ltd: Chichester, UK, 2007; pp 90–96, ISBN 9780470513651.
181. Schubert, S.; Keddig, N.; Hanel, R.; Kammann, U. Microinjection into zebrafish embryos (Danio rerio) - a useful tool in aquatic toxicity testing? *Environ Sci Eur* **2014**, *26*, 1, doi:10.1186/s12302-014-0032-3.
182. Kim, D.-H.; Hwang, C.N.; Sun, Y.; Lee, S.H.; Kim, B.; Nelson, B.J. Mechanical analysis of chorion softening in prehatching stages of zebrafish embryos. *IEEE Trans. Nanobioscience* **2006**, *5*, 89–94, doi:10.1109/tnb.2006.875054.
183. Xie, Y.; Sun, D.; Liu, C.; Tse, H.Y.; Cheng, S.H. A Force Control Approach to a Robot-assisted Cell Microinjection System. *The International Journal of Robotics Research* **2010**, *29*, 1222–1232, doi:10.1177/0278364909354325.

184. Chow, Y.T.; Chen, S.; Liu, C.; Liu, C.; Li, L.; Kong, C.W.M.; Cheng, S.H.; Li, R.A.; Sun, D. A High-Throughput Automated Microinjection System for Human Cells With Small Size. *IEEE/ASME Trans. Mechatron.* **2016**, *21*, 838–850, doi:10.1109/TMECH.2015.2476362.
185. Zhao, Y.; Sun, H.; Sha, X.; Gu, L.; Zhan, Z.; Li, W.J. A Review of Automated Microinjection of Zebrafish Embryos. *Micromachines (Basel)* **2018**, *10*, doi:10.3390/mi10010007.
186. Stainier, D.Y.R.; Raz, E.; Lawson, N.D.; Ekker, S.C.; Burdine, R.D.; Eisen, J.S.; Ingham, P.W.; Schulte-Merker, S.; Yelon, D.; Weinstein, B.M.; et al. Guidelines for morpholino use in zebrafish. *PLoS Genet.* **2017**, *13*, e1007000, doi:10.1371/journal.pgen.1007000.
187. Heasman, J.; Kofron, M.; Wylie, C. Beta-catenin signaling activity dissected in the early Xenopus embryo: a novel antisense approach. *Dev. Biol.* **2000**, *222*, 124–134, doi:10.1006/dbio.2000.9720.
188. Nasevicius, A.; Ekker, S. Effective targeted gene 'knockdown' in zebrafish. *nature genetics* **2000**, *26*, 216–220, doi:10.1038/79951.
189. Renninger, S.L.; Schonthaler, H.B.; Neuhauss, S.C.F.; Dahm, R. Investigating the genetics of visual processing, function and behaviour in zebrafish. *Neurogenetics* **2011**, *12*, 97–116, doi:10.1007/s10048-011-0273-x.
190. Phillips, J.B.; Westerfield, M. Zebrafish as a Model to Understand Human Genetic Diseases. *The Zebrafish in Biomedical Research*; Elsevier, 2020; pp 619–626, ISBN 9780128124314.
191. Moulton, J.D.; Yan, Y.-L. Using Morpholinos to control gene expression. *Curr. Protoc. Mol. Biol.* **2008**, *Chapter 26*, Unit 26.8, doi:10.1002/0471142727.mb2608s83.
192. Geller, B.L.; Deere, J.; Tilley, L.; Iversen, P.L. Antisense phosphorodiamidate morpholino oligomer inhibits viability of Escherichia coli in pure culture and in mouse peritonitis. *J. Antimicrob. Chemother.* **2005**, *55*, 983–988, doi:10.1093/jac/dki129.
193. Suwanmanee, T.; Sierakowska, H.; Fucharoen, S.; Kole, R. Repair of a splicing defect in erythroid cells from patients with beta-thalassemia/HbE disorder. *Mol. Ther.* **2002**, *6*, 718–726, doi:10.1006/mthe.2002.0805.
194. Liu, L.Y.; Alexa, K.; Cortes, M.; Schatzman-Bone, S.; Kim, A.J.; Mukhopadhyay, B.; Cinar, R.; Kunos, G.; North, T.E.; Goessling, W. Cannabinoid receptor signaling regulates liver development and metabolism. *Development* **2016**, *143*, 609–622, doi:10.1242/dev.121731.
195. Eisen, J.S.; Smith, J.C. Controlling morpholino experiments: don't stop making antisense. *Development* **2008**, *135*, 1735–1743, doi:10.1242/dev.001115.
196. Oppel, F.; Tao, T.; Shi, H.; Ross, K.N.; Zimmerman, M.W.; He, S.; Tong, G.; Aster, J.C.; Look, A.T. Loss of atrx cooperates with p53-deficiency to promote the development of sarcomas and other malignancies. *PLoS Genet.* **2019**, *15*, e1008039, doi:10.1371/journal.pgen.1008039.
197. van Rooijen, E.; van de Hoek, G.; Logister, I.; Ajzenberg, H.; Knoers, N.V.A.M.; van Eeden, F.; Voest, E.E.; Schulte-Merker, S.; Giles, R.H. The von Hippel-Lindau Gene Is

Required to Maintain Renal Proximal Tubule and Glomerulus Integrity in Zebrafish Larvae. *Nephron* **2018**, *138*, 310–323, doi:10.1159/000484096.

198. Zhang, Z.; Liu, F.; Chen, J. Molecular structure of the ATP-bound, phosphorylated human CFTR. *Proc. Natl. Acad. Sci. U. S. A.* **2018**, *115*, 12757–12762, doi:10.1073/pnas.1815287115.

Chapter 2.

Drug Administration Routes Impact the Metabolism of a Synthetic Cannabinoid in the Zebrafish Larvae Model

Previously published in:

Yu Mi Park[1,2], Markus R. Meyer[3], Rolf Müller[1,4,*] and Jennifer Herrmann[1,4,*]

Molecules, 2020 Sep 29; 25(19):4474. DOI: 10.3390/molecules25194474.

[1] Department of Microbial Natural Products, Helmholtz Institute for Pharmaceutical Research Saarland (HIPS), Helmholtz Centre for Infection Research (HZI) and Department of Pharmacy, Saarland University, Campus E8 1, 66123 Saarbrücken, Germany; Yu-Mi.Park@helmholtz-hips.de

[2] Environmental Safety Group, Korea Institute of Science and Technology (KIST) Europe, 66123 Saarbrücken, Germany

[3] Department of Experimental and Clinical Toxicology, Institute of Experimental and Clinical Pharmacology and Toxicology, Center for Molecular Signaling (PZMS), Saarland University, 66421 Homburg, Germany; m.r.meyer@mx.uni-saarland.de

[4] German Center for Infection Research (DZIF), Partner Site Hannover-Braunschweig Germany

[*] Correspondence: Rolf.Mueller@helmholtz-hips.de (R.M.); Jennifer.Herrmann@helmholtz-hips.de (J.H.); Tel.: +49-0681-98806-3000 (R.M.), +49-0681-98806-3101 (J.H.)

Contributions

Author's effort

The author significantly contributed to the concept of the study, designed and performed experiments, and evaluated and interpreted the resulting data. The author performed mating zebrafish, exposure experiment, sample preparations for LC-HRMS/MS and MALDI-FT-ICR, all data analysis of LC-HRMS/MS, and data processing and analysis of MALDI-FT-ICR, as well as HepaRG *in vitro* experiment. Furthermore, the author contributed significantly to the conceiving and writing of the manuscript.

Contributions by others

Markus R. Meyer contributed to the conception, validation, resource of the substrate, reviewing, and editing of the manuscript. Rolf Müller contributed by conceiving, reviewing, and editing this study. Jennifer Herrmann contributed to the concept, validation, writing, editing, and reviewing of this study. Rolf Müller and Jennifer Herrmann supervised this project, and all authors also contributed by proofreading the manuscript.

2.1 Abstract

Zebrafish (*Danio rerio*) larvae have gained attention as a valid model to study *in vivo* drug metabolism and to predict human metabolism. The microinjection of compounds, oligonucleotides, or pathogens into zebrafish embryos at an early developmental stage is a well-established technique. Here, we investigated the metabolism of zebrafish larvae after microinjection of methyl 2-(1-(5-fluoropentyl)-1*H*-pyrrolo[2,3-b]pyridine-3-carboxamido)-3,3-dimethylbutanoate (7'*N*-5F-ADB) as a representative of recently introduced synthetic cannabinoids. Results were compared to human urine data and data from the *in vitro* HepaRG model and the metabolic pathway of 7'*N*-5F-ADB were reconstructed. Out of 27 metabolites detected in human urine samples, 19 and 15 metabolites were present in zebrafish larvae and HepaRG cells, respectively. The route of administration to zebrafish larvae had a major impact and we found a high number of metabolites in when 7'*N*-5F-ADB was microinjected into the caudal vein, heart ventricle, or hindbrain. We further studied the spatial distribution of the parent compound and its metabolites by mass spectrometry imaging (MSI) of treated zebrafish larvae to demonstrate the discrepancy in metabolite profiles among larvae exposed through different administration routes. In conclusion, zebrafish larvae represent a superb model for studying drug metabolism, and when combined with MSI, the optimal administration route can be determined based on *in vivo* drug distribution.

2.2 Graphical Abstract

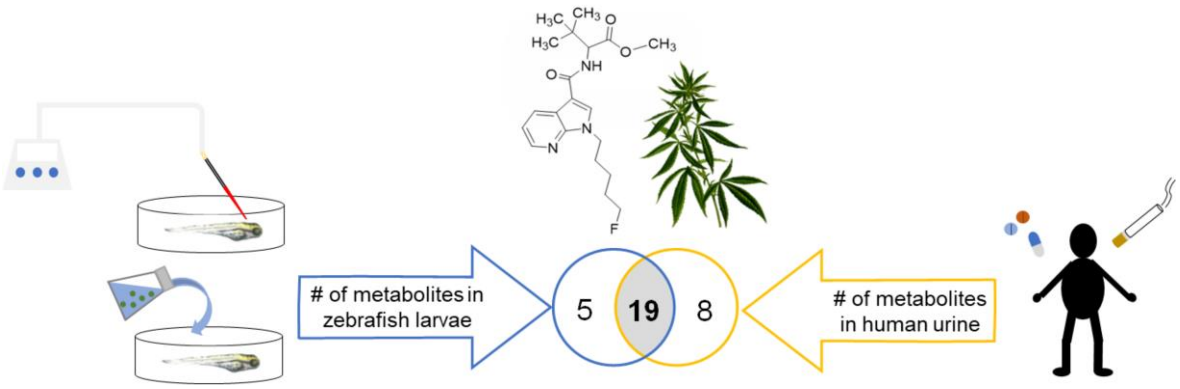

2.3 Introduction

Zebrafish *(Danio rerio*; ZF) has become a very prominent *in vivo* model organism in various research fields, such as toxicology, drug discovery, disease models, and neurobiology [1–5]. This has several reasons, such as ease of handling, predictivity of ZF assays, and their link to effects observed in humans. Importantly, the ZF genome shares 70% similarity to human genes and the similarity of potential human disease-related genes is even higher (82%) [6–8].

The use of self-feeding ZF embryos and larvae that are younger than 120 h post-fertilization (hpf) is particularly popular because such experiments are not considered as animal experiments according to European legislation (EU directive 2010/63/EU). Thus, experiments with larvae at ≤ 120 hpf are in compliance with the 3R principle (Replacement, Reduction, Refinement) as they contribute to the reduction of animal experiments. Consequently, ZF embryos and larvae have been widely applied in studies of e.g., human disease [9,10], infection [11,12], antibiotics [13,14], and human metabolism [15–17], to name just a few.

Microinjection has been used already for decades as a way of administering compounds to fish in early life stages, and this technique is still widely used in cellular microbiological research [18–20]. However, most laboratories use aquatic exposure in screening campaigns with ZF larvae, thus neglecting the potentially hindered uptake and absorption of lipophilic compounds which, in turn, can lead to a rather high rate of false negatives. More recently, some groups proposed to administer lipophilic compounds via microinjection into yolk sac due to easy and straightforward microinjection protocols that can be automated if required [21–23].

In an earlier study [24], we detected only one metabolite in ZF larvae after microinjection of a new psychoactive substance (NPS) into the yolk sac. In contrast, 18 metabolites were detected when we administered the compound to the ZF larvae through conventional aquatic exposure. This unexpected result prompted us to refine our protocols for metabolite identification in ZF larvae as part of our preclinical DMPK (drug metabolism and pharmacokinetics) assay pipeline.

The common sites for ZF microinjection are yolk sac, caudal vein, heart ventricle, and hindbrain. The corresponding techniques require different levels of expertise, with yolk sac injections being the simplest technique. However, more advanced microinjection techniques, such as caudal vein injections, provide the advantage of ensuring proper systemic distribution of a drug or other microinjected agents. For studying drug metabolism in ZF larvae, this appears to be crucial as test compounds need to reach the liver compartment where most metabolic reactions take place. Metabolic processing is mainly performed by cytochrome P450 (CYP) enzymes, and ZF larvae possess a full complement of CYP genes, which display functional similarity to the human orthologs. This similarity makes ZF a very promising model as its predictive value in comparison to human metabolism is thought to be high [25,26].

The spatial distribution of a drug can be checked by mass spectrometry imaging (MSI) as an outstanding visualization tool that enables label-free imaging in biological tissues. Here, we applied MSI in order to understand the distribution of a drug and its metabolites in ZF larval

bodies, which, in turn, enables an informed choice on the optimal administration route. However, sample preparation of ZF larvae sections is still challenging.

In this study, we present a new approach of employing various administration routes for drug exposure to ZF larvae to further improve metabolite identification resulting in a spectrum, which is widely in concordance with human metabolism. A new synthetic cannabinoid (SC), methyl 2-(1-(5-fluoropentyl)-1*H*-pyrrolo[2,3-b]pyridine-3-carboxamido)-3,3-dimethylbutanoate (7′*N*-5F-ADB, Figure 1), was chosen for this study because it appeared recently on the illicit drug market [27] as one of the most dangerous SCs with high potency and serious adverse effects resulting in hospitalizations and fatalities [28–31]. To characterize the circulation of 7′*N*-5F-ADB and its metabolites in the ZF larval body, the spatial distribution was visualized by matrix-assisted laser desorption/ionization (MALDI)-MSI as an emerging technique enabling the imaging of molecular species [32–34].

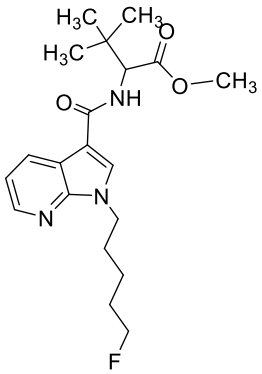

Figure 1. Chemical structure of 7′*N*-5F-ADB.

2.4 Results and Discussion

2.4.1. Zebrafish Larvae Metabolite Spectra of 7′*N*-5F-ADB Differ Depending on the Route of Administration

In a previous study [24], we investigated metabolites of 7′*N*-5F-ADB after addition of the compound to ZF larvae either through the larvae-surrounding water or through microinjection into yolk sac resulting in a reduction from 18 to only one detected metabolite when the yolk sac administration route was chosen. It is also worth mentioning that ZF larvae produced an authentic spectrum of metabolites as found in human biosamples after intake of 7′*N*-5F-ADB [27]. We initially expected that the lipophilic NPS would only be insufficiently taken up by the larvae when added to the water and that administration by microinjection should result in a larger number of detectable metabolites. This prompted us to investigate other injection sites and to compare ZF metabolism as part of the current study. Table 1 summarizes phase I and phase II metabolite data from microinjected larvae and HepaRG cells, the latter being used for comparison, along with data from previously published studies with 7′*N*-5F-ADB [24,27].

2.4 Results and Discussion

Table 1. Summary of 7′*N*-5F-ADB and its phase I and II metabolites and their detection in the different models.

Compound		Human Screening Data [27]		Zebrafish Larvae, Published Data [24]	Zebrafish Larvae, Data from This Study				HepaRG *In Vitro* Model
					Microinjection				
		Plasma	Urine	Aquatic Exposure	Yolk Sac	Caudal Vein	Heart Ventricle	Hindbrain	
Parent compound	7′*N*-5F-ADB	+++	+	+++	++	++	++	++	+++
Phase I	M1		+	+		+	+	+	+
	M2		+	+					+
	M3			+		+	+	+	+
	M4		+	+		+	+	+	+
	M5	++	+++	++		+	+	+	++
	M6		+	+		+	+	+	+
	M7			+		+	+	+	+
	M8		+			+ [nq]	+ [nq]	+ [nq]	
	M9					+ [nq]	+ [nq]	+ [nq]	
	M10		+	+		+	+	+	+
	M11	+	++			+	+ [nq]	+	+
	M12		+	+		+	+ [nq]	+	+
	M13		+	+	+++	+++	+++	+++	+
	M14		+						
	M15			+		+	+	+	+
	M16	+		+		+	+	+	+
	M17	+	+			+	+	+	+
	M18		+						
	M19		+						
	M20 [a]								
	M21		+	+		+	+	+	
	M22								+
	M23			+ [c]		+ [b]	+ [b]	+ [b]	
	M24		+ [c]						
	M25		+ [c]						
	M26								
Total number of Phase I metabolites		4	17	14	1	17	17	17	15
Phase II	M27		+	+		+		+	+
	M28		+			+	+ [nq]	+	
	M29		+			+	+	+	+
	M30		+	+		+	+	+	+
	M31		+			+	+	+	+
	M32		+						
	M33		+						
	M34		+			+	+	+	
	M35		+ [c]	+[c]		+ [b]	+ [b]	+ [b]	+ [b]
	M36		+ [c]	+[c]					
Total number of Phase II metabolites		-	10	4	-	7	6	7	5
Total number of detected Phase I/II metabolites		4	27	18	1	24	23	24	20

[a] Precursor metabolite of M26 that was not detected in this study. [b] Peaks of structural isomers were not separated in the chromatograms due to co-elution from the LC-HRMS/MS system used in this study, and accordingly, isomers were counted and quantified as one metabolite. [c] Isomers of the metabolite eluted as individual peaks using LC-HRMS/MS conditions utilized applied in the previous studies [24,27]. [nq] Confirmed mass, but not quantified due to peak detection below signal-to-noise ratio of 3. +: Peak detected, ++: second most abundant peak among metabolites, +++: most abundant peak among metabolites.

Among the different models used (human, cells, zebrafish), a total number of up to 27, 20, and 24 metabolites was found in human urine, HepaRG cells, and microinjected (caudal vein, heart ventricle, hindbrain) ZF larvae, respectively (Table 1 and Supplementary Table S1). In contrast, the microinjection of 7'*N*-5F-ADB into the yolk sac of ZF larvae or addition of the compound to the water resulted in fewer detected metabolites (Figure 2). Importantly, out of the 24 metabolites from ZF larvae, 19 metabolites represent human metabolites from urine samples, three were also detected in HepaRG cells, and only two were exclusively found in the larvae (Figure 3). Reviewing the comparability of the three models, metabolite data of ZF larvae treated through microinjection showed high similarity to human urine samples, with a 70% match rate, and to HepaRG cells with a 90% match rate.

The most abundant metabolites of 7'*N*-5F-ADB in human urine samples [27] were M5 (ester hydrolysis), M11 (ester hydrolysis in combination with hydroxylation of the tertiary butyl part), and M30 (ester hydrolysis in combination with glucuronidation). In the ZF larvae model, M5, M13 (oxidative defluorination in combination with oxidation to carboxylic acid), and M23/M24/M25/M26 (four isomers; dihydroxylation of 7'*N*-5F-ADB) were the main metabolites (Table 2), and M13 was the fifth most abundant in human urine as well. Moreover, to study potential differences in metabolite patterns after microinjection of 7'*N*-5F-ADB into different organs of ZF larvae, we compared the five most abundant metabolites (Figure 4) and 17 minor metabolites (Supplementary Figure S1) detected in microinjected ZF larvae. Regarding the major metabolite M13, caudal vein injections were most successful as the respective peaks were detected at significantly higher abundance than in the other samples (heart ventricle and hindbrain injections). For the other major and minor metabolites, we did not observe specific patterns depending on the route of administration, but overall, metabolite peak detection was most feasible from samples where the compound was injected into the caudal vein. Yolk sac data could not be considered for the comparison due to only one metabolite (M13) being detected.

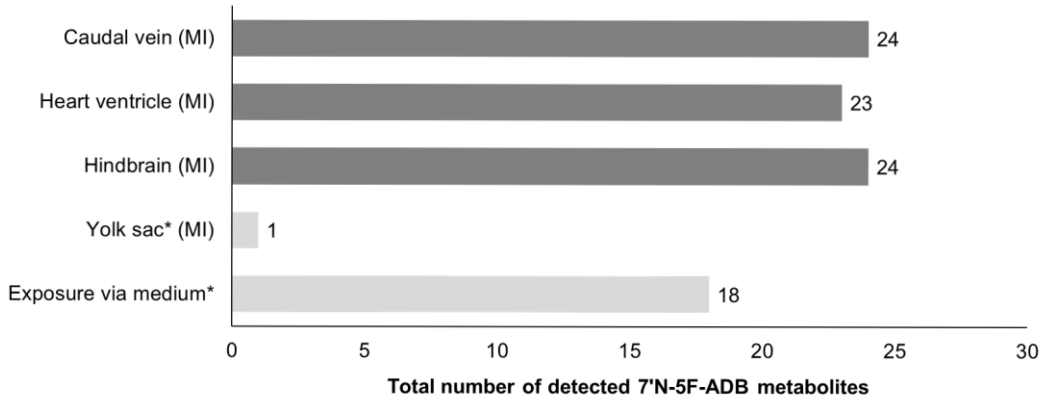

Figure 2. Comparison of the total number of metabolites produced depending on different administration routes in ZF larvae. Results for the samples investigated in this study are represented by the mean value of peak numbers of triplicates of 36 pooled larvae. (MI: microinjection, *these results were quoted from the previous study of 7'*N*-5F-ADB [24]).

2.4 Results and Discussion

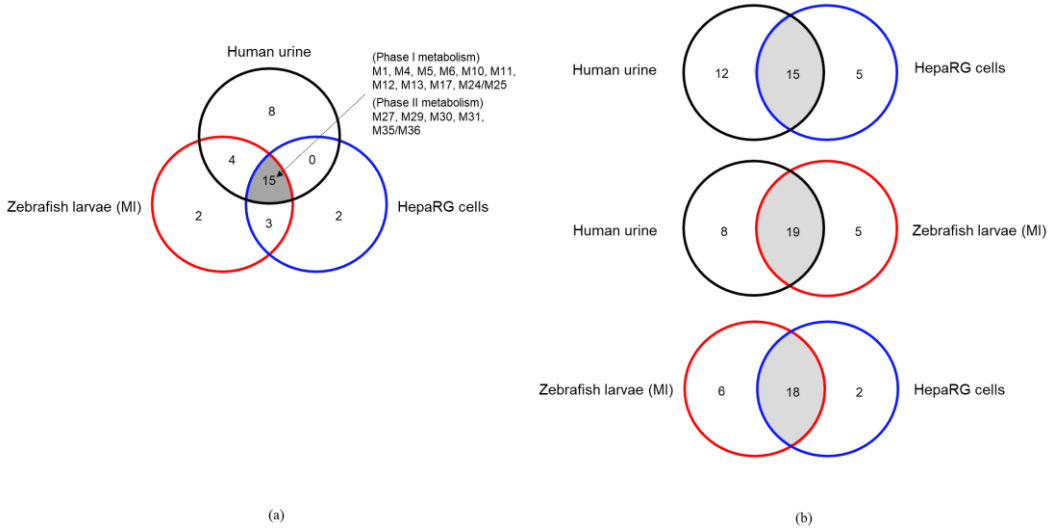

Figure 3. Comparison of the metabolites observed from the three models [human urine samples, zebrafish larvae (exposed via microinjection; MI), and HepaRG cells] using Venn diagrams. (a) Common metabolites detected among all models and (b) their mutual comparability.

Table 2. Comparison of the major metabolites detected in the investigated models using LC-HRMS/MS.

	Human Screening Data [27]		Zebrafish Larvae, Published Data [24]	Zebrafish Larvae, Data from this Study				HepaRG *In Vitro* Model
				Microinjection††				
	Plasma	Urine	Aquatic Exposure†	Yolk Sac	Caudal Vein	Heart Ventricle	Hindbrain	
most abundant peak	P	M5	P	M13	M13	P	M13	P
second most abundant peak	M5	M11	M5	P	P	M5	P	M5
third most abundant peak	M16	M30	M13	-*	M5	M13	M5	M4

P: Parent compound (7′*N*-5F-ADB). *Only one metabolite was produced from zebrafish larvae injected into yolk sac. † ZF larvae were treated via aquatic exposure from 4 day post-fertilization (dpf) to 5 dpf (1-day exposure) at 28 °C. †† ZF larvae after microinjection of 7′*N*-5F-ADB were incubated at 28 °C for 1 h.

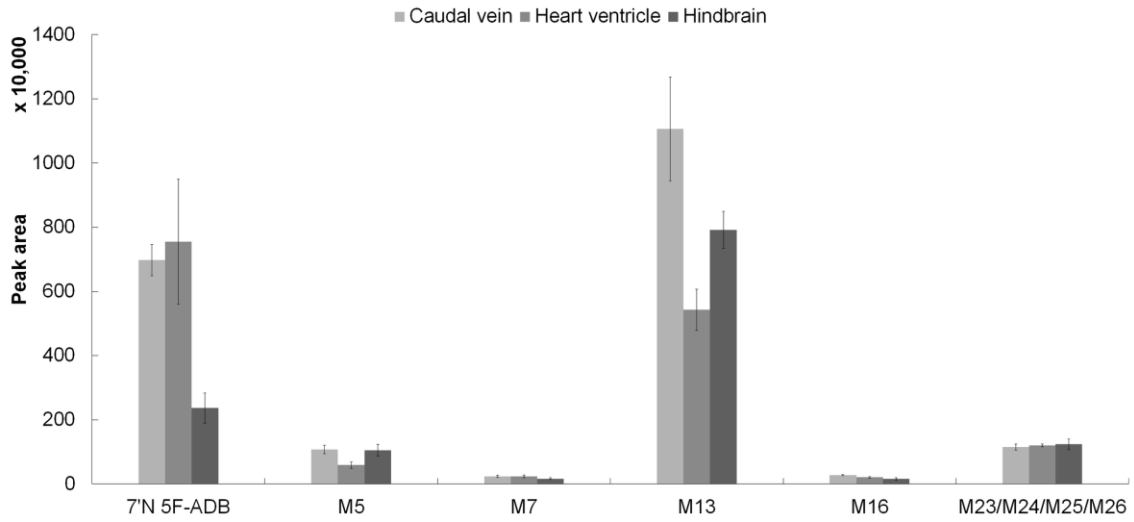

Figure 4. Detection profile of 7′*N*-5F-ADB and five major metabolites in microinjected ZF larvae (caudal vein, heart ventricle, and hindbrain). The most abundant metabolite, M13, was formed by

defluorination in combination with oxidation of the formed primary alcohol (M7) to a carboxylic acid moiety. The clustered columns are displayed as mean ± SD (n = 3). The four structural isomers (M23, M24, M25, and M26) at m/z 410.2075 are represented as one metabolite due to co-elution from the LC-HRMS/MS system.

ZF larvae exposed to 7′*N*-5F-ADB via microinjection into different organs also produced three metabolites [M3 (*N*-dealkylation), M7 (defluorination), M15 (defluorination in combination with oxidation to carboxylic acid)] that were not detected in human biosamples (Table 1). In addition, M9 (ester hydrolysis with combination with defluorination and hydroxylation of the pentyl chain) was found only in all microinjected ZF larvae except yolk sac compartment, and its detection was reported in rat urine of a published study [27]. M2 was uniquely observed in only ZF larvae treated by exposure medium, and seven out of 10 phase II glucuronidated metabolites detected in human urine were produced in ZF larvae microinjected into three internal organs excluding yolk sac.

The metabolic pathway of 7′*N*-5F-ADB was reconstructed with complementing the metabolites detected in all ZF larvae applied to different administration routes, including human urine samples [27] and HepaRG cells. The main pathways are displayed for phase I metabolism and phase II metabolism, which are centered on two abundant metabolites (M5, M13) found in the ZF larvae model (Table 2). Overall, we were able to construct the principal parts of the human metabolic pathway, as shown in Figure 5 based on the ZF larvae model.

Taken together, microinjection of 7′*N*-5F-ADB into caudal vein, heart ventricle, or hindbrain of ZF larvae resulted in a large number (24) of phase I and phase II metabolites that already formed as early as 1 h after compound administration with relatively high abundance. In contrast, detection of 18 metabolites after aquatic exposure with 7′*N*-5F-ADB required a much longer incubation period of 24 h. Microinjection into the yolk sac was not suitable for studying 7′*N*-5F-ADB metabolism in ZF larvae as demonstrated in a previous study [24]. Thus, direct injection into an internal organ of ZF larvae results in fast metabolism probably due to the fact that the NPS was able to reach functional metabolic organs, such as a liver and pancreas, through fast circulation inside of the larval body [35].

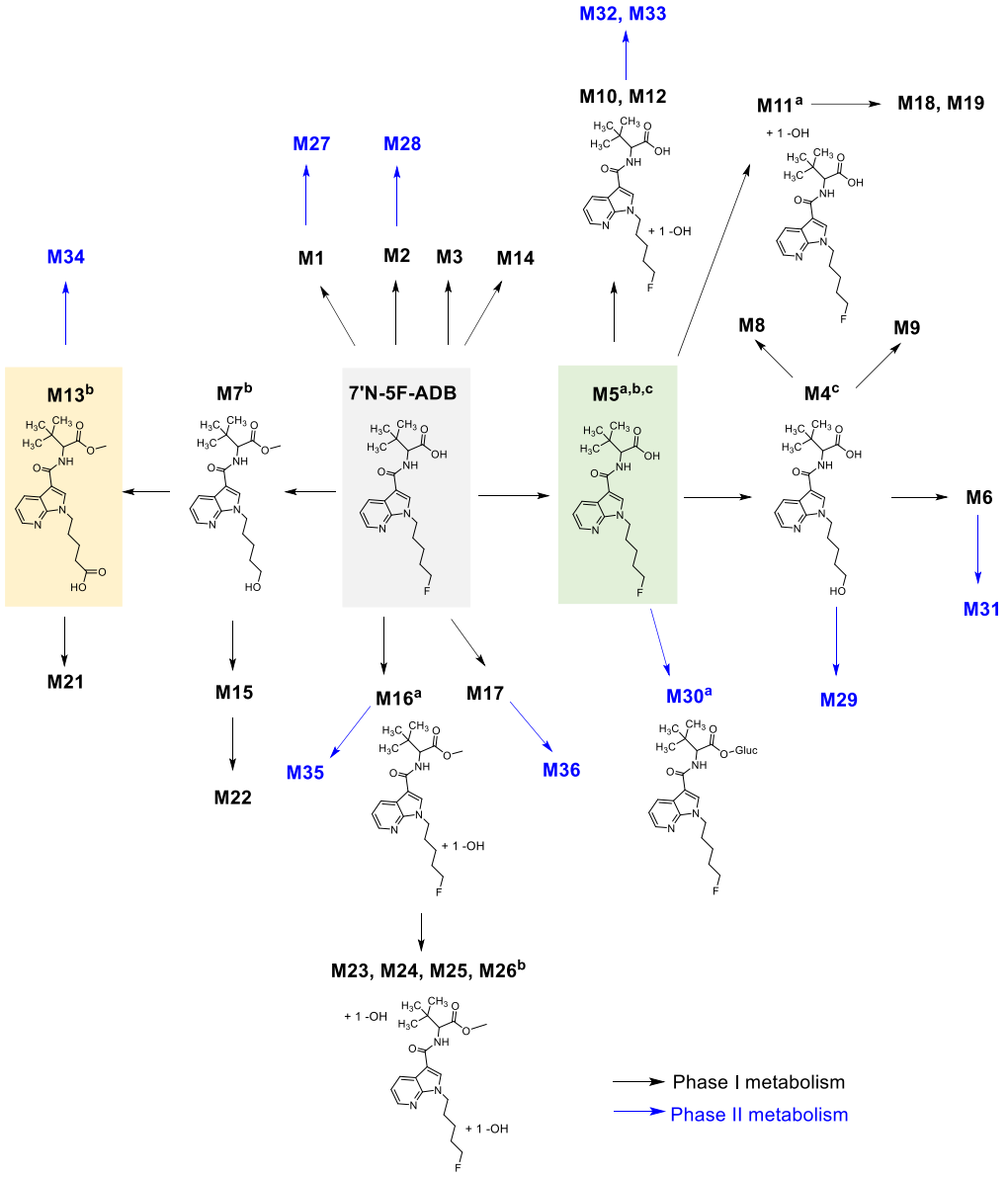

Figure 5. Overview of the reconstructed metabolic pathway of 7′*N*-5F-ADB based on the results from all investigated models. The progress of phase I metabolism is represented and the two major metabolites detected in all ZF larvae exposed to 7′*N*-5F-ADB, which were M5 and M13, are highlighted by a green and yellow box, respectively. Resulting phase II metabolites are displayed in blue. [a] Major metabolites in human samples; [b] major metabolites in microinjected ZF larvae; [c] major metabolites in HepaRG cells. A schematic representation of the reconstructed pathway from all three models can be found in Supplementary Figure S5.

2.4.2. The Spatial Distribution of 7′N-5F-ADB in ZF Larva is Visualized by MALDI-MSI

Mass spectrometry imaging (MSI) combined with MALDI enables coupling of high mass resolution data with visualized images of sample sections. Due to the results from metabolite detection following different administration routes for 7′*N*-5F-ADB into ZF larvae, we concluded that the drug distribution differs significantly if the NPS is given through the water, microinjected into yolk sac, or microinjected into caudal vein, heart ventricle, and hindbrain.

Thus, MALDI-MSI was used to study the distribution of the parent compound 7′*N*-5F-ADB in the ZF larval bodies. To our knowledge, this is the first concise study of drug distribution in ZF larvae following different routes of compound microinjection.

After 1-day exposure through medium, only 7′*N*-5F-ADB could be detected via MSI of sections of ZF larvae, and the parent compound exclusively accumulated inside the yolk sac. Therefore, we prepared ZF larvae that were treated for an extended period, from two days post-fertilization (dpf) to five dpf. In sections from these ZF larvae, we found the parent compound to be better distributed than in sections of one-day treated ZF larvae (Figure 6a, b). In summary, 7′*N*-5F-ADB and two major metabolites (M5 and M13; Figure 6c, d) appeared in dorsal and ventral regions at high abundances after 3 d treatment through aquatic exposure, but corresponding masses could not be detected in the tail end area of ZF larva.

In contrast, it was not possible to generate distribution images of the parent compound and M13 in ZF larvae that were treated by microinjecting into caudal vein, heart ventricle, and hindbrain (Table 3), and M5 was identified in only one section among heart ventricle samples. This might be indicative of a fast distribution and an accordingly fast metabolism. We thus analyzed the spatial distribution of other major metabolites and compared their distribution to MSI data from ZF larvae that were exposed to 7′*N*-5F-ADB through water. We were able to image five metabolites from microinjected ZF larvae, all of which were structural isomers as determined by LC-HRMS/MS: M8/M9 (two isomers at *m*/*z* 378.2013), M10/M11/M12 (three isomers at *m*/*z* 380.1970), M16/M17 (two isomers at *m*/*z* 394.2126), M18/M19/M20 (three isomers at *m*/*z* 396.1919), and M23/M24/M25/M26 (four isomers at *m*/*z* 410.2075). The main metabolites that we could visualize by MSI are also listed in Table 3, and exemplary images of the isomers M23/M24/M25/M26 from larvae that were exposed through microinjection into different organs are depicted in Figure 7. Interestingly, depending on the route of administration, the images show distinct distribution patterns inside the larval bodies. In the caudal vein slices, the metabolite was detected along the dorsal aorta and concentrated in the veins and arteries of ZF larva. ZF larva microinjected into heart ventricle showed full spread of M23/M24/M25/M26 from head region to tail region, and high concentrations were found throughout the larval body. In contrast, hindbrain slices indicated the best distribution of this metabolite at intermediate concentrations. Images of these isomeric metabolites visualized by MALDI-MSI are represented as the summed distribution of the multiple isomers, as these constitutional and isobaric isomers cannot be distinguished due to lack of chromatographic separation in MSI. However, the presence of several isomers probably improved mass detection and imaging above the method detection limit (MDL).

Table 3. Comparison of the major metabolites visualized in ZF larva by MALDI-FT-ICR.

	Aquatic Exposure		**Microinjection[+]**		
	1-Day Exposure (from 4 dpf to 5 dpf)	**3-Day Exposure (from 2 dpf to 5 dpf)**	**Caudal Vein**	**Heart Ventricle**	**Hindbrain**
most abundant peak	P	P	M23/M24/ M25/M26	M23/M24/ M25/M26	M23/M24/ M25/M26

second most abundant peak	M13*	M13	M16/M17	M18/M19/ M20	M16/M17
third most abundant peak	M5*	M5	M18/M19/M20	M16/M17	M18/M19/M20

P: Parent compound (7′*N*-5F-ADB) * Metabolites were detected at very low abundance and could not be visualized in the sections of ZF larvae. † Microinjected ZF larvae were incubated at 28 °C for 1 h.

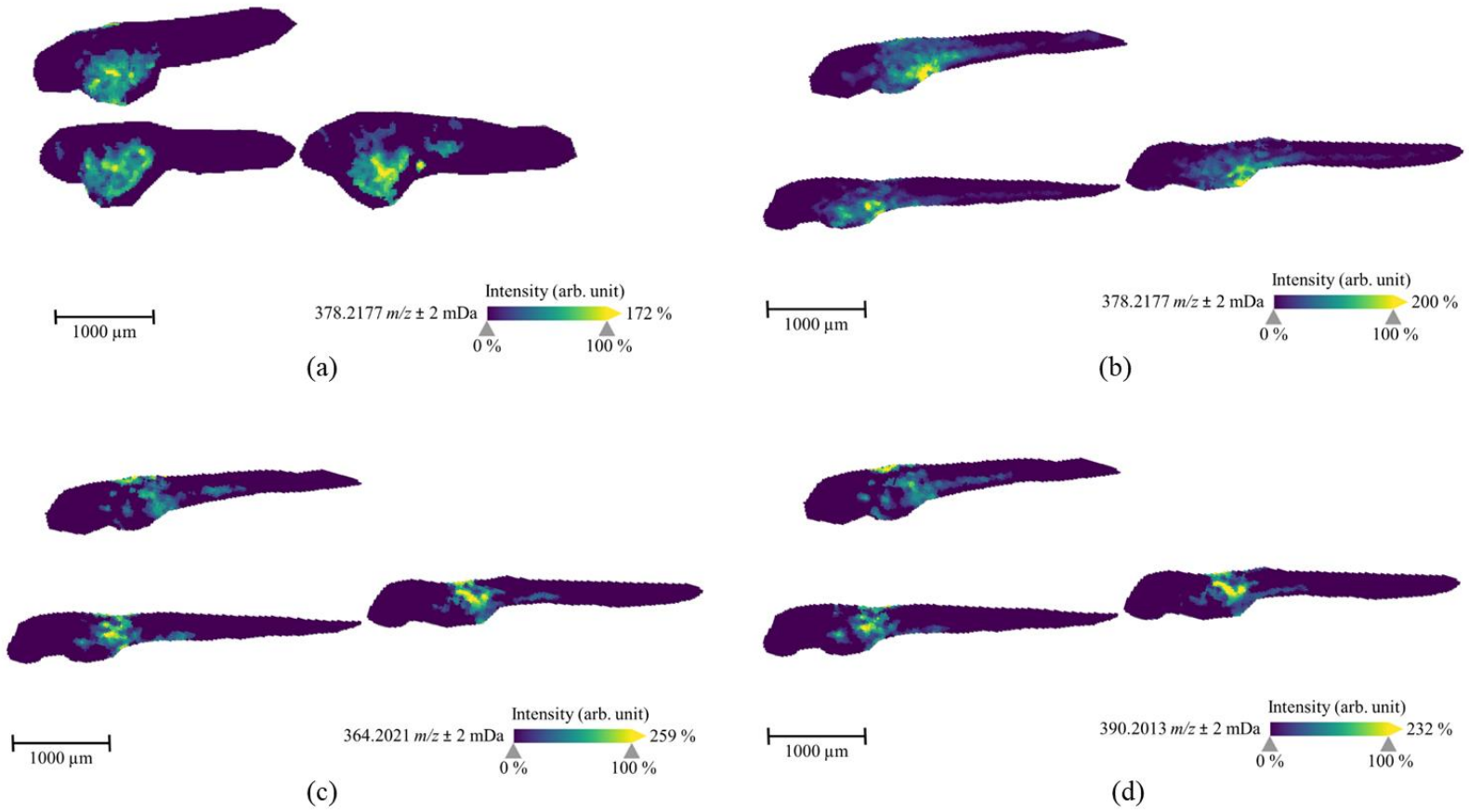

Figure 6. MALDI-MS images of the parent compound (7′*N*-5F-ADB, *m*/*z* 378.2177) in ZF larvae that were treated by aquatic exposure with 50 µM 7′*N*-5F-ADB for 1 d from 4 dpf to 5 dpf (**a**) or for 3 d from 2 dpf to 5 dpf (**b**). The MS images of two metabolites [M5, *m*/*z* 364.2021 (**c**) and M13, *m*/*z* 390.2013 (**d**)] visualized in the slices of B specimen. These metabolites were detected as the most abundant masses in all ZF larvae exposed via various administration routes. The presented sections originate from one representative larva per condition. The images were generated by preparing a colormap from blue (no detection) to yellow (high local concentration), and images were further processed by weak denoising in 96 dpi resolution with 24-bit color.

2.4 Results and Discussion

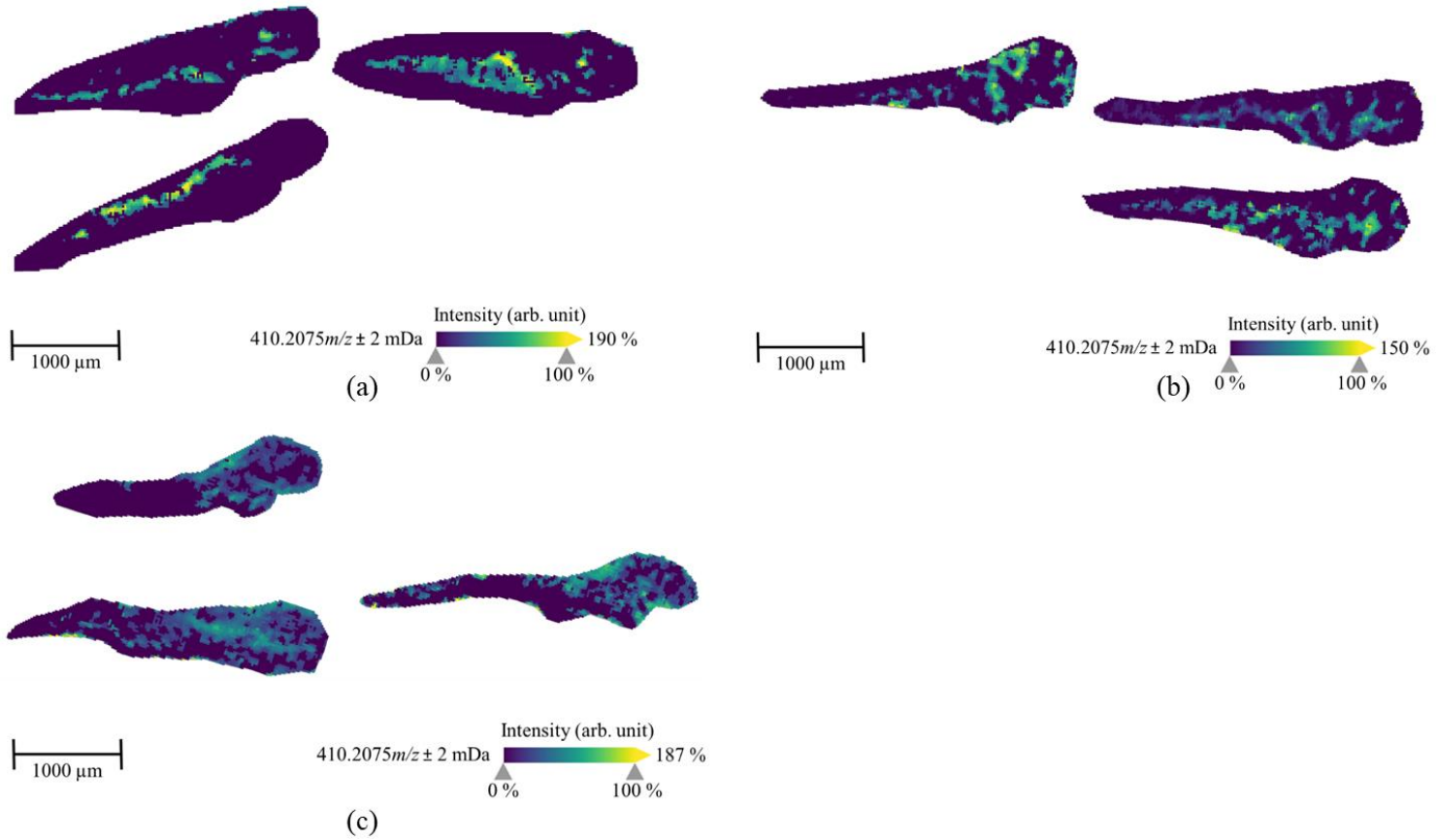

Figure 7. MALDI-MS images of the metabolite M23/M24/M25/M26 (four isomers, *m/z* 410.2075) in ZF larvae, which were exposed to 7′*N*-5F-ADB via microinjection into caudal vein (**a**), heart ventricle (**b**), and hindbrain (**c**) and then incubated at 28 °C for 1 h. These isomeric metabolites were the third most abundant in microinjected ZF larvae except ZF larvae treated through the yolk sac compartment. However, they cannot be differentiated in MSI due to lack of chromatographic separation. The presented sections originate from one representative larva per condition. The images were generated by preparing a colormap from blue (no detection) to yellow (high local concentration), and images were further processed by weak denoising in 96 dpi resolution with 24-bit color.

In the MSI study, we observed a certain discrepancy when we compared the detection of metabolites from LC-HRMS/MS and MSI. Although MSI is a highly sensitive method at trace level, it could not detect the masses in some cases that were clearly detected by LC-HRMS/MS in pooled larvae samples. This effect was caused by the spatial distribution of lower abundant metabolites in the ZF larva and their further dilution due to the preparation of on average more than ten cryosectioned slices per larva. In particular, several metabolites, including M5 and M13, from microinjected ZF larvae were confirmed by LC-HRMS/MS, but it was not possible to generate MS images displaying a specific pattern. Further studies to improve the MDL of MALDI-MSI for the analysis of ZF larvae are ongoing. In summary, the treatment of ZF larvae with 7'*N*-5F-ADB through aquatic exposure resulted in a strong accumulation of the lipophilic NPS in the yolk sac, thus, protecting the compound from being metabolized in metabolically active organs. In contrast, when 7'*N*-5F-ADB was microinjected into vital organs of the ZF larvae, this resulted in the fast distribution and metabolism of the drug, as demonstrated by LC-HRMS/MS and MSI measurements. Furthermore, the finding was confirmed by the spatial distribution analysis of 7'*N*-5F-ADB and its metabolites in ZF larvae treated via microinjection.

We could demonstrate the importance of choosing the right administration route when studying drug metabolism in ZF larvae, also taking the chemical properties of the investigated compound into consideration. Here, the lipophilic nature of 7'*N*-5F-ADB hindered its proper distribution inside the larval bodies when given through water or when microinjected into the yolk sac. Intriguingly, we could observe a large number of (human) phase I and phase II metabolites at relatively high abundance when we microinjected the NPS into organs that support faster distribution, such as the heart ventricle. Moreover, the MS images showed distinct distribution patterns of its metabolites throughout the ZF larva body, which might be linked in future studies to potential toxic effects of compounds and their *in vivo* metabolites. Further studies are in progress to refine protocols for the cryosectioning of ZF larva and subsequent MSI experiments as it appears to be crucial to initially investigate compound distribution before proceeding to metabolite identification and to general pharmacological studies.

2.4.3. Comparison of Metabolite Identification in the *In Vitro* HepaRG Model and from ZF Larvae

The hepatic stem cell line HepaRG expresses cytochrome P450 biotransformation enzymes, phase II enzymes, and several transporters, which make it a prominent screening tool in toxicology and drug discovery studies. Due to the easy handling of the HepaRG cell line, it is a good alternative to primary human hepatocytes which are also often used as predictive *in vitro* model [36,37].

The metabolism of 7'*N*-5F-ADB in HepaRG cells was investigated referring to a previous study [24], and compared to the zebrafish larvae model. Furthermore, the time-dependent metabolism of 7'*N*-5F-ADB and formation of its metabolites was studied by analyzing

cells after 0.1, 15, 60, 120, 240, 360, and 1,440 min of incubation. These time points were chosen based on waterborne exposure duration of ZF larvae (24 h) in order to study time-resolved metabolite formation within this period. HepaRG cells treated with 50 µM of 7′*N*-5F-ADB produced a total of twenty metabolites (Table 1). M5 formed by ester hydrolysis was the most abundant metabolite, which is in accordance to results from microinjected ZF larvae. M4 (ester hydrolysis in combination with oxidative defluorination), M10 and M11 (two isomers formed by ester hydrolysis in combination with hydroxylation of the tertiary butyl), and M30 (ester hydrolysis in combination with glucuronidation) were detected as the second-most abundant metabolites. However, M13, which was detected as a major metabolite in ZF larvae samples, was only found in minor amounts in HepaRG cells.

The concentration of 7′*N*-5F-ADB steadily increased up to 60 min and then declined significantly (Figure 8 and Supplementary Figure S2). Its metabolites had started to form markedly at this time point. Amounts of M5, M10, M11, and M30 were dramatically increased between 360 min and 1440 min, whereas M4 was increasing only slowly (Supplementary Figure S3).

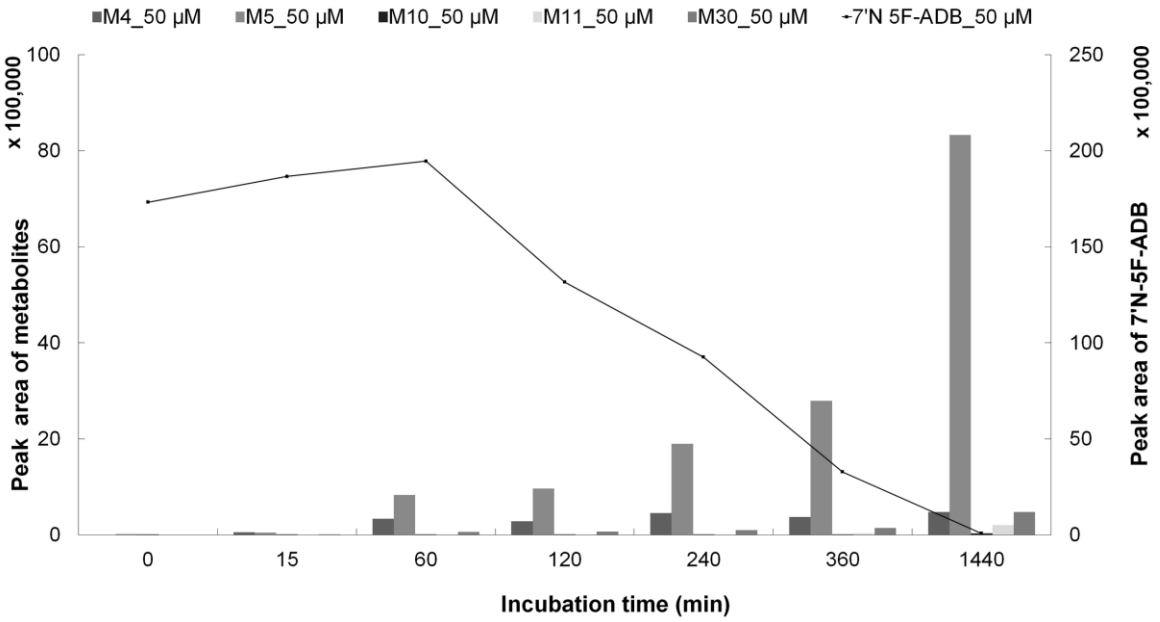

Figure 8. Internal amount-time profile of five main metabolites (M4, M5, M10, M11, and M30) in HepaRG cells incubated with 50 µM 7′*N*-5F-ADB (n = 2).

Twenty metabolites could be produced in HepaRG cells with M5 and M4 being the most abundant metabolites. Interestingly, M22 (oxidative defluorination in combination with dihydroxylation of the pentyl chain) was found only in HepaRG cells, which was not detected in the human biosamples and ZF larvae samples. However, the detection of M22 was reported in rat urine samples of a published study [27]. In contrast, M23/M24/M25/M26, M28 (ester hydrolysis in combination with *N*-dealkylation and glucuronidation), and M34 (oxidative defluorination in combination with oxidation to carboxylic acid and glucuronidation)

were not detected in HepaRG cells. The main metabolic pathway in HepaRG cells was constructed (Supplementary Figure S3) and 18 metabolites observed in HepaRG cells were also found in microinjected ZF larvae, corresponding to a 75% match rate. Fifteen metabolites from HepaRG were also detected in human urine samples, which corresponds to a 55% match rate (Table 1 and Figure 3). In conclusion, HepaRG cells constitute a valid *in vitro* model that can complement the *in vivo* ZF larvae model in drug metabolism studies.

2.5 Materials and Methods

2.5.1. Chemicals and Other Materials

7′*N*-5F-ADB was obtained from www.buyresearchchemicals.de tagged as 4′*N*-5F-ADB. However, NMR (nuclear magnetic resonance) studies confirmed it to be 7′*N*-5F-ADB. Dimethyl sulfoxide (DMSO), methylene blue, phenol red, tricaine (3-amino-benzoic acid ethyl ester), mineral oil, trifluoroacetic acid, gelatin from cold water fish skin, and 2,5-dihydroxybenzoic acid were obtained from Sigma-Aldrich (Taufkirchen, Germany). Methanol (LC-MS grade), acetonitrile (LC-MS grade), formic acid (LC-MS grade) were from VWR (Darmstadt, Germany). NaCl, KCl, $MgSO_4$, $Ca(NO_3)_2$, and HEPES were obtained from Carl Roth (Karlsruhe, Germany). The 10 mM stock solution of 7′*N*-5F-ADB was prepared in DMSO and it was stored for a maximum of one month at −20°C. The working solutions of 7′*N*-5F-ADB were freshly prepared prior to each experiment. Cell culture flasks, 24-well plates, and 6-well plates were purchased from Sarstedt (Nümbrecht, Germany). Basal hepatic cell medium MIL 700C and differentiation medium supplement with antibiotics ADD 720C were from Biopredic International (Saint-Grégoire, France). Glass capillaries TW100F-4 [4 inch (100 mm), 1/0.75 OD/ID (mm), Filament] were obtained from World Precision Instruments Germany GmbH (Friedberg, Germany). Undifferentiated HepaRG cells (HPR101) were purchased from Biopredic International (under MTA agreement No: 10528AHR10, Saint-Grégoire, France). Conductive indium-tin-oxide (ITO) coated glass slides were obtained from Bruker Daltonics (Bremen, Germany). ZF embryos of the AB wild-type line were initially obtained from the Luxembourg Center for Systems Biomedicine (Belvaux, Luxembourg). Dry small granulate food was purchased from SDS Deutschland (Limburgerhof, Germany), and *Artemia* cysts (> 230,000 nauplii per gram) were obtained from Coralsands (Wiesbaden, Germany).

2.5.2. Zebrafish Maintenance and Embryo Collection

ZF husbandry and all experiments with ZF larvae were carried out in accordance with EU Directive 2010/63/EU and the German Animal Welfare Act (§11 Abs. 1 TierSchG). All works were performed following internal standard-operating procedures (SOPs) based on published standard methods [38].

Adult zebrafish for breeding were kept in an automated aquatic eco-system (PENTAIR, Apopka, UK). The following parameters are continuously monitored: Temperature (27 ± 0.5 °C), pH (7.0 ± 0.1), conductivity (800 ± 50 μS), and light-dark cycle (14 h/10 h). Fish were fed twice a day with dry small granulate food and additionally once a day with freshly hatched live *Artemia* cysts. The ZF embryo medium (0.3× Danieau's solution) consisted of 17 mM NaCl, 2 mM KCl, 0.12 mM $MgSO_4$, 1.8 mM $Ca(NO_3)_2$, 1.5 mM HEPES, pH 7.1–7.3, and 1.2 μM methylene blue. For ZF embryo production, AB wild-type line pairs were kept overnight in standard mating cages, separated by gender. In the following morning, the separators were removed, and the zebrafish spawned immediately. Fertilized eggs of zebrafish were selected using a LEICA M205 FA stereo microscope (Leica Mikrosysteme Vertrieb GmbH,

Wetzlar, Germany), and embryos were raised in an incubator at 28 °C with daily medium change and cleaning of embryo cultures. ZF larvae at 4 dpf were used for drug metabolism studies.

2.5.3. Drug Treatment of ZF Larvae via Aquatic Exposure

The sample preparation following aquatic drug exposure is described in detail in a study by Richter et al. [24]. A non-toxic exposure concentration was chosen based on the survival rate as determined in *in vivo* maximum-tolerated concentration (MTC) experiments with 4 dpf ZF larvae. For metabolite studies, ten ZF larvae at 4 dpf were transferred to one well of a 6-well plate containing 3 mL of Danieau's medium with 50 µM 7'*N*-5F-ADB and a final concentration of 1% (*v*/*v*) DMSO, and ZF larvae were treated for 24 h in an incubator at 28 °C. Additional ten larvae were incubated in compound-free medium containing 1% (*v*/*v*) DMSO that served as negative control (background masses). Prior to sample extraction, ten larvae were pooled, and sample extractions were performed as described below (Section 2.5.5). All samples were prepared in six replicates.

2.5.4. Drug Treatment of ZF Larvae via Microinjection into Different Compartments

The glass microneedle for microinjection was prepared by a Flaming/Brown type micropipette puller (Model P-100, Sutter Instrument, Novato, CA, USA) using the following settings: heat: ramp value ± 10, pull: 80, velocity: 60, delay time: 90 ms, and pressure: 13.8 bar. For injections, a 5 mM solution of 7'*N*-5F-ADB was prepared in 50% (*v*/*v*) DMSO and 50% (*v*/*v*) of a 0.5% phenol red solution. The injection needle was filled with 10 µL of 5 mM 7'*N*-5F-ADB without air bubbles by a microloader pipette tip and it was placed in a M-152 manipulator (Narishige Group, Tokyo, Japan) connected to a FemtoJet 4× Microinjector (Eppendorf, Hamburg, Germany). Before microinjection, all microinjection needles were calibrated by single droplet injections onto mineral oil on a micrometer slide. The injection volume (nL) was calculated according to the sphere volume equation ($V = \pi\gamma^3\ 4/3$) based on the diameter (mm) of the droplet [39,40]. We have chosen to microinject 4.19 nL of 5 mM 7'*N*-5F-ADB per larvae, which corresponds to a total amount of 284.4 ng in a pool of 36 larvae.

ZF larvae at 4 dpf were anaesthetized by tricaine and then they were lined up on an agarose plate prepared using Z-MOLD (World Precision Instruments, Sarasota, USA). Excess medium was removed with a pipette. Microinjections were done into three different compartments of ZF larvae (caudal vein, heart ventricle, and hindbrain; Figure 9) under a stereo microscope (LEICA M205 FA stereo microscope). Larvae were directly transferred to fresh Danieau's medium and they were incubated at 28 °C for 1 h. Prior to sample extraction, 36 larvae were pooled. Sample extractions were performed as described below (Section 2.5.5). All samples were prepared in triplicates. The mortality rate of ZF larvae after microinjection was below 10% in all cases.

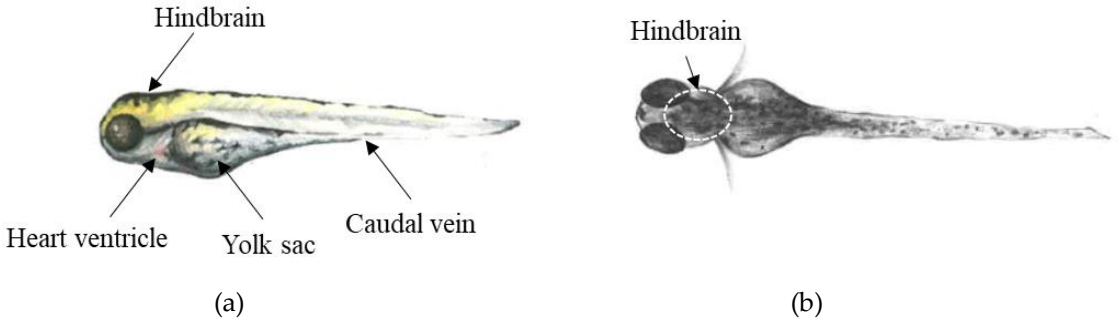

Figure 9. Microinjection sites used to administer 7′*N*-5F-ADB to 4 dpf ZF larvae in (**a**) lateral and (**b**) dorsal view.

2.5.5. ZF Sample Preparation and Metabolite Analysis by LC-HRMS/MS

After exposure (see Sections 2.5.3 and 2.5.4), all larvae were transferred into a tube using a pipette and then washed twice with 1 mL of Danieau's solution. The cleaned larvae were euthanized by placing the tubes in ice water for 15 min. Samples were snap-frozen in liquid nitrogen, followed by lyophilization for 4 h. The lyophilized larvae were stored for a maximum of one week at –20 °C until extraction. For metabolite identification, frozen larvae were thawed at room temperature for at least 30 min and extracted by vigorous vortexing for 2 min with 50 µL methanol. The sample was centrifuged at 10,000× *g* for 2 min at room temperature. All of the supernatant was transferred to an autosampler vial, and 5 µL was injected onto the LC-HRMS/MS system consisting of a Dionex Ultimate 3000 RSLC system (Thermo Fisher Scientific, Germering, Germany) and maXis 4G HR-QTOF mass spectrometer (Bremen, Germany) with the Apollo II ESI source. Separation was carried out on a Waters ACQUITY BEH C_{18} column (100 × 2.1 mm, 1.7 µm) equipped with a Waters VanGuard BEH C_{18} 1.7 µm guard column at 45 °C using 0.1% formic acid in water (*v*/*v*, eluent A) and 0.1% formic acid in acetonitrile (*v*/*v*, eluent B) at a flow rate of 600 µL/min. The linear gradient mode was as follows; 0–0.5 min, 5% eluent B; 0.5–18.5 min, 5–95% eluent B; 18.5–20.5 min, 95% eluent B; 20.5–21 min, 95–5% eluent B; 21–22.5 min, 5% eluent B.

Mass spectra were acquired in centroid mode ranging from 150–2,500 *m*/*z* at a 2 Hz full scan rate in the positive ion mode and MS/MS data were collected with automatic precursor selection including the masses of the inclusion list, which was set up for 7′*N*-5F-ADB and its expected metabolite. The precursor ion mass and MS^2 data (Supplementary Figure S4) were used to confirm the structures of the metabolites [24,27]. Mass spectrometry source parameters were set to 500 V as end plate offset; capillary voltage, 4000 V; nebulizer gas pressure, 1 bar; dry gas flow, 5 L/min, and dry temperature, 200 °C. Ion transfer and quadrupole settings were set to funnel RF 350 Vpp; Multipole RF, 400 Vpp as transfer settings; ion energy, 5 eV as well as a low mass cut of 300 *m*/*z* as quadrupole settings. Collision cell was set to 5 eV; pre-pulse storage time, 5 µs; spectra acquisition rate, 2 Hz. Calibration was carried out automatically before every LC-HRMS/MS run by injection of sodium formate and calibration on the sodium formate clusters forming in the ESI source. All MS analyses were acquired in the presence of the lock masses $C_{12}H_{19}F_{12}N_3O_6P_3$, $C_{18}H_{19}O_6N_3P_3F_2$, and

$C_{24}H_{19}F_{36}N_3O_6P_3$ which generate the $[M + H]^+$ ions of *m/z* 622.0290, 922.0098, and 1221.9906. DataAnalysis software version 4.2 (Bruker Daltonics, Bremen, Germany) was used for qualitative analysis. All data were presented as the range of mean and standard deviation (SD) using MS Excel 2016.

Analyzing metabolite data, structural isomers were numbered individually when their corresponding peaks could be separated by chromatography. When isomers where co-eluting, they were analyzed together as one peak as assigned in the tables of this study. In addition, the peak area of each metabolite was taken into consideration when constructing the metabolic pathway of 7'*N*-5F-ADB. Due to the lack of reference standards that would be needed for absolute quantification, our analyses of relative abundances of metabolites relies on the quantification of peak areas, assuming similar ionization behaviors of the individual metabolites.

2.5.6. *In Vitro* Metabolism Analyses Using HepaRG Cells

To compare the metabolism of an *in vitro* model to ZF larvae, HepaRG cells were investigated as already described by Richter et al. [24]. Undifferentiated cells frozen in a vial were thawed and seeded into T-75 flasks with a dilution factor of 10 (*v*/*v*) at 37 °C in a humidified incubator (95% air humidity, 5% CO_2). Cell medium was renewed every other day, and cells were sub-cultured to 2×10^6 cells/cm^2 in T-75 flasks in a total of 15 mL growth medium. After two weeks of proliferation, cells were seeded at a density of 1×10^5 cells/cm^2 with 2 mL growth medium in 6-well cell culture plates. For the process of cell differentiation, growth medium was replaced with differentiation medium for two more weeks and maintained with medium renewal every second day. Cells for drug metabolism experiments were at passage 18, and all the steps of cell preparation were performed under sterile conditions according to the manufacturer's instruction (Biopredic International).

Afterwards, the growth medium was composed of MIL 700C (basal hepatic cell medium) supplemented with ADD 720C (differentiation medium supplement with antibiotics), and it was pre-warmed to 37 °C before usage. 500 µL aliquots of medium were removed from the 6-well cell culture plate, and treatment was started by adding 500 µL of 7'*N*-5F-ADB solution. The solutions were prepared by the addition of compound to the growth medium at final concentrations of 20 µM with 0.2% (*v*/*v*) DMSO and 50 µM with 0.5% (*v*/*v*) DMSO.

Treatment was stopped after 0.1, 15, 60, 120, 240, 360, and 1,440 min (24 h), and 100 µL-supernatants of medium were transferred into a tube. 100 µL of cold acetonitrile with 0.1% formic acid was immediately added for extraction. Samples were vortexed and cooled in a freezer for 30 min at −20 °C. The samples were centrifuged at 10,000× *g* for 2 min at 4 °C and the supernatant was transferred to an autosampler vial. All samples were then dried *in vacuo* and resuspended with 50 µL of acetonitrile containing 0.1% formic acid. 5 µL was injected onto the LC-HRMS/MS system. All incubation conditions were done in duplicates. Data acquisition and analysis were performed as described in Section 2.5.5.

2.5.7. MSI Analysis of ZF Larva by MALDI-FT-ICR

Treated ZF larvae (see Sections 2.5.3 and 2.5.4) were directly frozen after embedding in 40% (*w*/*v*) gelatin solution and samples were stored at –20 °C until cryosectioning. Cuts with 10-µm thickness from single larvae were prepared using a cryostat (MEV; SLEE, Mainz, Germany) and they were put on a cold conductive indium-tin-oxide (ITO) coated glass slide. After scanning slides under a microscope to align the optical image of the sample in MALDI, the serial sections from one larva were deposited using TM-Sprayer (HTX M5; HTX Technologies, NC, USA) with 15 mg mL^{-1} 2,5-dihydroxybenzoic acid (2,5-DHB) in acetonitrile:water (9:1, *v*/*v*) containing 0.1% of trifluoroacetic acid, and then dried in a vacuum desiccator for 2 h. The dried glass slide was stored at –20 °C before MSI measurement.

MSI analysis was performed using MALDI and 7.0T SolariX FT-ICR (Bruker Daltonics, Bremen, Germany) in positive ion mode (*m*/*z* range 150–1,000), using 40 laser shots per pixel with a raster width of 20 µm. For auto-calibration of MALDI of each laser measurement, lock mass was set to *m*/*z* 273.039364 (2,5-DHB matrix), and mass calibration of FT-ICR was carried out using the calibration solution according to the manufacturer's manual. All MALDI-MSI data acquisitions and image analyses in two dimensions were processed using ftmsControl version. 2.2, flexImaging version 5.0, and SCiLS Lab version 2019b Pro softwares (Bruker Daltonics, Bremen, Germany).

2.6 Summary and Conclusions

ZF larvae were exposed to 7′*N*-5F-ADB by different administration routes and the total number of metabolites observed in these microinjected samples was higher than the number of metabolites detected after conventional waterborne exposure (Table 1). The only exception was the ZF larvae sample, where the NPS was microinjected into yolk sac. Here, only one metabolite was found [24], which we could later explain by the compound's lack of distribution in metabolically active organs of the larvae. Furthermore, the spatial distribution of 7′*N*-5F-ADB and its metabolites was investigated in detail by MSI and we found significant differences following aquatic exposure and microinjection into different organs (Figures 6 and 7).

Comparing the metabolite pattern from all investigated models (human [27], HepaRG cells, ZF larvae) using LC-HRMS/MS, metabolite M5, formed by ester hydrolysis, was among the most abundant peaks in human samples, HepaRG cells, and all ZF larvae samples prepared in this study. The parent compound was detected in high amounts in all samples except human urine samples, and the metabolites listed as next most abundant were M4 (oxidative defluorination of M5), M30 (glucuronidation of M5), M11 (hydroxylation of M5 in the tertiary butyl part), M13 (oxidation defluorination in combined with oxidation to carboxylic acid), and M16 (hydroxylation of the fluoro pentyl chain isomer 1) (Table 2). These results suggest that the major metabolites were produced sequentially from M5 and the main metabolic reactions were oxidation and hydroxylation as part of phase I metabolism. Interestingly, most of the glucuronidated conjugate metabolites found in human urine were also detected in significant amounts in microinjected ZF larvae (Table 1, Figure 5, Supplementary Figures S1 and S5). Fifteen phase I and phase II metabolites were commonly observed in the three models, which were generated by amide hydrolysis, ester hydrolysis, hydroxylation of the alkyl chains, and glucuronidation (Figure 3a and Table 1).

Remarkably, microinjected ZF larvae had a high concordance rate of 70% to human urine samples, compared to only 55% concordance of HepaRG cell metabolites to human metabolites (Figure 3b). While comparing the mutual similarity of metabolism among the three investigated models, ZF larvae were able to generate four metabolites also found in human urine, which were, however, not detected in HepaRG cells. Encouragingly, 18 out of 20 HepaRG metabolites were also found in ZF larvae, which included 15 compounds that were detected in all three models. It is noteworthy that it could be shown again that ZF larvae produce a metabolite spectrum which is highly similar to human *in vitro* and *in vivo* metabolism. Furthermore, the metabolic pathway of 7′*N*-5F-ADB [24,27] was refined and extended by addition of the results from ZF larvae and HepaRG cells (Figure 5).

Taken together, among the studied models, microinjected ZF larvae generated a high number of metabolites and the most authentic spectrum of human metabolites of 7′*N*-5F-ADB. Intriguingly, metabolic reactions could be observed already within one hour after microinjection. In contrast, at least 24 h waterborne treatment of ZF larvae was necessary to identify most common metabolites.

2.6 Summary and Conclusions

Due to its ease of handling and flexibility when it comes to the administration route of compounds, and because of being in accordance with results from human metabolism studies, the ZF larvae model is an excellent *in vivo* tool for drug metabolism and distribution studies. This is also owing to the fact that we could successfully prepare MS images of treated larvae, which allows us to rationally choose an appropriate route for compound administration. Although further optimization of MSI applied to ZF larvae [33] and the generation of metabolite images need to be done, it is already a unique tool to get a first impression on the distribution of a drug and its metabolites depending on the route of administration. Here, microinjection in vital organs, such as the heart ventricle, appeared to be most beneficial to achieve fast distribution and metabolism of the highly lipophilic 7'*N*-5F-ADB.

2.7 Acknowledgments

The authors would like to thank Mi Sun Park for the pictures of zebrafish larvae and Katarina Cirnski, Anastasia Andreas, Susanne Kirsch-Dahmen, and Lea Wagmann for skillful technical support and fruitful discussion.

2.8 Bibliography

1. Zhang, Q.; Ji, C.; Yan, L.; Lu, M.; Lu, C.; Zhao, M. The identification of the metabolites of chlorothalonil in zebrafish (Danio rerio) and their embryo toxicity and endocrine effects at environmentally relevant levels. *Environ. Pollut.* **2016**, *218*, 8–15, doi:10.1016/j.envpol.2016.08.026.
2. Kithcart, A.; MacRae, C.A. Using Zebrafish for High-Throughput Screening of Novel Cardiovascular Drugs. *JACC Basic Transl. Sci.* **2017**, *2*, 1–12, doi:10.1016/j.jacbts.2017.01.004.
3. Brugman, S. The zebrafish as a model to study intestinal inflammation. *Dev. Comp. Immunol.* **2016**, *64*, 82–92, doi:10.1016/j.dci.2016.02.020.
4. Shams, S.; Rihel, J.; Ortiz, J.G.; Gerlai, R. The zebrafish as a promising tool for modeling human brain disorders: A review based upon an IBNS Symposium. *Neurosci. Biobehav. Rev.* **2018**, *85*, 176–190, doi:10.1016/j.neubiorev.2017.09.002.
5. Kamel, M.; Ninov, N. Catching new targets in metabolic disease with a zebrafish. *Curr. Opin. Pharmacol.* **2017**, *37*, 41–50, doi:10.1016/j.coph.2017.08.007.
6. Howe, K.; Clark, M.D.; Torroja, C.F.; Torrance, J.; Berthelot, C.; Muffato, M.; Collins, J.E.; Humphray, S.; McLaren, K.; Matthews, L.; et al. The zebrafish reference genome sequence and its relationship to the human genome. *Nature* **2013**, *496*, 498–503, doi:10.1038/nature12111.
7. Goldstone, J.V.; McArthur, A.G.; Kubota, A.; Zanette, J.; Parente, T.; Jönsson, M.E.; Nelson, D.R.; Stegeman, J.J. Identification and developmental expression of the full complement of Cytochrome P450 genes in Zebrafish. *BMC Genom.* **2010**, *11*, 643, doi:10.1186/1471-2164-11-643.
8. van Wijk, R.C.; Krekels, E.H.J.; Hankemeier, T.; Spaink, H.P.; van der Graaf, P.H. Systems pharmacology of hepatic metabolism in zebrafish larvae. *Drug Discov. Today Disease Models* **2016**, *22*, 27–34, doi:10.1016/j.ddmod.2017.04.003.
9. Wu, J.-Q.; Fan, R.-Y.; Zhang, S.-R.; Li, C.-Y.; Shen, L.-Z.; Wei, P.; He, Z.-H.; He, M.-F. A systematical comparison of anti-angiogenesis and anti-cancer efficacy of ramucirumab, apatinib, regorafenib and cabozantinib in zebrafish model. *Life Sci.* **2020**, *247*, 117402, doi:10.1016/j.lfs.2020.117402.
10. Meijer, A.H. Protection and pathology in TB: Learning from the zebrafish model. *Semin. Immunopathol.* **2016**, *38*, 261–273, doi:10.1007/s00281-015-0522-4.
11. Gomes, M.C.; Mostowy, S. The Case for Modeling Human Infection in Zebrafish. *Trends Microbiol.* **2020**, *28*, 10–18, doi:10.1016/j.tim.2019.08.005.
12. Willis, A.R.; Moore, C.; Mazon-Moya, M.; Krokowski, S.; Lambert, C.; Till, R.; Mostowy, S.; Sockett, R.E. Injections of Predatory Bacteria Work Alongside Host Immune Cells to Treat Shigella Infection in Zebrafish Larvae. *Curr. Biol.* **2016**, *26*, 3343–3351, doi:10.1016/j.cub.2016.09.067.

13. Clatworthy, A.E.; Lee, J.S.-W.; Leibman, M.; Kostun, Z.; Davidson, A.J.; Hung, D.T. Pseudomonas aeruginosa infection of zebrafish involves both host and pathogen determinants. *Infect. Immun.* **2009**, *77*, 1293–1303, doi:10.1128/IAI.01181-08.
14. McVicker, G.; Prajsnar, T.K.; Williams, A.; Wagner, N.L.; Boots, M.; Renshaw, S.A.; Foster, S.J. Clonal expansion during Staphylococcus aureus infection dynamics reveals the effect of antibiotic intervention. *PLoS Pathog.* **2014**, *10*, e1003959, doi:10.1371/journal.ppat.1003959.
15. Papan, C.; Chen, L. Metabolic Fingerprinting Reveals Developmental Regulation of Metabolites during Early Zebrafish Embryogenesis. *OMICS* **2009**, *13*, 397–405.
16. Chng, H.T.; Ho, H.K.; Yap, C.W.; Lam, S.H.; Chan, E.C.Y. An investigation of the bioactivation potential and metabolism profile of Zebrafish versus human. *J. Biomol. Screen.* **2012**, *17*, 974–986, doi:10.1177/1087057112447305.
17. Jones, H.S.; Trollope, H.T.; Hutchinson, T.H.; Panter, G.H.; Chipman, J.K. Metabolism of ibuprofen in zebrafish larvae. *Xenobiotica* **2012**, *42*, 1069–1075, doi:10.3109/00498254.2012.684410.
18. Torraca, V.; Mostowy, S. Zebrafish Infection: From Pathogenesis to Cell Biology. *Trends Cell Biol.* **2018**, *28*, 143–156, doi:10.1016/j.tcb.2017.10.002.
19. Zhao, Y.; Sun, H.; Sha, X.; Gu, L.; Zhan, Z.; Li, W.J. A Review of Automated Microinjection of Zebrafish Embryos. *Micromachines* **2018**, *10*, 7, doi:10.3390/mi10010007.
20. Meijer, A.H.; Spaink, H.P. Host-Pathogen Interactions Made Transparent with the Zebrafish Model. *Curr. Drug Targets* **2011**, *12*, 1000–1017.
21. Schubert, S.; Keddig, N.; Hanel, R.; Kammann, U. Microinjection into zebrafish embryos (Danio rerio)—A useful tool in aquatic toxicity testing? *Environ. Sci. Eur.* **2014**, *26*, 1, doi:10.1186/s12302-014-0032-3.
22. Michiels, E.D.G.; Vergauwen, L.; Lai, F.Y.; Town, R.M.; Covaci, A.; van Nuijs, A.L.N.; van Cruchten, S.J.; Knapen, D. Advancing the Zebrafish embryo test for endocrine disruptor screening using micro-injection: Ethinyl estradiol as a case study. *Environ. Toxicol. Chem.* **2019**, *38*, 533–547, doi:10.1002/etc.4343.
23. Kim, S.-M.; Yoo, J.-A.; Baek, J.-M.; Cho, K.-H. Diethyl phthalate exposure is associated with embryonic toxicity, fatty liver changes, and hypolipidemia via impairment of lipoprotein functions. *Toxicol.* In Vitro **2015**, *30*, 383–393, doi:10.1016/j.tiv.2015.09.026.
24. Richter, L.H.J.; Herrmann, J.; Andreas, A.; Park, Y.M.; Wagmann, L.; Flockerzi, V.; Müller, R.; Meyer, M.R. Tools for studying the metabolism of new psychoactive substances for toxicological screening purposes—A comparative study using pooled human liver S9, HepaRG cells, and zebrafish larvae. *Toxicol. Lett.* **2019**, *305*, 73–80, doi:10.1016/j.toxlet.2019.01.010.
25. De Souza Anselmo, C.; Sardela, V.F.; de Sousa, V.P.; Pereira, H.M.G. Zebrafish (Danio rerio): A valuable tool for predicting the metabolism of xenobiotics in humans? *Comp. Biochem. Physiol. C. Toxicol. Pharmacol.* **2018**, *212*, 34–46, doi:10.1016/j.cbpc.2018.06.005.
26. MacRae, C.A.; Peterson, R.T. Zebrafish as tools for drug discovery. *Nat. Rev. Drug Discov.* **2015**, *14*, 721–731, doi:10.1038/nrd4627.

27. Richter, L.H.J.; Maurer, H.H.; Meyer, M.R. Metabolic fate of the new synthetic cannabinoid 7′ *N*-5F-ADB in rat, human, and pooled human S9 studied by means of hyphenated high-resolution mass spectrometry. *Drug Test. Anal.* **2019**, *11*, 305–317, doi:10.1002/dta.2493.
28. UNODC. Understanding the synthetic drug market: The NPS factor. *Global SMART Update* **2018**, *19*, 11.
29. UNODC. Special Segment Synthetic cannabinoids: Key facts about the largest and most dynamic group of NPS. *Global SMART Update* **2015**, *13*, 11.
30. Europäische Kommission; Europol. *EU Drug Markets Report*. *In-Depth Analysis: 2016*; Publications Office of the European Union: Luxembourg, 2016, ISBN 9789291688432.
31. Hasegawa, K.; Wurita, A.; Minakata, K.; Gonmori, K.; Yamagishi, I.; Nozawa, H.; Watanabe, K.; Suzuki, O. Identification and quantitation of 5-fluoro-ADB, one of the most dangerous synthetic cannabinoids, in the stomach contents and solid tissues of a human cadaver and in some herbal products. *Forensic Toxicol.* **2015**, *33*, 112–121, doi:10.1007/s11419-014-0259-0.
32. Buchberger, A.R.; DeLaney, K.; Johnson, J.; Li, L. Mass Spectrometry Imaging: A Review of Emerging Advancements and Future Insights. *Anal. Chem.* **2018**, *90*, 240–265, doi:10.1021/acs.analchem.7b04733.
33. Kirla, K.T.; Groh, K.J.; Steuer, A.E.; Poetzsch, M.; Banote, R.K.; Stadnicka-Michalak, J.; Eggen, R.I.L.; Schirmer, K.; Kraemer, T. From the Cover: Zebrafish Larvae Are Insensitive to Stimulation by Cocaine: Importance of Exposure Route and Toxicokinetics. *Toxicol. Sci.* **2016**, *154*, 183–193, doi:10.1093/toxsci/kfw156.
34. Dilillo, M.; Ait-Belkacem, R.; Esteve, C.; Pellegrini, D.; Nicolardi, S.; Costa, M.; Vannini, E.; Graaf, E.L.d.; Caleo, M.; McDonnell, L.A. Ultra-High Mass Resolution MALDI Imaging Mass Spectrometry of Proteins and Metabolites in a Mouse Model of Glioblastoma. *Sci. Rep.* **2017**, *7*, 603, doi:10.1038/s41598-017-00703-w.
35. Kimmel, C.B.; Ballard, W.W.; Kimmel, S.R.; Ullmann, B.; Schilling, T.F. Stages of embryonic development of the zebrafish. *Dev. Dyn.* **1995**, *203*, 253–310, doi:10.1002/aja.1002030302.
36. Sevior, D.K.; Pelkonen, O.; Ahokas, J.T. Hepatocytes: The powerhouse of biotransformation. *Int. J. Biochem. Cell Biol.* **2012**, *44*, 257–261, doi:10.1016/j.biocel.2011.11.011.
37. Andersson, T.B.; Kanebratt, K.P.; Kenna, J.G. The HepaRG cell line: A unique in vitro tool for understanding drug metabolism and toxicology in human. *Expert Opin. Drug Metab. Toxicol.* **2012**, *8*, 909–920, doi:10.1517/17425255.2012.685159.
38. Westerfield, M. *The Zebrafish Book. A Guide for the Laboratory Use of Zebrafish (Danio rerio)*; 4th ed., Univ. of Oregon Press, Eugene, OH, USA, **2000**.
39. Rosen, J.N.; Sweeney, M.F.; Mably, J.D. Microinjection of zebrafish embryos to analyze gene function. *J. Vis. Exp.* **2009**, doi:10.3791/1115.
40. Sive, H.L.; Grainger, R.M.; Harland, R.M. Calibration of the injection volume for microinjection of Xenopus oocytes and embryos. *Cold Spring Harb. Protoc.* **2010**, *2010*, pdb.prot5537, doi:10.1101/pdb.prot5537.

2.9 Supporting Information

Drug Administration Routes Impact the Metabolism of a Synthetic Cannabinoid in the Zebrafish Larvae Model

Previously published in:

Molecules, 2020 Sep 29; 25(19):4474. doi: 10.3390/molecules25194474.

Yu Mi Park[1,2], Markus R. Meyer[3], Rolf Müller[1,4,*] and Jennifer Herrmann[1,4,*]

[1]Department of Microbial Natural Products, Helmholtz Institute for Pharmaceutical Research Saarland (HIPS), Helmholtz Centre for Infection Research (HZI) and Department of Pharmacy, Saarland University, Campus E8 1, 66123 Saarbrücken, Germany; Yu-Mi.Park@helmholtz-hips.de

[2]Environmental Safety Group, Korea Institute of Science and Technology (KIST) Europe, 66123 Saarbrücken, Germany

[3]Department of Experimental and Clinical Toxicology, Institute of Experimental and Clinical Pharmacology and Toxicology, Center for Molecular Signaling (PZMS), Saarland University, 66421 Homburg, Germany; m.r.meyer@mx.uni-saarland.de

[4]German Center for Infection Research (DZIF), Partner Site Hannover-Braunschweig Germany

[*]Correspondence: Rolf.Mueller@helmholtz-hips.de (R.M.); Jennifer.Herrmann@helmholtz-hips.de (J.H.); Tel.: +49-0681-98806-3000 (R.M.), +49-0681-98806-3101 (J.H.)

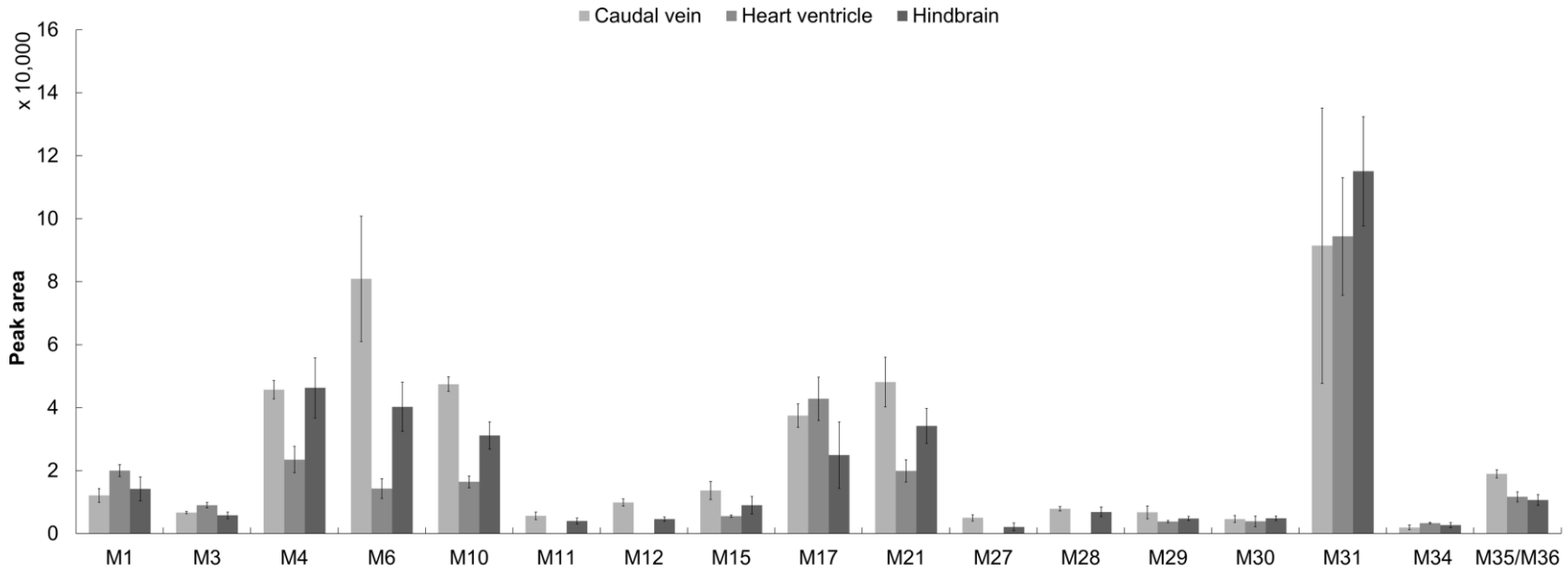

Figure S1. Detection profile of seventeen minor metabolites of 7′*N*-5F-ADB found in ZF larvae injected into three different organs (caudal vein, heart ventricle, and hindbrain). M11, M12, and M28 in the heart ventricle samples were observed with a low peak detection below signal-to-noise (S/N) ratio of 3, which resulted in no detectable peak area in this graph, but there was no detection of M27. Both, M8 and M9 in all microinjected ZF larvae were not quantified due to the low detection below S/N ratio of 3. The clustered columns are displayed as mean ± SD (*n*=3).

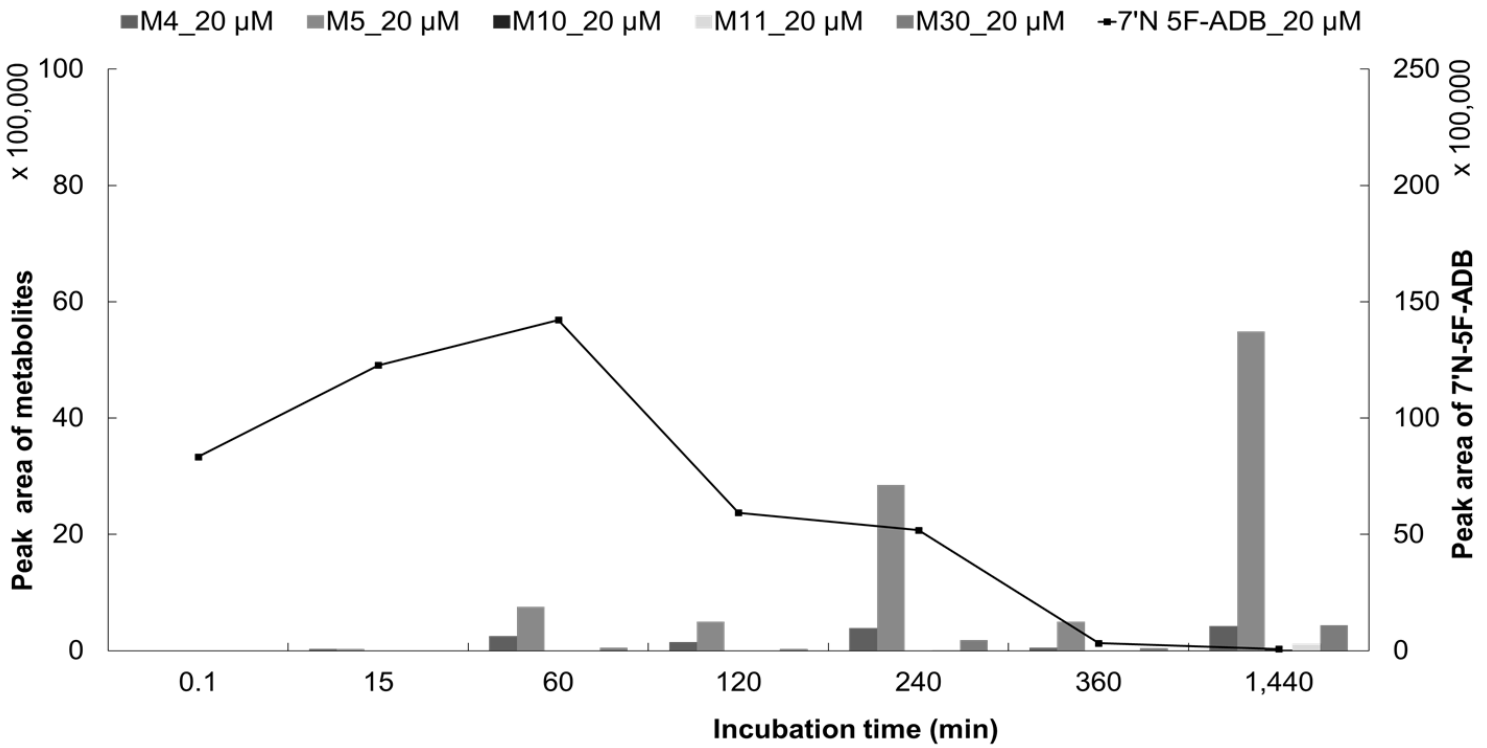

(a)

Figure S2. *Cont.*

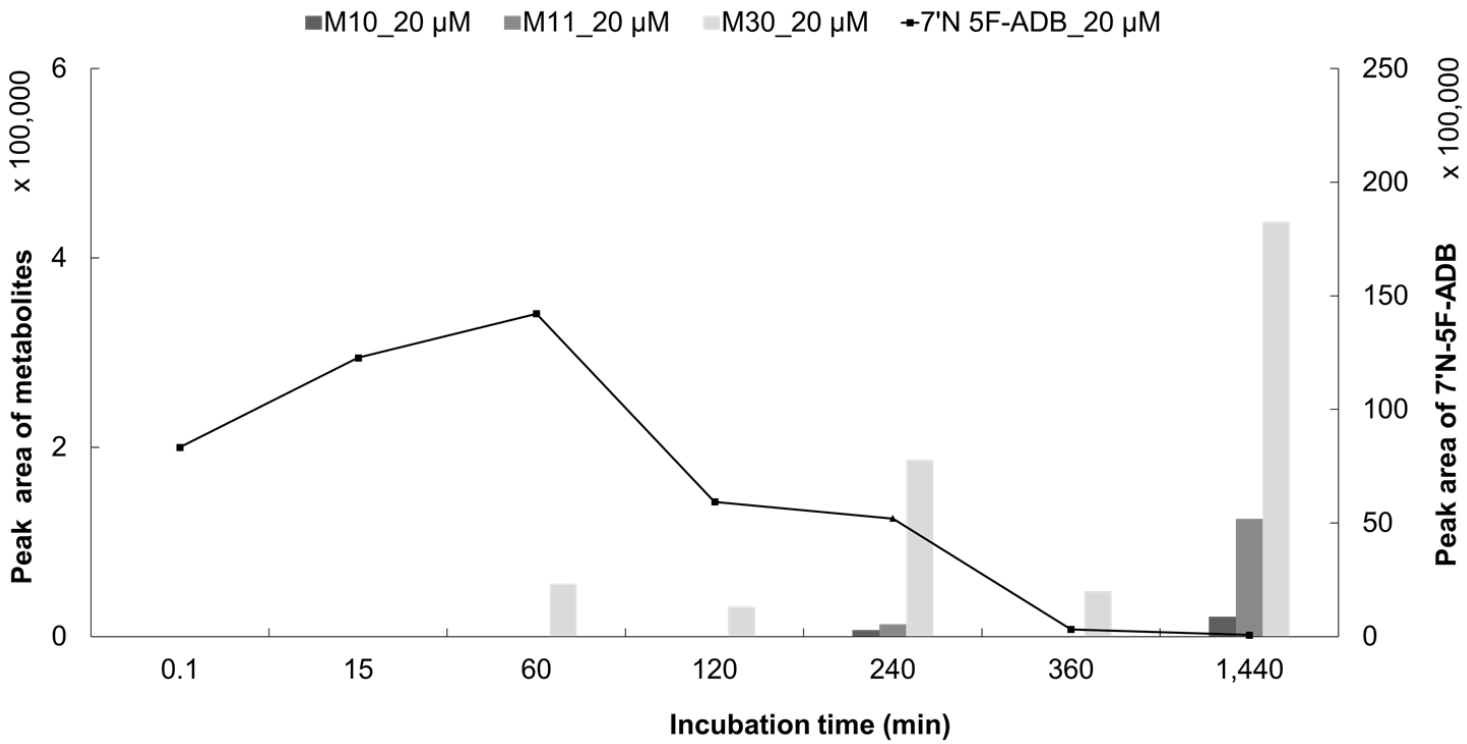

(b)

Figure S2. *Cont.*

2.9 Supporting Information

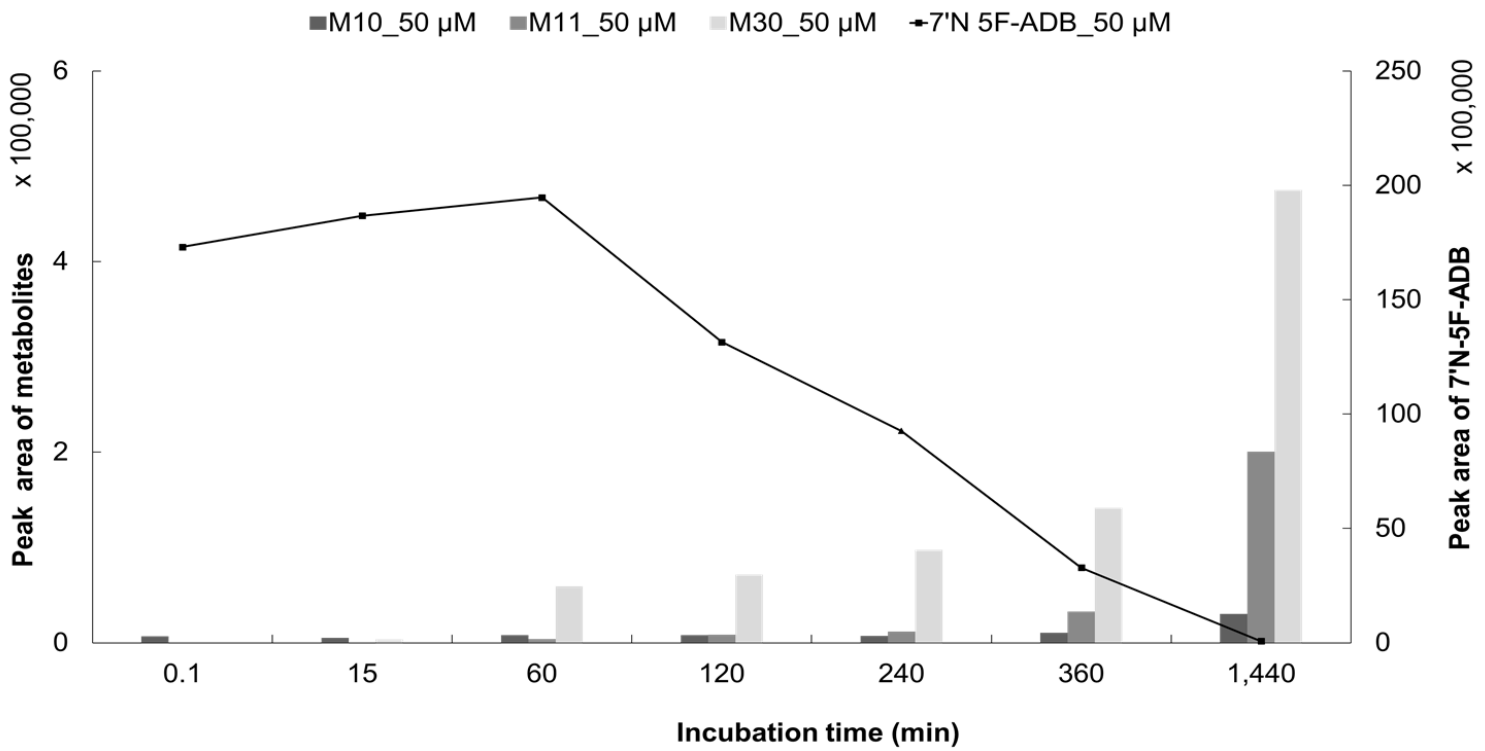

(c)

Figure S2. Internal amount-time profile of five main metabolites (M4, M5, M10, M11, and M30) in HepaRG cells incubated with 20 µM 7′*N*-5F-ADB (a) (n=2). (b) and (c) are the internal amount-time profiles of metabolites M10, M11, and M30. Incubation with 20 µM 7′*N*-5F-ADB (b) resulted in overall lower peak areas than incubation with 50 µM 7′*N*-5F-ADB (c).

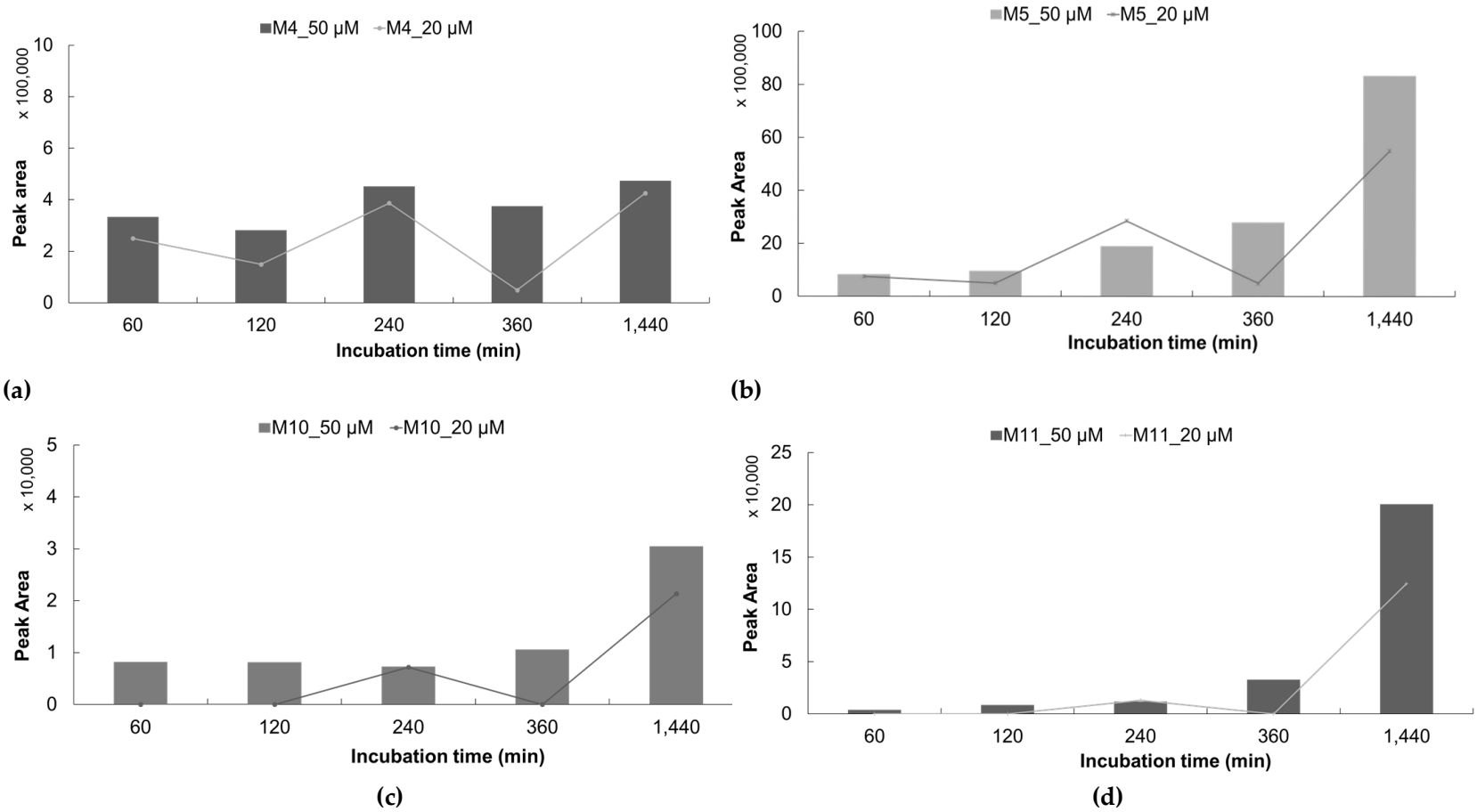

Figure S3. *Cont.*

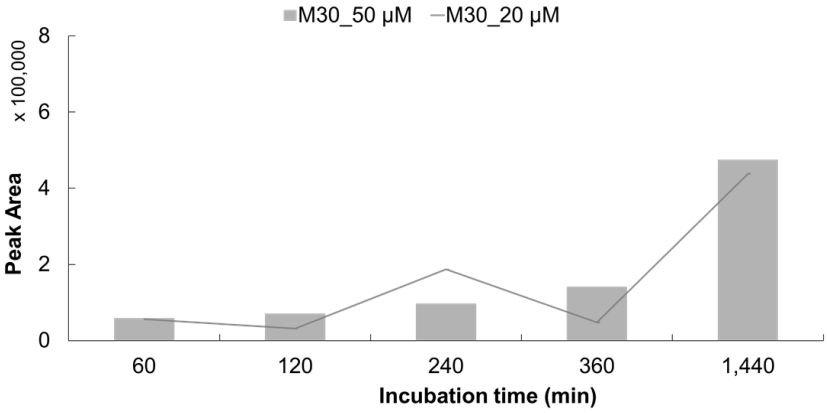

(e)

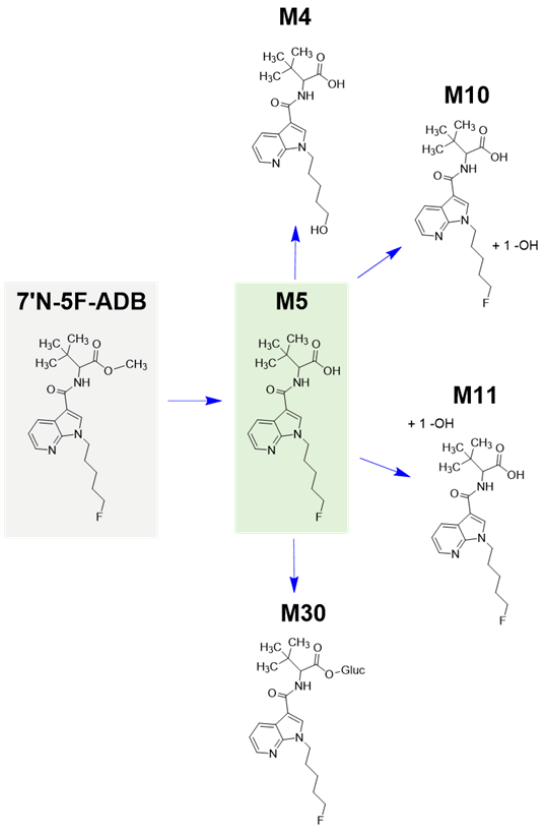

(f)

Figure S3. The effects of exposure time and concentration on the formation of five main metabolites (M4, M5, M10, M11, and M30; from (a) to (e)) in HepaRG cells. These graphs show the peak area of each metabolite during the incubation time from 60 min to 1,440 min following treatment with 20 μM (marked lines) and 50 μM (clustered columns) 7′*N*-5F-ADB. The main metabolic pathway in HepaRG cells was identified (f).

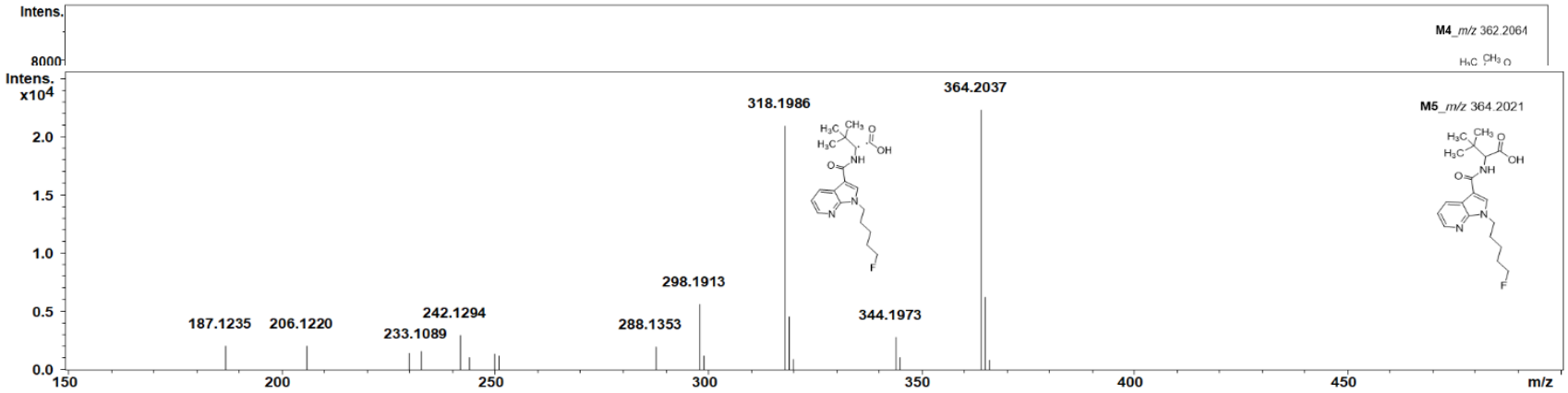

Figure S4. *Cont.*

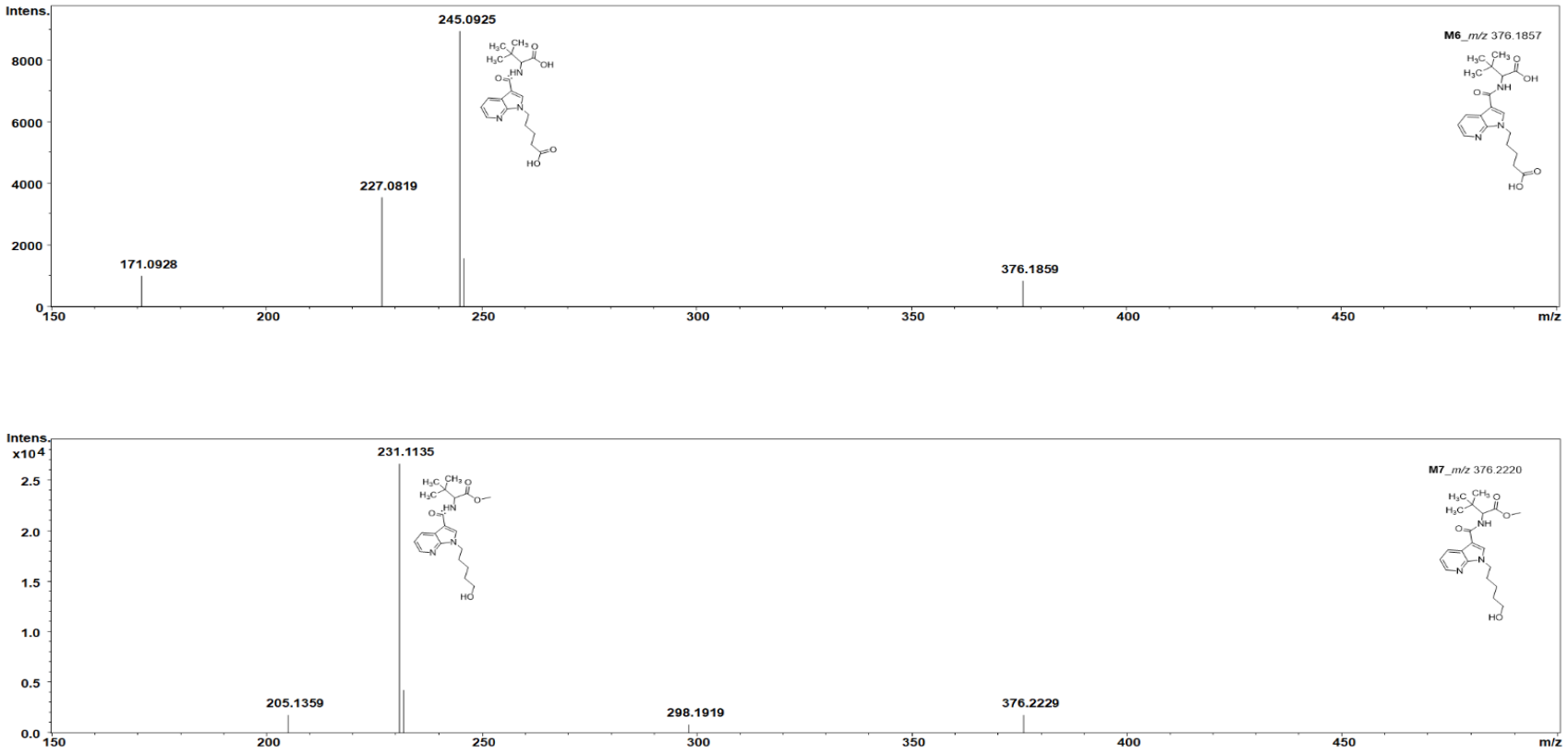

Figure S4. *Cont.*

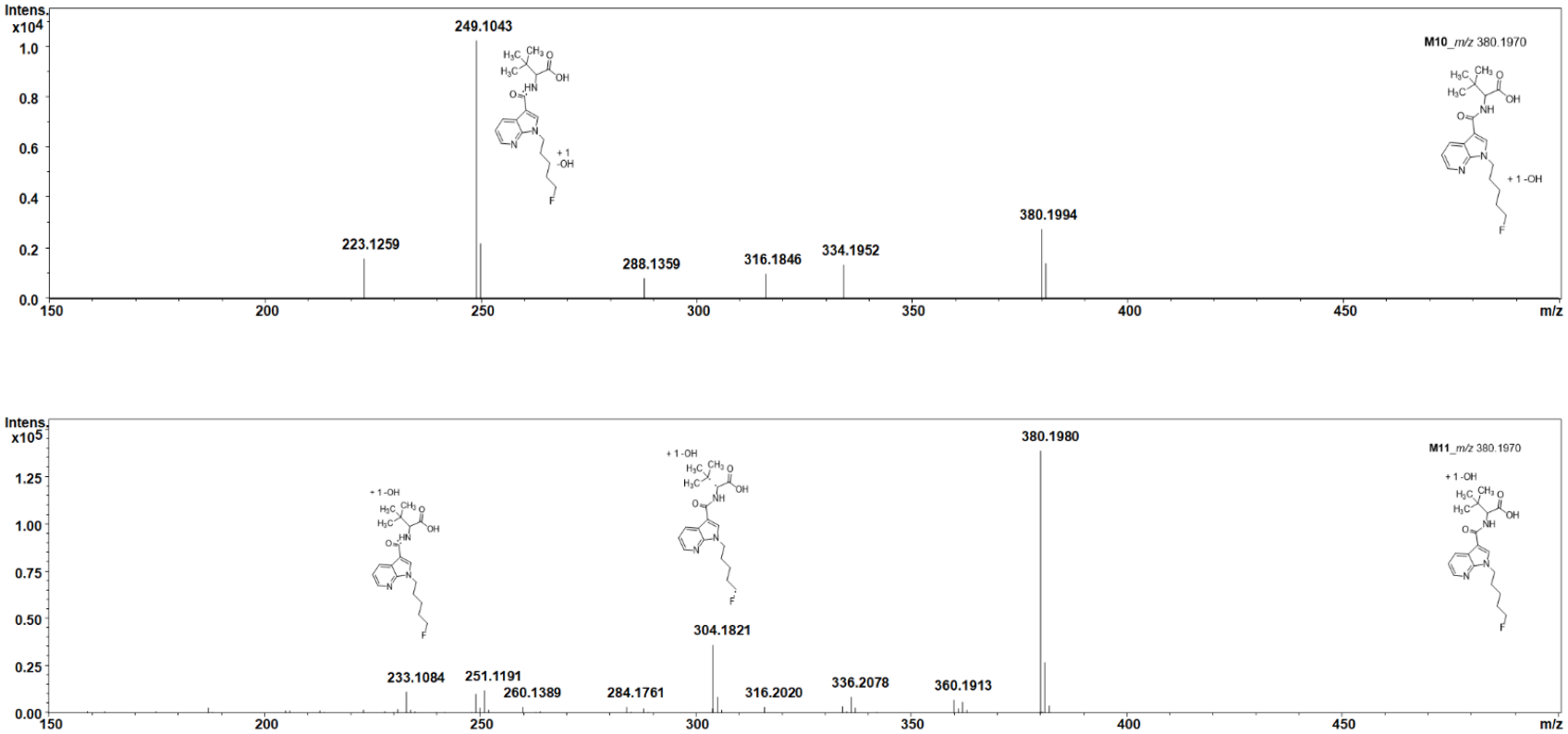

Figure S4. *Cont.*

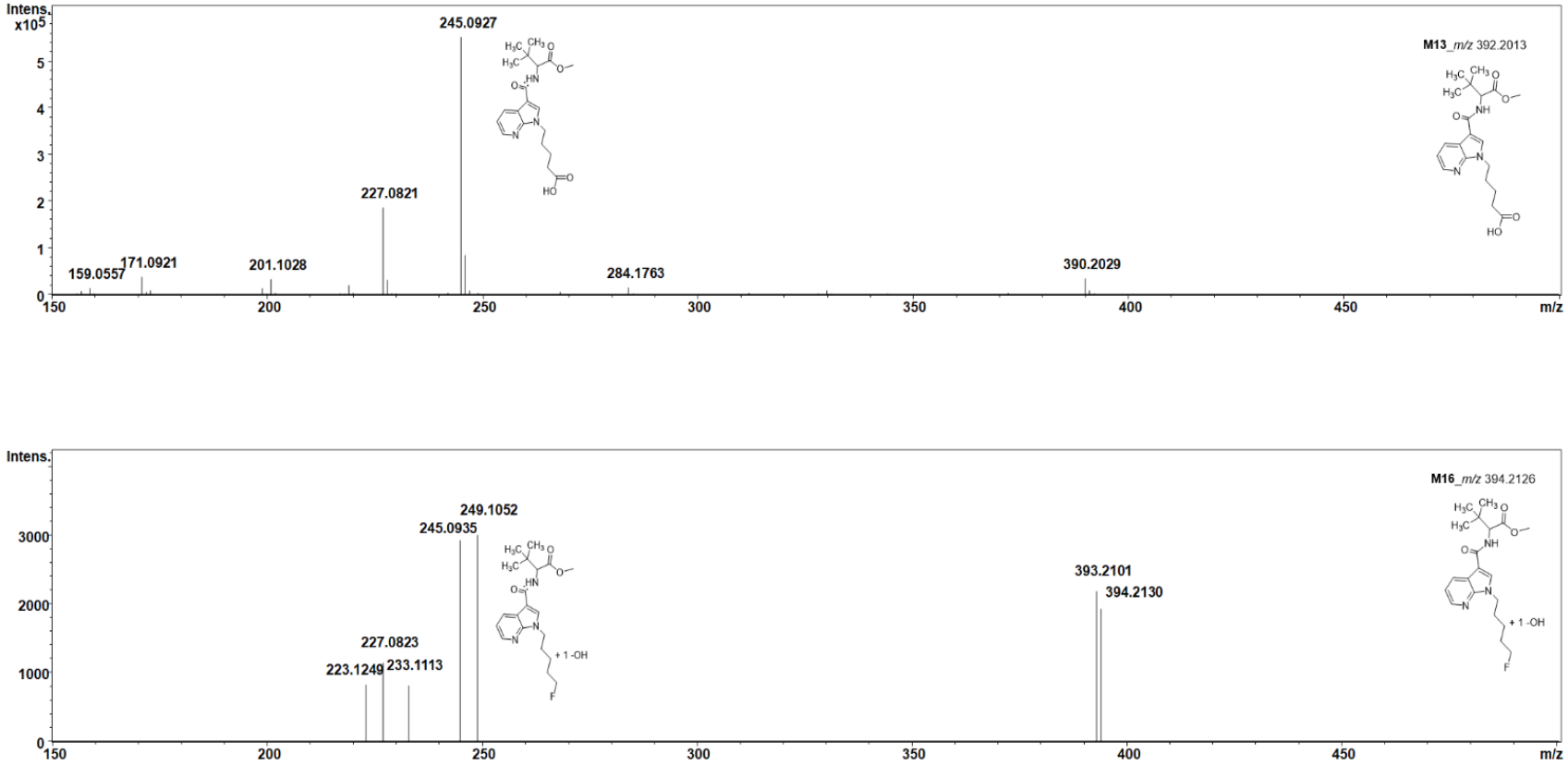

Figure S4. *Cont.*

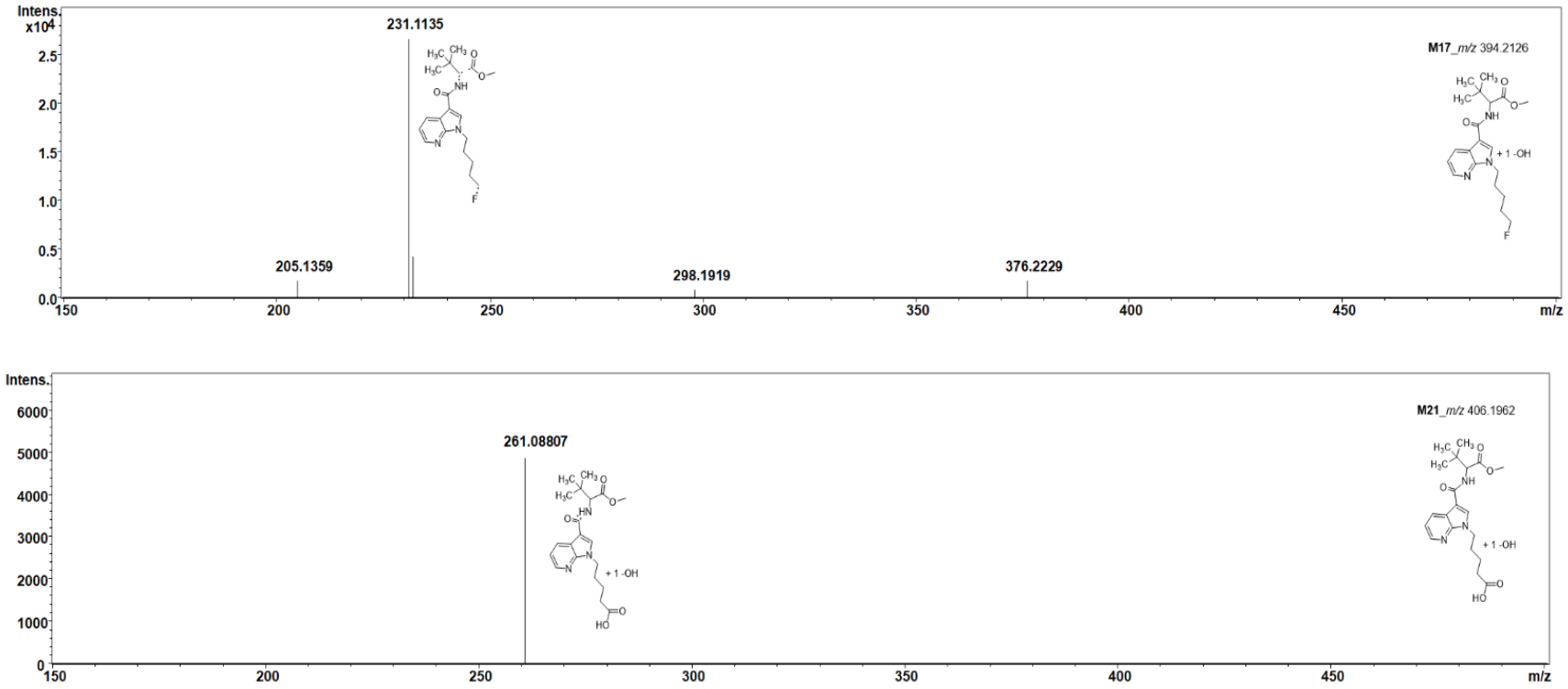

Figure S4. *Cont.*

2.9 Supporting Information

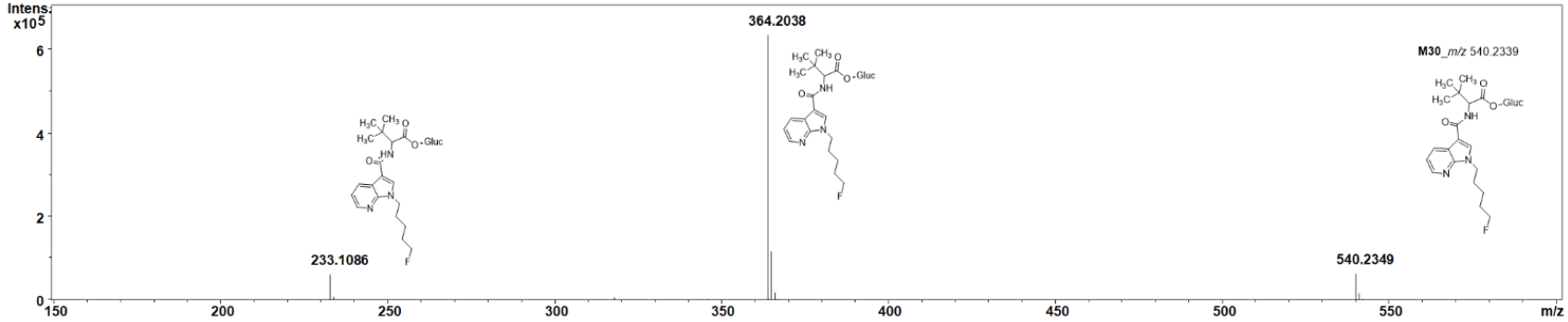

Figure S4. MS^2 spectra of 11 out of 24 metabolites detected in zebrafish larvae exposed to 7′*N*-5F-ADB, arranged by mass. The tentative structures of other metabolites, which are not displayed here, were confirmed by MS/MS^2 data in a published study [24, 27].

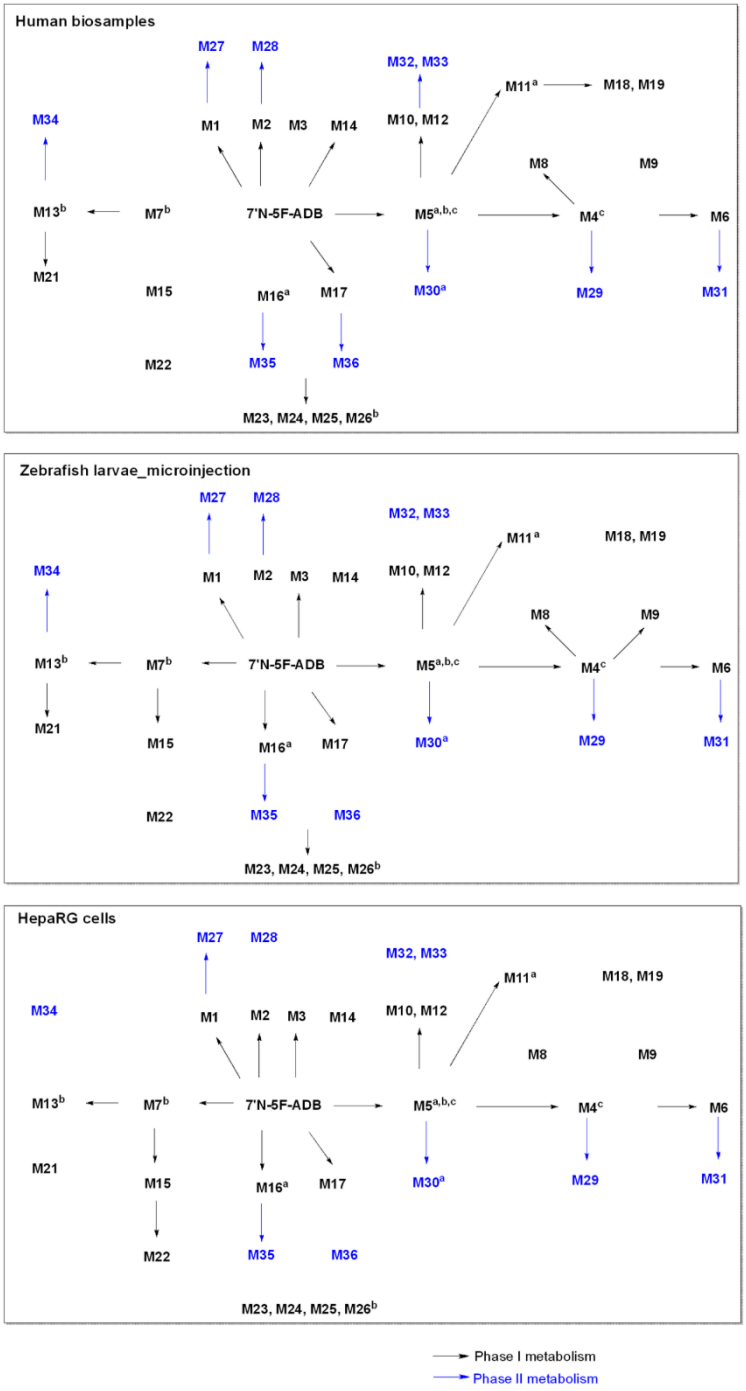

Figure S5. Schematic representation of 7'*N*-5F-ADB phase I and phase II metabolites in humans, ZF larvae, and HepaRG cells. [a] Major metabolites in human samples; [b] major metabolites in microinjected ZF larvae; [c] major metabolites in HepaRG cells.

2.9 Supporting Information

Table S1. Detailed information of 7′*N*-5F-ADB and its phase I and phase II metabolites in all investigated models.

Compound		Calculated exact masses (*m*/*z*)	Metabolic reaction	Human Screening Data [27]		Zebrafish Larvae, Published Data [24]	Zebrafish Larvae, Data from this Study				HepaRG *In vitro* Model (50 µM)
							Microinjection				
				Plasma	Urine	Aquatic Exposure (50 µM)	Yolk sac	Caudal Vein	Heart Ventricle	Hind-brain	
Parent compound	7'*N*-5F-ADB	378.2177	Parent compound	+++	+	+++	++	++	++	++	+++
Phase I	M1	251.1184	Amide hydrolysis		+	+		+	+	+	+
	M2	276.1335	Ester hydrolysis + *N*-dealkylation		+	+					+
	M3	290.1941	*N*-dealkylation			+		+	+	+	+
	M4	362.2064	Ester hydrolysis + oxidative defluorination		+	+		+	+	+	+
	M5	364.2021	Ester hydrolysis	++	+++	++		+	+	+	++
	M6	376.1857	Ester hydrolysis + oxidative defluorination + oxidation to carboxylic acid		+	+		+	+	+	+
	M7	376.2220	Oxidative defluorination			+		+	+	+	+
	M8	378.2013	Ester hydrolysis + oxidative defluorination + hydroxylation of the tertiary butyl part isomer 1		+			+nq	+nq	+nq	
	M9	378.2013	Ester hydrolysis + oxidative defluorination + hydroxylation of the pentyl chain isomer 2					+nq	+nq	+nq	
	M10	380.1970	Ester hydrolysis + hydroxylation of the fluoro pentyl chain isomer 1		+	+		+	+	+	+
	M11	380.1970	Ester hydrolysis + hydroxylation of the tertiary butyl part isomer 2	+	++			+	+nq	+	+
	M12	380.1970	Ester hydrolysis + hydroxylation of the fluoro pentyl chain isomer 3		+	+		+	+nq	+	+
	M13	390.2013	Oxidative defluorination + oxidation to carboxylic acid		+	+	+++	+++	+++	+++	+
	M14	392.1806	Ester hydrolysis + oxidative defluorination + oxidation to carboxylic acid + hydroxylation of the tertiary butyl part		+						
	M15	392.2169	Oxidative defluorination + hydroxylation of the pentyl chain			+		+	+	+	+

	M16	394.2126	Hydroxylation of the fluoro pentyl chain isomer 1	+		+		+	+	+	+
	M17	394.2126	Hydroxylation of the pyrrolo pyridine part isomer 2	+	+			+	+	+	+
	M18	396.1919	Ester hydrolysis + dihydroxylation of the fluoro pentyl chain and tertiary butyl part isomer 1		+						
	M19	396.1919	Ester hydrolysis + dihydroxylation of the fluoro pentyl chain and tertiary butyl part isomer 2		+						
	M20 [a]	396.1919	Ester hydrolysis + dihydroxylation of the fluoro pentyl chain isomer 3								
	M21	406.1962	Oxidative defluorination + oxidation to carboxylic acid + hydroxylation of the pentyl chain		+	+		+	+	+	
	M22	408.2118	Oxidative defluorination + dihydroxylation of the pentyl chain								+
	M23	410.2075	Dihydroxylation of the fluoro pentyl chain and tertiary butyl part isomer 1			+[c]					
	M24	410.2075	Dihydroxylation of the pyrrolo pyridine part and tertiary butyl part isomer 2		+[v]			+[b]	+[b]	+[b]	
	M25	410.2075	Dihydroxylation of the fluoro pentyl chain and pyrrolo pyridine part isomer 3		+[c]						
	M26	410.2075	Dihydroxylation of the fluoro pentyl part isomer 4								
Total number of phase I metabolites				4	17	14	1	17	17	17	15
Phase II	M27	427.1502	Amid hydrolysis + glucuronidation		+	+		+		+	+
	M28	452.1653	Ester hydrolysis + *N*-dealkylation + glucuronidation		+			+	+[nq]	+	
	M29	538.2382	Ester hydrolysis + oxidative defluorination + glucuronidation		+			+	+	+	+
	M30	540.2339	Ester hydrolysis + glucuronidation		+	+		+	+	+	+
	M31	552.2175	Ester hydrolysis + oxidative defluorination + oxidation to carboxylic acid + glucuronidation		+			+	+	+	+
	M32	556.2288	Ester hydrolysis + hydroxylation of the fluoro pentyl chain + glucuronidation isomer 1		+						
	M33	556.2288	Ester hydrolysis + hydroxylation of the fluoro pentyl chain + glucuronidation isomer 2		+						
	M34	566.2331	Oxidative defluorination + oxidation to carboxylic acid + glucuronidation		+			+	+	+	
	M35	570.2444	Hydroxylation of the fluoro pentyl chain + glucuronidation isomer 1		+[c]	+[c]		+[b]	+[b]	+[b]	+[b]
	M36	570.2444	Hydroxylation of the pyrrolo pyridine part + glucuronidation isomer 2		+[c]	+[c]					

Total number of phase II metabolites	-	10	4	-	7	6	7	5
Total number of detected phase I/II metabolites	**4**	**27**	**18**	**1**	**24**	**23**	**24**	**20**

[a] Precursor metabolite of M20 that was not detected in this study. [b] Peaks of structural isomers were not separated in the chromatograms due to co-elution from the LC-HRMS/MS system used in this study, and accordingly, isomers were counted and quantified as one metabolite. [c] Isomers of the metabolite eluted as individual peaks using LC-HRMS/MS conditions utilized applied in the previous studies [24, 27]. [nq] Confirmed mass, but not quantified due to peak detection below signal-to-noise ratio of 3. +: Peak detected, ++: second most abundant peak among metabolites, +++: most abundant peak among metabolites.

Chapter 3.

Induction of Liver Size Reduction in Zebrafish Larvae by the Emerging Synthetic Cannabinoid 4F-MDMB-BINACA and its Impact on Drug Metabolism

Previously published in:

Molecules, 2022 Feb 15; 27(4):1290. DOI: 10.3390/molecules27041290.

Yu Mi Park [1,2,3], Charlotte Dahlem [4], Markus R. Meyer [5], Alexandra K. Kiemer [4], Rolf Müller [1,3,6,*] and Jennifer Herrmann [1,6,*]

[1]Helmholtz Institute for Pharmaceutical Research Saarland (HIPS), Helmholtz Centre for Infection Research, Campus E8 1, Saarland University, 66123 Saarbrücken, Germany; Yu-Mi.Park@helmholtz-hips.de
[2]Environmental Safety Group, Korea Institute of Science and Technology (KIST) Europe, 66123 Saarbrücken, Germany
[3]Department of Pharmacy, Saarland University, 66123 Saarbrücken, Germany
[4]Department of Pharmacy, Pharmaceutical Biology, Campus C2 3, Saarland University, 66123 Saarbrücken, Germany; charlotte.dahlem@uni-saarland.de (C.D.); pharm.bio.kiemer@mx.uni-saarland.de (A.K.K.)
[5]Center for Molecular Signaling (PZMS), Institute of Experimental and Clinical Pharmacology and Toxicology, Department of Experimental and Clinical Toxicology, Saarland University, 66421 Homburg, Germany; m.r.meyer@mx.uni-saarland.de
[6]German Center for Infection Research (DZIF), 38124 Braunschweig, Germany
*Correspondence: Rolf.Mueller@helmholtz-hips.de (R.M.); Jennifer.Herrmann@helmholtz-hips.de (J.H.)

Contributions

Author's effort

The author significantly contributed to the concept of the study, designed and performed experiments, and evaluated and interpreted the resulting data. The author performed mating zebrafish, exposure experiment, liver size assessment, the genetically modified larvae creation using morpholino oligonucleotides, sample preparations for LC-HRMS/M and MALDI-FT-ICR, all data analysis of LC-HRMS/MS, and data processing and analysis of MALDI-FT-ICR. Furthermore, the author contributed significantly to the conceiving and writing of the manuscript.

Contributions by others

Charlotte Dahlem and Markus R. Meyer contributed to the conception, methodology, reviewing, and editing of this study and, in particular, attended the methodological development and analysis of the gene modification by morpholino oligonucleotides and validation of 4F-MDMB-BINACA metabolism, respectively. Alexandra K. Kiemer and Rolf Müller contributed by conceiving, reviewing, and editing this study. Jennifer Herrmann contributed to the concept, writing, editing, and reviewing of this study. Rolf Müller and Jennifer Herrmann supervised this project, and all authors also contributed by proofreading the manuscript.

[Additional Paper]

How to Study the Metabolism of New Psychoactive Substances for the Purpose of Toxicological Screenings—A Follow-Up Study Comparing Pooled Human Liver S9, HepaRG Cells, and Zebrafish Larvae

Previously published in:

Front. Chem., 2020 17 July;8:539. doi: 10.3389/fchem.2020.00539.

Lea Wagmann[1], Fabian Frankenfeld[1], Yu Mi Park[2,3], Jennifer Herrmann[2,4], Svenja Fischmann[5], Folker Westphal[5], Rolf Müller[2,4], Veit Flockerzi[6] and Markus R. Meyer[1*]

[1] Department of Experimental and Clinical Toxicology, Institute of Experimental and Clinical Pharmacology and Toxicology, Center for Molecular Signaling (PZMS), Saarland University, Homburg, Germany,
[2] Department of Microbial Natural Products (MINS), Helmholtz Institute for Pharmaceutical Research Saarland (HIPS), Saarland University, Saarbrücken, Germany,
[3] Environmental Safety Group, Korea Institute of Science and Technology (KIST) Europe, Saarbrücken, Germany,
[4] German Center for Infection Research (DZIF), Partner Site Hannover–Braunschweig, Saarbrücken, Germany,
[5] State Bureau of Criminal Investigation Schleswig–Holstein, Kiel, Germany,
[6] Department of Experimental and Clinical Pharmacology, Institute of Experimental and Clinical Pharmacology and Toxicology, Center for Molecular Signaling (PZMS), Saarland University, Homburg, Germany

[Additional Paper] Contributions

Author's effort

The author significantly contributed to the concept of the part in the study using zebrafish larvae, designed and performed experiments, and evaluated and interpreted the resulting data. The author performed mating zebrafish, *in vivo* maximum-tolerated concentration studies, exposure experiments, and sample preparations for identification of the metabolites. Furthermore, the author contributed significantly to the conceiving and writing of the manuscript.

Contributions by others

Lea Wagmann and Markus R. Meyer contributed to the conception, design, methodology, reviewing, and editing of this study. Fabian Frankenfeld contributed to performing experiments, further investigation, and data analysis. Jennifer Herrmann and Rolf Müller supervised zebrafish larvae experiments. Veit Flockerzi and Lea Wagmann performed HepaRG cell experiments, and Svenja Fischmann and Folker Westphal provided reference standard. Lea Wagmann and Fabian Frankenfeld wrote the first draft of the manuscript, and all authors also contributed by proofreading the manuscript.

3.1 Abstract

Zebrafish (*Danio rerio*) larvae have become a popular *in vivo* model in drug metabolism studies. Here, we investigated the metabolism of methyl 2-[1-(4-fluorobutyl)-1*H*-indazole-3-carboxamido]-3,3-dimethylbutanoate (4F-MDMB-BINACA) in ZF larvae after direct administration of the cannabinoid via microinjection, and we visualized the spatial distributions of the parent compound and its metabolites by mass spectrometry imaging (MSI). Furthermore, using genetically modified ZF larvae, the role of cannabinoid receptor type 1 (CB1) and type 2 (CB2) on drug metabolism was studied. Receptor-deficient ZF mutant larvae were created using morpholino oligonucleotides (MOs), and CB2-deficiency had a critical impact on liver development of ZF larva, leading to a significant reduction of liver size. A similar phenotype was observed when treating wild-type ZF larvae with 4F-MDMB-BINACA. Thus, we reasoned that the cannabinoid-induced impaired liver development might also influence its metabolic function. Studying the metabolism of two synthetic cannabinoids, 4F-MDMB-BINACA and methyl 2-(1-(5-fluoropentyl)-1*H*-pyrrolo[2,3-b]pyridine-3-carboxamido)-3,3-dimethylbutanoate (7′*N*-5F-ADB), revealed important insights into the *in vivo* metabolism of these compounds and the role of cannabinoid receptor binding.

3.2 Graphical Abstract

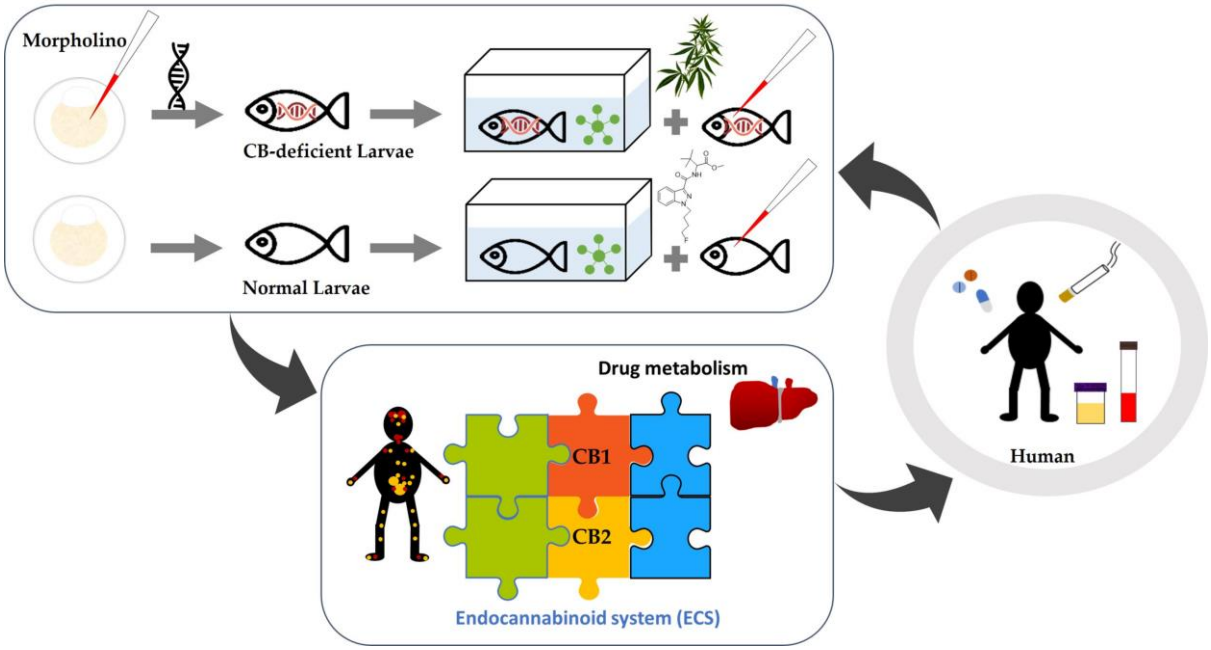

3.3 Introduction

In drug discovery and development, many non-clinical studies are performed using animal models to investigate pharmacokinetics (PK) and bioavailability, non-clinical toxicology, and efficacy of new drug candidates [1]. During these early phases, 40% to 80% of compounds fail, and their further development is stopped mainly due to safety concerns and/or insufficient PK properties [1–4]. In order to reduce the number of animal experiments in pre-clinical testing and increase the rate of success in such models, many alternative models are being developed [1–3]. Zebrafish (*Danio rerio*; ZF) has become an important pre-clinical *in vivo* vertebrate model, which is widely applied in drug discovery to study the pharmacology of new drug candidates [5–10]. Eight small molecules which were initially discovered in ZF models have proceeded into clinical trials during the past decade [1,11–18], demonstrating that the use of ZF models can contribute to successful translation [1,18]. Over the past few years, the ZF model has been increasingly used not only in functional and safety studies but also in drug metabolism studies, and its reproducibility and high coverage of human metabolites have been demonstrated [19]. Numerous studies have been published on ZF xenobiotic metabolites [19–24], and importantly, several new psychoactive substances (NPSs) and their phase I and phase II metabolites in ZF have been evaluated and were found to well correlate with human metabolism [25–28].

In our previous study [28], we assessed various administration routes into ZF larvae, and an authentic spectrum of metabolites of the synthetic cannabinoid (SC) methyl 2-(1-(5-fluoropentyl)-1*H*-pyrrolo[2,3-b]pyridine-3-carboxamido)-3,3-dimethylbutanoate (7′*N*-5F-ADB; Figure 1a) was obtained in ZF larvae. Using mass spectrometry imaging (MSI), the spatial distribution pattern in ZF larvae of 7′*N*-5F-ADB and its metabolites was studied and revealed the impact of different administration routes on *in vivo* distribution and drug metabolism.

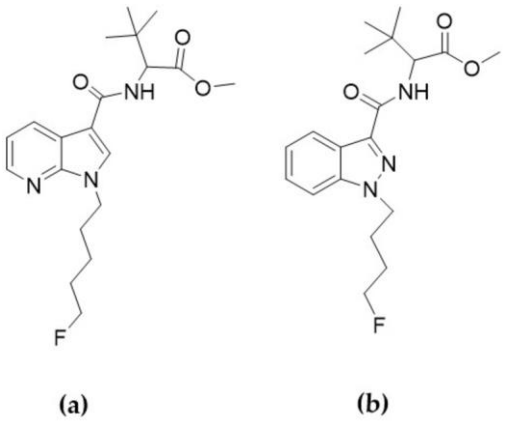

Figure 1. Chemical structures of 7′*N*-5F-ADB (a) and 4F-MDMB-BINACA (b).

SCs are investigated as pharmacological probes to study the endocannabinoid system (ECS), and they show some pharmaceutical potential, *e.g.*, in the treatment of inflammatory dis-

eases and in cancer pain management [19,29,30]. However, new emerging SCs are also potentially harmful psychoactive drugs of abuse, and they pose a severe threat to human health with numerous reported associated fatalities [31]. Detailed information on their metabolic fate and a mechanistic understanding is almost entirely lacking due to the rapid generation of new derivatives and the illegal distribution of these new SCs.

In this study, we aimed to investigate the metabolism of a newly emerging SC, methyl 2-[1-(4-fluorobutyl)-1*H*-indazole-3-carboxamido]-3,3-dimethylbutanoate (4F-MDMB-BINACA, Figure 1b). 4F-MDMB-BINACA was chosen for this study because it is an emerging and highly potent new SC for which a high number of seizure cases were reported in 2019 by the European Union Early Warning System [31,32]. Therefore, 4F-MDMB-BINACA has been controlled under Schedule II of the Convention on Psychotropic Substances of 1971, designed as a United Nations treaty, which came into force on 3 November 2020 [33,34].

Here, we relied on direct administration routes into the ZF larvae, basically following the optimized protocol of our previous study [28]. The detected ZF metabolites were then compared to recently published human metabolites [27,32,34,35]. In addition, we explored the circulation/distribution of 4F-MDMB-BINACA inside the ZF larval body following microinjection of the SCs into internal organs (caudal vein, heart ventricle, and hindbrain) and visualized molecular spatial images obtained from MSI. Furthermore, 4F-MDMB-BINACA was described as a potent agonist of cannabinoid receptor type 1 (CB1) [31,34,36]. In ZF larvae, it was shown that loss of CB1 and cannabinoid receptor type 2 (CB2) lead to a significant reduction of liver size, impaired hepatocyte proliferation, and reduced liver gene expression [37–39]. In turn, this liver pathophysiologic effect could impact the ZF metabolism of SCs since phase I and phase II metabolic enzymes are expressed in this compartment. We then studied the correlation between drug metabolism and non-functional CB1 and CB2. To achieve this, we utilized morpholino oligonucleotides (MO) as an antisense gene-knockdown tool, which is widely and successfully used for, *e.g.*, modeling human diseases in ZF [40–42]. The metabolic profiles of 4F-MDMB-BINACA and 7′*N*-5F-ADB (Figure 1) in ZF larvae mutants experiencing gene knock-down of either CB1 or CB2 were explored and compared to findings from our earlier studies [25,27,28].

3.4 Results and Discussion

3.4.1. Zebrafish Larvae Produce an Authentic Spectrum of 4F-MDMB-BINACA Metabaolites

In our previous study, we optimized the administration route for 7′*N*-5F-ADB into ZF larvae to study the SCs metabolism [28]. This was the first comprehensive evaluation of the impact of compound administration (waterborne exposure vs. microinjection into different organs) on the efficacy of drug metabolism. In the case of the studied SC, we could reveal that only one metabolite can be detected when the drug was microinjected into the yolk sac of the ZF larvae. In contrast, a significantly higher number of metabolites could be detected by adding 7′*N*-5F-ADB into ZF larvae medium or microinjecting the SC into vital organs. Thus, owing to the presumed similar physico-chemical properties of 7′*N*-5F-ADB and 4F-MDMB-BINACA (cp. Section 3.4.3), we assessed ZF larvae metabolism of the latter following microinjection of the drug into vital organs such as the caudal vein, heart ventricle, and hindbrain.

Wagmann et al. [27] studied the metabolism of five NPSs, including 4F-MDMB-BINACA, and compared the metabolite spectra found in ZF larvae (waterborne exposure), *in vitro* models (pooled human liver S9 fraction and HepaRG cells), and one authentic human plasma sample. In total, 14 phase I and four phase II metabolites were detected in the ZF larvae, and ZF larvae produced the highest number of 4F-MDMB-BINACA (and four other NPSs) metabolites among all investigated models. Here, we further investigated the metabolism of 4F-MDMB-BINACA in ZF larvae using direct administration routes, with the aim to deepen the knowledge on human metabolism of the NPS. For this, we also compared our findings to recently published studies of human biosamples (blood and urine), which were screened for 4F-MDMB-BINACA and its metabolites from 2019 to 2021 as part of routine toxicology [27,34,35] or forensic casework [32].

Table 1 summarizes phase I and phase II metabolite data from microinjected ZF larvae investigated in this study, and the integrated data of human screening results reported from other studies were added along [27,32,34,35]. More detailed information on the human screening data surveyed is provided in Supplementary Table S1, which also provides the metabolic reactions and exact masses of the detected metabolites. The structure elucidations of these detected metabolites based on their MS2 data are reported elsewhere [27].

While combining human data, we found that these studies show some deviations with respect to metabolite detection, especially in urine samples, as the number of reported metabolites varies from three to twelve detected, depending on the studied sample. This discrepancy is possibly caused by the lack of homogeneity and diversity in random sampling, where no medical and personal information on the patients is available. Thus, the 'integrated human samples' data of Table 1 represent abundant metabolites of 4F-MDMB-BINACA, which were detected at least twice in each of the samples. In short, out of the 26 metabolites identified from three different models in our previous study [27], nine metabolites were observed in human urine samples and three metabolites in blood samples (Table 1 and Supplementary Table S1).

3.4 Results and Discussion

Table 1. Summary of 4F-MDMB-BINACA and its phase I and II metabolites and their detection in human biosamples and microinjected zebrafish larvae.

Compounds	Metabolite ID	Integrated Human Screening Data * [27,32,34,35]		Data from Zebrafish Larvae			
				Aquatic Exposure, Published Data [27]	Microinjection		
		Blood	Urine		Caudal Vein	Heart Ventricle	Hindbrain
Parent compound	4F-MDMB-BINACA			+++	+++	+++	+++
Phase I metabolites	M1						
	M2			+	+ nq		+ nq
	M3		√√		+ nq	+ nq	+ nq
	M4	√√		+	+	+	+
	M5			+			
	M6	√	√√	++	+	+	+
	M7		√	+			
	M8	√	√	+			
	M9			+			
	M10		√√	+	+ nq	+ nq	+ nq
	M11		√√	+	+	+	+
	M12			+	+	+	+
	M13		√	+			
	M14		√				
	M15		√√	+	+	++	+
	M16			+			
	M17						
	M18			+			
	M19						
Total number of phase I metabolites		3	9	14	8	7	8
Phase II metabolites	M20			+	++	+	+
	M21						
	M22						
	M23						
	M24			+			
	M25			+	+ nq	+	+
	M26			+			
Total number of phase II metabolites		-	-	4	2	2	2
Total number of detected Phase I/II metabolites		3	9	18	10	9	10

* All human data were taken from recently published studies; integrated blood data were quoted from [27,32], integrated urine data from [27,32,34,35], and details are shown in Supplementary Table S1. √: detected at least twice among the samples in each respective human matrix; √√: detected in both the microinjected ZF larvae and human biosamples; nq: confirmed mass, but not quantified due to peak detection below signal-to-noise ratio of 3. +: Peak detected, ++: second most abundant peak among metabolites, +++: most abundant peak among metabolites.

Upon microinjection of 4F-MDMB-BINACA into the caudal vein and hindbrain of ZF larvae, ten metabolites were detected. Similarly, following microinjection into the heart ventricle, nine metabolites were found, whereas the previously found M2 metabolite (lactone formation in combination with *N*-dealkylation) was not detected (Table 1 and Figure 2). Two metabolites, M20 (hydroxylation of the indazole part in combination with sulfation) and M25 (hydroxylation of the tertiary butyl part in combination with glucuronidation isomer 1), out of seven phase II metabolites, were produced in all microinjected ZF larvae. In human biosamples, there was no detection of phase II metabolites except M22 (ester hydrolysis in combination with glucuronidation) detected only once from urine samples [27].

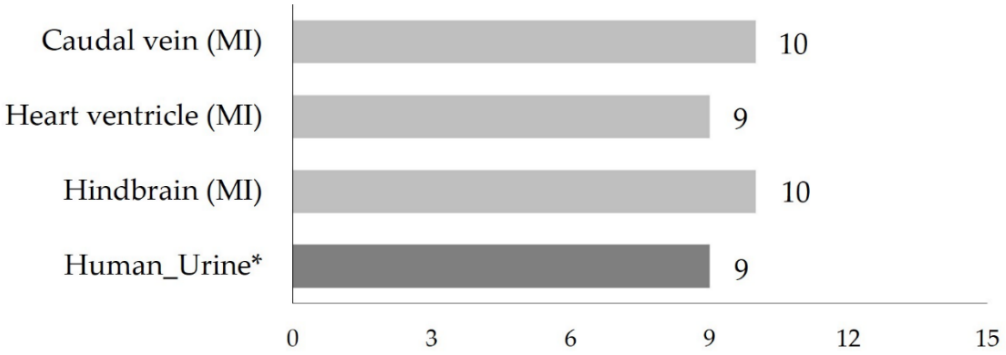

Figure 2. Total number of detected 4F-MDMB-BINACA metabolites following administration of the SC into ZF larvae through different microinjection routes. All results from ZF larvae in this study are represented as the mean value of peak numbers from triplicates of 30 pooled larvae. * Human urine data represent published integrated data of metabolites that were detected at least twice in all studied urine samples [27,32,34,35]. (MI: microinjection).

M2 and M12 (lactone formation in combination with hydroxylation of the tertiary butyl part), which originate from M6 (lactone formation), were uniquely detected in ZF larvae but not in human samples (Table 1 and Supplementary Table S1). Conversely, M6 is the second most abundant human metabolite, and it was also detected in all investigated ZF larvae samples. The most abundant metabolite in human urine and blood samples, M8 (ester hydrolysis), was not detected in the microinjected ZF larvae. M3 (ester hydrolysis in combination with *N*-dealkylation), M10 (ester hydrolysis in combination with oxidative defluorination and oxidation to carboxylic acid), M11 (oxidative defluorination), and M15 (oxidative defluorination in combination with oxidation to carboxylic acid) were observed in both microinjected ZF larvae and integrated urine samples. M8 is metabolized to M7 and then to M10, however, in the microinjected larvae, only M10 as the latest metabolite was found. In contrast, M4 (*N*-dealkylation) was commonly observed in the ZF larvae and integrated blood samples, but it was not found in human urine samples (Table 1 and Supplementary Table S1). Based on the detection pattern of these four metabolites (M2, M6, M10, and M12), we conclude that ZF larvae in the chosen setup display a faster metabolism than found in humans.

Assessing the mutual comparability between ZF larvae and human biosamples, the metabolism of the NPS in microinjected ZF larvae displays a high similarity, with a 67% match rate to integrated human blood samples and a 56% match rate to integrated human urine samples, respectively. In the microinjected ZF larvae, the three most abundant metabolites of 4F-MDMB-BINACA were M12, M15 (oxidative defluorination in combination with oxidation to carboxylic acid), and M20 (hydroxylation of the indazole part in combination with sulfation). The parent compound, 4F-MDMB-BINACA, still existed in the injected larvae, and it was the most abundant peak (Table 1 and Figure 3).

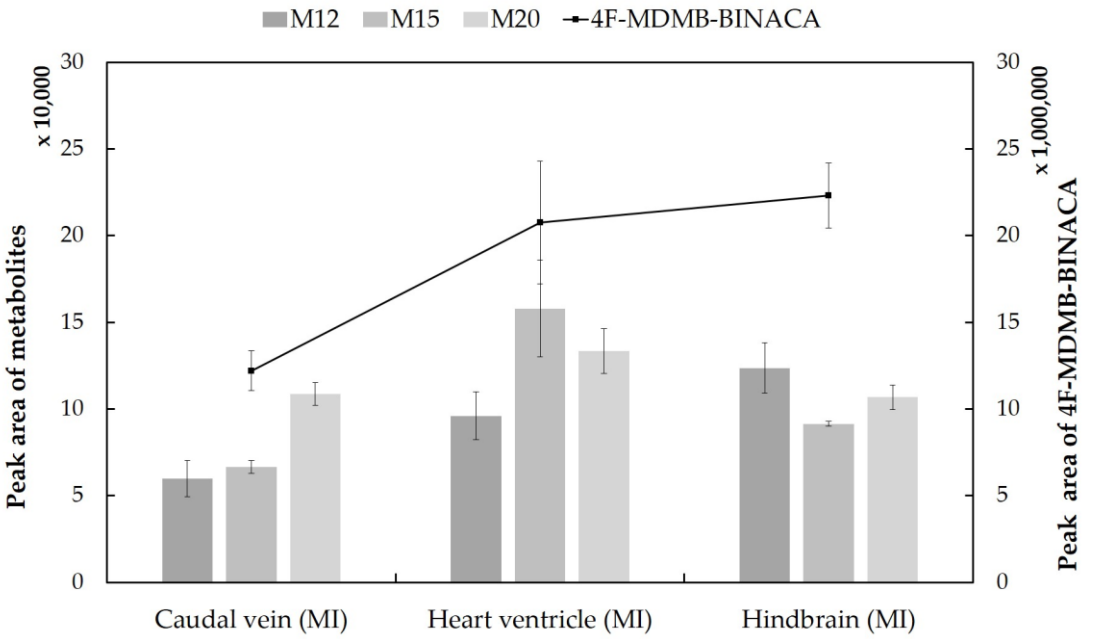

Figure 3. Detection profiles of the parent compound 4F-MDMB-BINACA and the three most abundant metabolites in microinjected ZF larvae (caudal vein, heart ventricle, and hindbrain). The most abundant metabolites (M12, M15, and M20) were formed by lactone formation, oxidative defluorination, and hydroxylation, respectively. The line chart represents the relative abundance of the parent compound, and three gray-colored clustered columns stand for its major metabolites. All data are displayed as mean ± standard deviation (SD) (n = 3).

Moreover, comparing the relative abundance of the three major ZF metabolites, their peak intensities varied depending on the site of microinjection. M20 was most abundant after caudal vein injection, M15 after heart ventricle injection, and M12 after injecting 4F-MDMB-BINACA into the hindbrain (Figure 3). The peak area of M20 was similar in all three microinjected ZF samples. However, the observed differences were mostly below statistical significance with $p >$ 0.05. Overall, peak intensities of the parent compound and its three major metabolites were lowest after injection into the ZF caudal vein, and this finding was also confirmed for the three minor metabolites M4, M11, and M25 (Supplementary Figure S1). This result can possibly be explained by the fast circulation of the parent compound as soon as it is injected into the caudal vein. This, in turn, might cause fast metabolism and excretion. However, the overall metabolite pattern seems to be barely influenced by the target organ of microinjection as direct administration routes for 4F-MDMB-BINACA (Table 1 and Figure 2). In contrast to the previously studied cannabinoid 7′*N*-5F-ADB, direct injection of 4F-MDMB-BINACA into ZF larvae did not increase the number of detected metabolites compared to waterborne exposure [28].

The main phase I metabolic pathways of 4F-MDMB-BINACA were reconstructed by complementing the metabolites detected in ZF larvae to integrated human biosamples [27,32,34,35], which contained M1 found by MALDI-MSI analysis (see Section 3.4.2). Conversely, the pathways for phase II metabolism were not constructed because the overall experimental metabolite detection in all investigated models was insufficient, with only two metabolites found in the

microinjected ZF larvae (M20, M25) and one metabolite (M22) found in human biosamples. In the microinjected ZF larvae, four minor metabolites (M7, M8, M13, and M14) in the left panel of the phase I metabolic pathway were not produced (Figure 4a), whereas three other metabolites (M1, M2, and M12) and the cross-connection between M3 and M4 in the right panel were absent in human urine samples (Figure 4b). In human blood samples, only three primary metabolites (M4, M6, and M8) were found at the center of the pathway.

M3 and M10 were detected in the microinjected ZF larvae despite the non-detection of two intermediates (M7 and M8). Among all detected metabolites, M6, formed by lactone formation, is a reliable metabolic biomarker as it was found with high abundance in the ZF larvae model as well as in all previously investigated human biosamples (Table 1 and Supplementary Table S1). M6 was previously recommended as a target for toxicological screening in two studies [27,35], and we could confirm its high peak intensity detection in the ZF larva model. Furthermore, M8 also seems to be another metabolic biomarker in humans since it is predominant in all human urine and blood samples (Supplementary Table S1). Taken together, we were able to construct the human metabolic phase I pathway of 4F-MDMB-BINACA by combining phase I metabolites from ZF larvae with already described human metabolites.

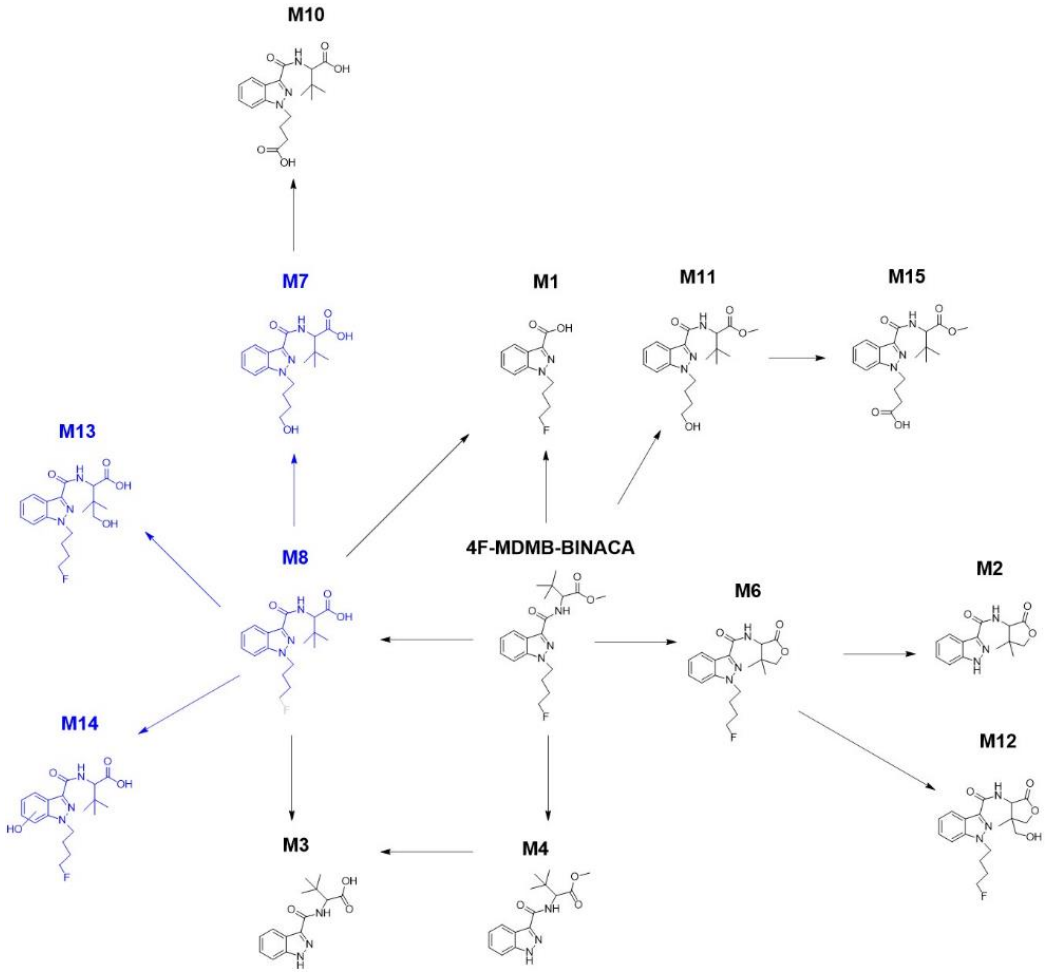

(a)

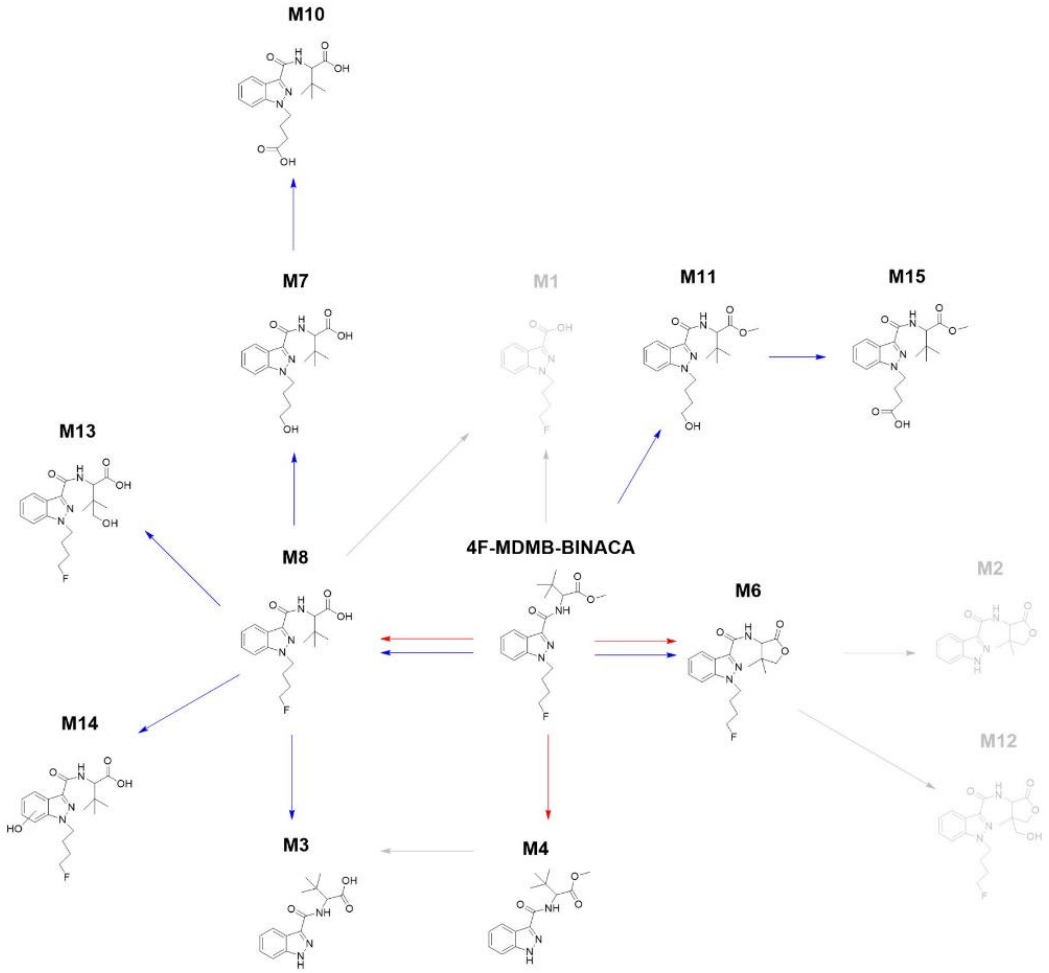

(b)

Figure 4. The main phase I metabolic pathway of 4F-MDMB-BINACA based on findings in the ZF larvae model (a) and from human screening (b). In panel (b), red arrows indicate results from human blood samples, and blue arrows indicate results from human urine samples. Metabolites in blue represent molecules not detected in the respective model. Four metabolites (M7, M8, M13, and M14) were not detected in the microinjected ZF larvae despite the detection of M3 and M10 as their following sequential metabolites. In contrast, terminal metabolites M1, M2, and M12 and a cross-connection between M3 and M4 were not found in human samples.

3.4.2. Spatial Distribution of 4F-MDMB-BINACA ant Its Metabolites in ZF Larvae

MSI is a powerful tool and label-free technology that enables visualization of the spatial distribution of molecules in biological specimens in a single experiment [43–47]. In combination with a high-resolution mass spectrometer such as Fourier-transform ion cyclotron resonance (FT-ICR), MSI can depict the localization of molecules, which can be identified with high confidence. Moreover, MSI mapping of molecules of interest (*e.g.*, drugs, metabolites, biomarkers) in biological tissues is critical for understanding their pharmacology [44,45]. In recent years,

MALDI-MSI is becoming a more established tool in clinical practice and the pharmaceutical industry [45–47]. However, its application to ZF larvae is still limited, mainly due to challenging and critical steps of sample preparation. Nevertheless, we were previously able to generate spatial distribution images of 7′*N*-5F-ADB metabolites in ZF larvae by MALDI-FT-ICR [28].

In this study, we used MALDI-MSI to study the distribution of 4F-MDMB-BINACA in the ZF larval bodies and investigated how spatial MS images of molecules can be utilized to provide reliable metabolism information along with LC-HRMS/MS data.

One hour after microinjections into three internal organs, the parent compound (Figure 5) and three metabolites (M1 (amide hydrolysis from M3; Figure 6), M3 (Supplementary Figure S2), and M4 (Supplementary Figure S3)) could be visualized in the sections from these injected ZF larvae. M1 was uniquely detected in the injected ZF larvae prepared for MALDI-MSI among all samples. Moreover, M3 and M4 were observed in all injected ZF larvae analyzed by LC-HRMS/MS and MALDI-MSI and these metabolites were also found in human urine samples and blood samples, respectively (Table 1). However, corresponding masses of M12, M15, and M20 as the major metabolites detected in LC-HRMS/MS were not found by MALDI-MSI.

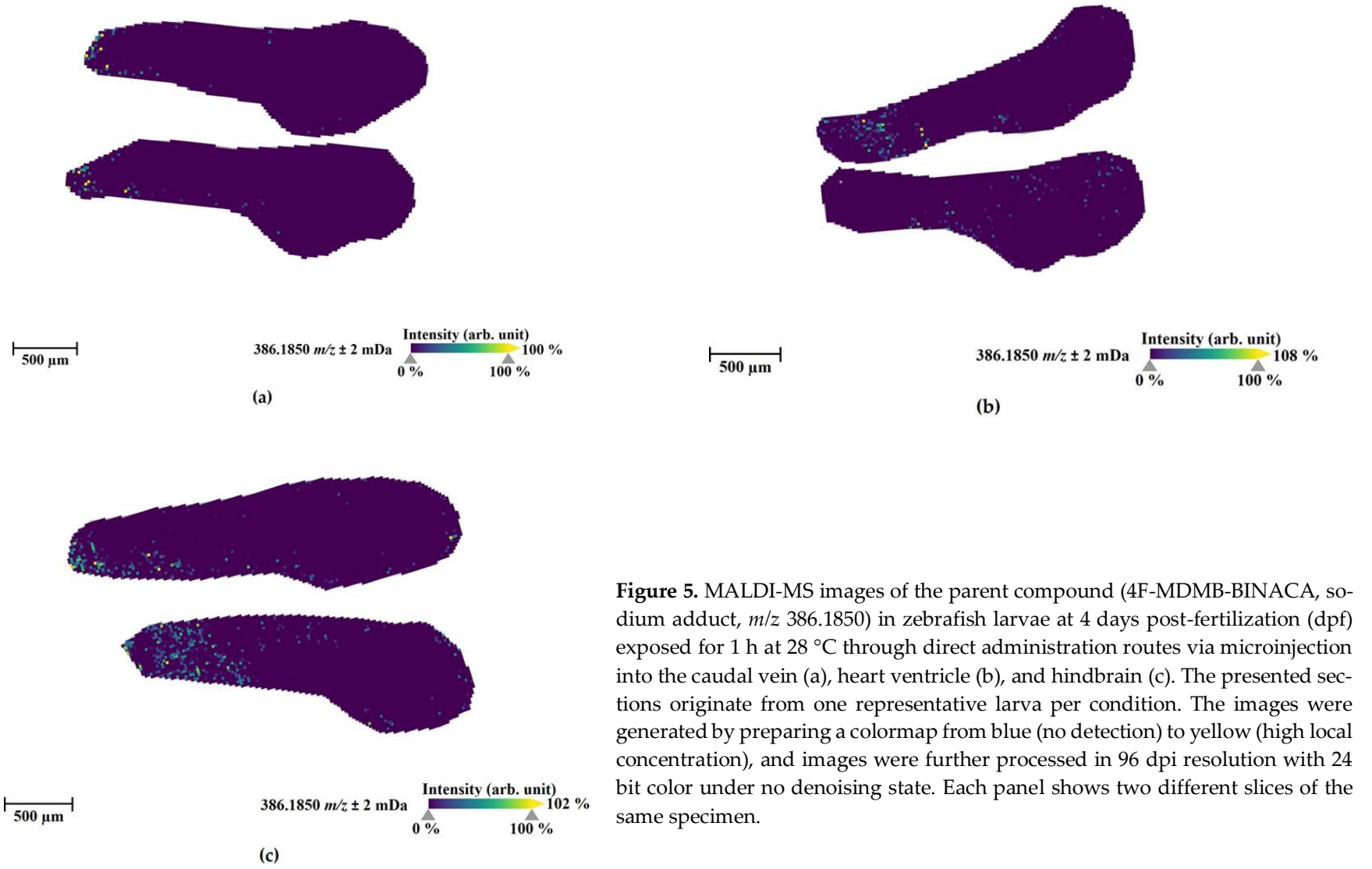

Figure 5. MALDI-MS images of the parent compound (4F-MDMB-BINACA, sodium adduct, *m/z* 386.1850) in zebrafish larvae at 4 days post-fertilization (dpf) exposed for 1 h at 28 °C through direct administration routes via microinjection into the caudal vein (a), heart ventricle (b), and hindbrain (c). The presented sections originate from one representative larva per condition. The images were generated by preparing a colormap from blue (no detection) to yellow (high local concentration), and images were further processed in 96 dpi resolution with 24 bit color under no denoising state. Each panel shows two different slices of the same specimen.

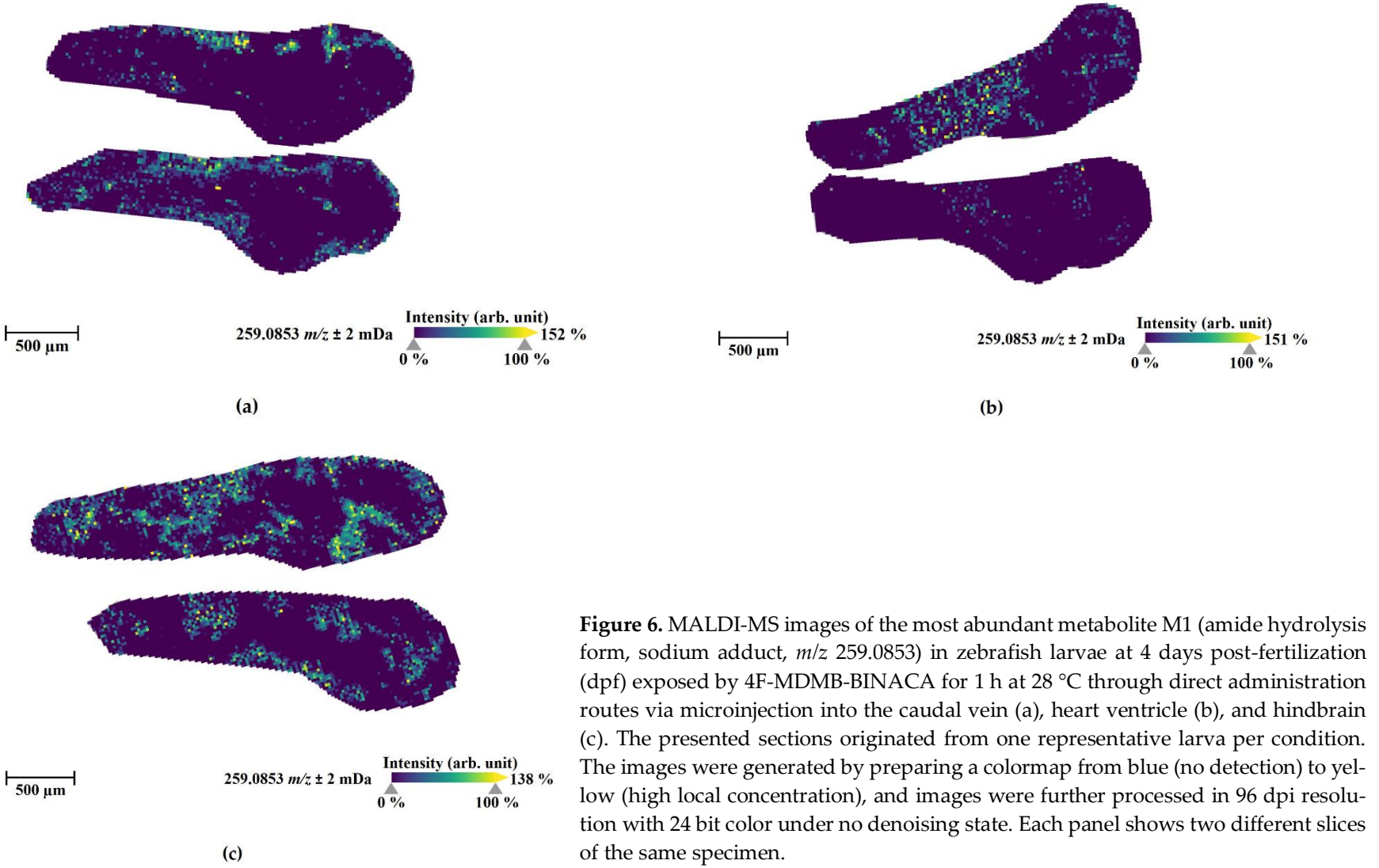

Figure 6. MALDI-MS images of the most abundant metabolite M1 (amide hydrolysis form, sodium adduct, *m/z* 259.0853) in zebrafish larvae at 4 days post-fertilization (dpf) exposed by 4F-MDMB-BINACA for 1 h at 28 °C through direct administration routes via microinjection into the caudal vein (a), heart ventricle (b), and hindbrain (c). The presented sections originated from one representative larva per condition. The images were generated by preparing a colormap from blue (no detection) to yellow (high local concentration), and images were further processed in 96 dpi resolution with 24 bit color under no denoising state. Each panel shows two different slices of the same specimen.

3.4 Results and Discussion

The parent compound, 4F-MDMB-BINACA, was mainly located at the ZF larva's peripheral region (Figure 5). In contrast, the most abundant metabolite in MSI, M1, was detected throughout the larval body, and it was distributed in all compartments spreading from the head to the tail region. ZF larva injected into the hindbrain showed the most prominent spread of M1, and in sections from ZF larvae injected into the heart ventricle, M1 somehow accumulated more in the dorsal section than in other sections (Figure 6). M3 and M4 were evenly distributed in the ZF larval bodies, showing some accumulation in the head region with relatively minor intensity (Supplementary Figures S2 and S3). Overall, hindbrain injection resulted in the best distribution of these metabolites, which is in line with the findings from LC-HRMS/MS measurements (Figure 3). The widely distributional detection of these metabolites inside the larvae, despite the local and low abundance detection of 4F-MDMB-BINACA, leads to the assumption that the circulation of the parent compound proceeded sufficiently within 1 h after microinjection, allowing for fast and efficient metabolism.

When we compared the detection of metabolites from MALDI-MSI experiments and LC-HRMS/MS studies, we observed a discrepancy with respect to the main ion adduct formation of the detected metabolites. Furthermore, different metabolites were detected as most abundant, and this dissimilarity could be explained by the use of entirely different workup steps and analytical methodologies, *e.g.*, sample preparation and separation, ionization techniques, and data collecting/processing, just to name a few.

Common adducts in MSI spectra are formed with protons, sodium, and calcium derived from inorganic salts or residual water, naturally present in all biological samples. Reducing the formation of inorganic salt adducts in MSI is therefore a crucial step for enhancing sensitivity [47,48]. For MALDI ionization preferably leading to $[M+H]^+$ ion species, a matrix deposition step is required. Here, we used 2,5-dihydroxybenzoic acid (DHB) [28], which is widely used, especially for metabolites and peptides in positive ionization mode [45,47,48]. As expected, in previous MALDI-MSI measurements of 7′*N*-5F-ADB, we mainly found protonated adducts of its metabolites, including the parent compound [28]. In contrast, MSI with 4F-MDMB-BINACA resulted in $[M+Na]^+$ as predominant ion species; however, $[M+H]^+$ ions were detected with high abundance. Thus, 4F-MDMB-BINACA and its metabolites were screened by MALDI-MSI, based on masses of their respective sodium adduct ions generated from structures identified by LC-HRMS/MS/MS2 [27] (Supplementary Table S2). In future studies, other matrices such as sinapinic acid (SA), α-cyano-4-hydroxycinnamic acid (CHCA), and commercial matrix mixtures (*e.g.*, DHB:CHCA = 1:1) could be considered to improve the detection of 4F-MDMB-BINACA in ZF samples. Another reason that MSI detection of metabolites was less successful than analyses based on LC-HRMS/MS could be the different sample size; for MSI, one ZF larva was sectioned into on average ten slices, whereas 30 ZF larvae were pooled for LC-HRMS/MS measurements. Further studies will be needed to optimize MSI for the assessment of ZF larvae considering various classes of drugs. We plan to further investigate MSI for ZF larvae by applying existing and optimized methods using ZF larvae homogenates [49–51] in order to account for possible deviations based on different tissue types [49] and local interfering molecules [45].

3.4.3. Differences in the Metabolism of 4F-MDMB-BINACA and 7′*N*-5F-ADB in Zebrafish Larvae and Influence of Cannabinoid Receptor Function on Drug Metabolism

While investigating the ZF larvae model employing various administration routes, we confirmed the highest number of metabolites of 7′*N*-5F-ADB, 4F-MDMB-BINACA, and other NPSs in the ZF larvae compared to other models [25–28]. The overall number of detected metabolites of 4F-MDMB-BINACA was lower than for 7′*N*-5F-ADB (Supplementary Table S3), despite their high structural similarity. Moreover, the calculated physicochemical properties of both SCs (Table 2) are similar. In particular, they have a similar predicted log p value (lipophilicity), which possibly could have influenced drug distribution and metabolism in the ZF larvae model. In detail, in human urine samples and the microinjected ZF larvae, 27 and 24 metabolites out of 36 possible metabolites for 7′*N*-5F-ADB, and nine and 11 out of 26 possible metabolites for 4F-MDMB-BINACA were observed, respectively.

Table 2. Comparison of calculated physicochemical properties [1] of 4F-MDMB-BINACA and 7′*N*-5F-ADB.

	4F-MDMB-BINACA	7′*N*-5F-ADB
Log *P* [2]	3.12	3.20
Strongest acidic pKa [3]	14.65	15.05
Strongest basic pKa [3]	−0.76	3.11
Log Intrinsic solubility (mol/L) [4]	−4.37	−4.50

[1] All data were calculated online at https://chemicalize.com (accessed on 31.10.2019). [2] Log P value refers to the logarithm of the partition coefficient of a compound in octanol and water. [3] pKa, the acid dissociation constant at logarithmic scale, refers to a specific equilibrium constant to represent the ability of an acid to dissociate protons from a heterocyclic core (acidic pKa) and the protonated tertiary base (basic pKa). [4] Intrinsic solubility is the basic solubility of a drug when it is entirely unionized.

Due to the relatively small number of detected 4F-MDMB-BINACA metabolites in the ZF larvae model, we investigated a possible correlation between (impaired) liver development and metabolic function in ZF larvae. Thus, we evaluated the SCs hepatotoxic effect along with 7′*N*-5F-ADB. The ZF liver toxicity of these two SCs was determined indirectly by measuring the liver size after treatment via conventional waterborne exposure using a transgenic ZF line (Tg(*fabp10a*:DsRed;*elaA*:EGFP)) (Figure 7). This transgenic line displays strong constitutive expression of red fluorescent protein (DsRed) in the liver and enhanced green fluorescent protein (EGFP) in the exocrine pancreas under the *fabp10a* promoter and the *elaA* promoter, respectively, and it is commonly used for fluorescence-based *in vivo* hepatotoxicity assays [52–54]. In these ZF larvae treated for 1 d with 7′*N*-5F-ADB, the liver size increased by 21%, whereas larvae treated with 4F-MDMB-BINACA displayed a 37% decrease in liver size. These findings in ZF larvae treated with 4F-MDMB-BINACA resembled a phenotype that was previously described by Liu et al., which was caused by the loss of two cannabinoid receptors (CB1 and CB2) in ZF larvae [38]. Despite a reduction of liver size, the authors also reported impaired hepatocyte differentiation and proliferation in these larvae, whereas the abnormal liver architecture influenced the development of ZF even up to the

adult stage. Based on the acute effect of 4F-MDMB-BINACA on liver development in 4 dpf larvae, we thought that this phenotype might explain the less efficient drug metabolism compared to 7′*N*-5F-ADB. Although treatment with the latter also induced a phenotype in ZF larvae the extent of the effect was less pronounced than observed in ZF larvae treated with 4F-MDMB-BINACA. The generally contrary effects of both SCs that serve as CB receptor agonists, with 4F-MDMB-BINACA reducing liver size and 7′*N*-5F-ADB increasing it cannot be currently explained. In principle, it was expected that 4F-MDMB-BINACA, due to its agonistic CB receptor activity, also increases the liver size in ZF larvae. However, complex regulation following activation of CB1 and/or CB2 and the balance between activity of both receptors might explain the differential phenotypes observed. For future studies, it would be interesting to study the influence of CB receptor antagonists reducing the liver size on ZF metabolism and to compare the results to our findings with 4F-MDMB-BINACA, for which we found an atypical phenotype.

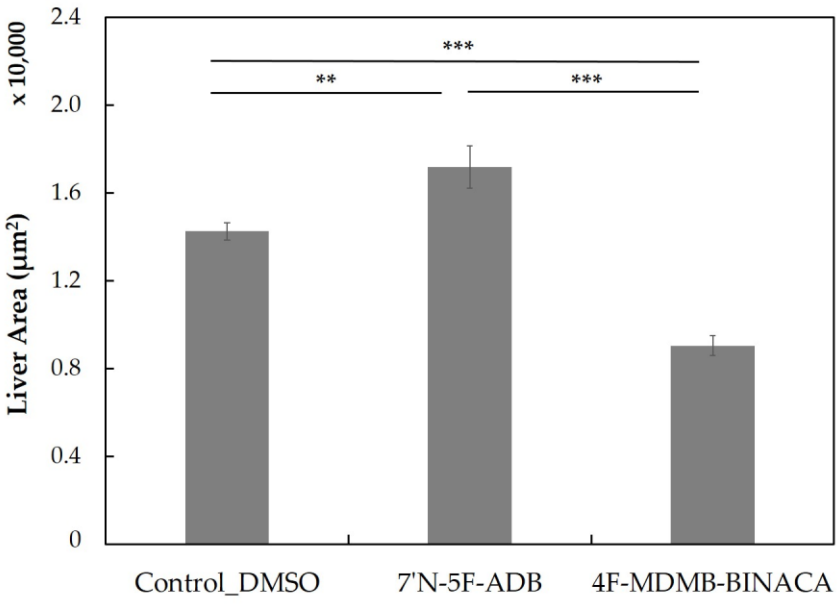

(a)

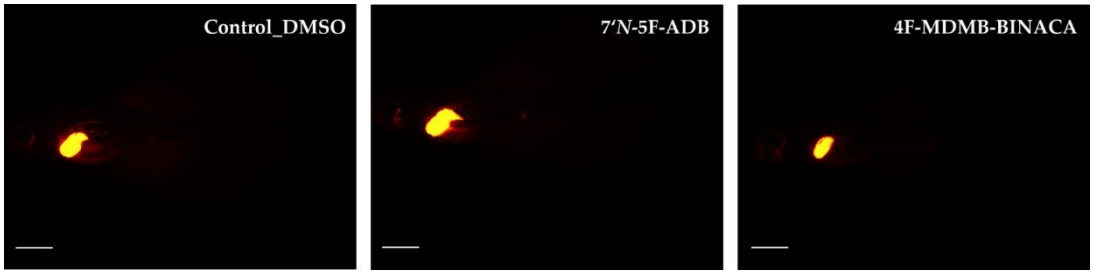

(b)

Figure 7. Liver size assessment (a) and red fluorescent liver morphologies (b) of transgenic ZF larvae (Tg(*fabp10a*:DsRed;*elaA*:EGFP)) treated by waterborne exposure with DMSO, 7′*N*-5F-ADB (50 μM), or 4F-MDMB-BINACA (25 μM) from 4 dpf to 5 dpf (n = 11–15). All data are represented by the mean ± standard error of the mean (s.e.m.) and p values were computed by one-way ANOVA (** $p < 0.01$, *** $p < 0.001$). Liver sizes were determined based on fluorescence microscopy images using ImageJ 1.53a. Scale bars: 500 μm.

In order to study the possible impact of CB1/2 receptor function on drug metabolism in more detail, we employed the morpholino (MO) technology to knock down cnr1 and cnr2 in ZF larvae. For determining the optimal non-toxic conditions for the gene knockdown, the survival rates of ZF larvae from 3 dpf to 4 dpf were examined after early-stage injection of three different concentrations of MOs (Supplementary Figure S4). Simultaneously, morphological malformations of larvae were recorded (Supplementary Table S4). CB2-deficient morphants showed morphological malformations, such as curved or vent spine, shortened tail, and edemas in the pericardial and yolk sac more frequently than the CB1-deficient morphants (Supplementary Figure S5). Considering these toxic effects of high MO dosage, we used an MO concentration of 100 μM for all subsequent experiments. Furthermore, since the random MO control 25-*N* still indicated some rare toxic effects on ZF larvae, control injections were performed with distilled water unless otherwise specified in the Supplementary Table S5.

Following *cnr1* and *cnr2* gene knockdown in embryos of the Tg(*fabp10a*:DsRed; *elaA*:EGFP) ZF line, we assessed the liver size of morphants from 3 to 5 dpf (Figure 8). We observed small effects on the liver size already at 3 and 4 dpf, whereas the impact of CB1 and CB2 deficiency was most obvious at 5 dpf, and CB2-deficient morphants showed a significantly reduced liver area compared to the control group (mock injection with distilled water). The extent of liver size reduction in 5 dpf CB2-deficient morphants (26% reduction compared to control) was similar to that observed in 5 dpf larvae treated for 1 d with 4F-MDMB-BINACA (37% reduction compared to untreated control).

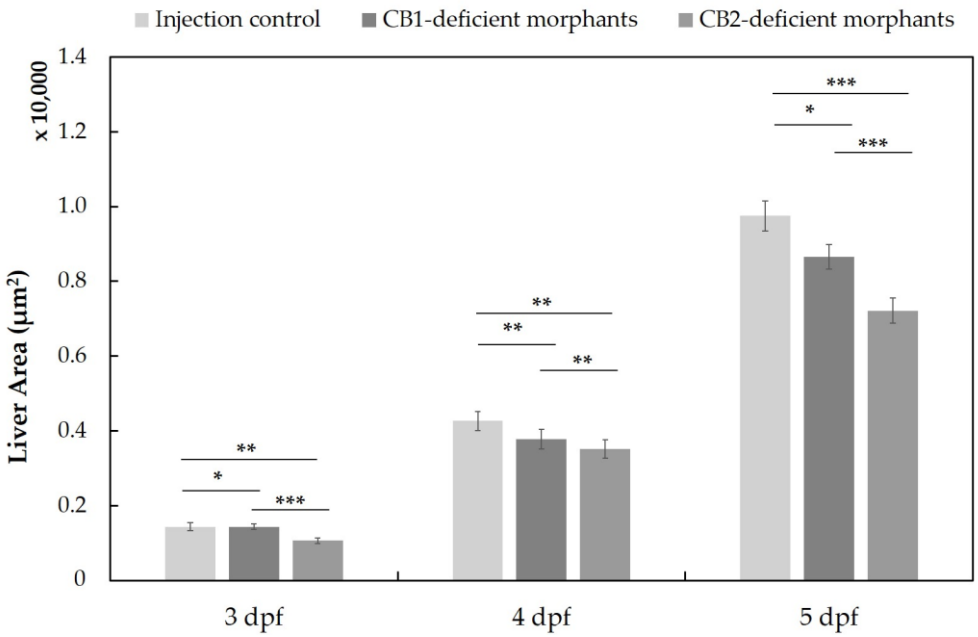

Figure 8. Liver size assessment in the transgenic ZF line (Tg(*fabp10a*:DsRed;*elaA*:EGFP)) after MO injection at one-cell stage to generate CB1- and CB2-deficient morphants (n = 43 (at 3 dpf), 41 (at 4 dpf), 55 (at 5 dpf)). All data are represented by the mean ± standard error of the mean (s.e.m.), and p values were computed with one-way ANOVA (* $p < 0.05$, ** $p < 0.01$, *** $p < 0.001$). Liver sizes were determined based on fluorescence microscopy images using ImageJ 1.53a.

To demonstrate the effect of CB1- and CB2-deficiency on SC metabolism, we exposed both morphants to 4F-MDMB-BINACA and 7′*N*-5F-ADB, respectively, from 4 to 5 dpf as described in previous studies, and we determined the metabolite profile by LC-HRMS/MS [25,27]. The direct administration route via injection was not considered in this study to avoid the stress of an additional injection. Remarkably, the influence of these two cannabinoid receptors on the overall number of detected metabolites of 4F-MDMB-BINACA and 7′*N*-5F-ADB compared to a control group (mock-injected MO control) was pronounced. We observed only ca. 80% and ca. 45% of metabolites of both SCs in the CB1-deficient and CB2-deficient morphants, respectively (Figure 9 and Supplementary Figure S6). SCs are generally described to mainly act as agonists of CB1 and as partial agonists of CB2 [30,55]. However, in the given example (Figure 9), dysfunctional CB2 seems to play a more critical role in liver metabolic efficiency of ZF larvae than CB1. As NPSs exert their psychoactive effects mostly via CB1, their activity on CB1 function was mainly investigated using *in vitro* assays [30,55,56]. Cannaert et al. reported 4F-MDMB-BINACA as one of the most potent CB1 agonists in recently detected twelve SCs with a half-maximal effective concentration (EC_{50}) of 7.37 nM, compared to 5,475 nM for 7′*N*-5F-ADB [55]. In this respect, it seems plausible that 4F-MDMB-BINACA might also serve as a stronger CB2 agonist in ZF larvae than 7′*N*-5F-ADB, and the strong activation of CB2 might have a similar effect on drug metabolism as CB2 deficiency, both leading to a hepatotoxic phenotype.

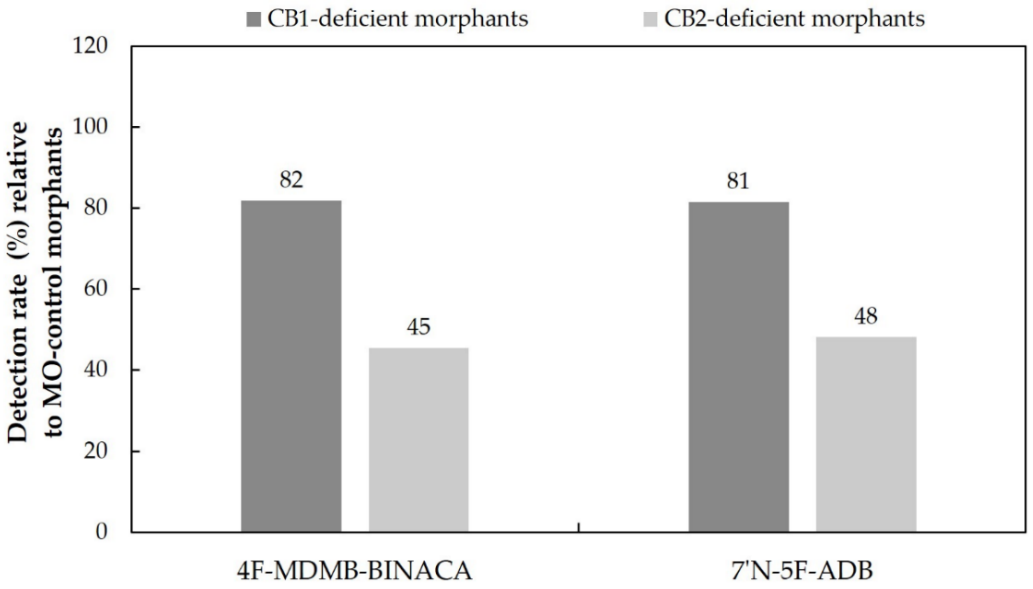

Figure 9. Comparison of the overall detection rates of phase I and phase II metabolites produced in CB1-deficient and CB2-deficient ZF larvae after waterborne exposure to 25 μM 4F-MDMB-BINACA and 50 μM 7′*N*-5F-ADB, respectively ($n = 3$). The detection rates were calculated based on the number of metabolites found in the respective control population (set to 100%).

3.5 Materials and Methods

3.5.1. Chemicals and Other Materials

4F-MDMB-BINACA was provided by the EU-funded project ADEBAR (IZ25-5793-2016-27) for research purposes. 7′*N*-5F-ADB was obtained from www.buyreserchchemicals.de (accessed on 19 January 2022) tagged as 4′*N*-5F-ADB, which was confirmed to be 7′*N*-5F-ADB by analysis of NMR (nuclear magnetic resonance) [25]. Dimethyl sulfoxide (DMSO), methylene blue, phenol red, tricaine (3-amino-benzoic acid ethyl ester), mineral oil, trifluoroacetic acid, gelatin from cold water fish skin, and 2,5-dihydroxybenzoic acid (2,5-DHB) were obtained from Sigma-Aldrich (Taufkirchen, Germany). Methanol (LC-MS grade), acetonitrile (LC-MS grade), formic acid (LC-MS grade) were from VWR (Darmstadt, Germany). NaCl, KCl, $MgSO_4$, $Ca(NO_3)_2$, and HEPES were obtained from Carl Roth (Karlsruhe, Germany). The 10 mM stock solutions for all standards were prepared in DMSO, and solutions were stored for a maximum of one month at −20 °C. The working solutions were freshly prepared prior to each experiment. Morpholino oligonucleotides (MOs) were purchased from Gene Tools, LLC (Philomath, OR, USA). The working solution of MOs was prepared at 1 mM in distilled water and stored according to the manufacturer's protocol, and the detailed information of MOs used in the present study is given in Section 3.5.5. 6-well plates were obtained from Sarstedt (Nümbrecht, Germany). Glass capillaries TW100F-4 (4 inches (100 mm), 1/0.75 OD/ID (mm), Filament) were from World Precision Instruments Germany GmbH (Friedberg, Germany). Conductive indium-tin-oxide (ITO) coated glass slides were purchased from Bruker Daltonics (Bremen, Germany). Zebrafish embryos of the AB wild-type line were initially obtained from the Luxembourg Center for Systems Biomedicine (Belvaux, Luxembourg). The ZF line Tg(*fabp10a*:DsRed;*elaA*:EGFP) was provided by the Goessling lab (Boston, MA, USA). Dry small granulate food was purchased from SDS Deutschland (Limburgerhof, Germany), and *Artemia cysts* (>230,000 nauplii per gram) were obtained from Coralsands (Wiesbaden, Germany).

3.5.2. Zebrafish Maintenance and Embryo Collection

Zebrafish husbandry and all experiments with ZF larvae were performed according to EU Directive 2010/63/EU and the German Animal Welfare Act (§11 Abs. 1 TierSchG). All works were accomplished following internal standard-operating procedures (SOPs) based on published standard methods [57]. Adult ZF were kept in an automated aquatic eco-system (PENTAIR, Apopka, UK) that is continuously monitored: Temperature (27 ± 0.5 °C), pH (7.0 ± 0.1), conductivity (800 ± 50 μS), and light–dark cycle (14 h/10 h). Fish were fed twice a day with dry small granulate food and freshly hatched live Artemia cysts once a day. The ZF embryo/larvae medium (0.3× Danieau's solution) was composed of 17 mM NaCl, 2 mM KCl, 0.12 mM $MgSO_4$, 1.8 mM $Ca(NO_3)_2$, 1.5 mM HEPES, pH 7.1–7.3, and 1.2 μM methylene blue. For ZF embryo production, ZF pairs were kept overnight in standard mating cages, separated by gender. The following morning, the adult ZF started spawning immediately after removing the separators. All fertilized eggs of ZF were sorted using a Zeiss Stemi 508

stereo microscope (Carl Zeiss Microscopy GmbH, Jena, Germany). All embryos were raised in an incubator at 28 °C with daily medium change to clean embryo cultures. ZF larvae at 4 dpf were used for drug metabolism studies.

3.5.3. Drug Treatment of Zebrafish Larvae via Medium Exposure

The sample preparation following aquatic drug exposure is described elsewhere [25,27,28]. A non-toxic exposure concentration was chosen based on the survival rate as determined by *in vivo* maximum-tolerated concentration (MTC) experiments with 4 dpf ZF larvae. For the two drugs (4F-MDMB-BINACA, 7′*N*-5F-ADB) investigated in the current study, the results of MTC are published in our previous papers [25,27]. For metabolite studies, 15 ZF larvae at 4 dpf were transferred to one well of a 6-well plate containing 3 mL of 0.3× Danieau's medium with 25 μM 4F-MDMB-BINACA and 50 μM 7′*N*-5F-ADB, respectively. All exposure media contained a final concentration of 1% (*v*/*v*) DMSO, and ZF larvae were treated for 24 h in an incubator at 28 °C. An additional 15 larvae were incubated in a compound-free medium containing only 1% DMSO (*v*/*v*) as negative control (background masses). Before sample extraction, 30 larvae were pooled, and sample extractions were performed as described below in Section 3.5.7. All pooled samples were prepared in triplicates.

3.5.4. Drug Treatment of Zebrafish Larvae via Microinjection into Different Compartments

For microinjections, the glass microneedle was produced by a Flaming/Brown type micropipette puller (Model P-100, Sutter Instrument, Novato, CA, USA). The microneedle can be fabricated to fit the purpose via changes of heating and pulling parameters. 4F-MDMB-BINACA solution at 5 mM was prepared in 50% DMSO and 50% of a 0.5% phenol red solution, and the microneedle was filled with this solution without air bubbles by a microloader pipette. The needle containing the solution was assembled in an M-152 manipulator (Narishige Group, Tokyo, Japan) connected to a FemtoJet 4× Microinjector (Eppendorf, Hamburg, Germany). Before starting injections, every microinjection needle was calibrated by a single droplet injection onto mineral oil on a micrometer slide. We chose to microinject 4.19 nL of 5 mM 4F-MDMB-BINACA per one larva, which corresponds to a total amount of 228.4 ng in a pool of 30 larvae. The detailed conditions of making the glass microneedle and needle calibration are given elsewhere [28].

Before starting the injection, ZF larvae at 4 dpf were anaesthetized by tricaine solution, and promptly, they were aligned on an agarose plate prepared using Z-MOLD (World Precision Instruments, Sarasota, FL, USA). The excess medium was removed with a pipette as much as possible to immobilize ZF larva during the injection. Microinjections were conducted into three different compartments of ZF larvae (caudal vein, heart ventricle, and hindbrain) under a stereo microscope (Zeiss Stemi 508 stereo microscope). The injected larvae were immediately transferred to fresh 0.3× Danieau's medium, and they were incubated at 28 °C for 1 h. Prior to sample extraction, all malformed larvae generated after the injection were excluded by sorting using a microscope, and 30 healthy larvae were pooled into one

tube. Sample extractions proceeded as described below (Section 3.5.7), and all pooled larvae were prepared in triplicates. In general, the mortality rate of ZF larvae after microinjection was below 10% in all cases.

3.5.5. Gene Knockdwon of Cannabinoid Receptor Type 1 and Type 2 via Microinjection of Morpholino Oligonucleorides in Zebrafish Embryos

The morpholino oligonucleotides (MOs; synthesized by Gene Tools) against cannabinoid receptor type 1 (CB1) and type 2 (CB2) were designed to target its splicing site (Supplementary Table S5), and these MOs were validated in earlier studies [38,58]. Each MO working solution, yielding final concentrations of 100, 200, and 500 μM, was freshly prepared from a 1 mM stock solution according to the manufacturer's recommendations and a previously published protocol [59] and mixed with 0.5% phenol red solution as described in Section 3.5.4. These MO solutions were injected into one-cell stage embryos with a volume of 4.19 nL. Embryos were maintained as described above (Section 3.5.2).

3.5.6. Measurement of the Fluorescent Liver Size in a Transgenic Zebrafish Larva

A transgenic zebrafish line Tg(*fabp10a*:DsRed; *elaA*:EGFP) was used to determine the liver size of ZF larva, which has been widely employed for liver studies [52–54]. This ZF line expresses the red fluorescent protein (DsRed) under control of the *fabp10a* promoter in the liver and the enhanced green protein (EGFP) under the elastase A (*elaA*) promoter in the exocrine pancreas. For the fluorescent liver measurement of ZF larvae from 3 dpf to 5 dpf, ZF larvae were anesthetized on ice. All ZF larvae were arranged directly in a manner to minimize measuring variances, in which the head part was positioned on the left side and the end tail on the right side. Images of ZF livers were taken using a Leica M205 FA stereo microscope (Leica Mikrosysteme Vertrieb GmbH, Wetzlar, Germany) connected with an X-Cite® 200DC illuminator (Excelitas technologies, Mississauga, ON, Canada) and appropriate filter sets for red fluorescent protein detection. The liver size of ZF larva was then quantified using ImageJ version 1.53a [60].

3.5.7. Zebrafish Sample Preparation and Metabolite Analysis by LC-HRMS/MS

All treated larvae (waterborne exposure and microinjection) were transferred into a tube using a pipette and then rinsed twice with 1 mL of 0.3× Danieau's solution. The washed larvae were euthanized by placing the tubes in ice water for 15 min. These larvae were snap-frozen in liquid nitrogen, followed by lyophilization for 4 h. The lyophilized larvae were stored for a maximum of one week at –20 °C before extraction. For metabolite identification, frozen larvae were thawed at room temperature for at least 30 min and extracted by vigorous vortexing for 2 min with 50 μL methanol. The sample was centrifuged at 10,000× *g* for 2 min at room temperature, and the supernatant was transferred to an autosampler vial. The extract from ZF larvae was kept in a freezer at −20 °C and analyzed within one week after extraction.

The LC-HRMS/MS system consisted of a Dionex Ultimate 3000 RSLC system (Thermo Fisher Scientific, Germering, Germany) and maXis 4G HR-QTOF mass spectrometer (Bremen, Germany) with the Apollo II ESI source. Separation of 5 μL aliquot from all larvae extracts was carried out by a linear gradient with 0.1% formic acid in water (*v*/*v*, eluent A) and 0.1% formic acid in acetonitrile (*v*/*v*, eluent B) at a flow rate of 600 μL/min. As stationary phase, a Waters ACQUITY BEH C_{18} column (100 × 2.1 mm, 1.7 μm) equipped with a Waters VanGuard BEH C_{18} 1.7 μm guard column at 45 °C was used. The gradient mode was programmed into these steps as follows; 0–0.5 min, 5% eluent B; 0.5–18.5 min, 5–95% eluent B; 18.5–20.5 min, 95% eluent B; 20.5–21 min, 95–5% eluent B; 21–22.5 min, 5% eluent B. UV spectra were recorded by a Diode array detector (DAD) in the range from 200 to 600 nm. Mass spectra were recorded in centroid mode ranging from 150–2,500 *m*/*z* at a 2 Hz full scan acquisition rate under auto MS/MS conditions in positive ionization mode. External calibration was automatically performed by injecting sodium formate and calibration on the respective clusters formed in the ESI source before every LC-HRMS/MS run. All MS analyses were acquired in the presence of the *m*/*z* 622.0290, 922.0098, and 1221.9906 ions as the lock masses generated with the $[M+H]^+$ ions of $C_{12}H_{19}F_{12}N_3O_6P_3$, $C_{18}H_{19}O_6N_3P_3F_2$, and $C_{24}H_{19}F_{36}N_3O_6P_3$. DataAnalysis software version 4.4 (Bruker Daltonics, Bremen, Germany) was used for qualitative analysis. All data were presented with the range of mean and standard deviation (SD) using MS Excel 2016.

All masses and MS2 data of four substrates, 4F-MDMB-BINACA, 7′*N*-5F-ADB, and its expected metabolites, were confirmed in our previous studies [25,27,28,61]. Accordingly, their structures and other detailed information were not included in the present study. With the absence of reference standards for using absolute quantification, the comparisons of the metabolites performed in this paper were executed by quantifying peak areas under the assumption of similar ionization behaviors of the individual metabolites.

3.5.8. Mass Spectrometry Imaging Analysis of Zebrafish Larva by MALDI-FT-ICR

The ZF larvae treated by the procedures described in Sections 3.5.3 and 3.5.4 were embedded in 40% (*w*/*v*) gelatin solution and were then frozen and stored at −20 °C until cryosectioning. A single larva was cut with 10-μm thickness at −20 °C using a cryostat (MEV; SLEE, Mainz, Germany), and every section was placed on a cold conductive indium-tin-oxide (ITO) coated glass slide. The slides were scanned under a microscope for alignment of the optical image of the sample in MALDI. The serial sections from one larva in one glass slide were deposited using TM-Sprayer (HTX M5; HTX Technologies, Chapel Hill, NC, USA) with 15 mg mL^{-1} 2,5-dihydroxybenzoic acid (2,5-DHB) in acetonitrile:water (9:1, *v*/*v*) solution containing 0.1% of trifluoroacetic acid, and then dried in a vacuum desiccator for ≥ 2 h. The dried glass slide was stored at –20 °C before MALDI measurement. Importantly, as the detachment of the sections from the glass slide happened during the thawing step prior to the MALDI analysis, it is recommended to analyze the samples within one week after matrix deposition. This phenomenon occurred mainly from the arid part of the section embedded in a 40% gelatin medium.

For MSI measurement, the sections of ZF larvae were analyzed by MALDI and 7T SolariX FT-ICR (Bruker Daltonics, Bremen, Germany) in positive ionization mode (*m*/*z* range 150–1,000), using 40 laser shots per pixel with a raster width of 20 μm. Before acquiring MALDI images, the mass calibration of FT-ICR was carried out using the calibration standard according to the manufacturer manual, and for auto-calibration of MALDI of each laser measurement, the lock mass was set to *m*/*z* 273.0394 (2,5-DHB matrix). ftmsControl version. 2.2.0, flexImaging version 5.0, and SCiLS Lab version 2021a Pro software (Bruker Daltonics, Bremen, Germany) were used for MALDI-MSI data acquisitions and image data analyses in two dimensions.

3.6 Summary and Conclusions

Our study aimed to strengthen the understanding of the human metabolism of 4F-MDMB-BINACA using the ZF larvae model as an alternative *in vivo* model. By predicting human metabolism based on results in the ZF larvae model, several issues caused by variance in human biosamples due to the lack of homogeneity and diversity among samples in random sampling could be overcome. ZF larvae were treated with the SC by direct injection into vital organs, and in total, ten metabolites were observed (Figure 2). Encouragingly, we found high matching rates of ZF metabolites of 67% for human blood samples and 56% for human urine samples, respectively. In conclusion, metabolite data sets from the ZF model, in combination with data from *in vitro* models such as HepaRG, can complement and extend human metabolism data.

Moreover, the spatial distribution of 4F-MDMB-BINACA and its metabolites in ZF larvae was analyzed by MALDI-MSI, and three metabolites were visualized inside ZF larval bodies by MSI (Figure 6 and Supplementary Figures S2 and S3). In the context of our study, this technology can be applied to analyze the biodistribution of drugs and their metabolites and it can help to investigate, *e.g.*, accumulation of compounds in specific organs. Here, we did not detect unusual local concentrations of the studied SC, but we were able to identify another metabolite (M1), which was not found in LC-HRMS-based screening of extracted larvae.

The overall metabolite detection between 4F-MDMB-BINACA and another SC, 7′*N*-5F-ADB [28], were contrasting despite the similarity of their physicochemical properties (Table 2). Consequently, we performed additional experiments to shed light on the observed differences in ZF metabolism with respect to the total number of detected metabolites for these two SCs. The liver toxicity of the SCs was determined indirectly by measuring the liver size of a transgenic ZF line, and 4F-MDMB-BINACA induced a pronounced liver size reduction despite its strong agonistic activity on CB2 (Figure 7). Thus, we investigated the role of cannabinoid receptors on liver development and drug metabolism in ZF larvae. We could show that CB2-deficient larvae showed a drastic decline in the overall number of detected metabolites of both SCs, which could be related to the simultaneously observed hepatotoxic effect (Figure 9 and Supplementary Figure S6). The role of CB2 deficiency (and dysregulation) in drug metabolism requires further research, and here, we provide first evidence that it might play a major role in the overall efficacy of drug metabolism in the liver.

In summary, we applied established methodologies for studying drug metabolism in ZF larvae. A concise evaluation in wild-type ZF allowed for refinement of the phase I metabolic pathways of 4F-MDMB-BINACA. Additionally, we investigated the role of cannabinoid receptor function in metabolism using genetically modified ZF larvae. We gained important insights into the relationship between liver function, cannabinoid receptor function, and the onset of drug metabolism. Although many questions associated with various biological systems for drug metabolism studies require further analyses, this study emphasizes the high potential of ZF larvae as a model to study complex human bioprocesses. We

expect that ZF will play a more prominent role in translational research in future. Importantly, applying state-the-art analytics contributes to a better understanding of drug pharmaco- and toxicokinetics, which, in turn, is necessary to understand complex biological processes in the *in vivo* model.

3.7 Bibliography

1. Cassar, S.; Adatto, I.; Freeman, J.L.; Gamse, J.T.; Iturria, I.; Lawrence, C.; Muriana, A.; Peterson, R.T.; van Cruchten, S.; Zon, L.I. Use of Zebrafish in Drug Discovery Toxicology. *Chem. Res. Toxicol.* **2020**, *33*, 95–118. https://doi.org/10.1021/acs.chemrestox.9b00335.
2. Waring, M.J.; Arrowsmith, J.; Leach, A.R.; Leeson, P.D.; Mandrell, S.; Owen, R.M.; Pairaudeau, G.; Pennie, W.D.; Pickett, S.D.; Wang, J.; et al. An analysis of the attrition of drug candidates from four major pharmaceutical companies. *Nat. Rev. Drug Discov.* **2015**, *14*, 475–486. https://doi.org/10.1038/nrd4609.
3. Blomme, E.A.G.; Will, Y. Toxicology Strategies for Drug Discovery: Present and Future. *Chem. Res. Toxicol.* **2016**, *29*, 473–504. https://doi.org/10.1021/acs.chemrestox.5b00407.
4. Swinney, D.C.; Anthony, J. How were new medicines discovered? *Nat. Rev. Drug Discov.* **2011**, *10*, 507–519. https://doi.org/10.1038/nrd3480.
5. MacRae, C.A.; Peterson, R.T. Zebrafish as tools for drug discovery. *Nat. Rev. Drug Discov.* **2015**, *14*, 721–731. https://doi.org/10.1038/nrd4627.
6. Ellis, L. Zebrafish as a High-Throughput In Vivo Model for Testing the Bioactivity of Cannabinoids. In *Recent Advances in Cannabinoid Research*; Costain, W.J., Laprairie, R.B., Eds.; IntechOpen: London, UK, 2019; ISBN 978-1-83880-151-9.
7. Katoch, S.; Patial, V. Zebrafish: An emerging model system to study liver diseases and related drug discovery. *J. Appl. Toxicol.* **2021**, *41*, 33–51. https://doi.org/10.1002/jat.4031.
8. Goessling, W.; Sadler, K.C. Zebrafish: An important tool for liver disease research. *Gastroenterology* **2015**, *149*, 1361–1377. https://doi.org/10.1053/j.gastro.2015.08.034.
9. Chakraborty, C.; Hsu, C.H.; Wen, Z.H.; Lin, C.S.; Agoramoorthy, G. Zebrafish: A Complete Animal Model for In Vivo Drug Discovery and Development. *Curr. Drug Metab.* **2009**, *10*, 116–124. https://doi.org/10.2174/138920009787522197.
10. Hill, A. Zebrafish in Drug Discovery: Safety Assessment. In *Drug Discovery and Evaluation: Safety and Pharmacokinetic Assays*; Vogel, H.G., Maas, J., Hock, F.J., Mayer, D., Eds.; Springer: Berlin/Heidelberg, Germany, 2013; pp. 605–629, ISBN 978-3-642-25239-6.
11. Cutler, C.; Multani, P.; Robbins, D.; Kim, H.T.; Le, T.; Hoggatt, J.; Pelus, L.M.; Desponts, C.; Chen, Y.-B.; Rezner, B.; et al. Prostaglandin-modulated umbilical cord blood hematopoietic stem cell transplantation. *Blood* **2013**, *122*, 3074–3081. https://doi.org/10.1182/blood-2013-05-503177.
12. Li, D.; March, M.E.; Gutierrez-Uzquiza, A.; Kao, C.; Seiler, C.; Pinto, E.; Matsuoka, L.S.; Battig, M.R.; Bhoj, E.J.; Wenger, T.L.; et al. ARAF recurrent mutation causes central conducting lymphatic anomaly treatable with a MEK inhibitor. *Nat. Med.* **2019**, *25*, 1116–1122. https://doi.org/10.1038/s41591-019-0479-2.
13. Mandelbaum, J.; Shestopalov, I.A.; Henderson, R.E.; Chau, N.G.; Knoechel, B.; Wick, M.J.; Zon, L.I. Zebrafish blastomere screen identifies retinoic acid suppression of MYB in adenoid cystic carcinoma. *J. Exp. Med.* **2018**, *215*, 2673–2685. https://doi.org/10.1084/jem.20180939.

14. North, T.E.; Goessling, W.; Walkley, C.R.; Lengerke, C.; Kopani, K.R.; Lord, A.M.; Weber, G.J.; Bowman, T.V.; Jang, I.-H.; Grosser, T.; et al. Prostaglandin E2 regulates vertebrate haematopoietic stem cell homeostasis. *Nature* **2007**, *447*, 1007–1011. https://doi.org/10.1038/nature05883.
15. Ryals, M.; Morell, R.J.; Martin, D.; Boger, E.T.; Wu, P.; Raible, D.W.; Cunningham, L.L. The Inner Ear Heat Shock Transcriptional Signature Identifies Compounds That Protect Against Aminoglycoside Ototoxicity. *Front. Cell. Neurosci.* **2018**, *12*, 445. https://doi.org/10.3389/fncel.2018.00445.
16. White, R.M.; Cech, J.; Ratanasirintrawoot, S.; Lin, C.Y.; Rahl, P.B.; Burke, C.J.; Langdon, E.; Tomlinson, M.L.; Mosher, J.; Kaufman, C.; et al. DHODH modulates transcriptional elongation in the neural crest and melanoma. *Nature* **2011**, *471*, 518–522. https://doi.org/10.1038/nature09882.
17. Yu, P.B.; Hong, C.C.; Sachidanandan, C.; Babitt, J.L.; Deng, D.Y.; Hoyng, S.A.; Lin, H.Y.; Bloch, K.D.; Peterson, R.T. Dorsomorphin inhibits BMP signals required for embryogenesis and iron metabolism. *Nat. Chem. Biol.* **2008**, *4*, 33–41. https://doi.org/10.1038/nchembio.2007.54.
18. Poon, K.L.; Wang, X.; Ng, A.S.; Goh, W.H.; McGinnis, C.; Fowler, S.; Carney, T.J.; Wang, H.; Ingham, P.W. Humanizing the zebrafish liver shifts drug metabolic profiles and improves pharmacokinetics of CYP3A4 substrates. *Arch. Toxicol.* **2017**, *91*, 1187–1197. https://doi.org/10.1007/s00204-016-1789-5.
19. Diao, X.; Huestis, M.A. New Synthetic Cannabinoids Metabolism and Strategies to Best Identify Optimal Marker Metabolites. *Front. Chem.* **2019**, *7*, 109. https://doi.org/10.3389/fchem.2019.00109.
20. van Wijk, R.C.; Krekels, E.H.J.; Hankemeier, T.; Spaink, H.P.; van der Graaf, P.H. Systems pharmacology of hepatic metabolism in zebrafish larvae. *Drug Discov. Today Dis. Models* **2016**, *22*, 27–34. https://doi.org/10.1016/j.ddmod.2017.04.003.
21. de Souza Anselmo, C.; Sardela, V.F.; Matias, B.F.; de Carvalho, A.R.; de Sousa, V.P.; Pereira, H.M.G.; de Aquino Neto, F.R. Is zebrafish (*Danio rerio*) a tool for human-like metabolism study? *Drug Test. Anal.* **2017**, *9*, 1685–1694. https://doi.org/10.1002/dta.2318.
22. Jones, H.S.; Trollope, H.T.; Hutchinson, T.H.; Panter, G.H.; Chipman, J.K. Metabolism of ibuprofen in zebrafish larvae. *Xenobiotica* **2012**, *42*, 1069–1075. https://doi.org/10.3109/00498254.2012.684410.
23. Brox, S.; Seiwert, B.; Haase, N.; Küster, E.; Reemtsma, T. Metabolism of clofibric acid in zebrafish embryos (*Danio rerio*) as determined by liquid chromatography-high resolution-mass spectrometry. *Comp. Biochem. Physiol. C Toxicol. Pharmacol.* **2016**, *185–186*, 20–28. https://doi.org/10.1016/j.cbpc.2016.02.007.
24. Kantae, V.; Krekels, E.H.J.; Ordas, A.; González, O.; van Wijk, R.C.; Harms, A.C.; Racz, P.I.; van der Graaf, P.H.; Spaink, H.P.; Hankemeier, T. Pharmacokinetic Modeling of Paracetamol Uptake and Clearance in Zebrafish Larvae: Expanding the Allometric Scale in Vertebrates with Five Orders of Magnitude. *Zebrafish* **2016**, *13*, 504–510. https://doi.org/10.1089/zeb.2016.1313.

25. Richter, L.H.J.; Herrmann, J.; Andreas, A.; Park, Y.M.; Wagmann, L.; Flockerzi, V.; Müller, R.; Meyer, M.R. Tools for studying the metabolism of new psychoactive substances for toxicological screening purposes—A comparative study using pooled human liver S9, HepaRG cells, and zebrafish larvae. *Toxicol. Lett.* **2019**, *305*, 73–80. https://doi.org/10.1016/j.toxlet.2019.01.010.
26. Gampfer, T.M.; Wagmann, L.; Park, Y.M.; Cannaert, A.; Herrmann, J.; Fischmann, S.; Westphal, F.; Müller, R.; Stove, C.P.; Meyer, M.R. Toxicokinetics and toxicodynamics of the fentanyl homologs cyclopropanoyl-1-benzyl-4′-fluoro-4-anilinopiperidine and furanoyl-1-benzyl-4-anilinopiperidine. *Arch. Toxicol.* **2020**, *94*, 2009–2025. https://doi.org/10.1007/s00204-020-02726-1.
27. Wagmann, L.; Frankenfeld, F.; Park, Y.M.; Herrmann, J.; Fischmann, S.; Westphal, F.; Müller, R.; Flockerzi, V.; Meyer, M.R. How to Study the Metabolism of New Psychoactive Substances for the Purpose of Toxicological Screenings—A Follow-Up Study Comparing Pooled Human Liver S9, HepaRG Cells, and Zebrafish Larvae. *Front. Chem.* **2020**, *8*, 539. https://doi.org/10.3389/fchem.2020.00539.
28. Park, Y.M.; Meyer, M.R.; Müller, R.; Herrmann, J. Drug Administration Routes Impact the Metabolism of a Synthetic Cannabinoid in the Zebrafish Larvae Model. *Molecules* **2020**, *25*, 4474. https://doi.org/10.3390/molecules25194474.
29. Pertwee, R.G. Cannabinoid pharmacology: The first 66 years. *Br. J. Pharmacol.* **2006**, *147* (Suppl. 1), S163–S171. https://doi.org/10.1038/sj.bjp.0706406.
30. Castaneto, M.S.; Gorelick, D.A.; Desrosiers, N.A.; Hartman, R.L.; Pirard, S.; Huestis, M.A. Synthetic cannabinoids: Epidemiology, pharmacodynamics, and clinical implications. *Drug Alcohol Depend.* **2014**, *144*, 12–41. https://doi.org/10.1016/j.drugalcdep.2014.08.005.
31. European Monitoring Centre for Drugs and Drug Addiction. *New Psychoactive Substances: Global Markets, Glocal Threats and the COVID-19 Pandemic*; European Monitoring Centre for Drugs and Drug Addiction: Lisbon, Portugal, 2020.
32. Krotulski, A.J.; Mohr, A.L.A.; Kacinko, S.L.; Fogarty, M.F.; Shuda, S.A.; Diamond, F.X.; Kinney, W.A.; Menendez, M.J.; Logan, B.K. 4F-MDMB-BINACA: A New Synthetic Cannabinoid Widely Implicated in Forensic Casework. *J. Forensic Sci.* **2019**, *64*, 1451–1461. https://doi.org/10.1111/1556-4029.14101.
33. European Monitoring Centre for Drugs and Drug Addiction. *4F-MDMB-BICA: EMCDDA Initial Report on the New Psychoactive Substance Methyl 2-({[1-(4-Fluorobutyl)-1H-indol-3-yl]carbonyl}amino)-3,3-dimethylbutanoate (4F-MDMB-BICA)*; European Monitoring Centre for Drugs and Drug Addiction: Lisbon, Portugal, 2020. https://doi.org/10.2810/221024.
34. Leong, H.S.; Watanabe, S.; Kuzhiumparambil, U.; Fong, C.Y.; Moy, H.Y.; Yao, Y.J.; Witting, P.K.; Fu, S. Monitoring metabolism of synthetic cannabinoid 4F-MDMB-BINACA via high-resolution mass spectrometry assessed in cultured hepatoma cell line, fungus, liver microsomes and confirmed using urine samples. *Forensic Toxicol* **2021**, *39*, 198–212. https://doi.org/10.1007/s11419-020-00562-7.

35. Haschimi, B.; Mogler, L.; Halter, S.; Giorgetti, A.; Schwarze, B.; Westphal, F.; Fischmann, S.; Auwärter, V. Detection of the recently emerged synthetic cannabinoid 4F-MDMB-BINACA in "legal high" products and human urine specimens. *Drug Test. Anal.* **2019**, *11*, 1377–1386. https://doi.org/10.1002/dta.2666.
36. Shafi, A.; Berry, A.J.; Sumnall, H.; Wood, D.M.; Tracy, D.K. New psychoactive substances: A review and updates. *Ther. Adv. Psychopharmacol.* **2020**, *10*, 1–21.
37. Bazwinsky-Wutschke, I.; Zipprich, A.; Dehghani, F. Endocannabinoid System in Hepatic Glucose Metabolism, Fatty Liver Disease, and Cirrhosis. *Int. J. Mol. Sci.* **2019**, *20*, 2516. https://doi.org/10.3390/ijms20102516.
38. Liu, L.Y.; Alexa, K.; Cortes, M.; Schatzman-Bone, S.; Kim, A.J.; Mukhopadhyay, B.; Cinar, R.; Kunos, G.; North, T.E.; Goessling, W. Cannabinoid receptor signaling regulates liver development and metabolism. *Development* **2016**, *143*, 609–622. https://doi.org/10.1242/dev.121731.
39. An, D.; Peigneur, S.; Hendrickx, L.A.; Tytgat, J. Targeting Cannabinoid Receptors: Current Status and Prospects of Natural Products. *Int. J. Mol. Sci.* **2020**, *21*, 5064. https://doi.org/10.3390/ijms21145064.
40. Stainier, D.Y.R.; Raz, E.; Lawson, N.D.; Ekker, S.C.; Burdine, R.D.; Eisen, J.S.; Ingham, P.W.; Schulte-Merker, S.; Yelon, D.; Weinstein, B.M.; et al. Guidelines for morpholino use in zebrafish. *PLoS Genet.* **2017**, *13*, e1007000. https://doi.org/10.1371/journal.pgen.1007000.
41. Phillips, J.B.; Westerfield, M. Zebrafish as a Model to Understand Human Genetic Diseases. In *The Zebrafish in Biomedical Research*; Elsevier: Amsterdam, The Netherlands, 2020; pp. 619–626, ISBN 9780128124314.
42. Renninger, S.L.; Schonthaler, H.B.; Neuhauss, S.C.F.; Dahm, R. Investigating the genetics of visual processing, function and behaviour in zebrafish. *Neurogenetics* **2011**, *12*, 97–116. https://doi.org/10.1007/s10048-011-0273-x.
43. Johnson, J.; Sharick, J.T.; Skala, M.C.; Li, L. Sample preparation strategies for high-throughput mass spectrometry imaging of primary tumor organoids. *J. Mass Spectrom.* **2020**, *55*, e4452. https://doi.org/10.1002/jms.4452.
44. Jeckel, A.M.; Matsumura, K.; Nishikawa, K.; Morimoto, Y.; Saporito, R.A.; Grant, T.; Ifa, D.R. Use of whole-body cryosectioning and desorption electrospray ionization mass spectrometry imaging to visualize alkaloid distribution in poison frogs. *J. Mass Spectrom.* **2020**, *55*, e4520. https://doi.org/10.1002/jms.4520.
45. Buchberger, A.R.; DeLaney, K.; Johnson, J.; Li, L. Mass Spectrometry Imaging: A Review of Emerging Advancements and Future Insights. *Anal. Chem.* **2018**, *90*, 240–265. https://doi.org/10.1021/acs.analchem.7b04733.
46. Addie, R.D.; Balluff, B.; Bovée, J.V.M.G.; Morreau, H.; McDonnell, L.A. Current State and Future Challenges of Mass Spectrometry Imaging for Clinical Research. *Anal. Chem.* **2015**, *87*, 6426–6433. https://doi.org/10.1021/acs.analchem.5b00416.

47. Asslan, M.; Lauzon, N.; Beus, M.; Maysinger, D.; Rousseau, S. Mass spectrometry imaging in zebrafish larvae for assessing drug safety and metabolism. *Anal. Bioanal. Chem.* **2021**, *413*, 5135–5146. https://doi.org/10.1007/s00216-021-03476-4.
48. Janda, M.; Seah, B.K.B.; Jakob, D.; Beckmann, J.; Geier, B.; Liebeke, M. Determination of Abundant Metabolite Matrix Adducts Illuminates the Dark Metabolome of MALDI-Mass Spectrometry Imaging Datasets. *Anal. Chem.* **2021**, *93*, 8399–8407. https://doi.org/10.1021/acs.analchem.0c04720.
49. Hansen, H.T.; Janfelt, C. Aspects of Quantitation in Mass Spectrometry Imaging Investigated on Cryo-Sections of Spiked Tissue Homogenates. *Anal. Chem.* **2016**, *88*, 11513–11520. https://doi.org/10.1021/acs.analchem.6b02711.
50. Hulme, H.; Fridjonsdottir, E.; Gunnarsdottir, H.; Vallianatou, T.; Zhang, X.; Wadensten, H.; Shariatgorji, R.; Nilsson, A.; Bezard, E.; Svenningsson, P.; et al. Simultaneous mass spectrometry imaging of multiple neuropeptides in the brain and alterations induced by experimental parkinsonism and L-DOPA therapy. *Neurobiol. Dis.* **2020**, *137*, 104738. https://doi.org/10.1016/j.nbd.2020.104738.
51. Zecchi, R.; Franceschi, P.; Tigli, L.; Amidani, D.; Catozzi, C.; Ricci, F.; Salomone, F.; Pieraccini, G.; Pioselli, B.; Mileo, V. Sample preparation strategy for the detection of steroid-like compounds using MALDI mass spectrometry imaging: Pulmonary distribution of budesonide as a case study. *Anal. Bioanal. Chem.* **2021**, *413*, 4363–4371. https://doi.org/10.1007/s00216-021-03393-6.
52. Goessling, W.; North, T.E.; Lord, A.M.; Ceol, C.; Lee, S.; Weidinger, G.; Bourque, C.; Strijbosch, R.; Haramis, A.-P.; Puder, M.; et al. APC mutant zebrafish uncover a changing temporal requirement for wnt signaling in liver development. *Dev. Biol.* **2008**, *320*, 161–174. https://doi.org/10.1016/j.ydbio.2008.05.526.
53. Zhang, X.; Li, C.; Gong, Z. Development of a convenient in vivo hepatotoxin assay using a transgenic zebrafish line with liver-specific DsRed expression. *PLoS ONE* **2014**, *9*, e91874. https://doi.org/10.1371/journal.pone.0091874.
54. Korzh, S.; Pan, X.; Garcia-Lecea, M.; Winata, C.L.; Pan, X.; Wohland, T.; Korzh, V.; Gong, Z. Requirement of vasculogenesis and blood circulation in late stages of liver growth in zebrafish. *BMC Dev. Biol.* **2008**, *8*, 84. https://doi.org/10.1186/1471-213X-8-84.
55. Cannaert, A.; Sparkes, E.; Pike, E.; Luo, J.L.; Fang, A.; Kevin, R.C.; Ellison, R.; Gerona, R.; Banister, S.D.; Stove, C.P. Synthesis and in Vitro Cannabinoid Receptor 1 Activity of Recently Detected Synthetic Cannabinoids 4F-MDMB-BICA, 5F-MPP-PICA, MMB-4en-PICA, CUMYL-CBMICA, ADB-BINACA, APP-BINACA, 4F-MDMB-BINACA, MDMB-4en-PINACA, A-CHMINACA, 5F-AB-P7AICA, 5F-MDMB-P7AICA, and 5F-AP7AICA. *ACS Chem. Neurosci.* **2020**, *11*, 4434–4446. https://doi.org/10.1021/acschemneuro.0c00644.
56. World Health Organization. Critical Review Report: 4F-MDMB-BINACA: Expert Committee on Drug Dependence, Forty-second Meeting Geneva. In Proceedings of the 42nd ECDD (2019): 4F-MDMB-BINACA, Geneva, Switzerland, 21–25 October 2019.

57. Westerfield, M. *The Zebrafish Book*: *A Guide for the Laboratory Use of Zebrafish (Danio rerio)*, 4th ed.; M. Westerfield: Eugene, OR, USA, 2000.
58. Esain, V.; Kwan, W.; Carroll, K.J.; Cortes, M.; Liu, S.Y.; Frechette, G.M.; Sheward, L.M.V.; Nissim, S.; Goessling, W.; North, T.E. Cannabinoid Receptor-2 Regulates Embryonic Hematopoietic Stem Cell Development via Prostaglandin E2 and P-Selectin Activity. *Stem Cells* **2015**, *33*, 2596–2612. https://doi.org/10.1002/stem.2044.
59. Hoppstädter, J.; Valbuena Perez, J.V.; Linnenberger, R.; Dahlem, C.; Legroux, T.M.; Hecksteden, A.; Tse, W.K.F.; Flamini, S.; Andreas, A.; Herrmann, J.; et al. The glucocorticoid-induced leucine zipper mediates statin-induced muscle damage. *FASEB J.* **2020**, *34*, 4684–4701. https://doi.org/10.1096/fj.201902557RRR.
60. Schneider, C.A.; Rasband, W.S.; Eliceiri, K.W. NIH Image to ImageJ: 25 years of image analysis. *Nat. Methods* **2012**, *9*, 671–675. https://doi.org/10.1038/nmeth.2089.
61. Richter, L.H.J.; Maurer, H.H.; Meyer, M.R. Metabolic fate of the new synthetic cannabinoid 7'N-5F-ADB in rat, human, and pooled human S9 studied by means of hyphenated high-resolution mass spectrometry. *Drug Test. Anal.* **2019**, *11*, 305–317. https://doi.org/10.1002/dta.2493.

3.8 Supporting Information

Induction of Liver Size Reduction in Zebrafish Larvae by the Emerging Synthetic Cannabinoid 4F-MDMB-BINACA and its Impact on Drug Metabolism

Previously published in:

Molecules, 2022 Feb 15; 27(4):1290. doi: 10.3390/molecules27041290.

Yu Mi Park [1,2,3], Charlotte Dahlem [4], Markus R. Meyer [5], Alexandra K. Kiemer [4], Rolf Müller [1,3,6,*] and Jennifer Herrmann [1,6,*]

[1]Helmholtz Institute for Pharmaceutical Research Saarland (HIPS), Helmholtz Centre for Infection Research, Campus E8 1, Saarland University, 66123 Saarbrücken, Germany; Yu-Mi.Park@helmholtz-hips.de
[2]Environmental Safety Group, Korea Institute of Science and Technology (KIST) Europe, 66123 Saarbrücken, Germany
[3]Department of Pharmacy, Saarland University, 66123 Saarbrücken, Germany
[4]Department of Pharmacy, Pharmaceutical Biology, Campus C2 3, Saarland University, 66123 Saarbrücken, Germany; charlotte.dahlem@uni-saarland.de (C.D.); pharm.bio.kiemer@mx.uni-saarland.de (A.K.K.)
[5]Center for Molecular Signaling (PZMS), Institute of Experimental and Clinical Pharmacology and Toxicology, Department of Experimental and Clinical Toxicology, Saarland University, 66421 Homburg, Germany; m.r.meyer@mx.uni-saarland.de
[6]German Center for Infection Research (DZIF), 38124 Braunschweig, Germany
*Correspondence: Rolf.Mueller@helmholtz-hips.de (R.M.); Jennifer.Herrmann@helmholtz-hips.de (J.H.)

3.8 Supporting Information

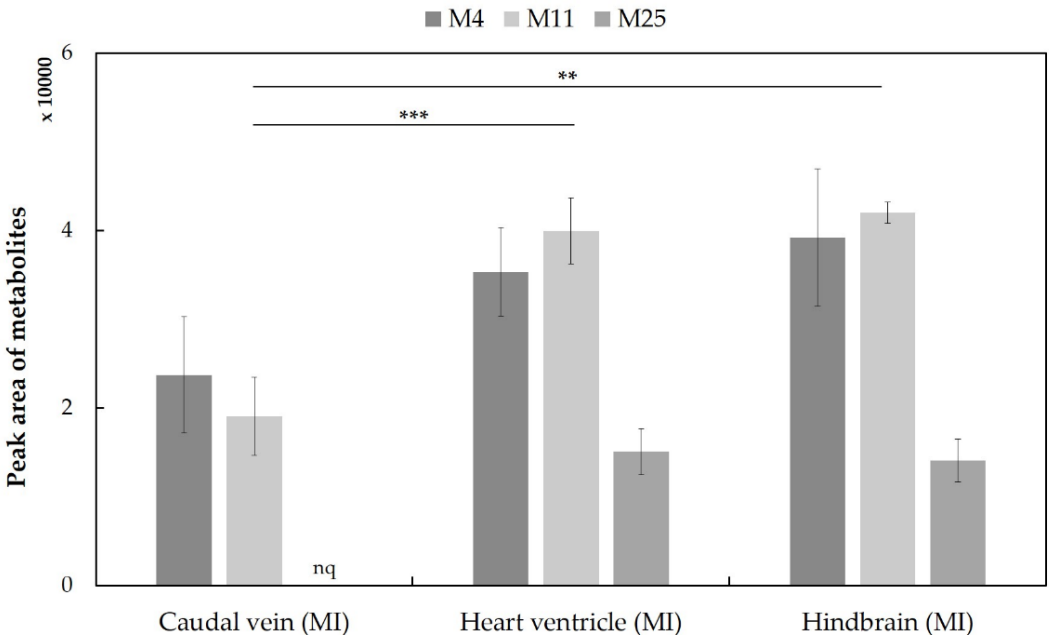

Figure S1. Detection profiles of the three minor abundant metabolites of 4F-MDMB-BINACA in microinjected zebrafish larvae (caudal vein, heart ventricle, and hindbrain). These three minor metabolites, M4, M11, and M25, were formed by *N*-dealkylation, oxidative defluorination, hydroxylation of the tertiary butyl part in combination with glucuronidation isomer 1, respectively. The clustered columns are displayed as mean ± SD using the peak areas detected from 30 pooled larvae (n=3). The p-values for M11 in the different groups were calculated by one-way ANOVA (**$p < 0.01$, ***$p < 0.001$). nq: Confirmed mass, but not quantified due to peak detection below signal-to-noise ratio of 3.

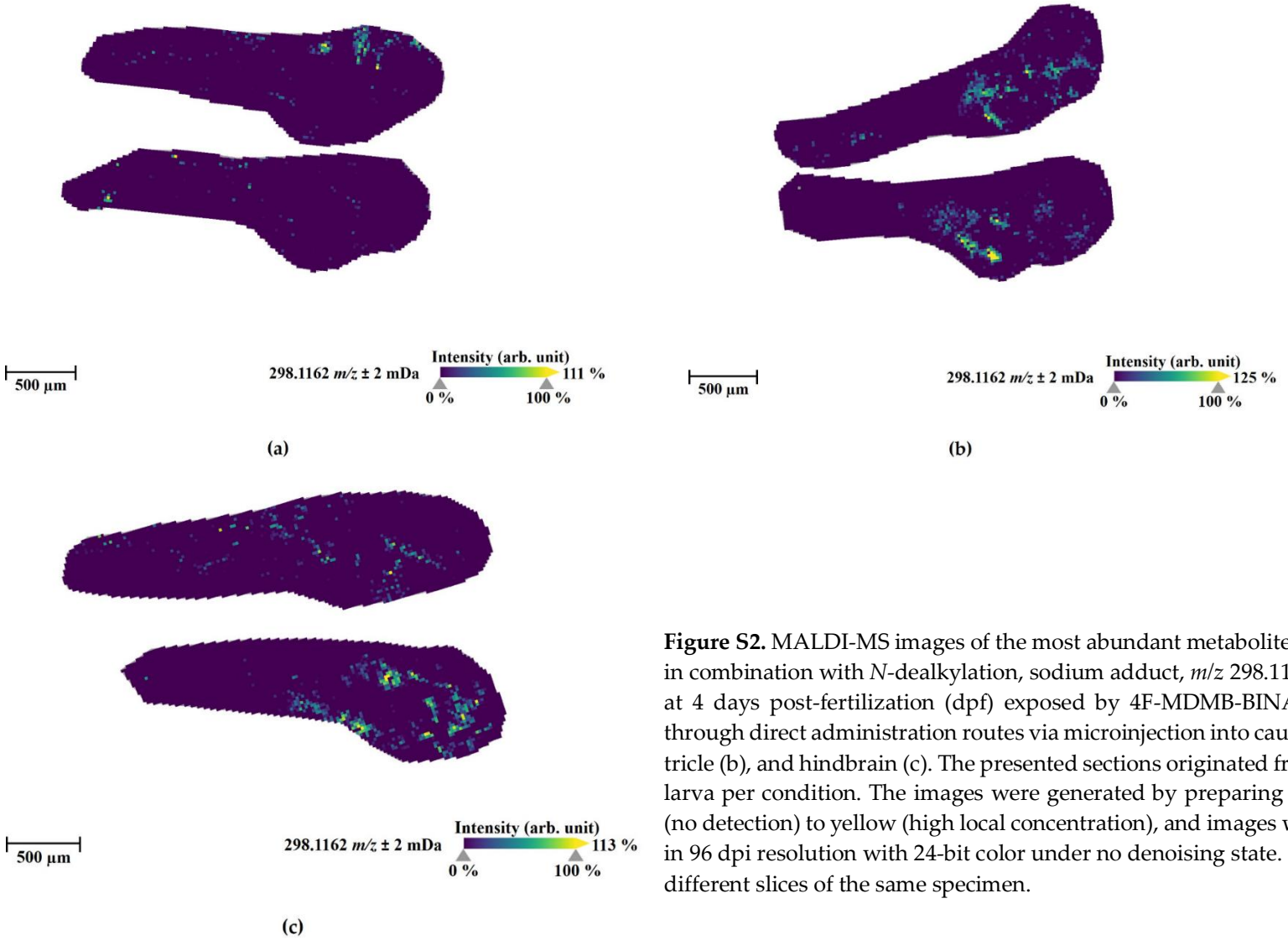

Figure S2. MALDI-MS images of the most abundant metabolites M3 (ester hydrolysis in combination with *N*-dealkylation, sodium adduct, *m/z* 298.1162) in zebrafish larvae at 4 days post-fertilization (dpf) exposed by 4F-MDMB-BINACA for 1 h at 28 °C through direct administration routes via microinjection into caudal vein (a), heart ventricle (b), and hindbrain (c). The presented sections originated from one representative larva per condition. The images were generated by preparing a colormap from blue (no detection) to yellow (high local concentration), and images were further processed in 96 dpi resolution with 24-bit color under no denoising state. Each panel shows two different slices of the same specimen.

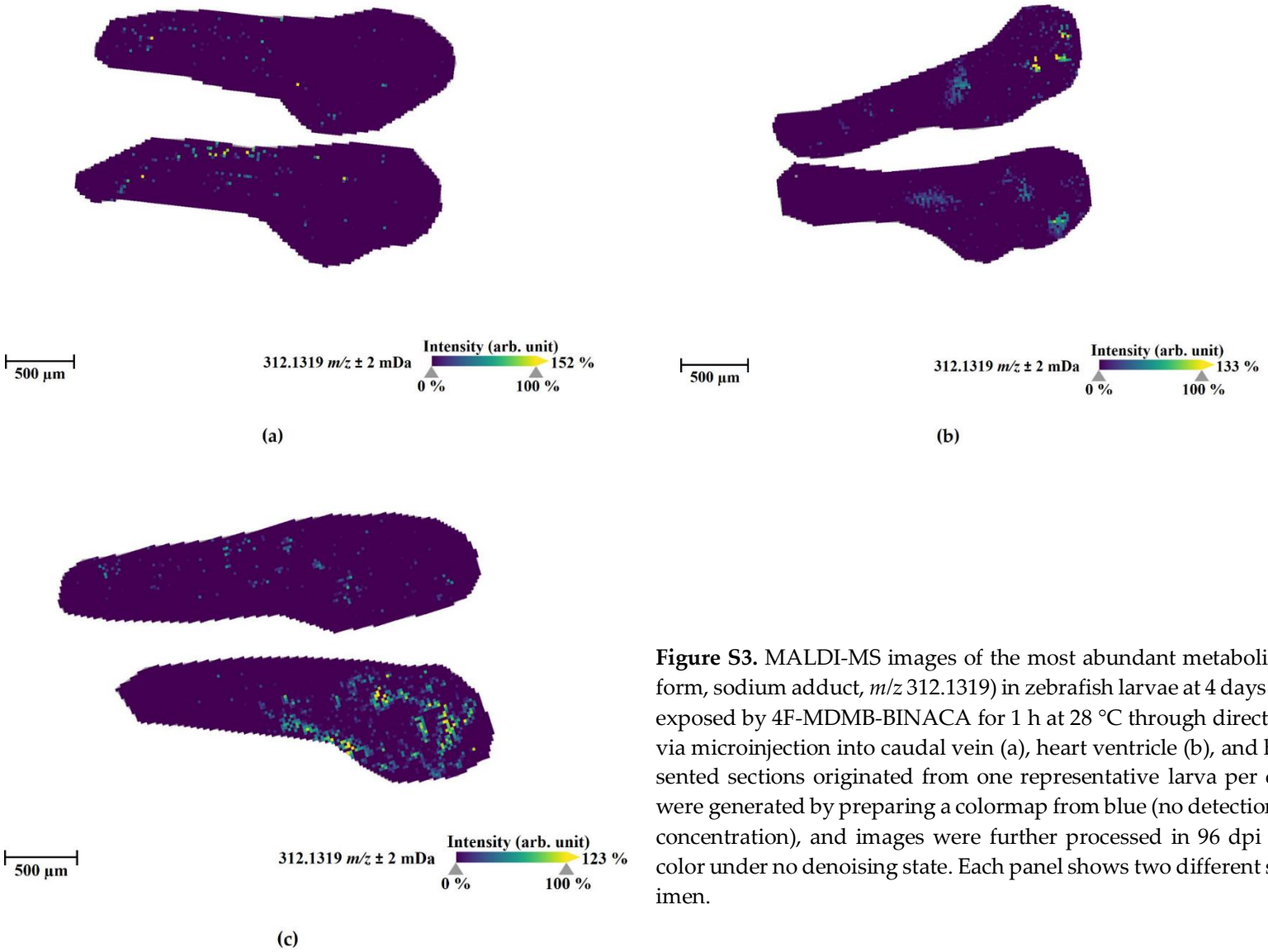

Figure S3. MALDI-MS images of the most abundant metabolite M4 (*N*-dealkylation form, sodium adduct, *m/z* 312.1319) in zebrafish larvae at 4 days post-fertilization (dpf) exposed by 4F-MDMB-BINACA for 1 h at 28 °C through direct administration routes via microinjection into caudal vein (a), heart ventricle (b), and hindbrain (c). The presented sections originated from one representative larva per condition. The images were generated by preparing a colormap from blue (no detection) to yellow (high local concentration), and images were further processed in 96 dpi resolution with 24-bit color under no denoising state. Each panel shows two different slices of the same specimen.

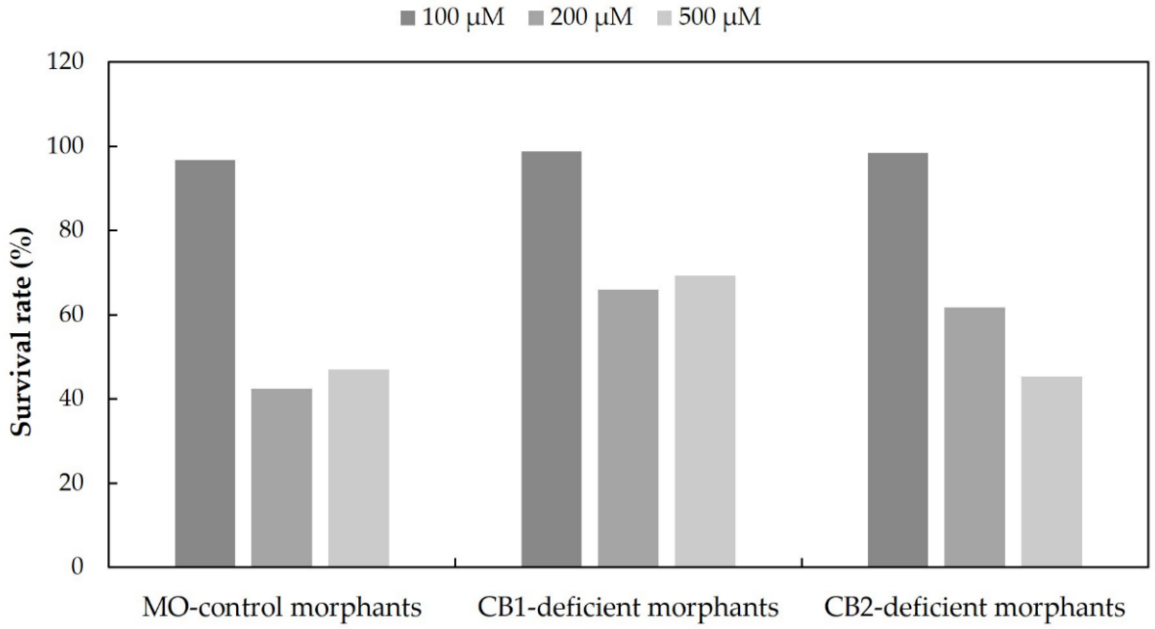

Figure S4. The survival rates of zebrafish mutant larvae at 4 days post-fertilization (dpf) according to the different concentrations of each morpholino oligonucleotide (MO) at 100 μM, 200 μM, and 500 μM with the fixed injection volume of 4.19 nL. All mutant larvae were prepared by 4.19 nL injections of MOs at a one-cell stage. Survival rates (%) were calculated based on the total numbers of ZF mutant larvae measured per condition due to the variance of offspring quality and quantity in parent fish. [n = 126-205 (at 100 μM), 80-136 (at 200 μM), 83-101 (at 500 μM)]. The p-values between the 100 μM group showing 100 % survival and the two other groups (200 μM, 500 μM) were computed by one-way ANOVA, and all p-values showed significance (*$p < 0.05$).

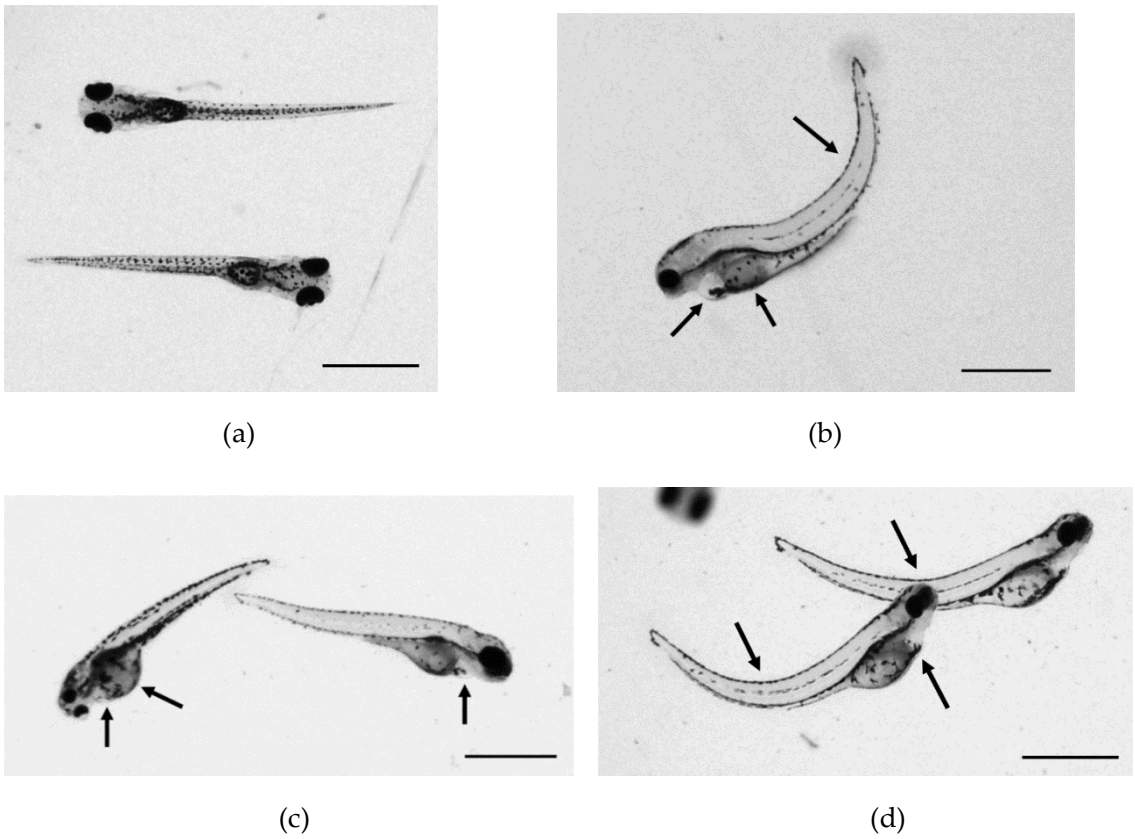

Figure S5. Representative images of morphological malformations and signs of toxicity (depicted by black arrows) in zebrafish larvae at 5 days post-fertilization (dpf) as observed in CB knockdown experiments (MO). The control group, which was left untreated (a), did not show any malformation, whereas some ZF larvae injected with the random MO control 25-*N* (b) displayed edema in the heart ventricle, an up-curved spine, and non-spherical yolk sac. Several CB1 knockdown ZF larvae (c) showed edemas in the heart ventricle and an abnormally large size of the yolk sac. Similarly, several CB2 knockdown ZF larvae (d) showed up-curved spines and heart ventricle edema. The displayed larvae in panel (b)-(d) were created by 4.19 nL injection of each MO (100 μM) at a one-cell stage. To study the impact of MO injection on larval development, all ZF larvae were checked daily under a microscope, and deformed morphants were excluded from the experiments for drug metabolisms studies. Scale bars: 1 mm.

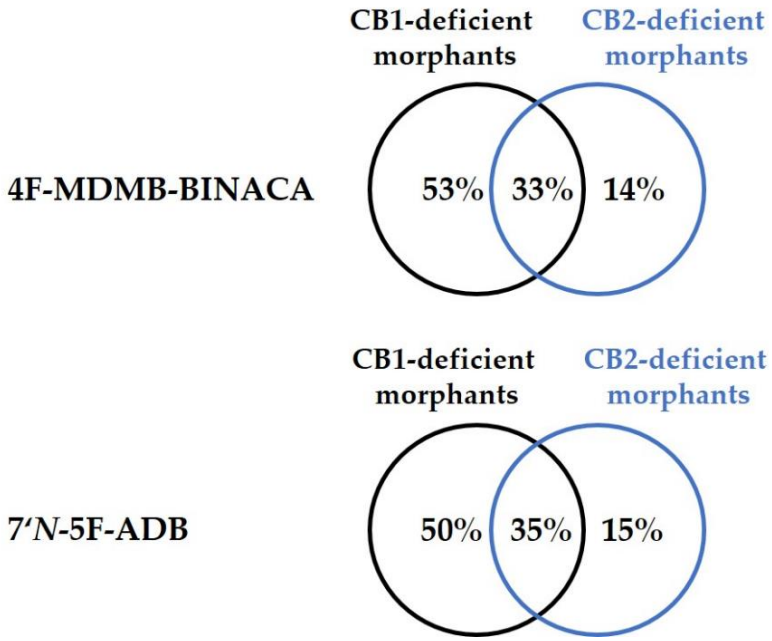

Figure S6. Mutual comparability of the overall metabolites detected in CB1-deficient and CB2-deficient ZF larvae after waterborne exposure of 4F-MDMB-BINACA (at 25 μM) and 7′*N*-5F-ADB (at 50 μM) using Venn diagrams (*n*=3).

3.8 Supporting Information

Table S1. Detailed information of 4F-MDMB-BINACA and its phase I and phase II metabolites and their detection in human biosamples from published literature and microinjected zebrafish larvae. All metabolites were identified from three different models in our previous study [27].

Compound	Metabolite ID	Calculated exact masses, *m/z*	Metabolic reaction	Integrated Human Screening Data* [27,32,34,35]								Data from Zebrafish Larvae			
												Aquatic Exposure, Published Data [27]	Microinjection		
				Plasma [27] (*n*=1)	Blood [32] (*n*=4)	Integrated Blood [27,32]	Urine [27] (*n*=1)	Urine [35] (*n*=17)	Urine [32] (*n*=4)	Urine [34] (*n*=20)	Integrated Urine [27,32,34,35]		Caudal Vein	Heart Ventricle	Hindbrain
Parent compound	4F-MDMB-BINACA	364.2031	Parent Compound	+++			+					+++	+++	+++	+++
Phase I	M1	237.1034	Amide Hydrolysis												
	M2	274.1186	Lactone formation + *N*-dealkylation									+	+nq		+nq
	M3	276.1343	Ester hydrolysis + *N*-dealkylation						+	++	√√		+nq	+nq	+nq
	M4	290.1499	*N*-Dealkylation	+	+	√√						+	+	+	+
	M5	346.1761	Lactone formation + oxidative defluorination									+			
	M6	348.1718	Lactone formation	+	+	√	+	++	+	+	√√	++	+	+	+
	M7	348.1918	Ester hydrolysis + oxidative defluorination					+	+	+	√	+			
	M8	350.1874	Ester hydrolysis	++	++	√	+	+++	+++	+++	√	+			
	M9	360.1554	Lactone formation + oxidative defluorination + oxidation to carboxylic acid									+			
	M10	362.1710	Ester hydrolysis + oxidative defluorination + oxidation to carboxylic acid					+	+	+	√√	+	+nq	+nq	+nq
	M11	362.2074	Oxidative defluorination		+++			+		+	√√	+	+	+	+
	M12	364.1667	Lactone formation + hydroxylation of the tertiary butyl part									+	+	+	++
	M13	366.1824	Ester hydrolysis + hydroxylation of the tertiary butyl part isomer 1				++	+	+		√	+			
	M14	366.1824	Ester hydrolysis + hydroxylation of the indazole part isomer 2					+		+	√				
	M15	376.1867	Oxidative defluorination + oxidation to carboxylic acid					+	++	+	√√	+	+	++	+
	M16	380.1980	Hydroxylation of the tertiary butyl part isomer 1	+				+				+			

	M17	380.1980	Hydroxylation of the butyl chain isomer 2					+							
	M18	380.1980	Hydroxylation of the indazole part isomer 3					+				+			
	M19	380.1980	Hydroxylation of the indazole part isomer 4					+							
Total number of Phase I metabolites				4	4	3	3	12	7	8	9	14	8	7	8
Phase II	M20	460.1548	Hydroxylation of the indazole part + sulfation									+	++	+	+
	M21	524.2239	Ester hydrolysis + oxidative defluorination + glucuronidation												
	M22	526.2196	Ester hydrolysis + glucuronidation				+++								
	M23	542.2144	Ester hydrolysis + hydroxylation of the indazole part + glucuronidation												
	M24	552.2188	Oxidative defluorination + oxidation to carboxylic acid+ glucuronidation									+			
	M25	556.2301	Hydroxylation of the tertiary butyl part + glucuronidation isomer 1									+	+nq	+	+
	M26	556.2301	Hydroxylation of the indazole part + glucuronidation isomer 2									+			
Total number of Phase II metabolites							1					4	2	2	2
Total number of detected Phase I/II metabolites				4	4	3	4	12	7	8	9	18	10	9	10

[1]All human data were integrated with the recently published studies; √: Detection at least twice among the samples in each respective human matrix; √√: detection in both the microinjected ZF larvae and each human biosample; [nq] confirmed mass, but not quantified due to peak detection below signal-to-noise ratio of 3. +: Peak detected, ++: second most abundant peak among metabolites, +++: most abundant peak among metabolites.

Table S2. Mass list of 4F-MDMB-BINACA and its phase I and phase II metabolites used for LC-HRMS/MS and MALDI-FT-ICR measurements.

Compounds	Metabolite ID	$[M+H]^+$ ion for LC-HRMS/MS [27]	$[M+Na]^+$ ion for MALDI-FT-ICR
Parent compound	4F-MDMB-BINACA	364.2031	386.1850
Phase I metabolites	M1	237.1034	259.0853
	M2	274.1186	296.1006
	M3	276.1343	298.1162
	M4	290.1499	312.1319
	M5	346.1761	368.1581
	M6	348.1718	370.1537
	M7	348.1918	370.1737
	M8	350.1874	372.1694
	M9	360.1554	383.1452
	M10	362.1710	384.1530
	M11	362.2074	384.1894
	M12	364.1667	386.1487
	M13	366.1824	388.1643
	M14	366.1824	388.1643
	M15	376.1867	398.1686
	M16	380.1980	402.1800
	M17	380.1980	402.1800
	M18	380.1980	402.1800
	M19	380.1980	402.1800
Phase II metabolites	M20	460.1548	482.1368
	M21	524.2239	546.2058
	M22	526.2196	548.2015
	M23	542.2144	564.1964
	M24	552.2188	574.2007
	M25	556.2301	578.2120
	M26	556.2301	578.2120

Table S3. Comparison of the total number of metabolites detected in zebrafish larvae and human urine samples for 7′*N*-5F-ADB and 4F-MDMB-BINACA.

Compound	Total number of metabolites	Human urine samples		Microinjected zebrafish larvae[1]	
		Phase I metabolites	Phase II metabolites	Phase I metabolites	Phase II metabolites
7′*N*-5F-ADB [28]	36	17	10	17 (12)[2]	7 (7)[2]
4F-MDMB-BINACA	26	9[3]	0[3]	8+1[4] (5)[2]	2 (0)[2]

[1] Zebrafish larvae were exposed to the parent compound via microinjection at a final concentration of 5 mM. [2] The values in parentheses stand for the number of overlapping metabolites to human urine samples per compound. [3] The human urine data for 4F-MDMB-BINACA was generated based on literature [27,32,34,35]. [4] The 4F-MDMB-BINACA metabolite M1 detected by MALDI-FT-ICR analysis was included in the ZF larvae data.

3.8 Supporting Information

Table S4. Number of morphological malformation cases (given in % of total population obeserved) in the zebrafish mutant larvae from 3 days post-fertilization (dpf) to 4 dpf after MOs injection at a one-cell stage with three different concentrations.

	at 3 dpf			at 4 dpf		
	100 μM	**200 μM**	**500 μM**	**100 μM**	**200 μM**	**500 μM**
MO-control morphants	11	10	7	11 (11+0)	10 (10+0)	7 (7+0)
CB1-deficient morphants	10	6	14	12 (10+2)	9 (6+3)	17 (14+3)
CB2-deficient morphants	12	15	17	16 (12+4)	15 (15+0)	20 (17+3)

All MOs were injected with a 4.19 nL volume into one-cell stage zebrafish embryos. The defect rates (%) were calculated based on the total sample number due to the difference in offspring quality and quantity used in the experiments. All values in parentheses are % of malformed larvae at 3 dpf + % of malformed larvae at 4 dpf. [*n* = 126-205 (at 100 μM), *n* = 80-136 (at 200 μM), *n* = 83-101 (at 500 μM)].

Table S5. Sequences of morpholino oligonucleotides (MOs) for the gene knockdown of CB1 and CB2 by binding its splicing site.

Gene	Morpholino sequence
cnr1	GTGCTATCAACAACATACCTTTGTG[a]
cnr2	GCCATGAAACAAACAGTACCTGTGG[a]
n.a. (random control 25-*N*)	NNNNNNNNNNNNNNNNNNNNNNNNN

[a] The sequences of MOs for CB1 and CB2 were validated in earlier studies [38,58].

Chapter 4.

Optimization of Mass Spectrometry Imaging for Drug Metabolism and Distribution Studies in the Zebrafish Larvae Model: A Case Study with the Opioid Antagonist Naloxone

Manuscript ready for Submission:

Yu Mi Park [1,2,3], Markus R. Meyer [4], Rolf Müller [1,3,5,*] and Jennifer Herrmann [1,5,*]

[1]Helmholtz Centre for Infection Research, Helmholtz Institute for Pharmaceutical Research Saarland (HIPS), Campus E8 1, Saarland University, 66123 Saarbrücken, Germany; yu-mi.park@helmholtz-hips.de
[2]Environmental Safety Group, Korea Institute of Science and Technology (KIST) Europe, 66123 Saarbrücken, Germany
[3]Department of Pharmacy, Saarland University, 66123 Saarbrücken, Germany
[4]Center for Molecular Signaling (PZMS), Institute of Experimental and Clinical Pharmacology and Toxicology, Department of Experimental and Clinical Toxicology, Saarland University, 66421 Homburg, Germany; m.r.meyer@mx.uni-saarland.de
[5]German Center for Infection Research (DZIF), 38124 Braunschweig, Germany
[*]Correspondence: Rolf.Mueller@helmholtz-hips.de (R.M.); Jennifer.Herrmann@helmholtz-hips.de (J.H.); Tel.: +49-681-98806-3000 (R.M.), +49-681-98806-3101 (J.H.)

Contributions

Author's effort

The author significantly contributed to the concept of the study, designed and performed experiments, and evaluated and interpreted the resulting data. The author performed mating zebrafish, exposure experiment, sample preparations for LC-HRMS/MS and MALDI-FT-ICR, all data analysis of LC-HRMS/MS, and data processing and analysis of MALDI-FT-ICR, as well as HepaRG cell *in vitro* experiment. Furthermore, the author contributed significantly to the conceiving and writing of the manuscript.

Contributions by others

Markus R. Meyer contributed to the conception, resource of the substrate, reviewing, and editing of the manuscript. Rolf Müller contributed by conceiving, reviewing, and editing this study. Jennifer Herrmann contributed to the concept, writing, editing, and reviewing of this study. Rolf Müller and Jennifer Herrmann supervised this project, and all authors also contributed by proofreading the manuscript.

4.1 Abstract

Zebrafish (ZF; *Danio rerio*) larvae have emerged as a promising *in vivo* model in drug metabolism studies. Here, we set out to ready this model for integrated mass spectrometry imaging (MSI) to comprehensively study the spatial distribution of drugs and their metabolites inside ZF larvae. In our pilot study with the overall goal to improve MSI protocols for ZF larvae, we investigated the metabolism of the opioid antagonist naloxone. We confirmed that the metabolic modification of naloxone are in high accordance to metabolites detected in HepaRG cells, human biosamples, rats, and some other *in vivo* models. In particular, all three major human metabolites were detected at high abundance in the ZF larvae model. Next, the *in vivo* distribution of naloxone was investigated in three body sections of ZF larvae using LC-HRMS/MS showing that the opioid antagonist is mainly present in the head and body section as suspected from published human pharmacological data. Having optimized sample preparation procedures for MSI, i.e. embedding layer composition, cryosectioning, and matrix composition and spraying, we were able to record MS images of naloxone and its metabolites in ZF larvae giving highly informative distributional images. In conclusion, and in conjunction with results from other studies, we could demonstrate that all major ADMET (absorption, distribution, metabolism, excretion, toxicity) parameters as part of *in vivo* pharmacokinetic studies can be assessed in the simple and cost-effective ZF larvae model. Our established protocols for ZF larvae using naloxone as a tool compound are broadly applicable, particularly for MSI sample preparation, to various types of compounds and will help to understand human metabolism and pharmacokinetics.

4.2 Graphical Abstract

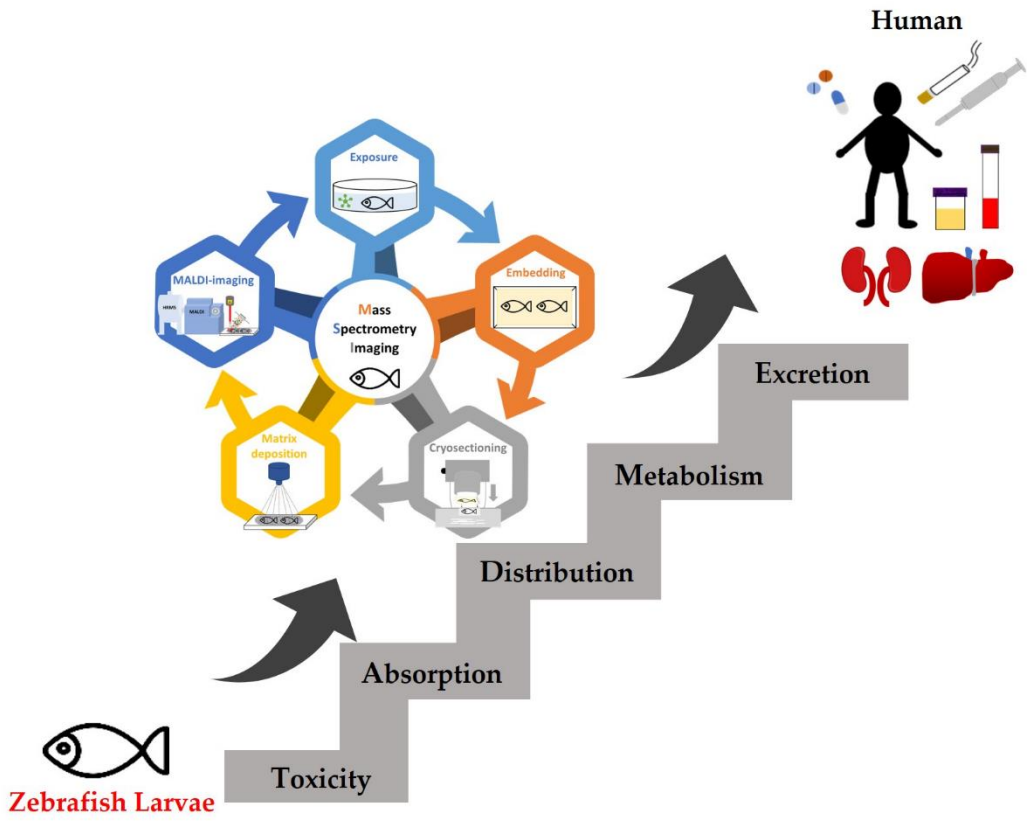

4.3 Introduction

Mass spectrometry imaging (MSI) is a state-of-the-art and label-free technology that allows investigating the localization and spatial distribution of diverse molecular species in one analysis in various biological specimens [1,2]. In general, MSI is an integrated approach offering the possibility to combine mass spectrometry (MS) [e.g., Time-of-flight (TOF), Fourier-transform ion cyclotron resonance (FT-ICR), Orbitrap] to spatial images generated from different ionization equipment [e.g., matrix-assisted laser desorption ionization (MALDI), desorption electrospray ionization (DESI), secondary ion mass spectrometry (SIMS)] to match specific needs for analyzing various types of samples [2–4]. In particular, visualizing the tissue distribution of a parent molecule and its metabolites has opened a new era to characterize physiological and pathological properties of drugs. Thus, MSI has been increasingly used in preclinical studies [1,5–7] and illicit drug testing [8–10].

Zebrafish (*Danio rerio*; ZF) models are gaining popularity as an *in vivo* model organism in many research studies of developmental biology [11–13], toxicology [14,15], pharmacological properties of drugs such as absorption, distribution, metabolism, and excretion (ADME) [16–20], human diseases [21,22], and neurobiology [23–25].

In our earlier studies [26,27], we demonstrated that MALDI-MS images were crucial for investigating the distribution of two new synthetic cannabinoids (SCs; 7'*N*-5F-ADB and 4F-MDMB-BINACA) inside the ZF larval body. Notably, ZF larvae metabolism of the two studied SCs was found to be very similar to reported human and rodent metabolism, and using various administration routes further helped to increase the number of detected metabolites. Combining routine metabolite identification studies with MSI analyses for deciphering the spatial *in vivo* distribution of investigated drugs in the ZF model is a promising tool with the potential to cover large parts of preclinical DMPK (drug metabolism and pharmacokinetics) typically done in rodent models [26–30]. However, preparation of ZF larval sections for MSI analysis is technically challenging, and the discrepancy in terms of metabolite detection between two representative analytical platforms that we used, LC-HRMS/MS and MALDI-MSI, still requires further investigation. Furthermore, there are so far only few reports on MSI studies with ZF larvae, in particular in the context of drug distribution and metabolism [31,32], since MSI is so far more commonly used for tissues [1,33] and tumors [34,35], rodent organs [3,36], and adult ZF [37,38].

In this study, we aimed to investigate the metabolism of the opioid antagonist naloxone (Figure 1) in ZF larvae and the common *in vitro* HepaRG model, and to compare our findings to already published data from humans [39–48] and other animal models [39,43,49–52]. Naloxone is widely used as emergency therapy upon risk of opioid overdose, and it is distributed through a global take-home program [39–42]. We have chosen naloxone as a model drug as it is known to cross the blood-brain barrier, and we were expecting to observe a distinct distribution pattern in the ZF larvae with a significant portion of the drug being accumulated in the brain region as suggested by other studies [39,41,43,44]. Studying a drug

with a distinct biodistribution pattern was considered as a prerequisite to further optimize the MSI workflow in ZF larvae.

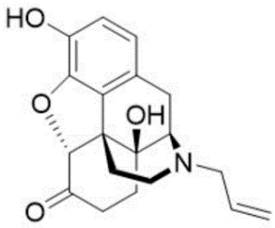

Figure 1. Chemical structure of naloxone.

4.4 Results and Discussion

4.4.1. In vivo Absorption, Metabolism and Excretion Properties of Naloxone in the Zebrafish Larvae Model

In previous studies, we demonstrated that the administration routes into ZF larvae for two rather lipophilic synthetic cannabinoids, 7'*N*-5F-ADB [26,30] and 4F-MDMB-BINACA [27,29], have a significant impact on observed metabolite patterns. For these substrates, direct administration via microinjection into different vital organs (i.e., heart ventricle, caudal vein, hindbrain, and yolk sac) was beneficial compared to conventional waterborne exposure. However, in this study, we mainly considered adding the water-soluble reference drug naloxone [39,42] to the embryo/larvae medium to treat ZF larvae in the course of *in vivo* ADME studies. Using this route for drug administration also significantly facilitates the MSI optimization procedures as proposed here since it allows for higher throughput (in terms of overall sample numbers) compared to setups where microinjection into ZF larvae is required.

Following previously established workflows [26–30], survival rates of ZF embryos and larvae after 5 d and 1 d treatment, respectively, were evaluated to determine a non-toxic concentration of naloxone that can be applied in subsequent *in vivo* ADME experiments. In parallel, the heartbeat of the exposed ZF larvae was measured at 5 days post-fertilization (dpf) as naloxone is described to induce cardiovascular events in humans (e.g., systolic blood pressure, respiratory stimulation, cardiovascular instability, and pulmonary edema) [39,43]. As a result, survival rates of naloxone-treated ZF larvae were 100% at maximum concentrations of 100 µM for 5 d exposure and 500 µM (highest assay concentration) for 1 d exposure. Also, we did not detect significant effects on the heartbeat rates of ZF larvae treated with non-lethal concentrations, and we only found a slightly reduced heartbeat rate for ZF larvae treated for 1 d with 500 µM naloxone (Table 1). Thus, a concentration of 300 µM naloxone (1 d treatment of 4 dpf ZF larvae) was chosen for the subsequent metabolism studies.

Table 1. Effects on heartbeat rates in ZF larvae at 5 days post-fertilization (dpf) following 1 d and 5 d waterborne exposure, respectively, to varying concentrations of naloxone.

Concentration of naloxone (µM)	Relative heartbeat rates (%) of 5 dpf ZF larvae after 1 d waterborne exposure	Relative heartbeat rates (%) of 5 dpf ZF larvae after 5 d waterborne exposure
0.01	98 ± 2.9^{ns}	$95 \pm 2.8^{***}$
0.1	96 ± 3.4^{ns}	$98 \pm 4.1^{***}$
1.0	$94 \pm 2.1^{*}$	$100 \pm 1.6^{***}$
10	$96 \pm 4.0^{**}$	$98 \pm 2.6^{***}$
30	$94 \pm 4.2^{*}$	$97 \pm 3.0^{***}$
50	$92 \pm 1.4^{**}$	$91 \pm 3.3^{***}$
80	$93 \pm 3.8^{*}$	$93 \pm 4.5^{***}$

100	93 ± 2.6*	98 ± 3.0***
300	91 ± 4.6**	-
500	87 ± 2.1***	-

Heartbeat was measured as beats per minute (BPM) using DanioScope software, version 1.2.206. Relative heartbeat rates (%) were calculated in comparison to the vehicle (1% DMSO, *v/v*) treated control group which was set to 100%. All data are represented as mean ± standard error of the mean (s.e.m.) (n = 8-13 for 1 d exposure groups, n = 10-12 for 5 d exposure groups). The p-values were calculated by one-way ANOVA ($^{ns}p > 0.05$, $^{*}p < 0.05$, $^{**}p < 0.01$, $^{***}p < 0.001$) in comparison to the respective control group.

The metabolite data of naloxone from the HepaRG *in vitro* model and from ZF larvae investigated in this study are summarized in Table 2, and published *in vivo* data from humans [41–43,45–51] and different animal models [39,45,48,52–54] were added for comparison. The metabolite screening of naloxone was carried out as described in previous studies [26,30]. More detailed information on human data and data from animal models is provided in Supplementary Table S1, which also contains the metabolic reactions and exact masses of the detected metabolites. Amount-time profiles for naloxone and its three major metabolites (M2, M4, M21) from HepaRG cells are given in Supplementary Figure S1.

Table 2. Summary of detection patterns of naloxone and its metabolites from human biosamples, animal models, HepaRG cells, and ZF larvae.

Compounds	Human [41–43,45–51]		Rat [39,45,48,52,53]	Rabbit, Chicken [45]	Dog [48,54]	Data from this study		
						HepaRG *in vitro* model [100 µM, 300 µM]	ZF larvae [300 µM]	
	Plasma	Urine	Plasma, urine, feces	Urine	Urine		Larvae	Medium
Naloxone	+	+	+	+	+	+	+	+
M2	+	+	+			+	+	+
M4	+	+	+	+	+	+	+[c]	
M5								+[b]
M7	+	+	+	+	+		+	+
M8							+[c]	
M9			+					
M10								+[a, b]
M12			+	+[d]			+[c]	
M14								+[a, b]
M17						+[e]		+[b]
M18								+[b]
M21			+			+	+	+
M23							+[c]	
M26								+[b]
M35			+				+[c]	
Total number of detected metabolites	3	3	7	3	2	4	8	8

All data from human samples and animal models were taken from published studies; Human plasma data were quoted from [47,49–51] and urine data from [41–43,45–48]. Rat plasma data were cited from [39,48,53] and urine and feces data from [47,48,52]. More details are shown in Supplementary Table S1; [a] The structural isomers M10 and M14 co-eluted in the LC-HRMS/MS setup used in this study, and accordingly, isomers were counted and quantified as one metabolite although they derive from different metabolic reactions (see Supplementary Figure S2); [b] the metabolites were only detected in the surrounding exposure medium and not from extracted ZF larvae; [c] the metabolites were detected only in extracted ZF larvae and not in the

surrounding exposure medium; [d] the metabolite was not detected in rabbit; [e] the metabolite was only detected at the higher exposure concentration of 300 µM naloxone. +: Peak detected. Metabolites M1, M3, M6, M11, M13, M15, M16, M19, M20, M22, M24, M25, M27-M34, M36, and M37 are not included in the table as these were not detected in any of the listed models.

Out of the total 37 theoretical metabolites of naloxone (see Supplementary Table S1), three and seven metabolites were detected in human biosamples (plasma and urine) and rats, respectively (Table 2). Primarily, three metabolic reactions, N-dealkylation (M2), ketone reduction (M4), and glucuronidation (M7) are described in literature on human metabolism of naloxone, whereas renal excretion of the glucuronic acid adduct is the major elimination route [39,41,42]. The other animal models, i.e. rabbit, chicken, and dog, produced two to three metabolites, whereas four metabolites were found in HepaRG cells. However, the structural isomers, M10 and M14, were counted as one metabolite due to co-elution from the LC system used in this study. Notably, 13 metabolites in total were detected in the ZF mode either extracted from the larvae or from the surrounding medium, whereas three metabolites [M2 (*N*-dealkylation), M7 (glucuronidation), and M21 (Sulfation)], were detected in both types of ZF samples (Table 2 and Supplementary Table S1). These findings highlight the superior performance of ZF larvae in metabolism studies with a high number of possible metabolites being detected, which, in turn, greatly facilitates the reconstruction of naloxone metabolism pathways (Supplementary Figure S2). Also, major metabolites from ZF larvae significantly overlap with those found in human and rodent models (Figure 2).

As detailed above, three metabolites, including the main human metabolite (M7), were found in both, ZF larvae extracts and the surrounding medium, (Figure 2a). In contrast, the commonly used *in vitro* HepaRG model did not reveal M7. However, two metabolites (M2 and M4) overlapped between human, ZF larvae, and HepaRG cells (Figure 2b). Encouragingly, metabolite data from the ZF larvae showed a 100% match rate in mutual comparability analyses with human data and with data from HepaRG cells (Figure 2c), and a match rate of 86% was determined when comparing ZF metabolite data to the rat model (Supplementary Figure S3). Analyzing mutual comparability on basis of the rat model we found 100%, 75%, and 46% match rates to humans, HepaRG cells, and ZF larvae, respectively (Supplementary Figure S3).

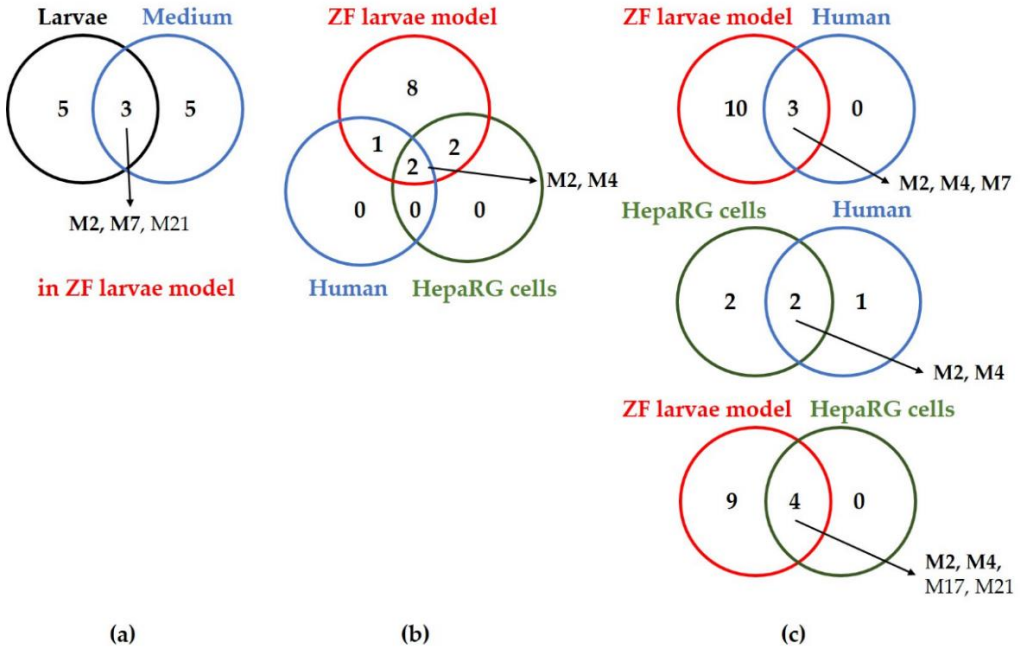

Figure 2. Comparison of the metabolites observed from three different models (human [41–43,45–51], ZF larvae, and HepaRG cells) using Venn diagrams. (a) Thirteen metabolites were found in the ZF larvae model with three metabolites being detected in both the larvae and surrounding medium, (b) common metabolites detected in three different models, and (c) their mutual comparability. Two metabolites (M2 and M4, in bold) were commonly found in all investigated models, and remarkably, the three most abundant human metabolites (M2, M4, and M7) were detected in the ZF larvae model.

Moreover, we assessed uptake kinetics and biotransformation in ZF larvae of naloxone over time through semi-quantitative analysis of relative peak intensities in order to explore its pharmacokinetic (PK) properties in ZF. From human PK it is known that naloxone is rapidly metabolized with ca. 30 min and 60 min elimination half-time in human plasma and serum, respectively [39,41,43]. In ZF larvae, the uptake of naloxone increased steadily, reaching a maximum at 24 h exposure. Along with a steady increase of naloxone amounts inside ZF larvae, the abundance of major metabolites, M7 and M21, dramatically increased from 6 h to 24 h of naloxone exposure, whereas M4 only slightly increased in the same observation period (Figure 3). A detailed assessment of the composition ratio among the parent drug naloxone and these major metabolites inside ZF larvae is given in Supplementary Figure S4. It is worth mentioning that the major human metabolite M7 (38% after 24 h) was found in nearly equal amounts to naloxone (40% after 24 h) in the ZF larvae. One of five minor metabolites in the exposed larvae, M12 (glucuronidation of M4), showed a similar pattern in terms of amount-time kinetics to the major metabolites, M7 and M21. The other four minor metabolites [M2, M8 (*N*-oxide in combination with glucuronidation), M23 (methoxylation in benzene ring), and M35 (rearrangement after elimination of hydroxyl group of M2)] showed a slow incline of their production over exposure time (Supplementary Figure S5a). Consistently with the data from ZF larvae and the most abundant internal metabolites, the

major metabolite detected in the residual surrounding medium, M17 (dihydroxylation/hydroxylation in combination with epoxidation/*N*-oxide in combination with epoxidation) displayed a strong increase in terms of relative amounts over time (Supplementary Figure S5b). In contrast, other external metabolites [M2, M5 (*N*-CH3; *N*-dealkylation), M10/M14 (N-oxidation/epoxidation/hydroxylation in benzene ring), and M18 (dihydroxylation in combination with epoxidation)] only slightly increased between 3 h and 24 h of exposure.

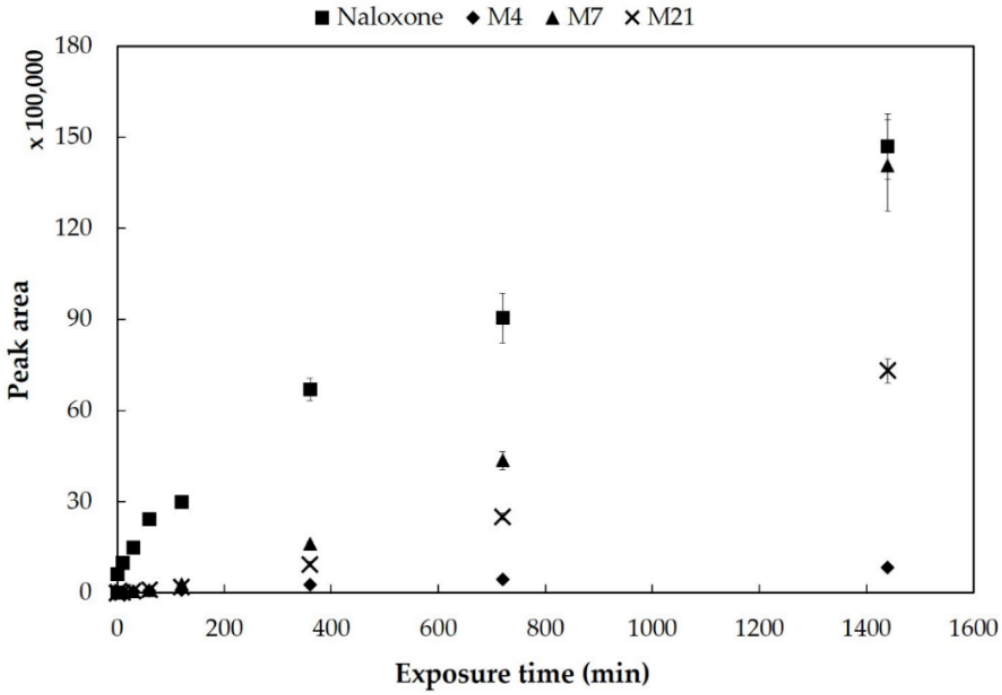

Figure 3. Internal amount-time profiles of naloxone and its most abundant metabolites (M4, M7, and M21) in ZF larvae exposed continuously with 300 µM naloxone. ZF larvae were exposed to the drug-containing medium for 0, 1, 10, 30, 60, 120, 360, 720, and 1,440 min, respectively ($n = 3$). All results from ZF larvae in this study are displayed as mean ± standard deviation from triplicates of 30 pooled larvae. The *p*-values between naloxone and its three abundant metabolites were computed by one-way ANOVA, and all *p*-values had statistical significance at all exposure times ($^{***}p < 0.001$).

To investigate elimination of naloxone in the ZF larvae model, exposed larvae were transferred into compound-free medium at 28°C after 1 h exposure to 300 µM naloxone. This time point was chosen since significant absorption and only minor conversion into metabolites of naloxone was observed in the uptake experiment (Figure 3). The internal peak intensity of naloxone showed an upward tendency until 10 min incubation in the drug-free medium (Figure 4), which could be explained by the balance of free fraction and bound naloxone. After the first 10 minutes, the amount of naloxone inside the ZF larvae declined until 6 h incubation (end of observation period), and intriguingly, the amount of the most abundant two metabolites (M7 and M21) decreased as well. In contrast, the third most abundant metabolite M4 that was analyzed in the previous uptake experiment was not quantified here

due to detection below a signal-to-noise ratio of 3. Comparing the composition ratio for naloxone and its major metabolites in ZF larvae upon transfer to the medium, the relative amount of naloxone was significantly reduced from 82% to 45% within 6 h, and in line with this, the relative amounts of M7 and M12 increased from 12% to 34% and from 7% to 21%, respectively (Supplementary Figure S6). In summary, we could confirm that data from the ZF larvae model on metabolism, absorption, and elimination of naloxone are well aligned, and thus already cover three integral parts of ADME experiments.

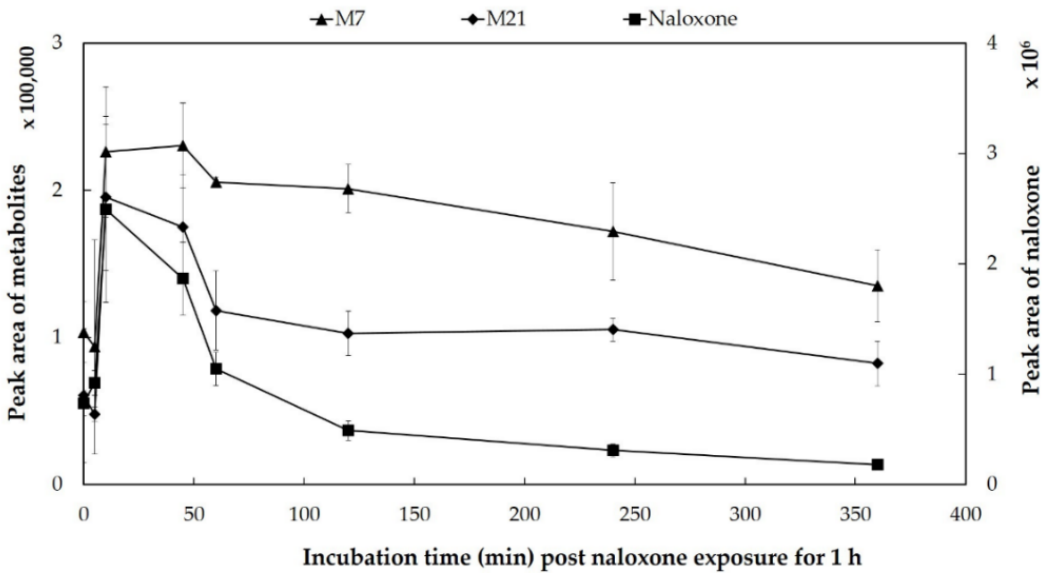

Figure 4. Elimination kinetics of naloxone and two abundant metabolites (M7 and M21) in ZF larvae following incubation in a compound-free medium post 1 h exposure with 300 µM naloxone. Incubations were performed at 0, 5, 10, 30, 45, 60, 120, 240, and 360 min (n=3). All data are depicted by mean ± standard deviation, and the p-values between naloxone and the two other metabolites were calculated by one-way ANOVA. All p-values showed significance at all incubation times ($^{***}p < 0.001$).

Taken together, in the ZF larvae model we observed fast circulation and efficient metabolism with a high similarity to human metabolism of naloxone as early as 10 min after compound exposure via conventional aqueous administration (Table 2 and Figure 3). In addition, the elimination of naloxone inside ZF larvae progressed further post 1 h continuous drug exposure (Figure 4), and a large portion of the initial naloxone amount in ZF larvae was excreted 6 h post-administration (Supplementary Figure S6).

4.4.2. Localization of Naloxone and its Metabolites in Whole Body Sections of Zebrafish Larvae

Opioids can act as receptor agonists leading to pharmacological effects as described for the archetypical opioid morphine. Naloxone is used as an opioid antagonist due to a non-selective and competitive affinity to opioid receptors in the central nervous system (CNS),

showing highest affinity to the μ-opioid receptor (MOR) located in brain, spinal cord, peripheral sensory neurons, and in the gastrointestinal tract [39,43,48]. In the present study, we examined the localization of naloxone and its metabolites inside ZF larval bodies initially using a simple dissection and extraction method. Naloxone exposed larvae (300 μM, 1 h) were sectioned into three parts (head, body, and tail sections) using a surgical blade (Supplementary Figure S7) with the goal to quantify levels of naloxone and its metabolites separately in these sections using methods as applied for the metabolism study detailed in Section 4.4.1. In order to obtain sufficient material for analyses, sections from 100 larvae were pooled for each individual sample. To account for differences in total weight of the separated fractions undergoing extraction and analysis by LC-HRMS/MS, peak intensities were normalized to the determined total weight of each section sample.

Five metabolites (M2, M4, M7, M12, and M21), out of initially eight metabolites detected in whole body ZF larvae, were detected using this experimental setup. Other ZF metabolites of naloxone (M8, M23, and M35) were not detected in the ZF larvae sections because their production requires ≥ 2 h exposure with the drug (Supplementary Figure S5a). Indeed, naloxone was mainly localized in the head section but it was also found in the body and tail sections, however, in lower amounts. In contrast, its most abundant metabolites, M7 and M21, were primarily found in the body section, whereas M4 was found in small amounts evenly distributed in all three prepared sections (Figure 5). The detection of two minor metabolites (M2 and M12) was consistent with the observed localization of M7 and M21 (Supplementary Figure S8). Encouragingly, these initial results were fully in line with presumed in vivo drug and metabolite distributions, with naloxone having a high affinity to the μ-opioid receptor found at high expression levels in the brain and metabolites being formed primarily in the liver. Thus, the data from whole body sections served as excellent starting point for the envisaged optimization of our MSI methods to study drug distribution in ZF larvae.

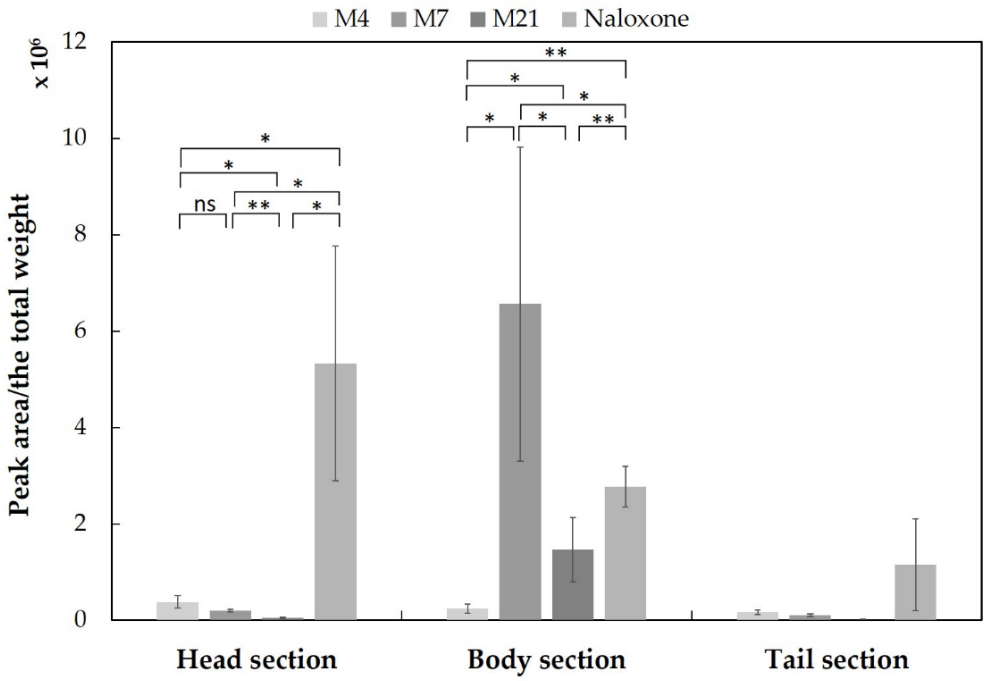

Figure 5. Sectional distributions of naloxone and its most abundant metabolites (M4, M7, and M21). The peak areas of individual compounds were normalized to the total weight of each section. Prior to sectioning, all ZF larvae were exposed to 300 μM naloxone for 1 h. The clustered columns are displayed as mean ± standard deviation ($n = 3$), and the p-values between naloxone and three metabolites were calculated by one-way ANOVA ($^{ns}p > 0.05$, $^{*}p < 0.05$, $^{**}p < 0.01$). All p-values were statistically significant in both the head and body sections, whereas the p-values for samples of the tail section could not be determined unambiguously due to the overall low peak intensities.

4.4.3. Optimization of MSI Methods to Study the Drug Distribution in Zebrafish Larvae – A Case Study Using Naloxone

Mass spectrometry imaging (MSI) provides a comprehensive method to study molecular distributions in a single experiment from biological specimens [1–3,25,55]. Over two decades, MALDI-MSI has been predominantly used, and in particular, it is still gaining popularity in biomedical and cancer research [1,3,56,57]. Nevertheless, MSI is only rarely used for analyzing ZF larvae samples, which is probably due to the fact that sample preparation from the tiny larvae poses significant technical challenges. In our previous studies [26,27], we were able to study the spatial distributions of two SCs, 7′*N*-5F-ADB and 4F-MDMB-BINACA, in ZF larval sections using MALDI-FT-ICR. These informative MS images supported our conclusions on how the route of drug administration impacts the *in vivo* distribution of a drug and its metabolism. However, there were some experimental challenges that still needed to be resolved prior to applying MSI for drug distribution studies in ZF larvae on a broader scale. In the current study, these issues were mainly related to discrepancies in MSI-based metabolite detection compared to routine LC-HRMS/MS measurements, which we contributed to non-uniform formation of adduct ions in the MALDI-MSI setup. In

detail, we generally observed the presence of three adduct ions (proton, sodium, and potassium) of the parent compound for naloxone and the two SCs (7′*N*-5F-ADB and 4F-MDMB-BINACA) in ZF larvae matrices. While evaluating optimal embedding procedures and matrix deposition steps for MALDI-MSI of ZF larvae as detailed below, the predominant adduct formed of naloxone and its metabolites in the ZF homogenates was $[M+K]^+$ and the $[M+Na]^+$ species was found at a similar intensity under non-optimized conditions. This result for naloxone differed unexpectedly from the previous results as 7′N-5F-ADB was found protonated and 4F-MDMB-BINACA was found as sodium adduct in the MS images of ZF larvae [26,27]. We assumed that this finding might be caused by different ionization efficiencies of molecules in MSI dependent on the composition of the surrounding matrix [56,58–61]. However, it is crucial for relative spatial compound quantification by MSI that a single primary ion of the target species is formed predominately in order to maximize the detection limit (MDL) of a substrate and to correlate compound abundance with MSI intensity plots.

Hence, further method optimization for MSI was done to better fit the needs for ZF larvae analyses. As a first step, we used homogenates from naloxone-exposed ZF larvae to reduce sample variability and overcome issues originating from the sample inhomogeneity in MSI of larval sections [56,58,59]. By spiking these ZF larval homogenates on the surface of blank embedding medium layer, we examined the optimal conditions in terms of sample preparation by varying the composition of the lower level embedding medium, cryosectioning, and matrix deposition steps for achieving more uniform ion detection patterns in MSI. Details on the studied conditions are summarized in Table 3. The listed parameters (steps) were assessed in sequential order.

Table 3. Detailed experimental conditions of MSI sample preparation using ZF larvae homogenates evaluated in this study.

Steps	Conditions	Variable parameters
1) Homogenate block*	Gelatin medium as lower sample layer**	**40% (*w*/*v*)**, 30% (*w*/*v*)
2) Cryosectioning	Thickness***	10 µm, (15 µm, 20 µm)
3) Matrix deposition****	Matrix reagent	**15 mg mL^{-1}**, 30 mg mL^{-1} (for DHB) 5 mg mL^{-1}, 15 mg mL^{-1} (for CHCA)
	Addition of TFA	**0.1%**, 0.5%, 1.0% (for DHB) 0.1% (for CHCA)
	Spray deposition passes	**14 passes**, 28 passes (for DHB) 8 passes, 14 passes (for CHCA)

The steps are listed in order of sample preparation for MSI. Conditions of our previously used protocol [26,27] are highlighted in bold. *The homogenate block is composed of a lower layer (the same thickness as the tested larvae section) of gelatin medium used as a blank layer for spiking ZF homogenates on top. **30% gelatin medium was additionally tested in this study since only 40% gelatin was tested for embedding a whole body of ZF larva in previous studies [26,27]. ***For cryosectioning, 15 µm and 20 µm thickness were also tested, however, these data are not shown due to many practical failures in the following matrix deposition step. Thus, all presented data are from 10 µm sections. ****The detailed deposition condition for each matrix reagent (DHB and CHCA) is described in Section 4.5.6. DHB: 2,5-Dihydroxybenzoic acid, CHCA: α-Cyano-4-hydroxycinnamic acid, TFA; Trifluoroacetic acid.

4.4 Results and Discussion

In the MS images of naloxone from homogenates of treated ZF larvae (waterborne exposure, 1 d, 300 μM), there were no specific distributional images, and naloxone was only detected as few random spots in the images using the matrix deposition conditions in Table 3. It also has to be noted that the initial issue of different ion species negatively impacting MSI of naloxone could not be resolved using DHB as matrix reagent; the sodium and the potassium ion of naloxone were present at similar abundance. In summary, 40% gelatin as embedding medium with a higher concentration of DHB (30 mg mL^{-1}) and 14 passes of spraying matrix deposition led to slightly better detection of naloxone compared to the other given conditions. Increasing the concentration of trifluoroacetic acid (TFA) in the DHB matrix solution led to slightly lower detectability, however, differences were not significant. In contrast, when using α-cyano-4-hydroxycinnamic acid (CHCA) as matrix, naloxone detection was significantly improved in both conditions using 30% and 40% gelatin as embedding medium (Figure 6). We determined eight passes of matrix spraying with 5 mg mL^{-1} CHCA solution containing 0.1% TFA as optimal condition (Figure 6a). Increasing the number of matrix spraying passes significantly reduced the intensity of naloxone, whereas generally lower detection intensity was found when using the matrix at a higher concentration (15 mg mL^{-1} CHCA; Figure 6b). Notably, in the CHCA matrix reagent, the potassium adduct ion was predominant in the MS images of the homogenates, whereas the sodium ion species was only observed in few small spots. Overall, using sections of 40% gelatin for spotting the homogenates prior to matrix deposition gave better results with less vacant space of the measured homogenate than 30% gelatin combined with a lower concentration of CHCA and higher spray deposition passes. In summary, the potassium adduct of naloxone ($[M+K]^+$) was uniformly detected using the optimized procedure for CHCA matrix deposition and encouragingly, the relative abundance of naloxone as $[M+Na]^+$ species was significantly reduced. In particular, the utilization of ZF larval homogenates as a pre-step before establishing optimal conditions for MSI of sectioned ZF larvae is convenient, and it diminishes many efforts required to accomplish MSI studies.

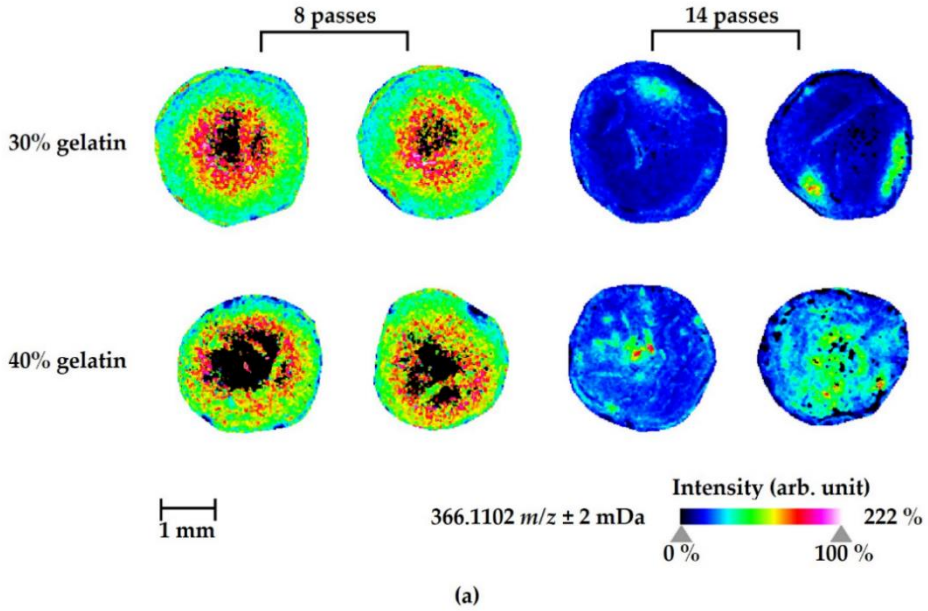

Figure 6. *Continued.*

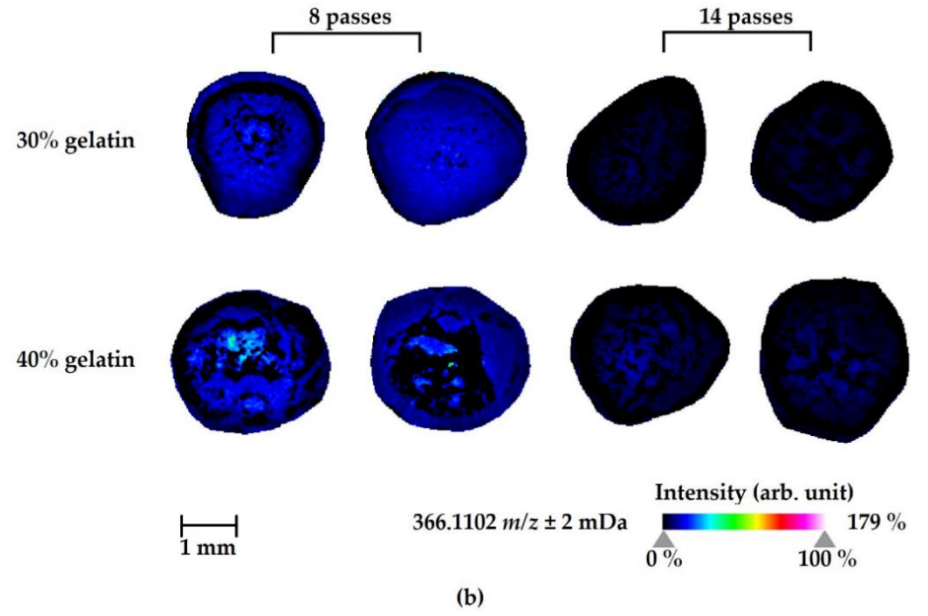

Figure 6. MALDI-MS images of the parent compound (naloxone, potassium adduct ion, *m/z* 366.1102) in ZF larvae homogenates. The optimal matrix deposition condition was determined as follows: (see upper left panel; a) 8 passes of spraying matrix deposition using 5 mg mL^{-1} CHCA containing 0.1% TFA and 40% gelatin as lower layer of the cryosectioned (10 μm) block. In panel b, 15 mg mL^{-1} CHCA containing 0.1% TFA was also investigated. ZF larvae at 4 days post-fertilization (dpf) were treated by waterborne exposure with 300 μM naloxone at 28 °C for 1 d prior to homogenization with an ultrasonic homogenizer (pools of 30 larvae each). Each homogenate sample was prepared by spotting 1 μL of total homogenate onto 30% and 40% gelatin layer,

respectively. The MS images were prepared in duplicates. The images were generated by preparing a colormap from blue (no detection) to purple (high local concentration), and they were further processed in 96 dpi resolution with 24-bit color under a weak denoising state.

Moreover, under the optimized condition for naloxone detection by MSI in ZF larvae homogenates, three sections (head, body, and tail) of exposed ZF larvae studied in Section 4.4.2 were homogenized and then analyzed by MALDI-FT-ICR, and results were compared to previously determined LC-HRMS/MS data. . Consistent with the MSI results from whole-body homogenates, naloxone was mainly detected as a potassium adduct ion. In addition, we could confirm by MALDI-MSI of these sectioned homogenates that naloxone showed highest abundance (on a qualitative scale) in the homogenate from the head region whereas amounts detected in the homogenate from the tail region were significantly lower (Figure 7).

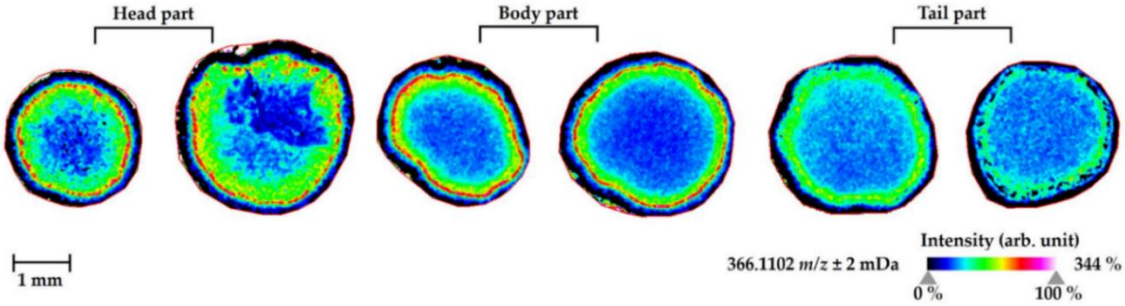

Figure 7. MALDI-MS images of the parent compound (naloxone, potassium adduct ion, *m/z* 366.1102) in three sectional homogenates of ZF larvae (head, body, and tail region) after 1 d treatment of ZF larvae at 4 dpf by waterborne exposure with 300 µM naloxone at 28 °C prior to sectioning and homogenization. Each homogenate sample was prepared by spotting 1 µL of total homogenate onto 10 µm slices of 40% gelatin followed by the matrix deposition step as detailed in the main text (optimized condition). The duplicate MS images originate from individual pools of 100 larvae. The images were generated by preparing a colormap from blue (no detection) to purple (high local concentration) and then were further processed in 96 dpi resolution with 24-bit color under weak denoising state.

Next, we attempted to quantify the relative naloxone amount in MSI experiments for a fixed volume of homogenate (1 µL) by external calibration through spiking naloxone into blank ZF larvae homogenates (Figure 8). Calibration curves of naloxone were generated by linear (≤ 33 ng/µL) and logarithmic regression (> 33 ng/µL) within different concentration ranges (Supplementary Figure S9). The narrow range of linearity might be caused by matrix effects and ion suppression induced by the overall complex composition of the homogenates. This effect is generally considered as a challenge in quantitative MSI studies [36,59,60,62], and it is assumed that it hinders the reproducible quantification of molecules in tissue sections through MSI. Thus, to produce reliable quantification data of a certain substance an appropriate internal standard (ISTD) is required in order to compensate for matrix effects to the same degree as for the unlabeled investigated substance [36,59–62]. However, such a setup is challenging to implement due to the lack and/or high price of custom-made ISTDs. Nevertheless, in future MSI studies, the use of an ISTD and additional washing steps by

submersion of sections with organic solvent or buffer [4,55,63,64] prior to matrix deposition should be considered for more accurate quantification of absolute naloxone amounts.

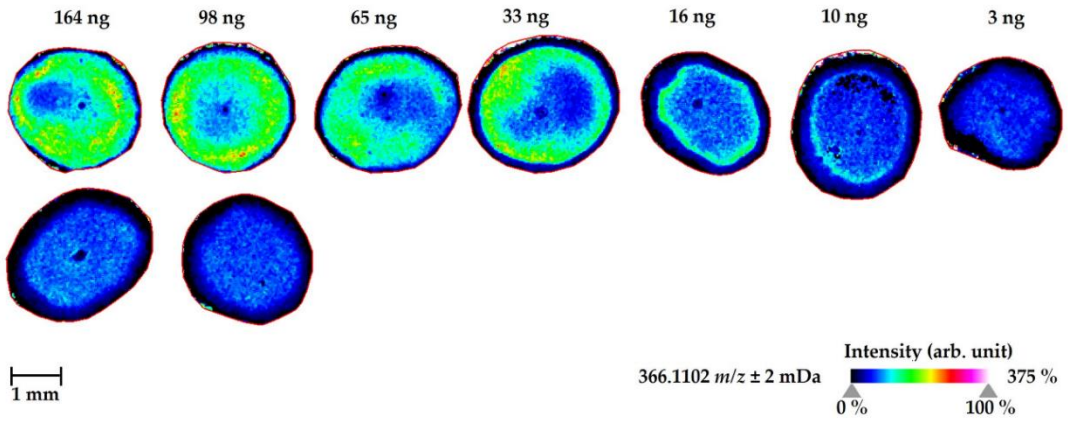

Figure 8. MALDI-MS images of naloxone (potassium adduct ion, *m/z* 366.1102) at different concentrations in 1 μL of blank ZF larvae homogenates (upper panel) and equal amounts of homogenates from ZF larvae pre-exposed to naloxone (lower panel). ZF larvae at 4 dpf were treated by waterborne exposure with 300 μM naloxone at 28 °C for 1 d and then homogenized with an ultrasonic homogenizer. Each homogenate sample was prepared by spotting 1 μL of total homogenate onto a 40% gelatin layer as described above. All homogenates used originate from individual pools of 100 ZF larvae, and the exposed larvae homogenates were analyzed in duplicates. All these samples were prepared using the optimized conditions for MSI of naloxone in ZF larvae homogenates as described above. The images were generated by preparing a colormap from blue (no detection) to purple (high local concentration) and then were further processed in 96 dpi resolution with 24-bit color under weak denoising state.

Having determined an improved protocol for the detection of naloxone in ZF larvae homogenates, we set out to test these conditions for distributional MS images of naloxone inside ZF larvae whole body sections. We compared these MS images to those generated by our previous protocol (Figure 9) [26,27]. In addition, the intensity of the three adduct ions of naloxone was analyzed in the larval sections to confirm an enrichment of a single ion species under the optimized conditions (Supplementary Figure S10). In particular, a 3-D view function for MS images was used to look over the distribution of molecules inside the small sized ZF larva and verify their localizations in specific organs without any loss of detection information. Since one representative slide cannot explain an entire body distribution of the substrate with stereoscopic vision, this 3-D function can reconstruct many cryosectioned larvae sections altogether into one entire larva MS image and also complement practical errors that occurred during embedding and cryosectioning processes. In practice, a sloping position of larva in an embedding medium occasionally occurs and then leads to partial or biased body sections.

In conclusion, optimizing sample preparation and using 3-D visualization for MS images of naloxone (predominant detection as potassium ion) in ZF larvae significantly enhanced intensity and detecting frequency (Figure 9b and 9d). Interestingly, when comparing

to MS images generated under the previous non-optimized condition (Figure 9a and 9c), several discrepancies are found, highlighting the need for compound and sample-specific optimization steps. In particular, the sodium adduct ion as major species was localized mostly in the tail part (Figure 9a), whereas the potassium ion was detected more or less randomly throughout the larval body at overall low abundance (Figure 9c). This distributional information, in turn, would have led to the conclusion that naloxone is accumulated in the tail of ZF larvae – a finding that can be hardly explained knowing that a significant proportion should be found particularly in the head region as detected through LC-HRMS/MS-based analyses of ZF larvae (Section 4.4.1 and 4.4.2). Having optimized the detection of naloxone in MSI we were able to revise this false-positive finding and indeed, analyzing the potassium adduct of naloxone under optimized conditions (Figure 9d) revealed a more reasonable distribution in view of the pharmacological properties of naloxone and our results from LC-HRMS/MS studies. In detail, naloxone was found at overall high abundance with accumulation in the head part of ZF larvae (in line with its property to cross the blood-brain barrier and high affinity binding to the μ-opioid receptor) and at other accumulation spots in the main body part, where major organs are located, and in the tail region, possibly reflecting drug distribution processes. Overall, these findings highlight how appropriate sample preparation plays a vital role in MSI studies and emphasizes the necessity of finding the best condition for analyzing a specific substrate.

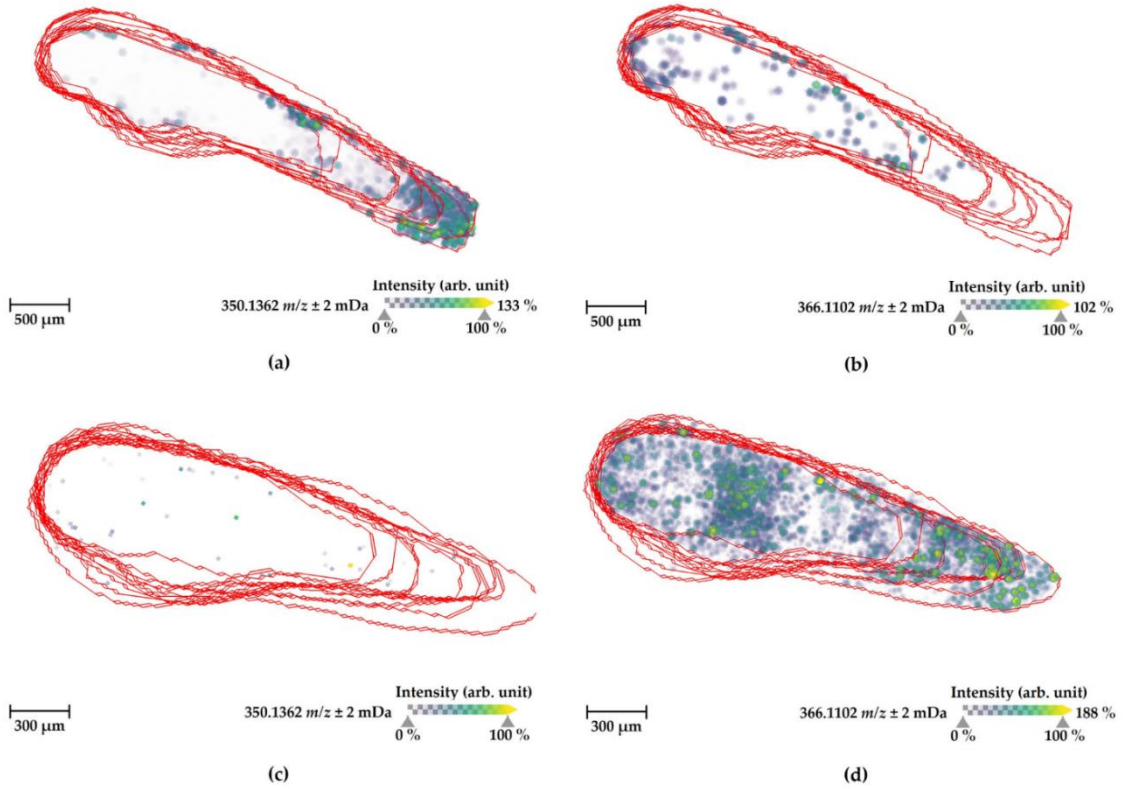

Figure 9. Comparison of the spatial distribution of naloxone [sodium adduct ion (*m/z* 350.1362) and potassium adduct ion (*m/z* 366.1102)] inside ZF larval whole body between (a,b) the protocol used in the previous studies [26,27] and (c,d) the optimal condition investigated in this study. All MS images were visualized with a 3-dimensional view function in SCiLS Lab version Premium 3-D software. These were the experimental conditions: (a,b) 14 passes of spraying matrix deposition using 15 mg mL^{-1} DHB containing 0.1% TFA and 40% gelatin embedding medium, a total of 10 slides for one respective larva; (c,d) 8 passes of spraying matrix deposition using 5 mg mL^{-1} CHCA containing 0.1% TFA and 40% gelatin embedding medium, a total of 11 slides for one respective larva. The images were generated by preparing a colormap from blue (no detection) to yellow (high local concentration) with a 50% transparency option, and then they were further processed in 96 dpi resolution with 24-bit color under denoising state.

Encouragingly, the overall inorganic salt adduct formation ($[M+K]^+$ and $[M+Na]^+$) of naloxone in the larvae sections prepared according to the newly developed protocol was approximately ten times higher than observed in MS images prepared according to the previously used method. Remarkably, through applying the optimized protocol, most naloxone signals derive from the highly abundant potassium adducted ion with only very little contribution of the protonated species and the sodium adduct (Supplementary Figure S10). In addition to the parent drug (Figure 9), five metabolites (M2, M4, M7, M10/M14, and M35) could also be visualized by MSI of the ZF larvae whole body sections (Figure 10). M2 was strongly detected in all areas of the ZF larval body except for the front head region, and M4

and M35 were distributed more in peripheral and yolk sac sections. Interestingly, glucuronidated naloxone, M7, which is the primary human metabolite, was uniquely detected in a specific region where ZF liver and pancreas are located, and M10/M14 was evenly distributed in the ZF larval body. Furthermore, these distributional properties of naloxone and its metabolites complemented findings of the whole body and sectional larvae samples analyzed by LC-HRMS/MS described in Section 4.4.1 and 4.4.2.

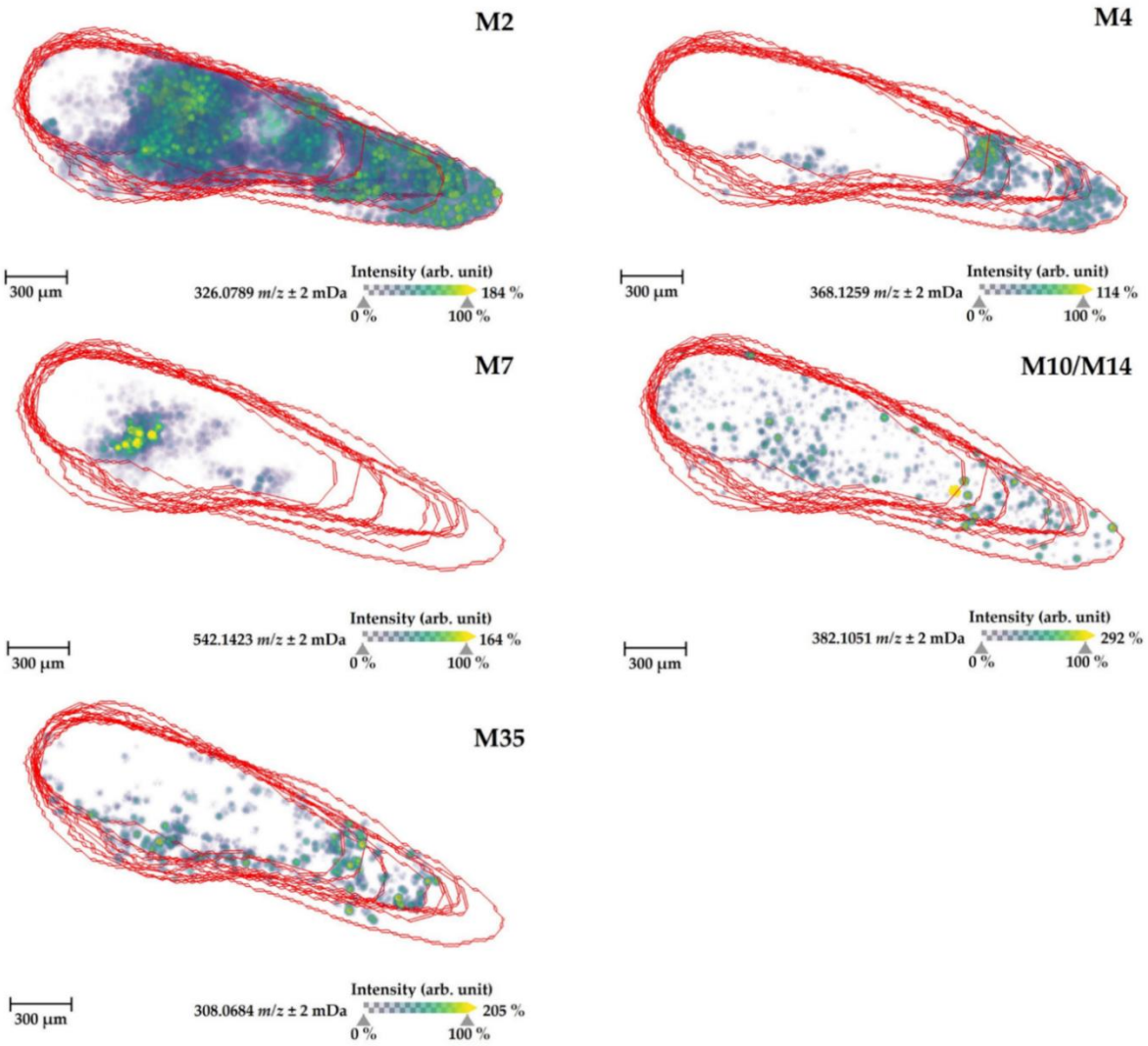

Figure 10. MALDI-MS images of the most abundant ZF metabolites of naloxone [M2 (*m/z* 326.0789), M4 (*m/z* 368.1259), M7 (*m/z* 542.1423), M10/M14 (*m/z* 382.1051), and M35 (*m/z* 308.0684), potassium adduct ions) detected inside ZF larvae (whole body) prepared under the optimal condition as described above. All MS images were visualized with a 3-dimensional view function in SCiLS Lab version Premium 3D software. The images were generated by preparing a colormap from blue (no detection) to yellow (high local concentration) with a 50% transparency option and then were further processed in 96 dpi resolution with 24-bit color under denoising state.

4.5. Materials and Methods

4.5.1. Chemicals and Other Materials

Naloxone, dimethyl sulfoxide (DMSO), tricaine (3-amino-benzoic acid ethyl ester), trifluoroacetic acid, gelatin from cold water fish skin, 2,5-dihydroxybenzoic acid (2,5-DHB), and α-cyano-4-hydroxycinnamic acid (CHCA) were obtained from Sigma-Aldrich (Taufkirchen, Germany). Methanol (LC-MS grade), acetonitrile (LC-MS grade), and formic acid (LC-MS grade) were from VWR (Darmstadt, Germany). NaCl, KCl, $MgSO_4$, $Ca(NO_3)_2$, and HEPES were purchased from Carl Roth (Karlsruhe, Germany). Stock solutions of all standards were prepared in DMSO at a concentration of 10 mM, and solutions were stored for a maximum of one month at −20 °C. The working solutions were freshly prepared prior to each experiment. 6-well plates were obtained from Sarstedt (Nümbrecht, Germany). Differentiated HepaRG cells® cryopreserved (HPR116), basal hepatic cell medium (MIL 600C), and thawing/plating/general purpose medium supplement (ADD 670C) were purchased from Biopredic International (Saint-Grégoire, France). 24-well plate coated with type I collagen was obtained from Life Technologies GmbH (Darmstadt, Germany), and conductive indium-tin-oxide (ITO) coated glass slides were from Bruker Daltonics (Bremen, Germany). Zebrafish embryos of the AB wild-type line were initially obtained from the Luxembourg Center for Systems Biomedicine (Belvaux, Luxembourg). Dry small granulate food was from SDS Deutschland (Limburgerhof, Germany), and *Artemia* cysts (> 230,000 nauplii per gram) were obtained from Coralsands (Wiesbaden, Germany).

4.5.2. ZF Maintenance and Embryo Collection

Zebrafish husbandry and all experiments with ZF larvae were executed according to EU Directive 2010/63/EU and the German Animal Welfare Act (§11 Abs. 1 TierSchG), in which all works were accomplished by following internal standard-operating procedures (SOPs) based on published standard methods [65]. Adult ZF were kept in an automated aquatic eco-system (PENTAIR, Apopka, UK), which is a continuous and real-time monitoring system under these conditions: Temperature (27 ± 0.5 °C), pH (7.0 ± 0.1), conductivity (800 ± 50 μS), and light-dark cycle (14 h/10 h). Fish were fed twice a day with dry small granulate food and freshly hatched live *Artemia* cysts once a day. The ZF embryo/larvae medium (0.3× Danieau's solution) is made up of 17 mM NaCl, 2 mM KCl, 0.12 mM $MgSO_4$, 1.8 mM $Ca(NO_3)_2$, 1.5 mM HEPES, pH 7.1–7.3, and 1.2 μM methylene blue. To reproduce ZF embryos, ZF pairs were kept overnight in standard mating cages, separated by gender. The following morning, the adult ZF started spawning as soon as the separators were removed. All fertilized eggs of ZF were collected and sorted using a Zeiss Stemi 508 stereo microscope (Carl Zeiss Microscopy GmbH, Jena, Germany). All embryos were raised in an incubator at 28 °C with daily medium change to clean embryo cultures. ZF larvae at 4 dpf were used for drug metabolism studies.

4.5.3. Drug Treatment of ZF Larvae via Medium Exposure

The sample preparation following waterborne drug exposure is described elsewhere [26–30]. A non-toxic exposure concentration was chosen based on the survival rate as determined by

in vivo maximum-tolerated concentration (MTC) experiments with 4 dpf ZF larvae. To measure the heartbeat of ZF larvae, ZF larvae were anesthetized on ice and arranged. Heartbeat rates were determined using DanioScope software version 1.2.206 based on imaging using a stereo microscope (Zeiss Stemi 508 stereo microscope). For metabolite studies, 15 ZF larvae at 4 dpf were transferred to one well of a 6-well plate containing 3 mL of 0.3× Danieau's medium with 300 μM naloxone. All exposure media contained a final concentration of 1% (*v*/*v*) DMSO, and ZF larvae were treated for 24 h in an incubator at 28 °C. Additional 15 larvae were incubated in a compound-free medium containing only 1% (*v*/*v*) DMSO as negative control (background masses). All treated larvae were rinsed twice with 1 mL of 0.3× Danieau's solution prior to subsequent analyses.

4.5.4. Manual Sectioning of ZF Larvae

After exposure and washing, all larvae were transferred into a petri dish using a pipette and then euthanized through cooling. Individual ZF larvae were aligned on a glass board for dissection. After removal of excess medium around the larvae by a pipette (but not all to prohibit dryness of the sections and loss of sections), the immobilized larvae were cut into three sections (head, body, and tail section; Supplementary Figure S7) using a sterilized surgical disposable scalpel (B. Braun; Tuttlingen, Germany) under a microscope (Zeiss Stemi 508 stereo microscope). All sections were collected into pre-cooled tubes and excess medium was removed with a pipette as much as possible. Each section sample was prepared from a pool of 100 larvae in triplicates.

4.5.5. ZF Sample Preparation and Metabolite Analysis by LC-HRMS/MS

The washed 30 larvae treated by the procedures described in Section 4.5.3 were pooled into a tube using a pipette and then euthanized by putting the tubes in ice water. After removing excess medium, these larvae or the sectional larvae samples prepared in Section 4.5.4 were snap-frozen in liquid nitrogen, followed by lyophilization for 4 h. The lyophilized larvae were stored for a maximum of one week at –20 °C before extraction. For metabolite identification, frozen larvae were thawed at room temperature for at least 30 min and extracted by vigorous vortexing for 2 min with 50 μL methanol. The sample was centrifuged at 10,000× *g* for 2 min at room temperature, and the supernatant was transferred to an autosampler vial. All pooled samples were prepared in triplicates. The extract from ZF larvae was kept in a freezer at -20 °C and analyzed within one week after extraction.

The LC-HRMS/MS system was composed of a Dionex Ultimate 3000 RSLC system (Thermo Fisher Scientific, Germering, Germany) and maXis 4G HR-QTOF mass spectrometer (Bremen, Germany) with the Apollo II ESI source. Separation of 5 μL-aliquots from all larvae extracts was carried out by a linear gradient with 0.1% formic acid in water (*v*/*v*, eluent A) and 0.1% formic acid in acetonitrile (*v*/*v*, eluent B) at a flow rate of 600 μL/min. Waters ACQUITY BEH C_{18} column (100 × 2.1 mm, 1.7 μm) equipped with a Waters VanGuard BEH C_{18} 1.7 μm guard column at 45 °C as stationary phase. The linear gradient mode was programmed as follows; 0–0.5 min, 5% eluent B; 0.5–18.5 min, 5–95% eluent B; 18.5–20.5 min, 95% eluent B; 20.5–21 min, 95–5% eluent B; 21–22.5 min, 5% eluent B. Complementarily, UV spectra measurement were recorded using a diode array detector (DAD) in the range from 200 to 600 nm.

Mass spectra were recorded in centroid mode ranging from 150–2,500 *m*/*z* at a 2 Hz full scan acquisition rate under auto MS/MS conditions in positive ionization mode. External calibration was automatically done by injecting sodium formate and calibration on the respective clusters formed in the ESI source before every LC-HRMS/MS run. All MS analyses were acquired in the presence of the *m*/*z* 622.0290, 922.0098, and 1221.9906 ions as the lock masses generated with the $[M+H]^+$ ions of $C_{12}H_{19}F_{12}N_3O_6P_3$, $C_{18}H_{19}O_6N_3P_3F_2$, and $C_{24}H_{19}F_{36}N_3O_6P_3$. DataAnalysis software version 4.4 (Bruker Daltonics, Bremen, Germany) was used for qualitative analysis.

With the limit of available reference standards, expected naloxone metabolites were tentatively identified using MS/MS data (Supplementary Figure S11). In addition, relative quantification of metabolites was done based on peak areas under the assumption of similar ionization behaviors of the individual metabolites due to the lacking of reference standards.

4.5.6. Mass Spectrometry Image Analysis of ZF Larva by MALDI-FT-ICR

The ZF larvae treated by the procedures described in Sections 4.5.3 were embedded in 30% and 40% (*w*/*v*) gelatin solution and then were frozen and stored at -20 °C until cryosectioning. A single larva was cut with 10-μm thickness at -20 °C using a cryostat (MEV; SLEE, Mainz, Germany), and every section was put on a cold conductive indium-tin-oxide (ITO) coated glass slide. In addition, 15-μm and 20-μm thickness were also tested, and however, this was not successful due to coarse quality of slides and rolling up/solidification at the rim of slides. All sections were scanned individually under a microscope for alignment of the optical image of the sample in MALDI. These serial sections from one larva on one glass slide were deposited using TM-Sprayer (HTX M5; HTX Technologies, Chapel Hill, NC, USA) with 2,5-dihydroxybenzoic acid (2,5-DHB; 15 mg mL^{-1} and 30 mg mL^{-1}) and α-cyano-4-hydroxycinnamic acid (CHCA; 5 mg mL^{-1} and 15 mg mL^{-1}) in acetonitrile:water (9:1, *v*/*v*) solution containing trifluoroacetic acid (TFA; 0.1%, 0.5%, and 1.0%) as described in Table 3 and then dried in a vacuum desiccator for ≥ 2 h. Spray nozzle temperature and flow rate of the pump were set up according to the manufacturer's recommendations based on the chemical property of each matrix reagent: 60 °C and 0.125 mL min^{-1} for DHB and 75 °C and 0.20 mL min^{-1} for CHCA. The dried glass slide was stored at –20 °C before MALDI-FT-ICR measurement. In practice, as the detachment of the sections from the glass slide often happened during the thawing step prior to the MALDI analysis, we recommend analyzing the samples within one week after matrix deposition. This issue occurred mainly from the arid part of the sections embedded in both 30% and 40% gelatin medium, and we assumed that it might be caused by the loss of water in the slides due to more extended storage in a freezer.

For MSI measurement, the sections of ZF larvae were analyzed by MALDI and 7T SolariX FT-ICR (Bruker Daltonics, Bremen, Germany) in positive ionization mode (*m*/*z* range 150–1,000), using 40 laser shots per pixel with a raster width of 20 μm. Before acquiring MALDI images, the mass calibration of FT-ICR was performed by the calibration standard according to the manufacturer manual, and for auto-calibration of MALDI of each laser measurement, the lock mass was set to *m*/*z* 273.0394 (for 2,5-DHB matrix) and *m*/*z* 212.0381 (for CHCA matrix). MALDI-MSI data acquisitions and image data analyses in three dimensions were processed using ftmsControl version. 2.2.0, flexImaging version 5.0, and SCiLS Lab version 2022a Premium 3D softwares (Bruker Daltonics, Bremen, Germany).

4.5.7. ZF Larval Homogenate Preparation

The pooled 30 whole-body larvae and 100 sectional larvae samples were treated as described above in Section 4.5.3 and 4.5.4, respectively, prior to homogenization for seven times using an ultrasonic homogenizer (ZINSSER ANALYTIC GmbH; Frankfurt am Main, Germany) under the condition of five sec/interval of 10 sec with 75% amplitude. These larval homogenate samples for MSI measurements were prepared by spotting 1 µL of total homogenate aliquots onto 30% and 40% gelatin and then dried in a vacuum desiccator for ≥ 1 h. To prepare external calibration in ZF larvae homogenate matrices, each calibration point was freshly prepared from a 5 mM stock solution, yielding a final concentration of 3, 10, 16, 33, 65, 98, and 164 ng, respectively. The larvae homogenates for the calibration were pooled from 100 ZF larvae. All homogenates were scanned followed by a matrix deposition procedure as described in Section 4.5.6.

4.5.8. *In Vitro* Metabolism Analyses Using HepaRG Cells

For further understanding of the naloxone metabolism in an *in vitro* model, differentiated HepaRG cells were investigated. According to the manufacturer's instruction, the metabolism studies were implemented using adherent cells at 4 h after cell seeding (Biopredic International; Saint-Grégoire, France). All the steps of cell preparation were performed under sterile conditions. Differentiated cells frozen in a vial were thawed and seeded at a density of 4.8×10^5 cells/cm^2 in collagen-coated 24-well plates with 0.5 mL of thawing and seeding medium. These cell cultures were maintained at 37 °C in a humidified incubator (95% air humidity, 5% CO_2). The thaw and seed medium was composed of MIL 600 (basal hepatic cell medium) supplemented by ADD 670C (thawing/plating/general purpose medium supplement with antibiotics) and pre-warmed to 37 °C before usage. For the cell exposure of naloxone, 150 µL aliquots of medium were removed from the 24-well cell culture plate, and treatment was started by adding 150 µL of the naloxone-contained medium. These mediums were prepared by adding naloxone into the thaw and seed medium, yielding final concentrations of 100 µM with 0.2% (*v*/*v*) DMSO and 300 µM with 0.6% (*v*/*v*) DMSO in the total medium of one well.

Treatment was stopped after 0.1, 10, 30, 60, 120, 240, 360, and 1,440 min, and blank group (as a negative control) and two control groups [as a DMSO control; 0.2% and 0.6% (*v*/*v*)] were also prepared. All samples were prepared in duplicates. An aliquot of 30 µL-supernatants of all medium was transferred into a tube, and for extraction, 30 µL of cold acetonitrile containing with 0.1% formic acid was immediately added. Samples were vortexed and cooled in a freezer for 30 min at −20 °C. After centrifuging at 10,000× g for 2 min at 4 °C, the 30 µL-supernatant of the samples was transferred to an autosampler vial, and all samples were then dried *in vacuo* and resuspended with 30 µL of acetonitrile containing 0.1% formic acid. All incubation conditions were done in duplicates. The analysis of these extracts and data acquisition were performed by the LC-HRMS/MS system conditions explained in Section 4.5.5.

4.6 Summary and Conclusions

In this study, we aimed to improve the understanding of metabolism and drug pharmacokinetics using the ZF larvae model as an alternative *in vivo* model for predicting human metabolism with the opioid antagonist naloxone as a tool drug. Intriguingly, we could demonstrate that the ZF model can reliably predict human metabolism of naloxone; ZF larvae produced all three described main human metabolites along with ten additional ones, which were used to refine the metabolic pathways of the opioid receptor antagonist (Table 2 and Supplementary Figure S2). In summary, while comparing the mutual similarity of metabolism, ZF larvae showed a 100% match rate to both humans and the common *in vitro* HepaRG cells (Figure 2c). Moreover, ZF larvae showed an 86% match rate to rat, as one renowned *in vivo* model in pharmacology and toxicology (Supplementary Figure S3). Moreover, the uptake and biotransformation kinetics of naloxone over time were assessed (Figures 3 and 4 and Supplementary Figure S6).

The localization of naloxone inside ZF larval bodies was first determined by manual sectioning of larvae into head, body, and tail regions, and we could demonstrate through LC-HRMS/MS analyses that naloxone can be found in each body part with a certain accumulation in the head region (Figure 5). Given the pharmacological properties of naloxone as an opioid receptor antagonist this result was fully conclusive and also consistent with reports on morphine-like PK properties of naloxone in humans [39,43,48]. To optimize naloxone detection in MSI, ZF larvae homogenates were utilized and we could optimize detection methods for naloxone distribution inside ZF larvae using the MSI approach (Figure 6 and Table 3), although FT-ICR-based quantification still needs further optimization in terms of reducing matrix effects and availability of internal standards for reliable quantitative analyses (Figure 8). Importantly, we could demonstrate that MSI of naloxone in ZF larvae under non-optimized conditions resulted in false-negative results with respect to the spatial distribution of the drug, a phenomenon which could be completely overcome when the newly developed sample preparation protocol was applied (Figure 9). Using the latter, we could not only reliably predict *in vivo* distribution of naloxone but were also able to characterize the spatial distribution of major metabolites (M2, M4, M7, M10/M14, and M35; Figure 10). Furthermore, the discrepancy between MALDI-MSI and LC-HRMS/MS due to the formation of three different adduct ions – which was indeed the major rationale for undertaking the presented study with naloxone – could be overcome as we were able to implement protocols for MSI sample preparation that support the preferential formation of single ion species (Figure 9 and Supplementary Figure S10).

Taken together, with the naloxone example we demonstrate that ZF larvae model is a promising *in vivo* model, which can be broadly applied to study DMPK properties of a drug. In particular, drug metabolism in ZF larvae has been shown to reliably predict human metabolism and we could further consolidate this finding in the presented study with naloxone. Having detailed information on the *in vivo* distribution of drugs and metabolites in ZF larvae would largely increase the impact of this model in routine screening and early preclinical profiling of investigational new drugs. In the presented case study with naloxone, we were able to significantly improve MSI protocols giving reliable images of the *in vivo* distribution of naloxone. Importantly, the general workflows applied here for optimizing MSI detection of naloxone inside ZF larvae is

broadly applicable and will help to improve analytics of any other investigated molecule as part of DMPK studies in the ZF larvae model.

4.7 Bibliography

1. Davoli, E.; Zucchetti, M.; Matteo, C.; Ubezio, P.; D'Incalci, M.; Morosi, L. THE SPACE DIMENSION AT THE MICRO LEVEL: MASS SPECTROMETRY IMAGING OF DRUGS IN TISSUES. *Mass Spectrom. Rev.* **2021**, *40*, 201–214, doi:10.1002/mas.21633.
2. Buchberger, A.R.; DeLaney, K.; Johnson, J.; Li, L. Mass Spectrometry Imaging: A Review of Emerging Advancements and Future Insights. *Anal. Chem.* **2018**, *90*, 240–265, doi:10.1021/acs.analchem.7b04733.
3. Zemaitis, K.J.; Izydorczak, A.M.; Thompson, A.C.; Wood, T.D. Streamlined Multimodal DESI and MALDI Mass Spectrometry Imaging on a Singular Dual-Source FT-ICR Mass Spectrometer. *Metabolites* **2021**, *11*, doi:10.3390/metabo11040253.
4. Gorzolka, K.; Kölling, J.; Nattkemper, T.W.; Niehaus, K. Spatio-Temporal Metabolite Profiling of the Barley Germination Process by MALDI MS Imaging. *PLoS One* **2016**, *11*, e0150208, doi:10.1371/journal.pone.0150208.
5. Sphamandla Ntshangase; Sipho Mdanda; Tricia Naicker; Hendrik G. Kruger; Sooraj Baijnath; Thavendran Govender. Spatial distribution of elvitegravir and tenofovir in rat brain tissue: Application of matrix-assisted laser desorption/ionization mass spectrometry imaging and liquid chromatography/tandem mass spectrometry. *Rapid Communications in Mass Spectrometry* **2019**, *33*, 1643–1651, doi:10.1002/rcm.8510.
6. Tang, W.; Chen, J.; Zhou, J.; Ge, J.; Zhang, Y.; Li, P.; Li, B. Quantitative MALDI Imaging of Spatial Distributions and Dynamic Changes of Tetrandrine in Multiple Organs of Rats. *Theranostics* **2019**, *9*, 932–944, doi:10.7150/thno.30408.
7. Giordano, S.; Pifferi, V.; Morosi, L.; Morelli, M.; Falciola, L.; Cappelletti, G.; Visentin, S.; Licandro, S.A.; Frapolli, R.; Zucchetti, M.; et al. A Nanostructured Matrices Assessment to Study Drug Distribution in Solid Tumor Tissues by Mass Spectrometry Imaging. *Nanomaterials (Basel)* **2017**, *7*, doi:10.3390/nano7030071.
8. Costa, C.; Jang, M.; Jesus, J. de; Steven, R.T.; Nikula, C.J.; Elia, E.; Bunch, J.; Bellew, A.T.; Watts, J.F.; Hinder, S.; et al. Imaging mass spectrometry: a new way to distinguish dermal contact from administration of cocaine, using a single fingerprint. *Analyst* **2021**, *146*, 4010–4021, doi:10.1039/d1an00232e.
9. Bailey, M.J.; Bradshaw, R.; Francese, S.; Salter, T.L.; Costa, C.; Ismail, M.; P Webb, R.; Bosman, I.; Wolff, K.; Puit, M. de. Rapid detection of cocaine, benzoylecgonine and methylecgonine in fingerprints using surface mass spectrometry. *Analyst* **2015**, *140*, 6254–6259, doi:10.1039/c5an00112a.
10. Ifa, D.R.; Manicke, N.E.; Dill, A.L.; Cooks, R.G. Latent fingerprint chemical imaging by mass spectrometry. *Science* **2008**, *321*, 805, doi:10.1126/science.1157199.
11. Lawson, N.D.; Weinstein, B.M. In vivo imaging of embryonic vascular development using transgenic zebrafish. *Dev. Biol.* **2002**, *248*, 307–318, doi:10.1006/dbio.2002.0711.

12. Carten, J.D.; Bradford, M.K.; Farber, S.A. Visualizing digestive organ morphology and function using differential fatty acid metabolism in live zebrafish. *Dev. Biol.* **2011**, *360*, 276–285, doi:10.1016/j.ydbio.2011.09.010.
13. Rasheed, S.; Fries, F.; Müller, R.; Herrmann, J. Zebrafish: An Attractive Model to Study Staphylococcus aureus Infection and Its Use as a Drug Discovery Tool. *Pharmaceuticals (Basel)* **2021**, *14*, doi:10.3390/ph14060594.
14. Zhang, Q.; Ji, C.; Yan, L.; Lu, M.; Lu, C.; Zhao, M. The identification of the metabolites of chlorothalonil in zebrafish (Danio rerio) and their embryo toxicity and endocrine effects at environmentally relevant levels. *Environ. Pollut.* **2016**, *218*, 8–15, doi:10.1016/j.envpol.2016.08.026.
15. Wiegand, C.; Krause, E.; Steinberg, C.; Pflugmacher, S. Toxicokinetics of atrazine in embryos of the zebrafish (Danio rerio). *Ecotoxicol. Environ. Saf.* **2001**, *49*, 199–205, doi:10.1006/eesa.2001.2073.
16. Barros, T.P.; Alderton, W.K.; Reynolds, H.M.; Roach, A.G.; Berghmans, S. Zebrafish: an emerging technology for in vivo pharmacological assessment to identify potential safety liabilities in early drug discovery. *Br. J. Pharmacol.* **2008**, *154*, 1400–1413, doi:10.1038/bjp.2008.249.
17. Papan, C.; Chen, L. Metabolic fingerprinting reveals developmental regulation of metabolites during early zebrafish embryogenesis. *OMICS* **2009**, *13*, 397–405, doi:10.1089/omi.2009.0023.
18. Chng, H.T.; Ho, H.K.; Yap, C.W.; Lam, S.H.; Chan, E.C.Y. An investigation of the bioactivation potential and metabolism profile of Zebrafish versus human. *J. Biomol. Screen.* **2012**, *17*, 974–986, doi:10.1177/1087057112447305.
19. Jones, H.S.; Trollope, H.T.; Hutchinson, T.H.; Panter, G.H.; Chipman, J.K. Metabolism of ibuprofen in zebrafish larvae. *Xenobiotica* **2012**, *42*, 1069–1075, doi:10.3109/00498254.2012.684410.
20. van Wijk, R.C.; Krekels, E.H.J.; Hankemeier, T.; Spaink, H.P.; van der Graaf, P.H. Systems pharmacology of hepatic metabolism in zebrafish larvae. *Drug Discovery Today: Disease Models* **2016**, *22*, 27–34, doi:10.1016/j.ddmod.2017.04.003.
21. Wu, J.-Q.; Fan, R.-Y.; Zhang, S.-R.; Li, C.-Y.; Shen, L.-Z.; Wei, P.; He, Z.-H.; He, M.-F. A systematical comparison of anti-angiogenesis and anti-cancer efficacy of ramucirumab, apatinib, regorafenib and cabozantinib in zebrafish model. *Life Sci.* **2020**, *247*, 117402, doi:10.1016/j.lfs.2020.117402.
22. Meijer, A.H. Protection and pathology in TB: learning from the zebrafish model. *Semin. Immunopathol.* **2016**, *38*, 261–273, doi:10.1007/s00281-015-0522-4.
23. Shams, S.; Rihel, J.; Ortiz, J.G.; Gerlai, R. The zebrafish as a promising tool for modeling human brain disorders: A review based upon an IBNS Symposium. *Neurosci. Biobehav. Rev.* **2018**, *85*, 176–190, doi:10.1016/j.neubiorev.2017.09.002.
24. Martín-Jiménez, R.; Campanella, M.; Russell, C. New zebrafish models of neurodegeneration. *Curr. Neurol. Neurosci. Rep.* **2015**, *15*, 33, doi:10.1007/s11910-015-0555-z.

25. Gonzalez-Nunez, V.; Rodríguez, R.E. The zebrafish: a model to study the endogenous mechanisms of pain. *ILAR J.* **2009**, *50*, 373–386, doi:10.1093/ilar.50.4.373.
26. Park, Y.M.; Meyer, M.R.; Müller, R.; Herrmann, J. Drug Administration Routes Impact the Metabolism of a Synthetic Cannabinoid in the Zebrafish Larvae Model. *Molecules* **2020**, *25*, doi:10.3390/molecules25194474.
27. Park, Y.M.; Dahlem, C.; Meyer, M.R.; Kiemer, A.K.; Müller, R.; Herrmann, J. Induction of Liver Size Reduction in Zebrafish Larvae by the Emerging Synthetic Cannabinoid 4F-MDMB-BINACA and Its Impact on Drug Metabolism. *Molecules* **2022**, *27*, 1290, doi:10.3390/molecules27041290.
28. Gampfer, T.M.; Wagmann, L.; Park, Y.M.; Cannaert, A.; Herrmann, J.; Fischmann, S.; Westphal, F.; Müller, R.; Stove, C.P.; Meyer, M.R. Toxicokinetics and toxicodynamics of the fentanyl homologs cyclopropanoyl-1-benzyl-4′-fluoro-4-anilinopiperidine and furanoyl-1-benzyl-4-anilinopiperidine. *Arch. Toxicol.* **2020**, *94*, 2009–2025, doi:10.1007/s00204-020-02726-1.
29. Wagmann, L.; Frankenfeld, F.; Park, Y.M.; Herrmann, J.; Fischmann, S.; Westphal, F.; Müller, R.; Flockerzi, V.; Meyer, M.R. How to Study the Metabolism of New Psychoactive Substances for the Purpose of Toxicological Screenings-A Follow-Up Study Comparing Pooled Human Liver S9, HepaRG Cells, and Zebrafish Larvae. *Front. Chem.* **2020**, *8*, 539, doi:10.3389/fchem.2020.00539.
30. Richter, L.H.J.; Herrmann, J.; Andreas, A.; Park, Y.M.; Wagmann, L.; Flockerzi, V.; Müller, R.; Meyer, M.R. Tools for studying the metabolism of new psychoactive substances for toxicological screening purposes - A comparative study using pooled human liver S9, HepaRG cells, and zebrafish larvae. *Toxicol. Lett.* **2019**, *305*, 73–80, doi:10.1016/j.toxlet.2019.01.010.
31. Kirla, K.T.; Groh, K.J.; Steuer, A.E.; Poetzsch, M.; Banote, R.K.; Stadnicka-Michalak, J.; Eggen, R.I.L.; Schirmer, K.; Kraemer, T. From the Cover: Zebrafish Larvae Are Insensitive to Stimulation by Cocaine: Importance of Exposure Route and Toxicokinetics. *Toxicol. Sci.* **2016**, *154*, 183–193, doi:10.1093/toxsci/kfw156.
32. Nguyen, D.D.; Saharuka, V.; Kovalev, V.; Stuart, L.; Del Prete, M.; Lubowiecka, K.; Mot, R. de; Venturi, V.; Alexandrov, T. Facilitating Imaging Mass Spectrometry of Microbial Specialized Metabolites with METASPACE. *Metabolites* **2021**, *11*, doi:10.3390/metabo11080477.
33. Abdelmoula, W.M.; Pezzotti, N.; Hölt, T.; Dijkstra, J.; Vilanova, A.; McDonnell, L.A.; Lelieveldt, B.P.F. Interactive Visual Exploration of 3D Mass Spectrometry Imaging Data Using Hierarchical Stochastic Neighbor Embedding Reveals Spatiomolecular Structures at Full Data Resolution. *J. Proteome Res.* **2018**, *17*, 1054–1064, doi:10.1021/acs.jproteome.7b00725.
34. Fuso Nerini, I.; Morosi, L.; Zucchetti, M.; Ballerini, A.; Giavazzi, R.; D'Incalci, M. Intratumor heterogeneity and its impact on drug distribution and sensitivity. *Clin. Pharmacol. Ther.* **2014**, *96*, 224–238, doi:10.1038/clpt.2014.105.

35. Jove, M.; Spencer, J.; Clench, M.; Loadman, P.M.; Twelves, C. Precision pharmacology: Mass spectrometry imaging and pharmacokinetic drug resistance. *Crit. Rev. Oncol. Hematol.* **2019**, *141*, 153–162, doi:10.1016/j.critrevonc.2019.06.008.
36. Huizing, L.R.S.; McDuffie, J.; Cuyckens, F.; van Heerden, M.; Koudriakova, T.; Heeren, R.M.A.; Vreeken, R.J. Quantitative Mass Spectrometry Imaging to Study Drug Distribution in the Intestine Following Oral Dosing. *Anal. Chem.* **2021**, *93*, 2144–2151, doi:10.1021/acs.analchem.0c03956.
37. Villacrez, M.; Hellman, K.; Ono, T.; Sugihara, Y.; Rezeli, M.; Ek, F.; Marko-Varga, G.; Olsson, R. Evaluation of Drug Exposure and Metabolism in Locust and Zebrafish Brains Using Mass Spectrometry Imaging. *ACS Chem. Neurosci.* **2018**, *9*, 1994–2000, doi:10.1021/acschemneuro.7b00459.
38. Nelson, K.A.; Daniels, G.J.; Fournie, J.W.; Hemmer, M.J. Optimization of whole-body zebrafish sectioning methods for mass spectrometry imaging. *J. Biomol. Tech.* **2013**, *24*, 119–127, doi:10.7171/jbt.13-2403-002.
39. Committee for Medicinal Products for Human Use (CHMP), European Medicines Agency. Assessment report: Nyxoid **2017**, 1–59.
40. UNODC. World Drug Report 2021: Booklet 5 - COVID-19 AND DRUGS: IMPACT AND OUTLOOK **2021**.
41. van Dorp, E.L.A.; Yassen, A.; Dahan, A. Naloxone treatment in opioid addiction: the risks and benefits. *Expert Opin. Drug Saf.* **2007**, *6*, 125–132, doi:10.1517/14740338.6.2.125.
42. Haidari, M.; Mansani, S.; Ponds, D.; Romero, L.; Alsaab, S. Consumption of Movantik™ (Naloxegol) results in detection of naloxone in the patient's urine evaluated by confirmatory urine drug testing. *Clin. Biochem.* **2019**, *67*, 48–53, doi:10.1016/j.clinbiochem.2019.03.006.
43. Rzasa Lynn, R.; Galinkin, J.L. Naloxone dosage for opioid reversal: current evidence and clinical implications. *Ther. Adv. Drug Saf.* **2018**, *9*, 63–88, doi:10.1177/2042098617744161.
44. Teklezgi, B.G.; Pamreddy, A.; Ntshangase, S.; Mdanda, S.; Singh, S.D.; Gopal, N.D.; Naicker, T.; Kruger, H.G.; Govender, T.; Baijnath, S. Mass Spectrometric Imaging of the Brain Demonstrates the Regional Displacement of 6-Monoacetylmorphine by Naloxone. *ACS Omega* **2020**, *5*, 12596–12602, doi:10.1021/acsomega.9b03570.
45. Fujimoto, J.M. Isolation of naloxone-3-glucuronide from human urine. *Proc. Soc. Exp. Biol. Med.* **1970**, *133*, 317–319, doi:10.3181/00379727-133-34465.
46. Weinstein, S.H.; Pfeffer, M.; Schor, J.M.; Indindoli, L.; Mintz, M. Metabolites of naloxone in human urine. *J. Pharm. Sci.* **1971**, *60*, 1567–1568, doi:10.1002/jps.2600601030.
47. FDA Advisory Committee on the Most Appropriate Dose or Doses of Naloxone to Reverse the Effects of Life-threatening Opioid Overdose in the Community Settings: ADVISORY COMMITTEE BRIEFING MATERIALS. *Joint Meeting of the Anesthetic and Analgesic Drug Products Advisory Committee and the Drug Safety and Risk Management Advisory Committee on October 5, 2016* **2016**.

48. kaleo, I.B.D. Joint Meeting of the Anesthetic and Analgesic Drug Products and the Drug Safety and Risk Management Advisory Committees October 5, 2016: Advisory Committee Briefing Materials **2016**.
49. CHIANG, C. Pharmacokinetics of the combination tablet of buprenorphine and naloxone. *Drug Alcohol Depend.* **2003**, *70*, S39-S47, doi:10.1016/S0376-8716(03)00058-9.
50. Wiegand, S.L.; Swortwood, M.J.; Huestis, M.A.; Thorp, J.; Jones, H.E.; Vora, N.L. Naloxone and Metabolites Quantification in Cord Blood of Prenatally Exposed Newborns and Correlations with Maternal Concentrations. *AJP Rep.* **2016**, *6*, e385-e390, doi:10.1055/s-0036-1593993.
51. Swortwood, M.J.; Scheidweiler, K.B.; Barnes, A.J.; Jansson, L.M.; Huestis, M.A. Simultaneous quantification of buprenorphine, naloxone and phase I and II metabolites in plasma and breastmilk by liquid chromatography-tandem mass spectrometry. *J. Chromatogr. A* **2016**, *1446*, 70–77, doi:10.1016/j.chroma.2016.03.076.
52. Misra, A.L.; Pontani, R.B.; Vadlamani, N.L.; Mulé, S.J. Physiological disposition and biotransformation of allyl-1', 3' - 14C naloxone in the rat and some comparative observations on nalorphine. *J. Pharmacol. Exp. Ther.* **1976**, *196*, 257–268.
53. Joshi, A.; Parris, B.; Liu, Y.; Heidbreder, C.; Gerk, P.M.; Halquist, M. Quantitative determination of buprenorphine, naloxone and their metabolites in rat plasma using hydrophilic interaction liquid chromatography coupled with tandem mass spectrometry. *Biomed. Chromatogr.* **2017**, *31*, doi:10.1002/bmc.3785.
54. Garrett, E.R.; Shyu, W.C.; Ulubelen, A. Pharmacokinetics of morphine and its surrogates. VIII: Naloxone and naloxone conjugate pharmacokinetics in dogs as a function of dose and as affected by simultaneously administered morphine. *J. Pharm. Sci.* **1986**, *75*, 1127–1136, doi:10.1002/jps.2600751203.
55. Asslan, M.; Lauzon, N.; Beus, M.; Maysinger, D.; Rousseau, S. Mass spectrometry imaging in zebrafish larvae for assessing drug safety and metabolism. *Anal. Bioanal. Chem.* **2021**, doi:10.1007/s00216-021-03476-4.
56. Hulme, H.; Fridjonsdottir, E.; Gunnarsdottir, H.; Vallianatou, T.; Zhang, X.; Wadensten, H.; Shariatgorji, R.; Nilsson, A.; Bezard, E.; Svenningsson, P.; et al. Simultaneous mass spectrometry imaging of multiple neuropeptides in the brain and alterations induced by experimental parkinsonism and L-DOPA therapy. *Neurobiol. Dis.* **2020**, *137*, 104738, doi:10.1016/j.nbd.2020.104738.
57. Balluff, B.; Hopf, C.; Porta Siegel, T.; Grabsch, H.I.; Heeren, R.M.A. Batch Effects in MALDI Mass Spectrometry Imaging. *J. Am. Soc. Mass Spectrom.* **2021**, *32*, 628–635, doi:10.1021/jasms.0c00393.
58. Zecchi, R.; Franceschi, P.; Tigli, L.; Amidani, D.; Catozzi, C.; Ricci, F.; Salomone, F.; Pieraccini, G.; Pioselli, B.; Mileo, V. Sample preparation strategy for the detection of steroid-like compounds using MALDI mass spectrometry imaging: pulmonary distribution of budesonide as a case study. *Anal. Bioanal. Chem.* **2021**, *413*, 4363–4371, doi:10.1007/s00216-021-03393-6.

59. Hansen, H.T.; Janfelt, C. Aspects of Quantitation in Mass Spectrometry Imaging Investigated on Cryo-Sections of Spiked Tissue Homogenates. *Anal. Chem.* **2016**, *88*, 11513–11520, doi:10.1021/acs.analchem.6b02711.
60. Taylor, A.J.; Dexter, A.; Bunch, J. Exploring Ion Suppression in Mass Spectrometry Imaging of a Heterogeneous Tissue. *Anal. Chem.* **2018**, *90*, 5637–5645, doi:10.1021/acs.analchem.7b05005.
61. Lanekoff, I.; Stevens, S.L.; Stenzel-Poore, M.P.; Laskin, J. Matrix effects in biological mass spectrometry imaging: identification and compensation. *Analyst* **2014**, *139*, 3528–3532, doi:10.1039/c4an00504j.
62. Barry, J.A.; Groseclose, M.R.; Castellino, S. Quantification and assessment of detection capability in imaging mass spectrometry using a revised mimetic tissue model. *Bioanalysis* **2019**, *11*, 1099–1116, doi:10.4155/bio-2019-0035.
63. Angel, P.M.; Caprioli, R.M. Matrix-assisted laser desorption ionization imaging mass spectrometry: in situ molecular mapping. *Biochemistry* **2013**, *52*, 3818–3828, doi:10.1021/bi301519p.
64. Zaima, N.; Yoshioka, S.; Sato, Y.; Shinano, S.; Ikeda, Y.; Moriyama, T. Enhanced specificity for phosphatidylcholine analysis by positive ion mode matrix-assisted laser desorption/ionization imaging mass spectrometry. *Rapid Commun. Mass Spectrom.* **2014**, *28*, 1453–1458, doi:10.1002/rcm.6917.
65. Westerfield, M. *The zebrafish book*: *A guide for the laboratory use of zebrafish (Danio rerio)*, 4th edition; [M. Westerfield]: Eugene, OR 97403, 2000.

4.8 Supporting Information

Optimization of Mass Spectrometry Imaging for Drug Metabolism and Distribution Studies in the Zebrafish Larvae Model: A Case Study with the Opioid Antagonist Naloxone

Manuscript ready for Submission:

Yu Mi Park [1,2,3], Markus R. Meyer [4], Rolf Müller [1,3,5,*] and Jennifer Herrmann [1,5,*]

[1]Helmholtz Centre for Infection Research, Helmholtz Institute for Pharmaceutical Research Saarland (HIPS), Campus E8 1, Saarland University, 66123 Saarbrücken, Germany; yu-mi.park@helmholtz-hips.de
[2]Environmental Safety Group, Korea Institute of Science and Technology (KIST) Europe, 66123 Saarbrücken, Germany
[3]Department of Pharmacy, Saarland University, 66123 Saarbrücken, Germany
[4]Center for Molecular Signaling (PZMS), Institute of Experimental and Clinical Pharmacology and Toxicology, Department of Experimental and Clinical Toxicology, Saarland University, 66421 Homburg, Germany; m.r.meyer@mx.uni-saarland.de
[5]German Center for Infection Research (DZIF), 38124 Braunschweig, Germany
[*]Correspondence: Rolf.Mueller@helmholtz-hips.de (R.M.); Jennifer.Herrmann@helmholtz-hips.de (J.H.); Tel.: +49-681-98806-3000 (R.M.), +49-681-98806-3101 (J.H.)

4.8 Supporting Information

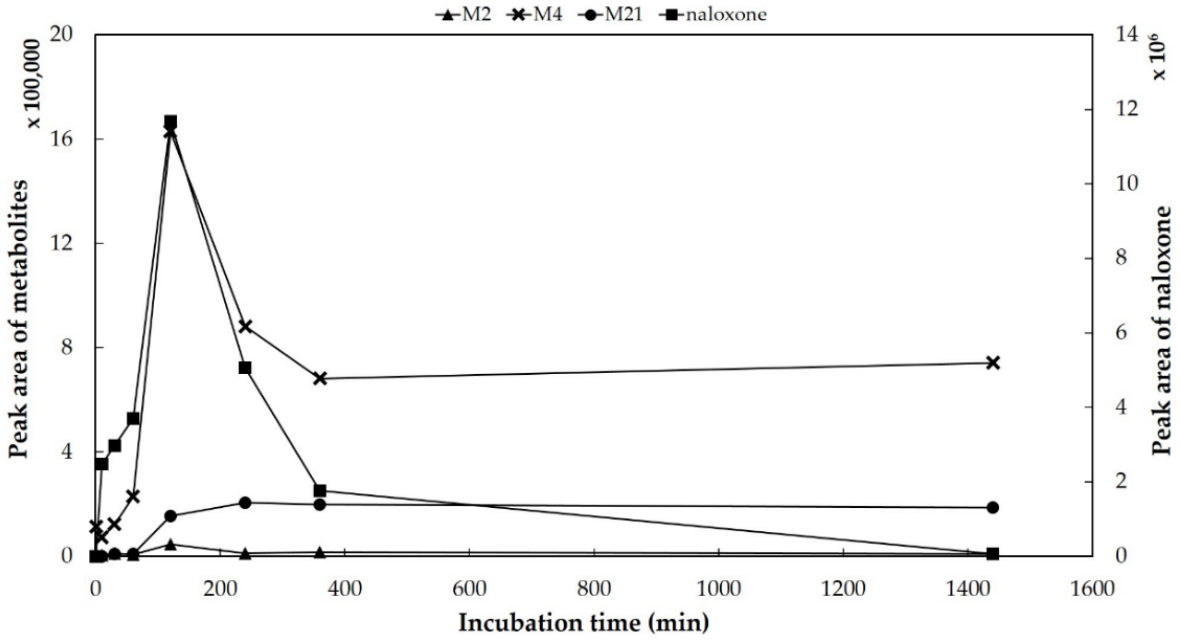

(a)

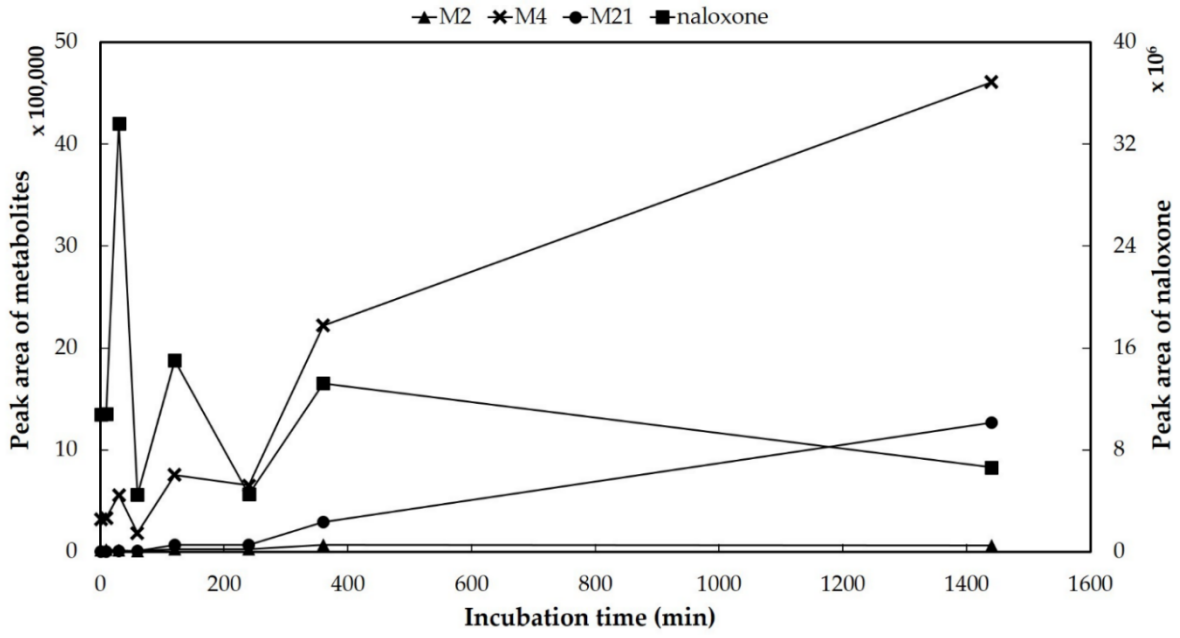

(b)

Figure S1. Internal amount-time profiles of naloxone and its main three metabolites (M2, M4, and M21) in HepaRG cells incubated with (a) 100 μM and (b) 300 μM naloxone, respectively. The cell medium was collected after 0.1, 10, 30, 60 120, 240, 360, 1,440 min of incubation (n = 3). The p-values between naloxone and these three metabolites at both concentrations were computed by one-way ANOVA, and all p-values represented significance at all incubation times, respectively ($^{***}p < 0.001$).

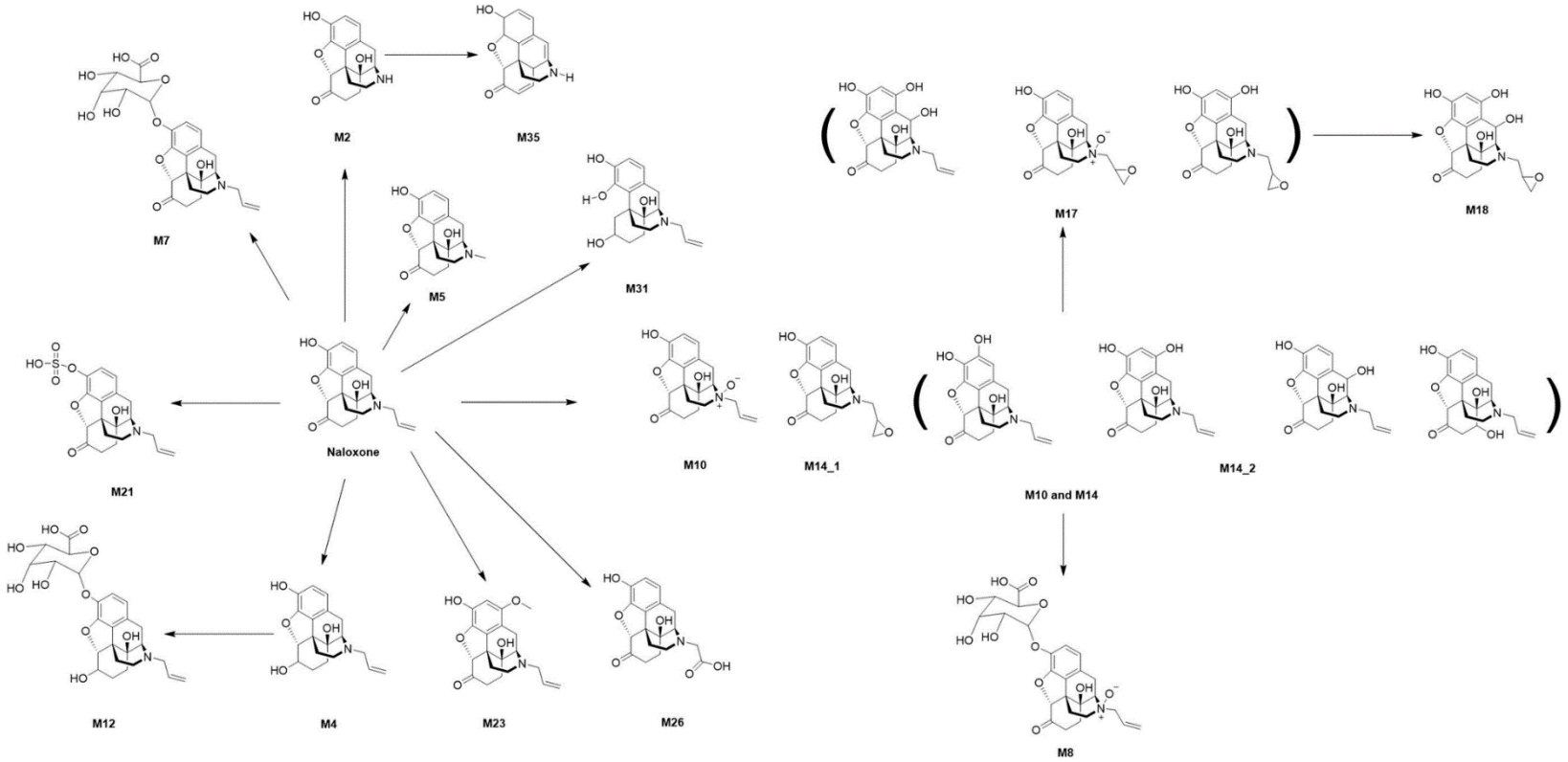

Figure S2. The reconstructed metabolic pathway of naloxone based on the metabolites detected in the ZF larvae model.

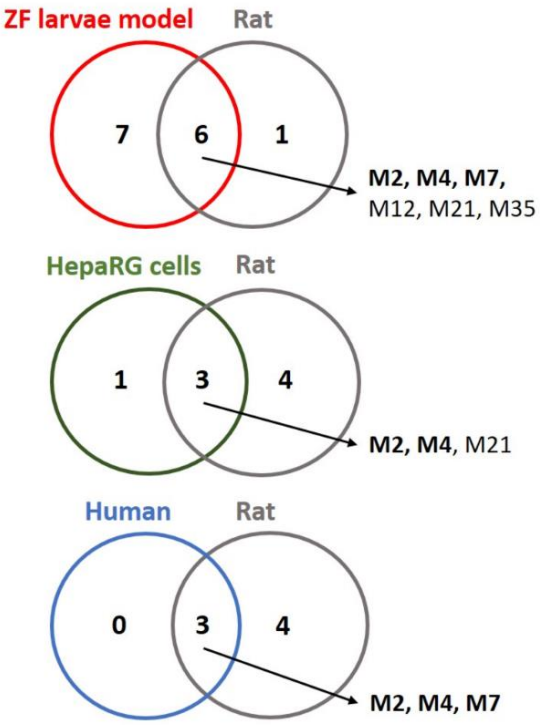

Figure S3. Mutual comparison of detected metabolites based on the rat model [39,48,53] with three different models (ZF larvae, HepaRG cells, and humans [41–43,45–51]). Two metabolites (M2 and M4, in bold) were commonly detected in all investigated models, and the dominant three human metabolites (M2, M4, and M7) were found in both ZF larvae and the rat models.

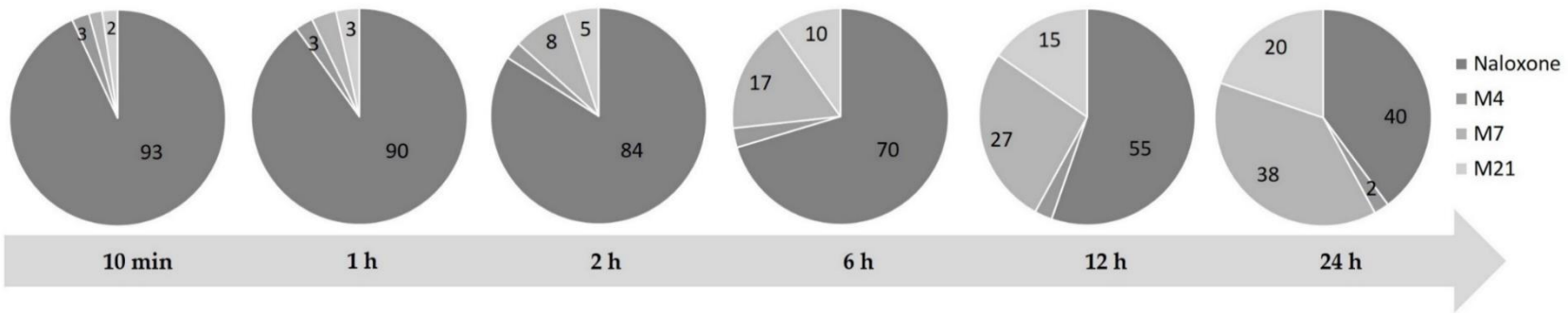

Figure S4. Composition pattern changes of internal naloxone and its major three metabolites (M4, M7, and M21) in ZF larvae after 10 min to 24 h exposure time of naloxone. All data are represented as mean of three replicates of 30 pooled larvae.

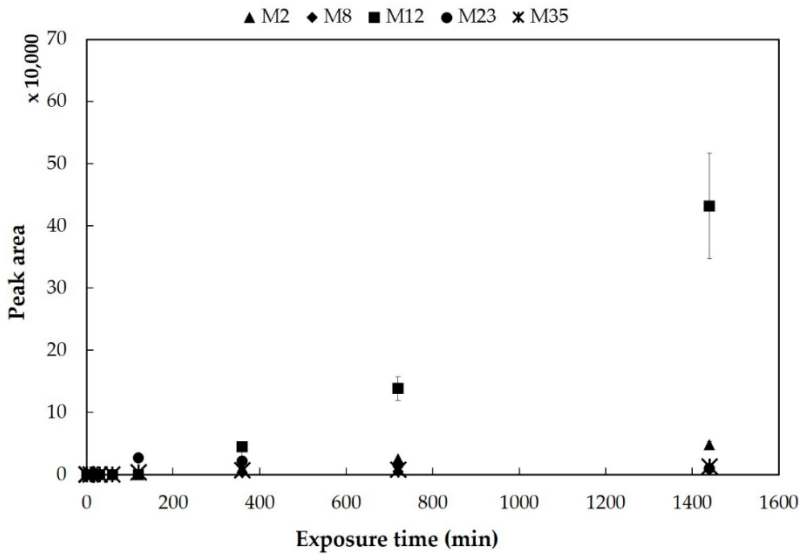

(a)

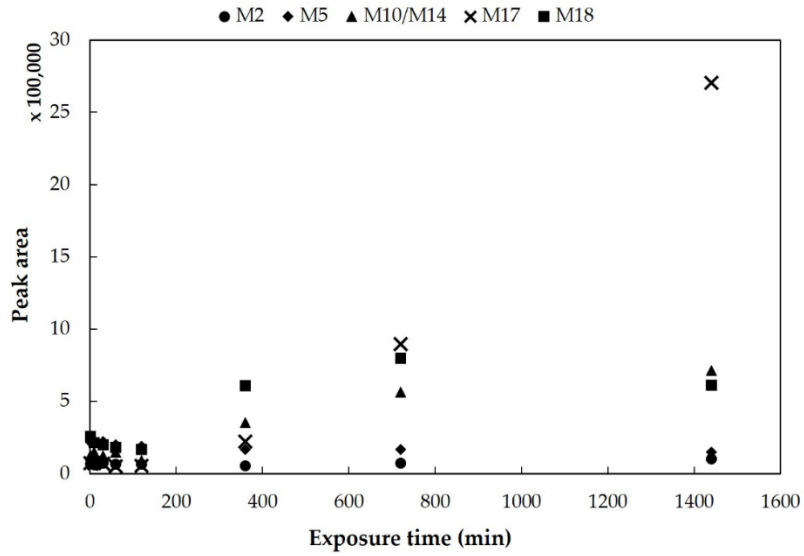

(b)

Figure S5. Internal amount-time profile of (a) five minor metabolites (M2, M8, M12, M23, and M35) in ZF larvae exposed to 300 μM naloxone and (b) detection of five metabolites (M2, M5, M10/M14, M17, and M18) in the surrounding medium after exposure of larvae to naloxone. ZF larvae were exposed to the drug-containing medium for 0, 1, 10, 30, 60, 120, 360, 720, and 1,440 min, respectively ($n = 3$). The residual medium is collected directly from each larvae sample at the given exposure time ($n = 1$). All results from ZF larvae in panel (a) are given as mean ± standard deviation from triplicates of 30 pooled larvae, and the p-values between naloxone and the respective five metabolites in the larvae were computed by one-way ANOVA. All p-values had statistical significance at all exposure times ($^{***}p < 0.001$).

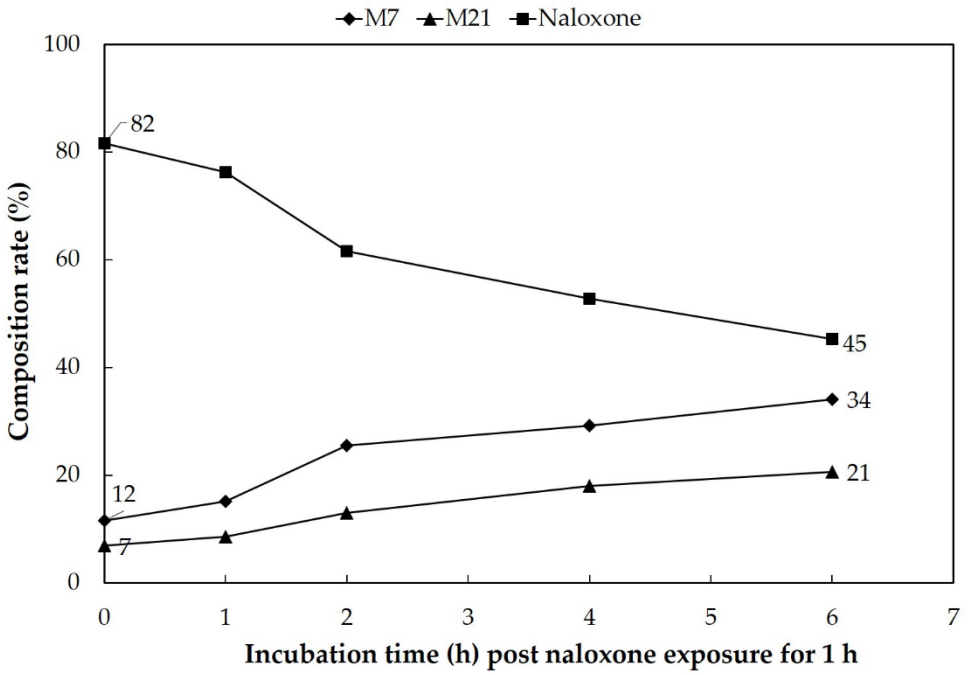

Figure S6. Composition rate changes of the relative amounts of naloxone and two major metabolites (M7 and M21) inside ZF larval bodies following incubation in a compound-free medium post 1 h exposure to 300 μM naloxone. Data were calculated on the basis of mean values given in Figure 4 of the main text ($n = 3$). All p-values between naloxone and these two metabolites were computed by one-way ANOVA and were statistically significant at all incubation times after 1 h naloxone exposure ($^{***}p < 0.001$).

4.8 Supporting Information

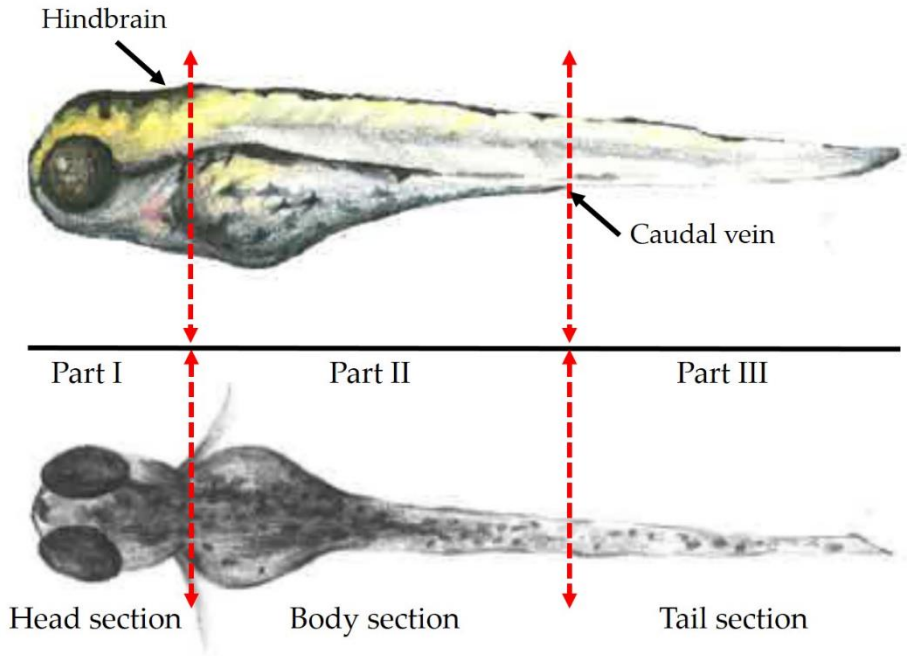

Figure S7. Prepared sections of ZF larvae at 5 days post-fertilization (dpf) in lateral (upper panel) and dorsal (lower panel) view. The head section includes hindbrain, eyes, and heart. Yolk sac and other intestinal organs (e.g., liver, pancreas, and kidney) are part of the body section. The tail part does not contain any major organ compartment.

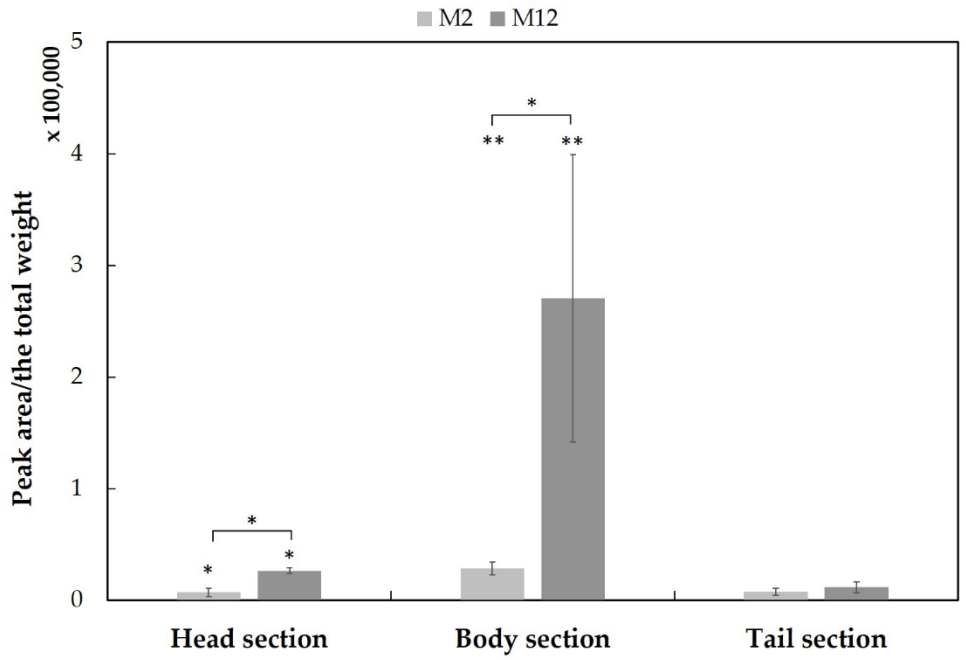

Figure S8. Sectional distributions of two minor metabolites (M2 and M12). The peak area of the substrate detected in the chromatogram was normalized individually with the total weight of each section, and the clustered columns are displayed as mean ± standard deviation (n = 3), and the p-values between naloxone and its two metabolites were calculated by one-way ANOVA ($^{*}p$<0.05, $^{**}p$<0.01). The p-values in the tail section could not be determined due to low intensity of M2 and M12.

4.8 Supporting Information

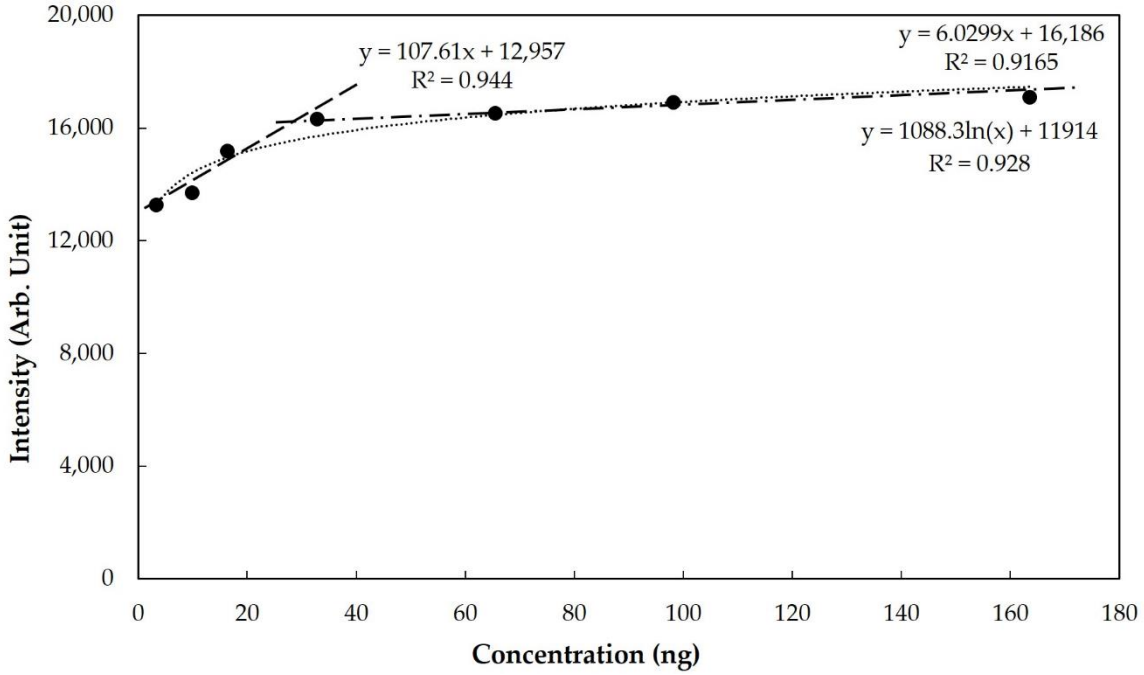

Figure S9. Calibration curves for naloxone (potassium adduct ion, *m/z* 366.1102) spiked into ZF larvae homogenates at 3, 10, 16, 33, 65, 98, and 164 ng per 1 µL homogenate (n = 7). The obtained data were either analyzed by logarithmic regression (full concentration range; round dotted line; n=7) or by linear regression of different concentration ranges (3-33 ng, long dashed line and 33-164 ng, long dash-dot line; n = 4). The resulting calibration curves all showed a high degree of R-squared ($R^2 \geq 0.92$).

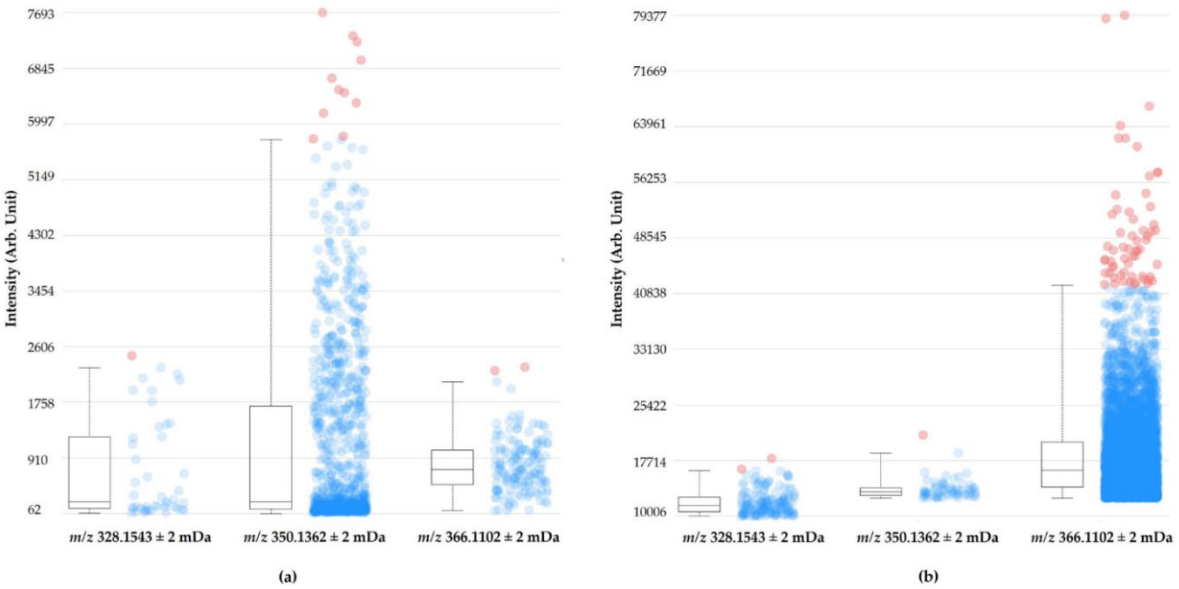

Figure S10. Comparison of the intensity of three naloxone adduct ions [proton (*m*/*z* 328.1549), sodium (*m*/*z* 350.1362), and potassium adduct ion (*m*/*z* 366.1102)] in the MS images of drug-treated ZF larvae whole body sections visualized with a 3-dimensional view function in SCiLS Lab version Premium 3D software. ZF larvae samples were prepared according to (a) the protocol used in the previous studies [26] and (b) the optimized protocol developed as part of this study. In detail, the following conditions were used: (a) 40% gelatin embedding medium, 15 mg mL^{-1} DHB containing 0.1% TFA, 14 passes of matrix spraying, composed up of 10 slides from one respective larva; (b) 40% gelatin embedding medium, 5 mg mL^{-1} CHCA containing 0.1% TFA, 8 passes of matrix spraying, composed up of 11 slides from one respective larva. The intensity box part is depicted by the lower and upper boundaries representing the second and the third quartile, and the line extending vertically from the boxes indicates lower and upper quantiles whose relative values are set at 99% quantile. The cloud part shows how the intensity of the molecular image distributes in spectra of a sample. Blue dots represent the spectra between the lower and upper quantiles, and red dots represent outliers distributed outside these intensity intervals.

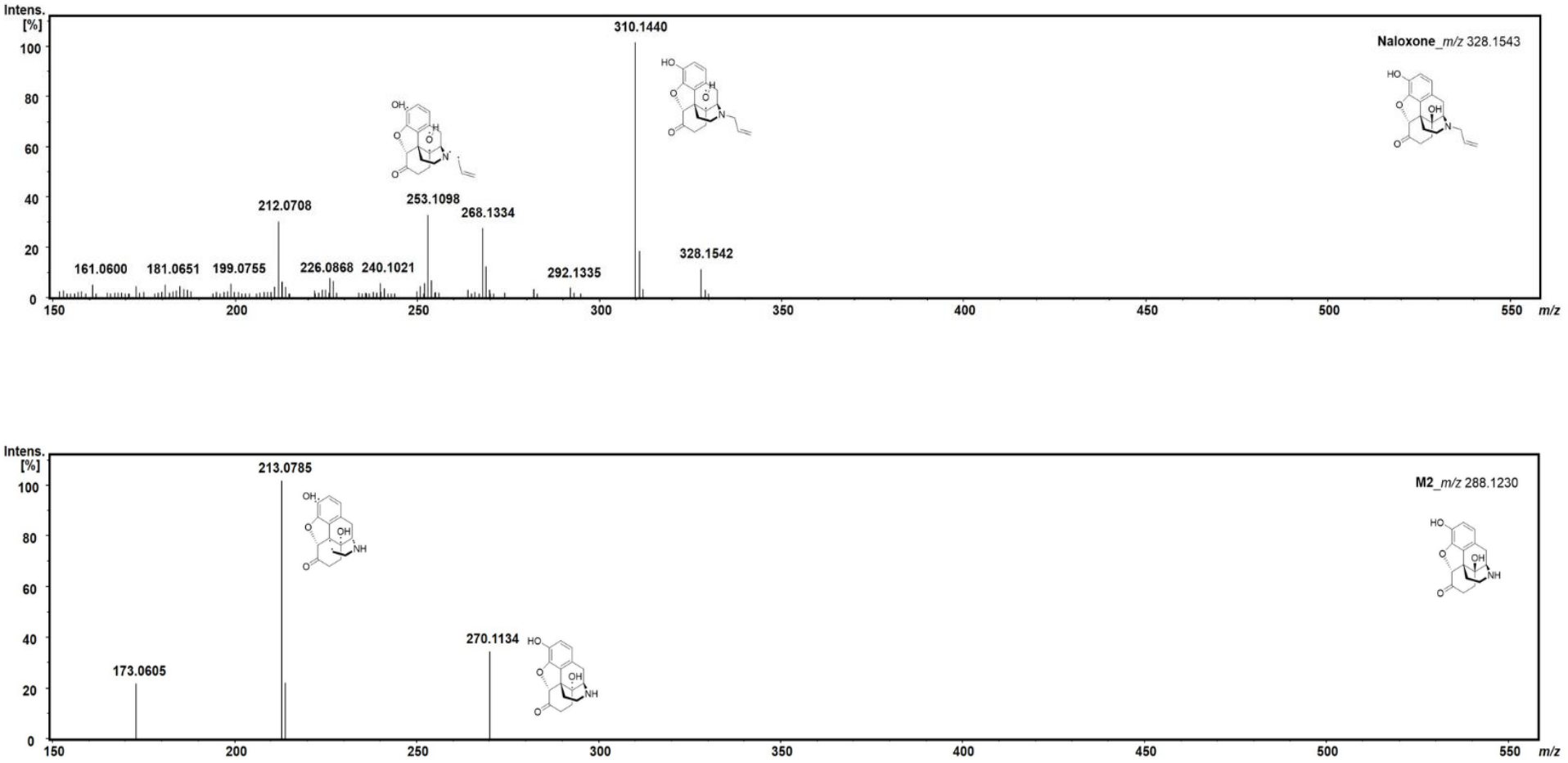

Figure S11. *Continued.*

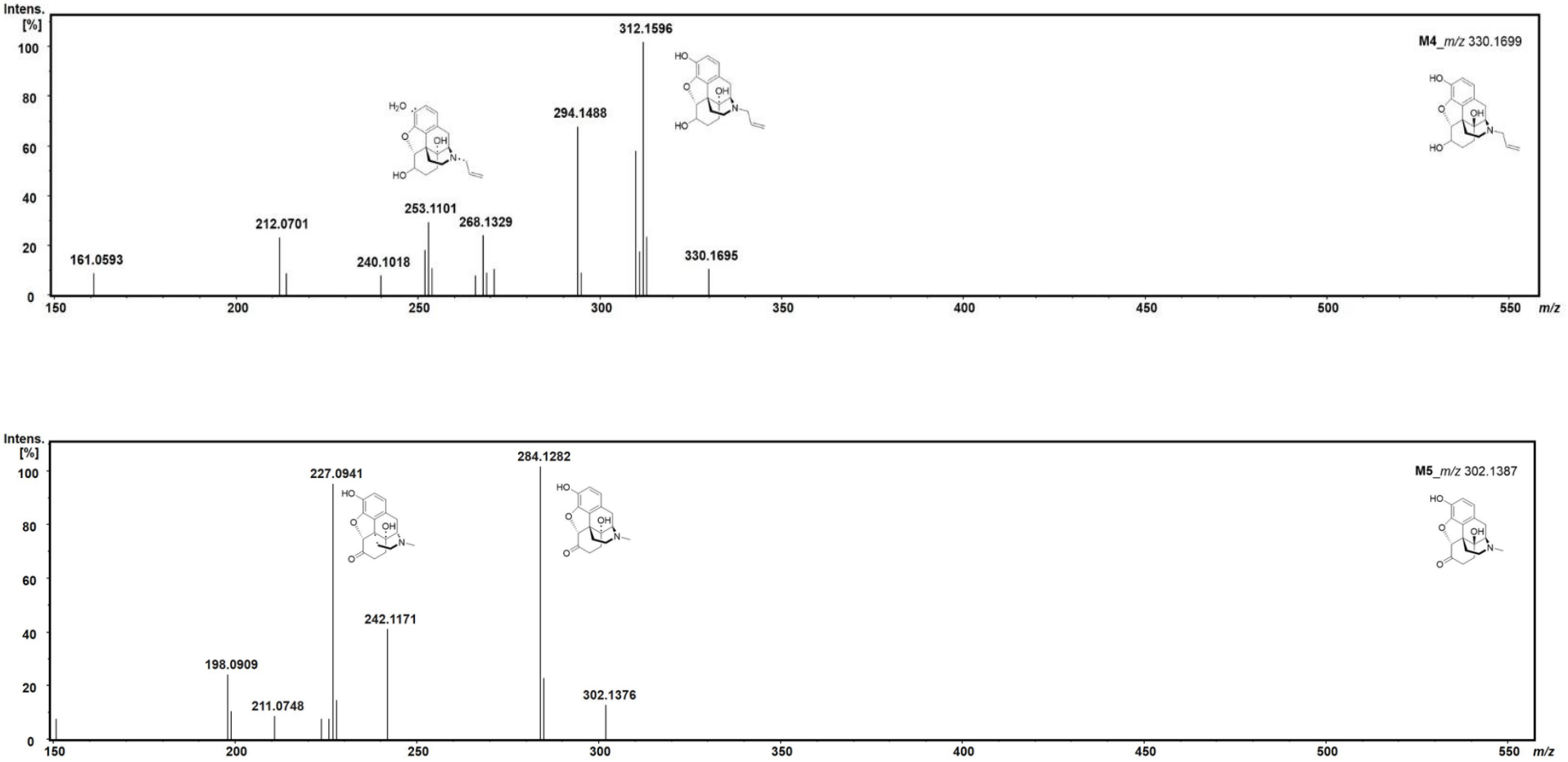

Figure S11. *Continued.*

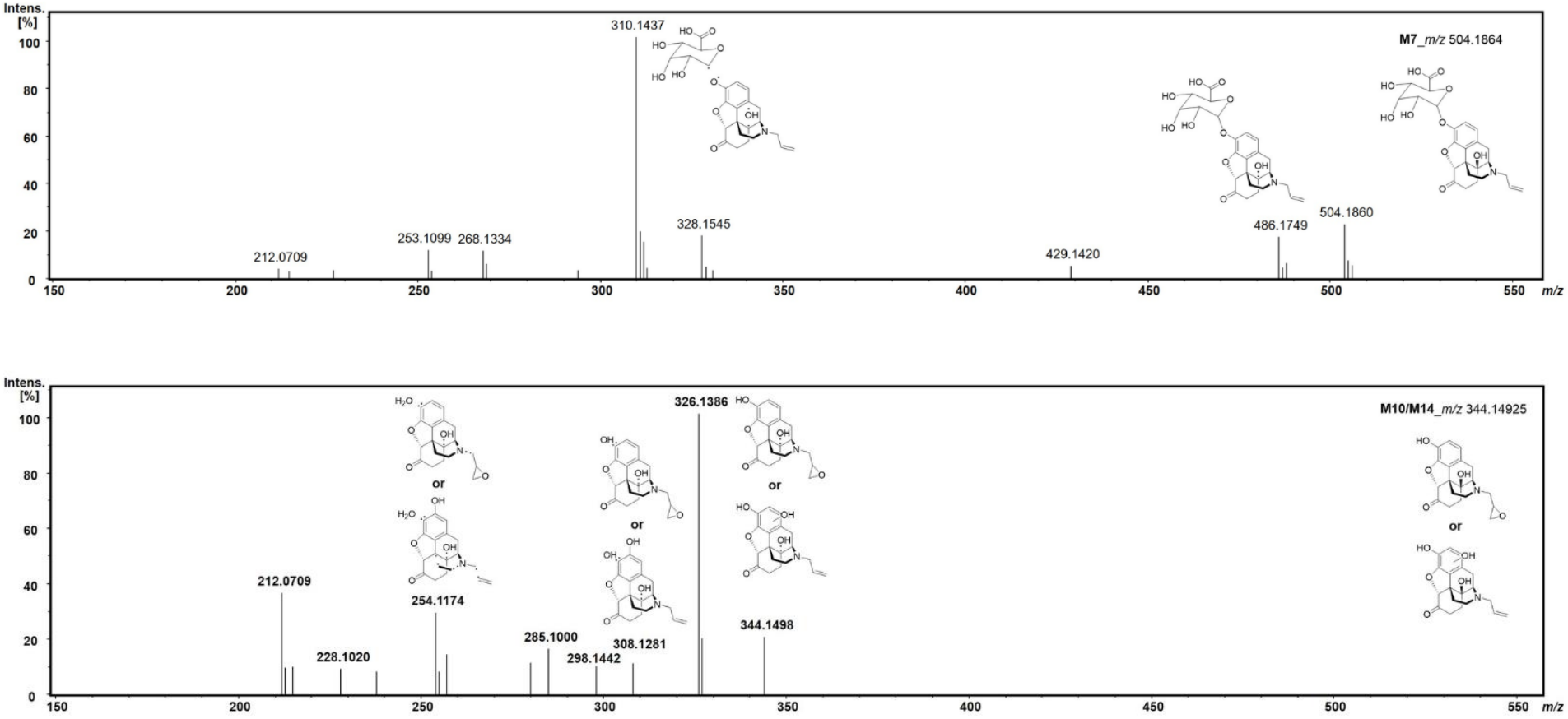

Figure S11. *Continued.*

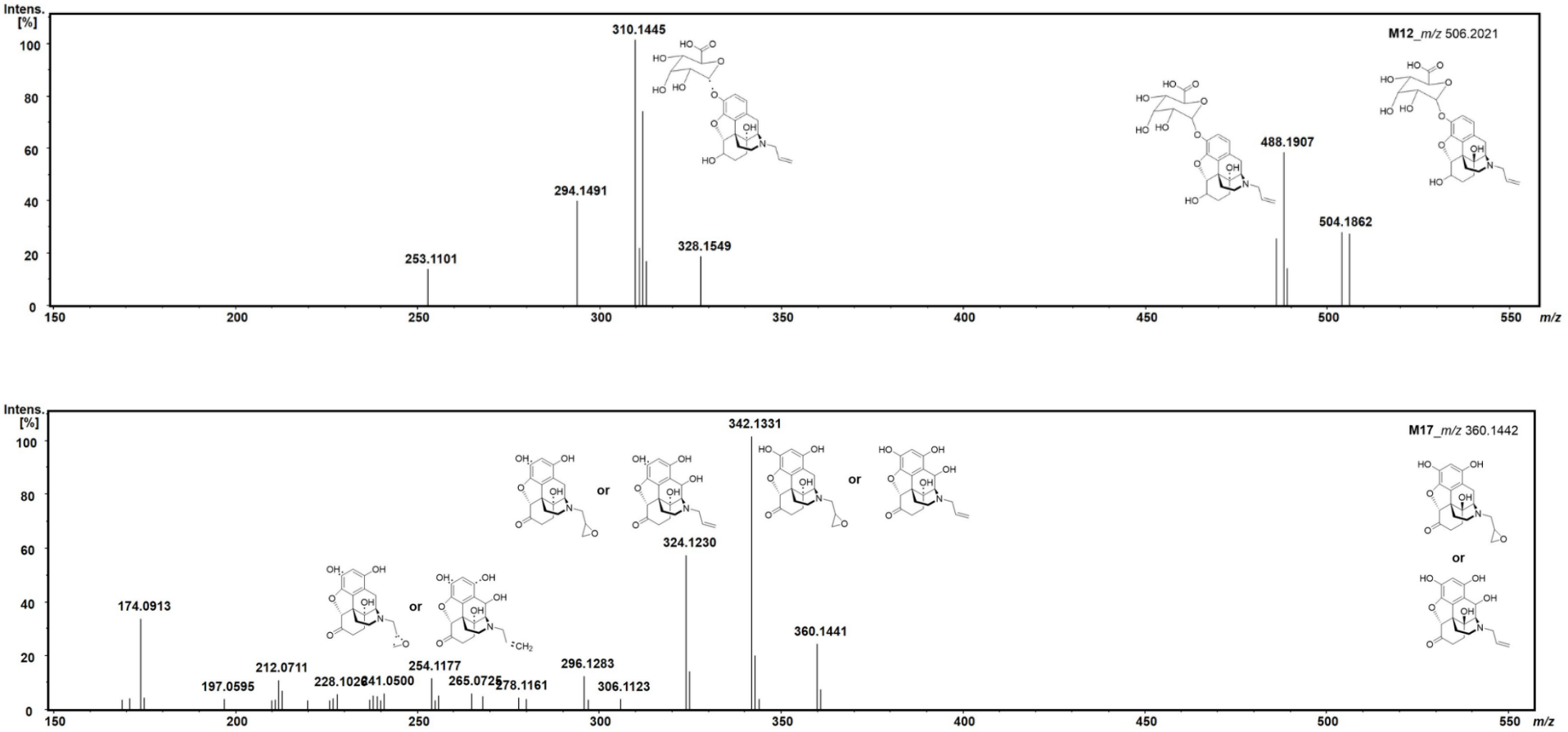

Figure S11. *Continued.*

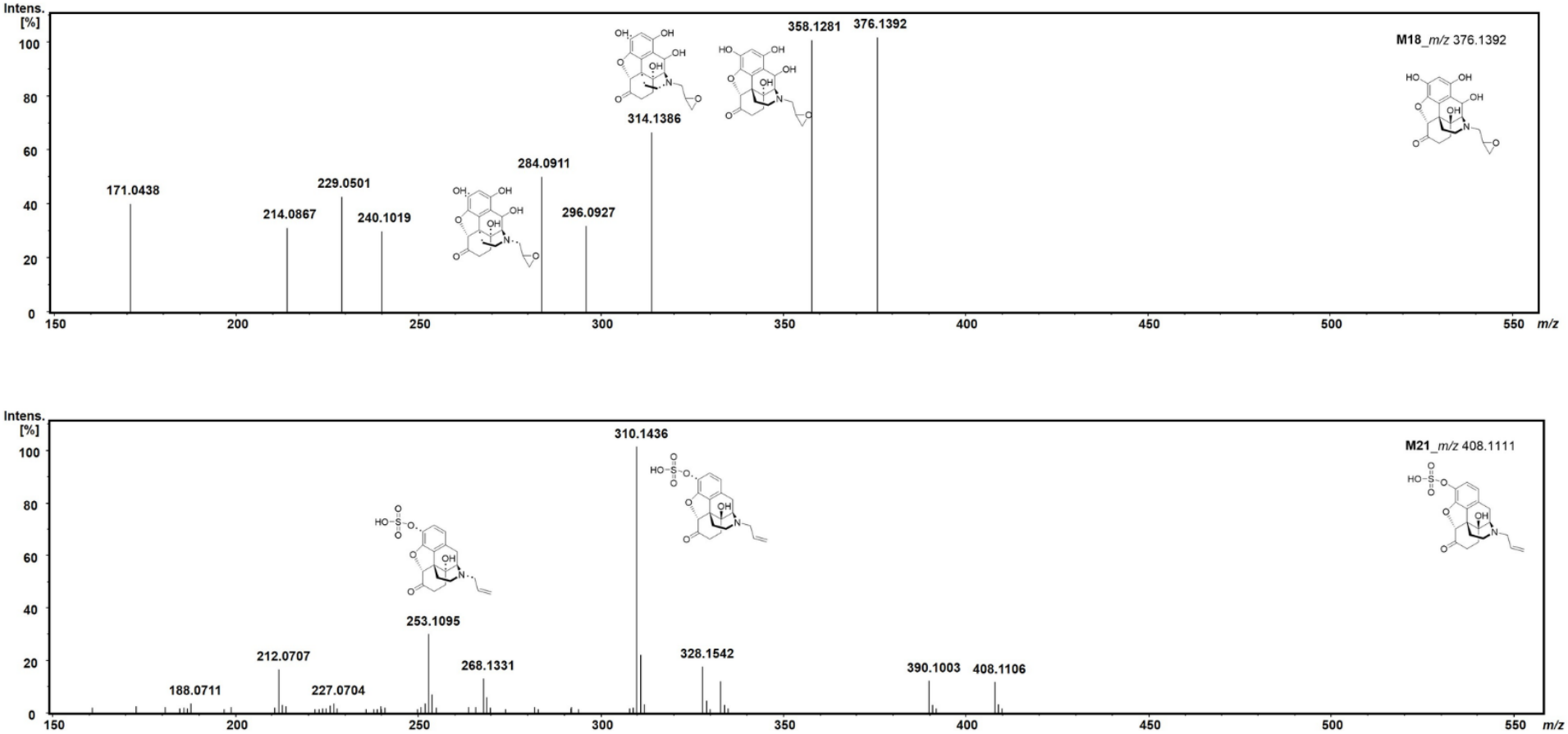

Figure S11. *Continued.*

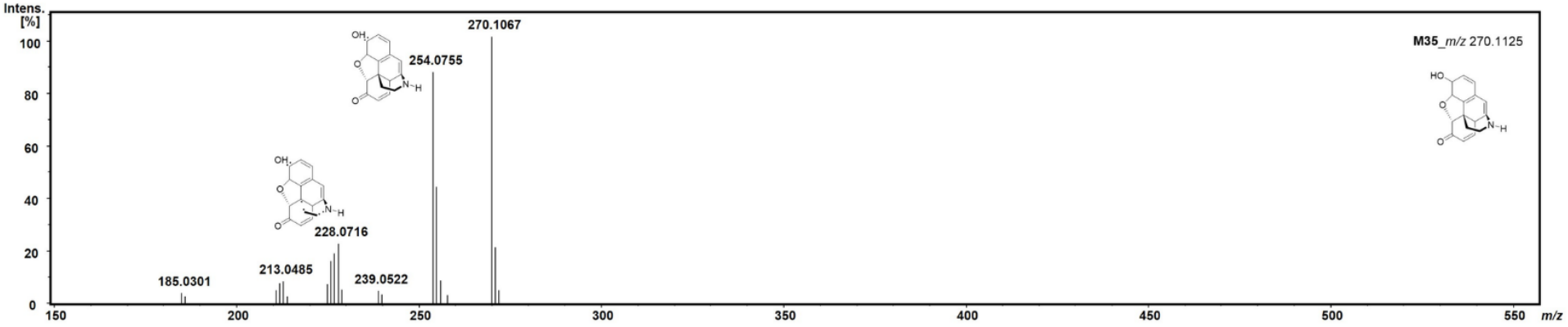

Figure S11. MS^2 spectra of naloxone and its ten metabolites detected in the exposed zebrafish larvae and the residual exposure medium, arranged by the labeling number in this study. The 13 metabolites were found in ZF larvae and residual exposure medium: M2, M4, M7, M12, M21, and M35 in the larvae, and M5, M10/M14, M17, and M18 in the medium. In the case of M10/M14 and M17, their MS^2 fragments were generated with two possible structures due to anticipating several structural isomers. The minor three metabolites (M8, M23, and M26) are not displayed here because their MS^2 spectra were not unavailable due to the low intensity of peaks.

4.8 Supporting Information

Table S1. Detailed information on naloxone and its metabolites identified from human biosamples and animal models (published data) and data of additional metabolite candidates from zebrafish larvae and HepaRG cells (this study).

Compounds	Metabolic reaction	Calculated exact masses (*m*/*z*)	Human [41–43,45–51]]		Rat [39,45,48,52,53]	Rabbit, Chicken [45]	Dog [48,54]	Data from this study		
								HepaRG *in vitro* models [100 µM, 300 µM]	Zebrafish larvae [300 µM]	
			Plasma	Urine	Plasma, urine, feces	Urine	Urine		Larvae	Medium
Naloxone	Unchanged form	328.1543	+	+	+	+	+	+	+	+
M1	*N*-hydroxylation	345.1571								
M2	*N*-dealkylation (nornaloxone)	288.1230	+	+	+			+	+	+
M3	*N*-dealkylation + hydroxylation	304.1179								
M4	*N*-allyl-7,8-dihydro-14-hydroxynormorphine (naloxol)	330.1700	+	+	+	+	+	+	+[c]	
M5	*N*-CH_3 (*N*-dealkylation; oxymorphone)	302.1387								+[b]
M6	*N*-CH_2CH_3 (*N*-dealkylation)	316.1543								
M7	Glucuronidation	504.1864	+	+	+	+	+		+	+
M8	*N*-oxide + glucuronidation	520.1813							+[c]	
M9	Glucuronidation of M2	464.1551			+					
M10	*N*-oxidation	344.1492								+[a,b]
M11	Glucuronidation of M3	480.1500								
M12	Glucuronidation of M4	506.2021			+	+[d]			+[c]	
M13	2*glucuronidation of M4	682.2342								
M14	Epoxidation Hydroxylation in the benzene ring	344.1492								+[a,b]
M15	Epoxidation in alkene group of M4	346.1649								
M16	Epoxidation + methylation of M5	359.1727								
M17	Dihydroxylation Hydroxylation + epoxidation *N*-oxide + epoxidation	360.1442						+[e]		+[b]
M18	Dihydroxylation + epoxidation	376.1391								+[b]
M19	Glucuronidation of M14	536.1763								
M20	2*glucuronidation	680.2185								
M21	Sulfation	408.111			+			+	+	+
M22	2*sulfation	488.0680								
M23	Methoxylation in benzene ring	358.1649							+[c]	
M24	Glucuronidation of M23	534.1970								
M25	Hydroxylation in alkene group	332.1492								
M26	Carboxylation in alkene group	346.1285								+[b]

M27	Naloxegol	652.3691									
M28	Addition of *S*-methyl	374.1421									
M29	Glutathione conjugate	633.2225									
M30	Cysteine conjugate	447.1584									
M31	Di-hydrogenation with the cleavage of carbon-oxygen bond in cyclopentane moiety	332.1856									
M32	Di-hydrogenation of M7with the cleavage of carbon-oxygen bond in cyclopentane moiety Glucuronidation of M31	508.2177									
M33	Glucuronidation of M32	684.2498									
M34	2 hydroxylation in benzene ring and alkene part	348.1442									
M35	Rearrangement after elimination of hydroxyl group of M2	270.1125			+				+[c]		
M36	*N*-CH_2CH_3 of M4	318.1700									
M37	Glucuronidation of M1	521.1892									
	Total number of detected metabolites		3	3	7	3	2	4	8	8	

All data from human samples and animal models were taken from published studies; Human plasma data were quoted from [47,49–51] and urine data from [41–43,45–48]. Rat plasma data were cited from [39,48,53] and urine and feces data from [47,48,52]. [a] The structural isomers M10 and M14 co-eluted in the LC-HRMS/MS setup used in this study, and accordingly, isomers were counted and quantified as one metabolite although they derive from different metabolic reactions (see Supplementary Figure S2); [b] the metabolites were only detected in the surrounding exposure medium and not from extracted ZF larvae; [c] the metabolites were detected only in extracted ZF larvae and not in the surrounding exposure medium; [d] the metabolite was not detected in rabbit; [e] the metabolite was only detected at the higher exposure concentration of 300 µM naloxone. +: Peak detected.

Table S2. Mass list of 4F-MDMB-BINACA and its phase I and phase II metabolites used for LC-HRMS/MS and MALDI-FT-ICR measurements.

Compounds	Metabolite ID	$[M+H]^+$ ion for LC-HRMS/MS [27]	$[M+Na]^+$ ion for MALDI-FT-ICR
Parent compound	4F-MDMB-BINACA	364.2031	386.1850
Phase I metabolites	M1	237.1034	259.0853
	M2	274.1186	296.1006
	M3	276.1343	298.1162
	M4	290.1499	312.1319
	M5	346.1761	368.1581
	M6	348.1718	370.1537
	M7	348.1918	370.1737
	M8	350.1874	372.1694
	M9	360.1554	383.1452
	M10	362.1710	384.1530
	M11	362.2074	384.1894
	M12	364.1667	386.1487
	M13	366.1824	388.1643
	M14	366.1824	388.1643
	M15	376.1867	398.1686
	M16	380.1980	402.1800
	M17	380.1980	402.1800
	M18	380.1980	402.1800
	M19	380.1980	402.1800
Phase II metabolites	M20	460.1548	482.1368
	M21	524.2239	546.2058
	M22	526.2196	548.2015
	M23	542.2144	564.1964
	M24	552.2188	574.2007
	M25	556.2301	578.2120
	M26	556.2301	578.2120

Table S2. Mass list of 4F-MDMB-BINACA and its phase I and phase II metabolites used for LC-HRMS/MS and MALDI-FT-ICR measurements.

Compounds	Metabolite ID	$[M+H]^+$ ion for LC-HRMS/MS [27]	$[M+Na]^+$ ion for MALDI-FT-ICR
Parent compound	4F-MDMB-BINACA	364.2031	386.1850
Phase I metabolites	M1	237.1034	259.0853
	M2	274.1186	296.1006
	M3	276.1343	298.1162
	M4	290.1499	312.1319
	M5	346.1761	368.1581
	M6	348.1718	370.1537
	M7	348.1918	370.1737
	M8	350.1874	372.1694
	M9	360.1554	383.1452
	M10	362.1710	384.1530
	M11	362.2074	384.1894
	M12	364.1667	386.1487
	M13	366.1824	388.1643
	M14	366.1824	388.1643
	M15	376.1867	398.1686
	M16	380.1980	402.1800
	M17	380.1980	402.1800
	M18	380.1980	402.1800
	M19	380.1980	402.1800
Phase II metabolites	M20	460.1548	482.1368
	M21	524.2239	546.2058
	M22	526.2196	548.2015
	M23	542.2144	564.1964
	M24	552.2188	574.2007
	M25	556.2301	578.2120
	M26	556.2301	578.2120

Chapter 5.

Discussion

5.1 Summary

The zebrafish (*Danio rerio*) larvae model is as a powerful *in vivo* model for drug discovery and development, pharmacological studies, and for studying human diseases. A survey performed by Zhang *et al*. in 2020 demonstrated that the model was applied in 114 published studies between 2000 and 2017 covering eleven major research fields, including twelve publications (10.5%) on zebrafish metabolism as the second most abundant research field after tissue-specific studies (56 publications) [1,2]. In this thesis, the zebrafish larvae model was the primary organism model for studying the metabolism of three different drugs. Moreover, three enabling methodological approaches (mass spectrometry imaging, microinjection, and morpholino oligonucleotide) were optimized for zebrafish larvae, and all procedures are described in detail in three individual chapters. These approaches were crucial to strengthen and further validate the zebrafish larvae model for predicting human drug metabolism. Ultimately, the usefulness of zebrafish larvae for expanding the current set of common ADMET (absorption, distribution, metabolism, excretion, toxicity) assays was successfully demonstrated.

In Chapter 2, 7′*N*-5F-ADB, an emerging synthetic cannabinoid (SC), well-known as a new psychoactive substance, was studied and various administration routes to deliver the drug to zebrafish larvae were evaluated. For example, direct microinjection into a vital organ (yolk sac, caudal vein, heart ventricle, or hindbrain) was compared to conventional waterborne exposure. Remarkably, from 27 metabolites detected in human urine samples, 19 metabolites were present in microinjected larvae, and 15 metabolites were detected using the *in vitro* HepaRG cells model. In addition, seven out of the ten glucuronidated conjugate phase II metabolites that were detected in human urine samples were also observed in the injected larvae. In summary, all of the detected metabolites in the zebrafish larvae represent a high concordance rate of 70% to human urine samples and 90% to HepaRG cells. Overall, it was found that microinjection of the SC into caudal vein, heart ventricle, or hindbrain of zebrafish larvae was most successful in terms of drug absorption and metabolism, whereas microinjection into the yolk sac and aquatic exposure to 7′*N*-5F-ADB resulted in only one and 18 metabolites, respectively. Furthermore, the spatial distributions of 7′*N*-5F-ADB and its metabolites were visualized by mass spectrometry imaging, and significant differences regarding their localization and abundance between aquatic exposure of 7′*N*-5F-ADB and/or microinjections into three different organs were revealed. The spatially resolved MS images helped to figure out that metabolism within 1 h after microinjection is as efficient as compared to waterborne exposure for 24 h in terms of identifying the most common metabolites of 7′*N*-5F-ADB detected in all investigated models.

In Chapter 3, studies on zebrafish drug metabolism were extended based on the findings of 7′*N*-5F-ADB metabolism studied in Chapter 2, using the newly emerged SC 4F-MDMB-BINACA, which was first reported in 2019 by the EU Early Warning System [3,4]. Interestingly, despite the similar physicochemical properties of both SCs, 7′*N*-5F-ADB and

4F-MDMB-BINACA, the number of detected metabolites of 4F-MDMB-BINACA was significantly lower than that of previously studied 7′*N*-5F-ADB. That contrasting result raised the question, whether there is a correlation between the efficacy of metabolism and the function of cannabinoid receptors, which possibly induces abnormal liver development. Thus, the liver sizes of zebrafish larvae treated with the two SCs were determined and compared to the liver sizes in genetically modified zebrafish larvae by gene knockdown of cannabinoid receptors type 1 and type 2 (CB1 and CB2) via antisense morpholino oligonucleotides. In particular, as CB2-deficient larvae showed a pronounced liver size reduction similar to non-CB-deficient larvae treated with 4-MDMB-BINACA, the effect of CB1- and CB2-deficiency on SC metabolism was investigated, and the overall number of detected metabolites of 7′*N*-5F-ADB and 4F-MDMB-BINACA was compared to a control group. The CB2-deficient larvae retained ca. 45% of both SC metabolites compared to ca. 80% for CB1-deficient larvae. Furthermore, given that SCs act as agonists of CB1 and partial agonists of CB2 [5–7] and in light 4F-MDMB-BINACA being a highly potent CB1 agonist as reported by Cannaert *et al*. [6], 4F-MDMB-BINACA might act as a more potent CB2 agonist than 7′*N*-5F-ADB. In turn, the strong activation of CB2 might lead to a similar effect on drug metabolism as CB2 deficiency in the larvae, concurrent with the reduction of liver size and fewer metabolites being generated.

Chapter 4 focuses on exploring the applicability of mass spectrometry imaging (MSI) for studying zebrafish larvae and on optimizing methods that are still considered challenging [8,9]. The opioid antagonist naloxone has been widely used for preventing overdose death due to opioid intake, cases of which have been increasing in recent years [10,11]. First, naloxone and its metabolites were investigated in the zebrafish model and results were compared to human data. Second, these findings were complemented with naloxone uptake and biotransformation kinetics in the larvae. Moreover, in three main body parts sectioned from the entire larval body, the specific localizations of naloxone and its metabolites were characterized using LC-HRMS/MS without additional imaging equipment. Ultimately, after optimization of the MSI method using zebrafish larvae homogenates, the distributional images of the parent compound and its metabolites inside a complete larval body were significantly improved as compared to MS images generated using previously applied protocols. The MS images revealed a detailed view on the localization of naloxone and its metabolites by combining the distributions of naloxone and its metabolites detected separately in different slides onto one entire larva image, thus, providing a 3-dimensional view. The results from MS images were consistent with data from sectioned larvae being analyzed by LC-HRMS/MS. Notably, the overall findings of naloxone metabolism in zebrafish larvae from two different analytical platforms (MALDI-FT-ICR and LC-HRMS/MS) were well aligned.

In summary, this thesis contributes to broadening the scope of zebrafish larvae model application, in particular in the field of drug metabolism studies, using three enabling methodological approaches: Mass spectrometry imaging, microinjection, and gene knock-down

via morpholino oligonucleotides. Using three tool drugs each approach was efficiently optimized in the present work. Taken together, zebrafish larvae are a promising and powerful *in vivo* model that can complement and/or replace conventional ADMET studies.

5.2 Challenges in the Use of Zebrafish Larvae for Drug Metabolism Studies

The zebrafish larvae model is one of the most promising *in vivo* models for drug metabolism studies mainly out of three reasons; it helps to reduce the number of animal studies, reliably predicts human metabolism, and additional data on *e.g.*, toxic events, pharmacokinetics (PK), and the pharmacology of drugs can be recorded simultaneously in the same model. Currently, the model is primarily used for profiling of drug candidates at the early phase of drug discovery and development and for deepening the knowledge on effects caused by substances to which humans are exposed. In the current work, three enabling methodologies for successfully applying the zebrafish larvae model were further refined and improved with a focus on optimizing the outcome of drug metabolism studies. Various routes of drug administration to zebrafish larvae, *i.e.* conventional waterborne exposure and microinjection into different organs, were studied and it was found that this step is crucial to ensure efficient *in vivo* distribution and in turn, efficient drug metabolism [12]. In fact, the majority of reported studies where zebrafish larvae were used as screening tool rely on adding test substances directly to the water, thereby neglecting potential issues with compound uptake and in turn, presumably producing a high rate of false-negatives [13]. Notably, we found fast circulation of drugs and a high number of drug metabolites in microinjected larvae, which surpassed or equaled results from different models (rodents, HepaRG cells, and humans). Despite the high success of the metabolism studies presented here, other factors beyond drug absorption and pharmacokinetics were found to impact drug metabolism in the model. As exemplified for the SC 4F-MDMB-BINACA [14], compounds can induce *e.g.* non-lethal toxic effects, which in turn, can influence their pharmaceutical effects and metabolism. In cases where such complex pharmacological events resemble those observed in humans this can be seen as beneficial. However, the complex *in vivo* events need to be assessed carefully on a case-by-case basis and lack of human data can hamper a differentiated evaluation of findings from the zebrafish larvae model. Nevertheless, various tools are available for genetic manipulation of zebrafish larvae such as gene knock-downs which, in turn, facilitates detailed studies on the *in vivo* pharmacology of compounds *e.g.* in the context of target validation and studying downstream effects [13,15,16]. In addition, analytical methods such as MSI can further help to understand what happens to a compound inside zebrafish larvae thereby covering in particular drug metabolism and distribution as part of ADME [12,14].

The following first part of this chapter summarizes the main obstacles observed during drug metabolism studies in zebrafish larvae along with an outlook on how such studies can be further improved on a technological level. New technical and methodological trends for drug metabolism studies are discussed and advancements and prospects for the use of MSI are detailed.

5.2.1 Obstacles and Prospects of Studies with Zebrafish Larvae from a Methodological Point of View

As early as in the mid-nineteenth century, scientific interest in drug metabolism arose, and this was further fueled by the discovery of the function of hepatic drug-metabolizing oxido-reductases, characterized as a cytochrome in the 1960s [17]. Interestingly, the first human study of drug metabolism occurred in 1841 while isolating the hippuric acid from the urine after benzoic acid ingestion. Since then, the number of drug metabolism studies steadily increased, and the Global 'Drug Discovery Market' Survey report 2022 anticipates an 8% growth rate in the market from 2019 to 2027 [18,19], and the global ADMET testing market is predicted to increase by 5-fold from 2020 to 2027 [20].

Studies of drug metabolism are mostly conducted during the drug discovery and development process for a basic understanding of a drug and precisely predicting its effects in humans (*e.g.*, the time course of drugs in the human body, the structuring of dosage regimens, and the pharmacology and toxicology of a drug and its metabolites) [17,21]. Moreover, drug metabolism studies are also required for controlling and monitoring emerging illegal drugs of concern in forensic and clinical toxicology research fields [21–23], and they are also applied for studying *e.g.* environmental toxins [13,24–26].

As part of this thesis, the zebrafish larvae model for *in vivo* drug metabolism was applied and further refined using three tool compounds (two synthetic cannabinoids and an opioid antagonist) with the overall goal to improve data quality and develop methodologies that are widely applicable for various types of compounds being studied in the model. One major obstacle is the administration of compounds to the zebrafish larvae. Although the model offers the possibility of fast and easy drug administration through adding compounds directly to the larvae-surrounding water, uptake into the organism is often not achieved although this has not yet been studied in detail. However, studying SC metabolism in the zebrafish model it became obvious that microinjection – and coupling of biological assessment with state-of-the-art analytical techniques – is crucial for the one or other compound to successfully administer it to the larvae. Encouragingly, when using the optimal route of administration of a certain compound zebrafish larvae produce a large number of phase I and phase II metabolites depicting an authentic spectrum of human metabolites. In general, it is advisable to explore various types of administration into zebrafish larvae prior to studying new compounds in the model, and the routes tested here (caudal vein, hindbrain, heart ventricle, yolk sac) could be even expanded to also testing microinjection into *e.g.* otic vesicle, muscle, or mouth [12,14]. However, it has to be acknowledged that only microinjection into the yolk sac of early stage zebrafish embryos and larvae can be automated with currently available technology [27–29]. In turn, performing a concise study of compound administration prior to the actual experiment requires access to analytical equipment, which is often not available in academic biology laboratories, and bears some other difficulties such as longer preparation time (not feasible for higher throughput screening), partly challenging

time management , and the need for adequate injection skills. The latter includes glass needle preparation and its volumetric calibration, an anaesthetizing step of larvae with *e.g.* tricaine, and alignment of zebrafish larvae on an agarose plate. In particular, the microinjection into small and vulnerable compartments such as the caudal vein requires extended training and expert knowledge. Such experiments should be carefully conducted as an unskilled injection can easily damage these compartments. Besides, we observed that due to the relatively long time needed for the microinjection into sensitive organs the skin of zebrafish larvae tends to dry out causing adhesion to the plate. Many injected larvae were, in turn, not available anymore after injections. In contrast, injection into the yolk sac of zebrafish embryo at 0 dpf as done with morpholino oligonucleotides (MOs; see Chapter 3) is straightforward and it is also amenable for automation [28,30],

Although these challenges could be overcome by a thoughtful protocol, as we developed throughout the studies of Chapter 2 and 3, the exact amount of injected compound is unclear, while drug delivery through injection of defined amounts is obviously much more reliable than waterborne exposure. Despite the fact the needle used for microinjection can be precisely calibrated some loss of injection solution while pulling out the needle from the zebrafish larvae can be barely avoided. Cocchiaro *et al*. introduced a method for microgavage of zebrafish larvae for oral delivery of compounds directly in the gut [31]. In theory, this method overcomes (or at least improves) loss of compound during injection due to deeper injection and less tissue disruption. Nevertheless, it is only applicable for compounds for which it is expected that they are efficiently resorbed from the gastrointestinal tract of zebrafish larvae. In contrast to studies involving compound addition and observations within live larvae, advanced methods for delivering various types of compounds and reagents are available which are, however, not applicable for drug metabolism studies. As an example, He *et al.* developed a protocol for *in situ* hybridization and antibody staining in zebrafish larvae (3 dpf to 4 dpf) to detect the localization of mRNAs and proteins [32]. They developed Triton X-100 treatment and skin removal (easily removed by fine tweezers) to permeate tissues and preserve antigen epitopes instead of proteinase K digestion used in general. They could overcome the lacking of available antibodies in zebrafish larvae with enough detection of multiple mRNAs and proteins with high sensitivity. However, all investigated techniques to deliver exact amounts of compounds into zebrafish larvae are generally quite time-consuming, need expert knowledge, and they potentially lead to inconsistency in data from different laboratories. Even the simple method of waterborne exposure, already considering that unknown amounts of compound are absorbed by the larvae, can be complicated by insufficient aqueous solubility of test items. In conclusion, it would be desirable to significantly extend compound delivery studies in zebrafish larvae. Ideally, having studied a large variety of compounds and drug classes with different physico-chemical properties, this would allow *in silico* predictions of suitable administration routes for newly studied compounds.

Despite the partly challenging aspect of precise drug administration to zebrafish larvae, which is not as much of an issue in larger animals, the model offers various unique advantages one of which is the availability of various tools for genetic manipulations. Here, morpholino oligonucleotides were applied in our study with 4F-MDMB-BINACA (Chapter 2) in order to explore the impact of cannabinoid receptor function on drug metabolism. The knock-down of CB1 and CB2 in zebrafish larvae through this methodology was easily achieved and contributed to a detailed understanding of the SCs metabolism. In general, zebrafish larvae models using MOs significantly contributed to understanding gene functions [15]. Overall, this genetic technique is convenient but it was reported that MOs often causes side effects (i.e., relatively high mortalities even for control groups) [30,33].

Indeed, as described in Chapter 2, the random MO control 25-*N* induced some rare toxic effects in zebrafish larvae at time points 24 h to 48 h post injection, even though this standard control MO has been used reliably as a negative control. Alternatively, in our study of Chapter 2, the control 25-*N* MO was replaced by mock injection with distilled water, which was more relevant compared to the random MO control. This phenomenon might be explained by off-target effects of MOs, giving strong and deleterious phenotypes unrelated to the targeted specific gene [34,35]. However, exact mechanisms are yet unknown, and we speculated that the observed toxic effect is instead a technical failure than anything related to biological issues. In fact, very few studies [14,36] investigated drug metabolism in genetically modified zebrafish larvae despite its relevance, in particular when the studied drug is suspected to have an impact *e.g.* on liver function as the major metabolizing organ. Such integrated studies can indeed become quite complex and time-consuming but the gain in knowledge of *in vivo* biological processes is clearly beneficial.

Throughout the studies with 4F-MDMB-BINACA, we could demonstrate that, especially in drug metabolism studies, transgenic zebrafish larvae offer the unique possibility to study *e.g.* compound-induced liver pathophysiology in real-time in the living organism. In case of adverse effects (as seen with 4F-MDMB-BINACA), further genetic modifications can be easily introduced to concisely study pharmacological effects in a systematic approach. Besides MOs, various other tools are available (CRISPR-Cas9, TALENs, TILLINGs, and CRISPR).

5.2.2 New Techniques and Methods for Drug Metabolism Studies

In order to improve drug metabolism studies in general and in the in zebrafish larvae model, novel techniques should be continuously explored. Recently, ambitious and underexplored methods, such as artificial intelligence (AI) computers and 3D-printed organs are being applied in drug discovery and development [37]. The GlobalData media survey in 2021 revealed that over 70% of pharmaceutical industry respondents anticipate intelligent technologies to impact drug development significantly [37]. In practice, AI models are applied in various fields and significant progress has been made *e.g.* in prediction of drug-protein interactions and efficacy, defining safety biomarkers, and the prediction of drug metabolites [38,39]. The vice president of the US supercomputer company NVIDIA predicted

that AI simulation could support model target and drug interactions *in silico*. Also, the breakthroughs of AI deep-learning programs, such as AlphaFold and RoseTTAFold, can generate a thousand-fold expression of known protein structures and increase the chances for drug discovery by a million times [37].

As a most prominent example, Zhavoronkov *et al*. published a proof-of-concept study for hit discovery using AI technology in 2019 [40]. This study successfully used a deep learning model, generative tensorial reinforcement learning (GENTRL), for *de novo* small-molecule design, and the authors discovered four potent inhibitors of discoidin domain receptor 1 (DDR1) after optimization of GENTRL algorithms (Figure 1)[40]. Moreover, a trend towards AI-driven decision making in pharmaceutical industry is anticipated as a competitive tool for faster and cheaper development of new drugs [41]. However, even though data from actual measurements are essential for validation and training of AI to improve clinically relevant decision-making, they are still lacking, particularly from drug efficacy and safety *in vivo* models [38,39,42]. In summary, vast experimental data of drug candidates from *in vitro* and *in vivo* models for drug discovery and development are still required, and the applicability of AI for predicting such data still needs to be demonstrated on a larger scale. Notably, advancements in assay technology also apply to the zebrafish larvae model generating comprehensive datasets, which can largely increase knowledge on investigational new drugs in an *in vivo* setting thereby reducing the number of animal models in the discovery stage.

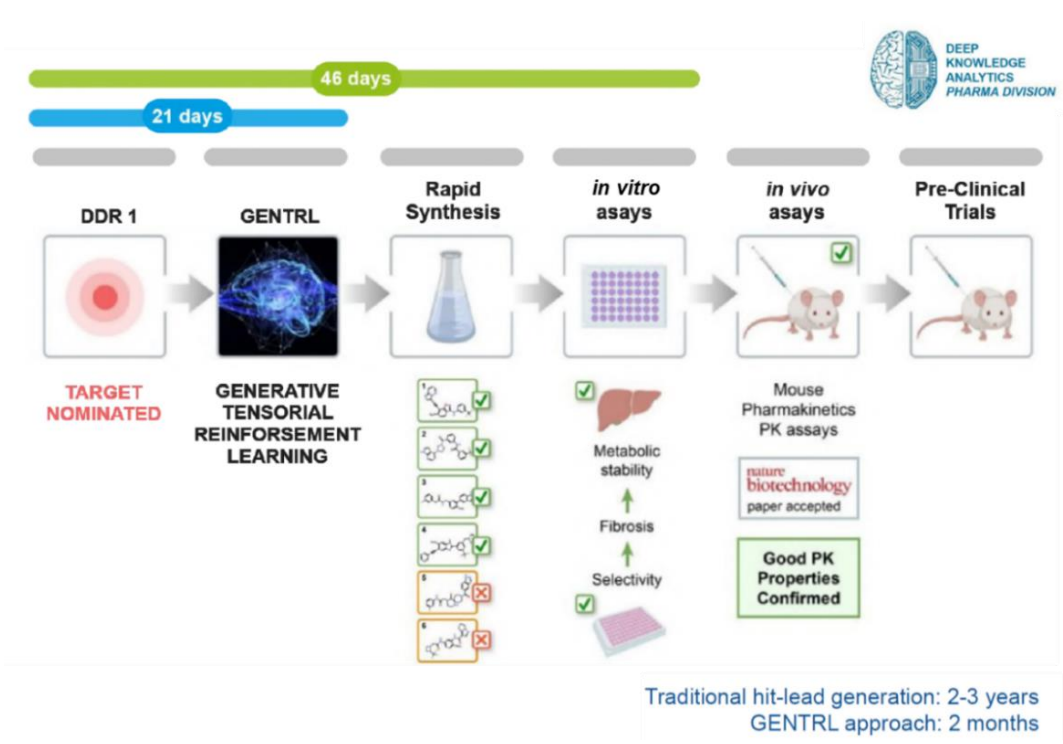

Figure 1. Flow chart of one success story using artificial intelligence (AI) for identifying potent discoidin domain receptor 1 (DDR1) kinase inhibitors in 2019 [40].

In reviews related to the 2022 forecast of drug discovery and development, it was common that the COVID-19 pandemic significantly altered the clinical trials landscape and emphasized the importance and necessity for better prediction of success in clinical trials [37,43,44]. Notably, failure of drug candidates in clinical trials is most often caused by unexpected toxicity and/or insufficient pharmacokinetic (PK) properties in humans [45,46]. One important aspect when optimizing human PK is a detailed understanding of possible metabolic reactions in humans, which, in turn, necessitates a concise evaluation of drug candidates at the pre-clinical stage in order to remove liabilities such as insufficient *in vivo* half-time at an early stage. Besides the importance of DMPK studies in the drug development process they also play a major role in clinical toxicology and forensics [21,47,48]. The European Monitoring Centre for Drugs and Drug Addiction (EMCDDA) published the "European Drug Report 2021: Trends and Developments", which reported ca. 5,769 overdose deaths driven by illicit drugs in the EU, Norway, and Turkey in 2019. The mortality by age (15-64 years) in the EU from 2012 to 2019 is shown in Figure 2. Numbers have been relatively stable in most countries but the reported increase in the age group 15-19 is worrisome [49]. Thus, the improvement of monitoring systems for illicit drugs is needed for prompt detection in the drug of abuse (DOA) field. Taken together, the demand for drug metabolism studies with the ultimate aim to protect public health and well-being of humans is anticipated to increase significantly in the next years [21,49]. This is another reason why alternative and highly predictive DMPK models such as zebrafish larvae are needed to complement the battery of already applied ADEMT assays .

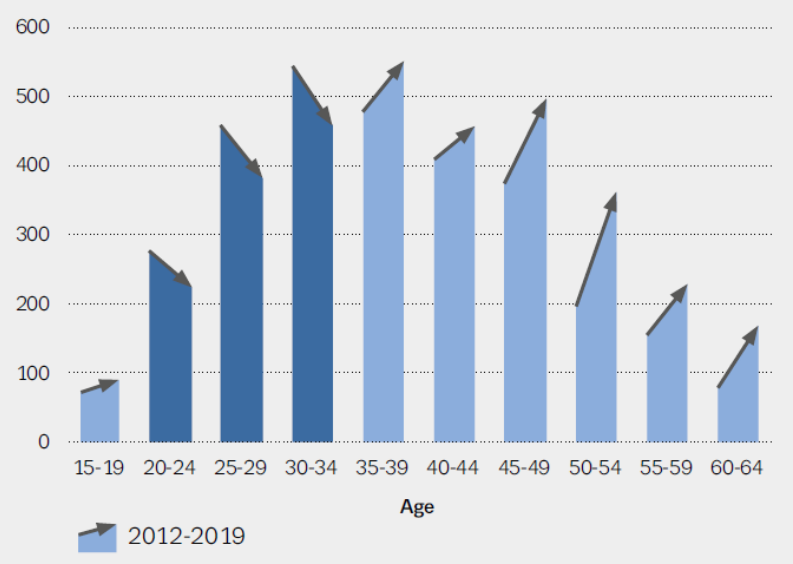

Figure 2. Analysis of drug-induced deaths among different age groups in 2012-2019 [49].

One of the ambitious methods mentioned above, 3D printing technology, has advanced with various printable and biocompatible materials [50,51]. In particular, 3D bioprinting of tissue models using biomaterials such as cells and biomolecules has improved the existing drug screening platform and drug delivery system by depositing biomaterials containing

patient-derived cells and generating the natural environment of the human body [51,52]. A state-of-art *in vitro* tissue model construction based on 3D bioprinting (e.g., heart, liver, and muscle) has been broadened, and Serra *et al.* demonstrated that 3D-based liver systems were physiologically relevant to human hepatic-specific function. Interestingly, they were sustainable for more extended periods than the 2D counterparts in paracetamol, diclofenac, and troglitazone toxicities studies [53]. In addition, Souza *et al.* recently developed the rapid and reproducible protocol of 3D cultures of two different zebrafish cell lines for high-throughput toxicity testing [54]. However, a mechanistic understanding of multi-organ systems for drug metabolism is almost entirely lacking because most research using 3D technology focuses on specific organs such as brain [55], heart [56], and liver [57] for human disease studies. Thus, 3D *in vitro* models based on zebrafish embryos and larvae may be a further challenge in expanding drug metabolism applications using zebrafish larvae model.

The development and application of analytical techniques for drug metabolism studies in both fields (drug discovery and illicit drug monitoring) have addressed several challenges and opened up new opportunities to identify unknown molecules or xenobiotics in human biosamples (*e.g.*, a drug and its biomarkers, illicit NPSs, and hazardous substances) [58]. The identification and purification of drug candidates, their structural identification, and DMPK properties in biosamples [*e.g.*, clearance, $T_{1/2}$ (half-time), C_{max} (peak concentration), AUC (area under the curve)] in the drug discovery process can only be accomplished with the support of several analytical instruments. In particular, analytical screening procedures in the monitoring system for DOAs are critical for implementing national regulations and in clinical and forensic toxicology and related fields such as doping control [22].

5.2.3 Analytical Challenges using the Zebrafish Larvae Model for Drug Metabolism

Currently, various advanced platforms, including GC-flame ionization detector (FID)-MS, GC-MS/MS, GCxGC or LCxLC–time-of-flight (TOF) MS, LC-HRMS, ^{1}H NMR, and ^{13}C NMR have been developed to enlarge the detecting coverage for unknown substances [59,60]. In addition, innovation of other powerful analytical platforms [e.g., ion mobility spectrometry (IMS), electrochemical surface enhanced Raman spectroscopy (EC-SERS), and desorption based methods: matrix-assisted laser desorption ionization (MALDI), desorption electrospray ionization (DESI), and direct analysis in real time (DART)] is currently taking place intending to contribute to the detection of the unknown substances [47,59,61]. Therefore, advanced analytical technologies speed up drug discovery and illegal drug screening by precise and accurate measurements in complex biological matrices, such as crude extracts from organisms and different biosamples (e.g., blood, urine, feces, and tissues) from humans or animal models. Nevertheless, the high cost of these analytical instruments can suppress their utilization in various scientific fields, particularly in the academic setting.

Considering studies as part of this thesis, these technical innovations can reinforce the zebrafish larvae model overcoming *e.g.* the low detection of metabolites in extracts due to extremely low body weight of zebrafish larva (ca. 3 mg per pool of 50 larvae).

Moreover, to analyze a compound in biological samples, a clean-up procedure - most likely liquid-liquid or solid-phase extraction (e.g., C_{18} carbon, silica, or florisil column) - is required to remove various interferences from the sample matrix. The more complex the matrix is, the more complicated the clean-up steps will get. However, in the case of zebrafish larvae extraction as presented in this thesis, optimizing this step was not considered as it appeared acceptable in this model to lose data on compounds present in minute amounts only. In addition, the surrounding medium was analyzed to detect as many hydrophilic metabolites (possibly rapid excretion from the larvae) as possible. All our analyses of the larvae extracts without clean-up or concentration steps would have been impossible if advanced analytical instruments (e.g., Q-TOF MS and FT-ICR MS instruments; see Chapter 5.2.3) were not available. However, such additional sample preparation steps would have possibly increased detection limits, and in turn, data depth. In future, clean-up methods for zebrafish larvae extracts, such as using a mixture of solid-phase materials (*e.g.*, C_{15} carbon and silica or silica and florisil) with a smaller volume to fit larvae extract (ca. 50 µL volume) could further improve sample analyses [62].

While analyzing metabolite spectra of three different drugs in zebrafish larvae, the abundances of a drug and its metabolites were determined by relative their peak areas due to the non-availability of reference standards and isotope-labeled internal standards (ISTDs) along with a limited amount of the parent compounds. For a concise evaluation and quantification as part of PK studies such standards will be crucial in the future in order to calculate absolute *in vivo* concentrations.

Within the three independent drug metabolism studies, the zebrafish larvae model reliably predicted metabolic patterns as reported from human studies (and other *in vitro* and *in vivo* models). In particular, while comparing the mutual similarity of metabolism among all investigated models, zebrafish larvae represented the highest concordance to humans. Despite this encouraging result, still some discrepancies in the metabolic profile of each drug to human biosamples (plasma and urine samples) were observed in zebrafish larvae and the HepaRG *in vitro* model. This might be possibly caused by species differences between humans and zebrafish larvae and differences between *in vitro* and *in vivo* models of the same species [63,64]. Besides, it is currently not easy to anticipate due to a lack of datawhether quantitative comparisons between human and zebrafish larvae metabolites will match each other. For the further development of zebrafish larvae as a suitable model to predict human DMPK as the final goal, the issue of quantitativing a drug and its metabolites should be investigated as part of future studies. This would enable the determination of *e.g.* plasma concentration-time curves of a drug in zebrafish larvae and help to explore the potential superiority of the model in early pre-clinical testing and determination of DMPK parameters that closely resemble those found in humans.

When tackling the issue of lacking required standards for quantifying a drug, standard operating procedures using a variety of isotope-labeled compounds could be set up. In turn, , typical quality assurance and quality control (QA/QC) procedures throughout all sample preparation processes could be performed with respect to *e.g* recovery rates (%) from the

zebrafish larvae preparations. With the recovery of ISTDs from larvae extract, the loss of a drug during sample preparation can be calculated indirectly and then the absolute amount of the substrate in the pooled zebrafish larvae can be determined using a direct comparison to STDs. A surrogate standard having similar chemical properties (e.g., acidic, neutral, or base pH and polar or non-polar properties) than the investigated drug could be another possibility to overcome this issue.. In summary, the most crucial analytical challenges in zebrafish larvae as model for human drug metabolism are obtaining high reproducibility of the sample preparation steps and ensuring quantification of a drug through using diverse classes of ISTDs and surrogate standards.

5.2.4 Current Trends, Outputs, and Future Directions of Mass Spectrometry Imaging in Pharmaceutical Research

The creation of molecular images with mass spectrometry imaging (MSI) has opened a new era for pharmacologists to characterize the distribution of a wide range of molecules (proteins, lipids, endogenous metabolites, and drugs) accurately inside tissues and their substructures. Analytes are identified based on the molecular mass and fragmentation pattern without the need of additional labeling steps [8,65]. Among the many available MSI techniques [e.g. secondary ion mass spectrometry (SIMS), desorption electrospray ionization (DESI), matrix-assisted laser desorption/ionization (MALDI), laser ablation electrospray ionization (LAESI)], the use of MALDI-MSI has shown the steepest growth curve in the past years [66]. In addition, fourier-transform ion cyclon resonance mass spectrometry (FT-ICR MS) currently provides the highest mass resolving power (> 100,000), accuracy (< 1 ppm), and offers multistage MS/MS capabilities thereby improving selectivity. These capabilities allow MS images of mass channel features with a bin size as small as $\Delta\ m/z = 0.005$ and structural identification throughout only one measurement [67,68]. As part of this thesis, MSI methods for zebrafish larvae using MALDI-FT-ICR MS were developed (Chapters 2 and 3), which were further refined and optimized successfully (Chapter 4).

Remarkably, MSI is used increasingly in pre-clinical stages and clinical practice, but its usage is still limited since most studies analyzing human samples in proof-of-concept studies proceed only rather slowly due to ethical concerns and practical difficulties [8,65]. In the context of this thesis, theapplication of MSI to zebrafish larvae (or adults) is still challenging due to the critical sample preparation, and especially, the use of tiny larva (ca. 4 mm body length) requires more sophisticated skills and technical equipment in order to generate high-quality sections for imaging, compared to adult fish or other tissues from animal models. However, since the zebrafish larvae model is particularly promising to predict human metabolism and since first trials assessing different administration routes (7'*N*-5F-ADB studies in Chapter 2) were successful, we started investigating MSI in this model to characterize drug distribution and metabolism. In fact, more than eight months were invested for dealing with zebrafish larvae and setting up of the whole MSI process for these samples.

Overall, the scope of MSI has been expanding beyond drug disposition studies into target engagement, drug metabolism, PK/PD, drug delivery, and studies on drug-induced toxic effects on organs[8,65]. Moreover, many efforts in the MSI community aimed at providing quantitative information along with relevant distributional images even though MSI technique has been considered mainly for qualitative assessments providing a semi-quantitative relationship between the amount of substance and detected ion intensity in the measured region rather than absolute concentrations [67,69,70].

Balluf *et al*. mentioned that MALDI-MSI technology was critically assessed twice in 2009 [71] and 2015 [72], which pointed out specific intrinsic challenges regarding ion suppression, sample throughput, homogeneity of matrix application, enzymatic tissue processing, spatial resolution, analyte delocalization, and the availability of validated/standardized protocols [66,73]. Since then, there have been noteworthy progresses in detection speed, spatial resolution, sensitivity, and various developed/upgraded MSI data analysis software tools with multi-dimensional viewing functions (3-D and 4-D visualization) [66,66,74–77]. As demonstrated here (Chapter 4), the 3-D view of zebrafish larva for MSI enabled us to look over the distribution of molecules inside the small-sized zebrafish larva without any loss of detection information, and 4-D visualization is expected to bring even more positive effects in MSI.

One of the invaluable analytical platforms in drug discovery and development is liquid chromatography-mass spectrometry (LC-MS) as it revolutionized analyzing and screening novel drug candidates for supporting DMPK and especially providing data for both qualitative and quantitative analyses [78,79]. In particular, the triple quadrupole MS system (called a low-resolution MS; LRMS) has been the gold standard for many decades for quantifying parent drug, metabolites, or biomarkers.

Moreover, high-resolution MS (HRMS) is also applied providing a wealth of information on isotope distribution, in-source fragmentation, adduct information, background ions, unknown drug metabolites, and new biomarkers in cases where the selectivity and sensitivity of LC-LRMS are insufficient. HRMS has gradually replaced a part of LC-MS systems for PK and other quantitative analyses [80–82]. In view of this, the MSI application faces the challenge of demonstrating its quantitative capability and competitive advantages over LC-HRMS.

In brief, the main four limitations of MSI (*i.e.* ion suppression (as a part of matrix effects), matrix effects, batch effects, and validation of quantification) are still under investigation to reveal the causes and provide solutions for overcoming these hurdles at least partially during sample preparation for MSI. Importantly, these factors impede the reliability and reproducibility of MSI data from inhomogeneous biological samples. In practice and as part of this thesis, some of the issues were addressed sequentially with a focus on improving MSI for sections of drug-treated zebrafish larvae. However, there are still many unsolved questions necessitating additional future optimization steps. Accordingly, such optimization will require a detailed understanding on how these issues manifest in MSI data in order to explore adapted methods and protocols [66,77].

First, ion suppression can be induced by many factors, such as the sample extraction, desorption, and ionization of a chosen molecule of interest [69,83]. In addition, this impact is tissue-specific and found to a greater extent in heterogeneous tissues such as the intestines [75] and, in turn, its effect can vary between the different areas of the investigated biosample. With the degree of ion suppression, the quantitative performance of MSI is disturbed because of lacking the analyte separation procedure in MSI [70], and consequently, this effect alleviates sensitivity loss of a substrate in the ionization step of MSI [84]. The issues caused by ion suppression effect mentioned above have been often considered in the context of assessing normalization strategies [69,75,84,85]. In general, ion suppression was primarily used to account for its effect on a substrate level, such as small molecule drugs and endogenous lipids commonly discussed in MSI studies [69].

As one approach to reducing ion suppression, Li *et al.* systematically assessed the ion suppression effect-induced sensitivity degradation of neuropeptides and lipids on whole mouse brain tissue sections and developed the new subatmospheric pressure-MALDI source [84]. Moreover, some studies underlined the importance of tissue washing procedures such as acetone and ammonium formate to enhance sensitivity and reduce ion suppression in MSI [86–88]. In particular, these studies focused on analyzing ion suppression effect on MSI within one specific tissue (e.g., brain, pancreas, and spleen). In contrast, the zebrafish larva section for MSI studies, which we investigated in this thesis, contains various internal organs in a measuring MSI area and can get influenced by the complexity of multi-organs in the larva. Thus, an additional step for reducing ion suppressions that occurred in the MSI zebrafish larva section should be considered to generate MS images precisely and interpret them. The washing step with organic solvent could be conveniently implemented for a further experiment in conjunction with the optimized MSI method studies in Chapter 4.

Secondly, an understanding of and correction for matrix effects is vital for MSI of biological samples because of its impact on the observed spatial distribution of molecules in biological systems. The analyte ionization efficiency in the ionization source of MSI system (e.g., MALDI, DESI, and SIMS) relies on the chemical composition of the surrounding matrix, causing vulnerability to matrix effects [89]. Looking through ion suppression and matrix effect, one organ/tissue can generally present diverse biological compositions (it initially causes different matrix effects). That fact may induce different levels of ion suppressions and then lead to different ionization of species or adduct forms [90]; different analyte suppression across a sample may cause false spatial distributions, and it occurs mainly in inhomogeneous tissues with high probability. Since matrix effects obstruct the quantitative approaches of molecules in MSI data due to leading the fluctuated detection, MSI pixel-wise generally normalizes ion intensities using total ion intensity, median, and root mean square (RMS) for preprocessing spectra. However, alternative normalizing techniques applied for data processing are still under study, and their effect on the final result is not yet apparent [69,91,92]. In practice, we applied different normalization processes to the MSI dataset of

zebrafish larvae generated in Chapter 2, 3, and 4, and no signficant gap was observed. However, it depended on the vendor of MSI data analysis since we only used SCiLS Lab software tool in this thesis. It was also limited due to expensive cost and different software tools incompatible with each other. This approach should be continued to be an area of focus for further study.

Indeed, we observed the presence of three adduct ions (proton, sodium, and potassium) of the parent compound for naloxone and the two SCs (7′*N*-5F-ADB and 4F-MDMB-BINACA) in zebrafish larvae matrices investigated in this thesis. Overall the predominant adduct formed of naloxone (detected with similar intensity of sodium and potassium species under non-optimal conditions) differed unexpectedly from the previous results as 7′*N*-5F-ADB was found protonated and 4F-MDMB-BINACA was found as sodium adduct in the MS images of zebrafish larvae. That finding was driven to determine the method optimization of the MSI for zebrafish larvae (Chapter 4). Notably, after optimizing naloxone, MS images of naloxone significantly enhanced intensity and detection inside zebrafish larvae. In particular, its potassium adduct ion as the most common adduct was detected and visualized to informative distributional images of naloxone and its metabolites. Above all, the false-positive finding of the sodium adduct ion visualized before optimization could be revised, analyzing potassium adduct of naloxone by the optimization study of naloxone. Besides, the optimal MSI condition of the two drugs formed only one potassium ion and represented the difference from the previous studies (Chapter 2 and 3).

As in the current work, the impact of adduct formation by these two factors (ion suppression and matrix effect) mentioned above will be acute when selecting precursor ions for tandem MS (MS/MS) imaging experiments. Moreover, the abundance of individual adducts obviously affects the method detection and quantification limit (LOD and LOQ, respectively) of a molecule of interest in MSI images [89,90,93]. Especially, it is crucial for relative spatial compound quantification by MSI that a single primary ion of the target species is formed predominately to maximize the detection of a substrate and enhance the characterization of its detection with the spatial distribution. For this reason, we should consider sample preparation for MSI, and especially matrix deposition process. To generate MS images by MADLI-FT-ICR, matrix deposition is required for proper ionization and production of the molecules, as MALDI ionization technique uses a pulsed and focused laser beam at the tissue surface [9,94]. One molecule can form multiple adducts with the matrix and other metal ions, which metal adduct ions in MALDI are generated from the salt dissolution in the matrix spotted by the laser [95]. The matrix choice is crucial to produce appropriate analyte extraction, small crystal size, and homogenous application in MALDI measuring spots [9]. Several matrices for MALDI analyses are popular for their general analysis: 2,5-dihydroxybenzoic acid (DHB), α-cyanohydroxy-cinnamic acid (CHCA), and sinapic acid (SA) in positive mode and 1,5-diaminonaphthalene (DAN) and 9-aminoacridine (9-AA) for negative mode [9,86,94]. Automated sprayer systems have been utilized to implement the consistency and reproducibility of matrix deposition [86,96]. In summary, matrix deposition could influence the ionization efficiency of a chosen analyte from the sample surface and

directly affect the detection and visualization in MSI. For continued MSI development using zebrafish larvae, other matrix reagents would be our next challenge to be investigated with diverse conditions of matrix sprayer (e.g., flow rate of pump, matrix deposition passes, and spray nozzle temperature) as we only compared two different matrix reagents (CHB and CHCA) by adding trifluoroacetic acid (TFA) in this thesis.

Another influencing factor mentioned at the beginning of Chapter 5.2.4, batch effect, should be reviewed comprehensively to understand the systematic effect caused by an individual process in MSI and to further develop its new application in zebrafish larvae model for drug metabolism studies. The batch effect was already found in large-scale studies in translational clinical research, mainly hampering the interpretation and comparison of results, especially from large-scale studies [66,97,98]. Moreover, Balluff *et al.* investigated this effect critically and underlined how batch effects were exhibited in MSI data and how we could mitigate batch effects [66]. As the term indicates, batch effects are considered as technical variations and a potential systematic source of false interpretation of MSI data [66]. All batch effects can either increase variance or induce confounding differences between samples. In the first case, batch effects can mask the actual biological variation between samples leading to false-negative results. And then, as the technical variation accumulates from the pixel (the beginning practical step) to the location level (the final spatial image visualized after MSI run), it is unknown how much the individual factor contributes to the total sum of variation in the whole process of sample preparation. Consequently, this technical variation can cause systematic bias and generate false-positive correlations despite the generation of the specific images.

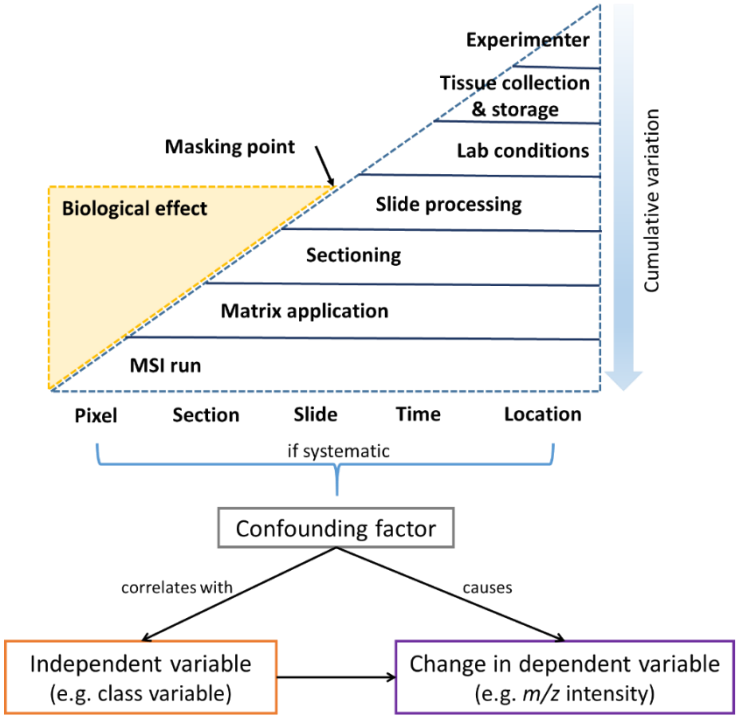

Figure 3. Diagram of batch effects in the entire MALDI-MSI procedure. The technical variation caused by batch effects can be masked by biological effect size (yellow reverse-right triangle) individually or in combination with cumulative batch effects. Systematic bias caused from any level can hence result in spurious correlations, where the observed correlation between an independent and dependent variable resulted from a confounding factor [66].

The fourth challenge of MSI, *i.e.* generating quantitative data, is an overarching issue, which cannot be solved if large data variance caused by matrix and batch effects is observed. Particularly in our MSI studies when working with complex larvae sections this might induce a significant batch effects due to technical challenges in reliably producing uniform sections from the tiny sample. In addition, also matrix effects probably play a role when analyzing compound abundance in physiologically different compartments. Each larva can be generally cryosectioned into ca. 20 sections with 10 μm-thickness, containing different organs and body parts per each section. In turn, each section has different ion suppression patterns depending on the individual matrix composition and additionally, different adduct ion ratios might be observed making a predictive analyses of compound distribution throughout the entire larvae sample complicated.

Interestingly, Barry *et al*. investigated three scenarios to emphasize potential issues of using LC-MS to validate quantitative MSI, in which the tissue is categorized as homogeneous, localized, or sporadic distribution [73]. The MSI results from multiple sections were compared to serial sections and whole tissues analyzed by LC-MS. Importantly, in the scenario of uniform distribution throughout all sections, MSI and LC-MS data were in good agreement. On the contrary, in the case of compounds being localized in specific regions and sub-compartments of the tissue, the whole tissue concentration by LC-MS is not relevant to the localized region, and the tissue concentration from a whole tissue homogenate is of little value in a sporadic distribution, respectively [73]. In addition, a mimetic tissue model was designed consisting of seven layers spiked with serial concentrations of test compound mixed in either rat liver, kidney, or brain tissue homogenate, respectively, to investigate the influence of tissue types. The linearity and slope of the calibration curve in the different mimetic tissue models (in three different organ matrices) were compared, and their calibration curve got a noticeable impact on the intercept. This result could be accounted for matrix effects caused by different tissue types [73]. Despite the successful development of the mimetic tissue models, some challenges for matrix effect, quantification, and LC-MS validation still remain. Through the findings of this study, the MSI challenges faced in the zebrafish larvae model are shared, to an extent, in MSI field, and its outlook seems to be promising.

For overcoming these negative factors, such as ion suppression, matrix effect, and batch effect, in MSI setups, a tissue-specific normalization factor called tissue extinction coefficient (TEC) was introduced and investigated using whole-body or single heterogeneous organ (brain, eye, and liver of mice) sections. Encouragingly, a comparison between MSI and LC-MS revealed good linearity of the calibration curves [85,99]. Moreover, to obtain precise and reproducible MSI data, more conventional methods such as spotting a compound dilution series onto the control tissue and a set of tissue homogenates of different tissue types (lung,

liver, kidney, heart, and brain) from animals were investigated and developed for easy preparation of standard curve with spiked tissue homogenates [70,75]. However, it was emphasized that quantitative MSI data from whole-body sections involving several tissue types should be interpreted with caution to avoid new faulty effects [70,73]. Also, additional attention needs to be paid if any tissue-specific variations in the signal response may be dependent on the sub-compartment in a tissue [70,75,85,99]. The trouble with this application, however, is that it cannot be practically applied to small animal models, particularly zebrafish larvae, because it is difficult to unambiguously visualize tissues of the 2 mm-length larvae separately due to the limitations of pixel resolution and laser repetition rate to ionize molecules in MALDI.

Alternatively, ISTDs for normalization have become common in MSI where absolute quantitation is required; for MSI, isotopically labeled compounds with ^{2}H, ^{13}C, ^{15}N, or ^{17}O should be used depending on the purpose of the study. Application of ISTDs yielded superb linearity of calibration curves and was superior to normalizations using the unlabeled compound for covering matrix effects [69,100]. Based on the results of these studies, ISTD usage may be the most optimal solution to compensate for discrepancies in intensities caused by the limitations from the sample itself, the overall MSI system, or inconsistency with LC-MS mentioned above. However, appropriate commercial or customized ISTDs for qualitative and quantitative analyses are mostly not available or too expensive, especially for non-targeted screening of xenobiotics and new illicit drugs by MSI and screening new drug candidates. Interestingly, well-characterized endogenous compounds (e.g. lipids), ubiquitous impurities (e.g., phthalates, butylated hydroxytoluene), and abundant matrix ions in every MSI spectrum are employed as references for internal mass calibration [101]. However, there are no generally applicable protocols yet, but these studies give some specific grounds for future research on optimizing MSI with the zebrafish larvae model.

So far, we lack an universal solution for avoiding tissue-specific variations in MSI signals, even though initial technical limitations of MSI of zebrafish larvae sections have mainly been overcome in the work presented here. However, further optimization of ionization patterns in MSI is of utmost importance because it can shift the interpretation of MSI visualization and cause potentially falsified information content [66,70]. Therefore, sufficiently large numbers of biological replicates for integrating all findings across different tissue sites [102], standardized and robust MSI protocols, and quality control (QC) methods throughout the complete procedure need to be implemented in MSI routines (Figure 3). Additionally, new normalization methods or advanced statistical approaches with clear guidelines will also help to further optimize MSI and ready this methodology for broad application *e.g.* in the clinical setting [92,103]. The final aim of all efforts described above is to reposition MSI as a convincing and effective technique for providing distributional information of a molecule in various tissues.

5.3 Conclusion

In this thesis, the zebrafish larvae model was characterized as a powerful *in vivo* model in drug metabolism studies due to some unique advantages, such as reproducibility, fast development, high coverage of human genomes, and ethical perspective as a non-animal experiment, over other common ADME methods. This work was particularly dedicated to further strengthening the model by applying three enabling methodologies: microinjection, genetic manipulation via morpholino oligonucleotides, and mass spectrometry imaging (MSI) in three independent, yet interconnected, studies. In the microinjection approach, we demonstrated that a direct administration route induced a fast distribution of 7′*N*-5F-ADB inside zebrafish larvae and produced an authentic metabolite spectrum, indicating the high potential of zebrafish larvae model for the prediction of human metabolism. In the second study, genetic modification of zebrafish larvae, *i.e.* knock-down of cannabinoid receptors CB1 and CB2, allowed us to establish a correlation between drug-modulated liver function and the onset of 4F-MDMB-BINACA. Both studies with the SCs, 7′*N*-5F-ADB and 4F-MDMB-BINACA, involved the spatial analysis of drug and metabolite distributions inside zebrafish larvae through MSI. Some discrepancies were found between routine LC-HRMS/MS datasets and data obtained from MSI, which fostered a third study specifically dedicated to further improving MSI protocols for studying drug distribution in zebrafish larvae. For this, the opioid antagonist naloxone was used as a reference compound in a case study for improving MSI protocols. Importantly, the developed methods, in particular the stepwise assessment of crucial steps of sample preparation procedures, are generally applicable also for other analytes. In conclusion, the zebrafish larvae model has great potential as a preclinical vertebrate animal model to predict human metabolism. The schematic approach presented here will also be relevant to developing other animal models for drug metabolism studies.

5.4 Bibliography

1. Zhang, T.; Peterson, R.T. Zebrafish as a Platform for Drug Screening. *The Zebrafish in Biomedical Research*; Elsevier, 2020; pp 659–675, ISBN 9780128124314.
2. van Wijk, R.C.; Krekels, E.H.J.; Hankemeier, T.; Spaink, H.P.; van der Graaf, P.H. Systems pharmacology of hepatic metabolism in zebrafish larvae. *Drug Discovery Today: Disease Models* **2016**, *22*, 27–34, doi:10.1016/j.ddmod.2017.04.003.
3. Krotulski, A.J.; Mohr, A.L.A.; Kacinko, S.L.; Fogarty, M.F.; Shuda, S.A.; Diamond, F.X.; Kinney, W.A.; Menendez, M.J.; Logan, B.K. 4F-MDMB-BINACA: A New Synthetic Cannabinoid Widely Implicated in Forensic Casework. *J. Forensic Sci.* **2019**, *64*, 1451–1461, doi:10.1111/1556-4029.14101.
4. European Monitoring Centre for Drugs and Drug Addiction. 4F-MDMB-BICA: EMCDDA initial report on the new psychoactive substance methyl 2-({[1-(4-fluorobutyl)-1H-indol-3-yl]carbonyl}amino)-3,3-dimethylbutanoate (4F-MDMB-BICA) **2020**, doi:10.2810/221024.
5. Castaneto, M.S.; Gorelick, D.A.; Desrosiers, N.A.; Hartman, R.L.; Pirard, S.; Huestis, M.A. Synthetic cannabinoids: epidemiology, pharmacodynamics, and clinical implications. *Drug Alcohol Depend.* **2014**, *144*, 12–41, doi:10.1016/j.drugalcdep.2014.08.005.
6. Noble, C.; Cannaert, A.; Linnet, K.; Stove, C.P. Application of an activity-based receptor bioassay to investigate the in vitro activity of selected indole- and indazole-3-carboxamide-based synthetic cannabinoids at CB1 and CB2 receptors. *Drug Test. Anal.* **2019**, *11*, 501–511, doi:10.1002/dta.2517.
7. World Health Organization. Critical Review Report: 4F-MDMB-BINACA. Expert Committee on Drug Dependence, Forthy-second Meeting, Geneva. In Proceeding of the 42nd ECDD (2019): 4F-MDMB-BINACA, Geneva, Switzerland, 21-25 October 2019. **2019**, 24.
8. Davoli, E.; Zucchetti, M.; Matteo, C.; Ubezio, P.; D'Incalci, M.; Morosi, L. THE SPACE DIMENSION AT THE MICRO LEVEL: MASS SPECTROMETRY IMAGING OF DRUGS IN TISSUES. *Mass Spectrom. Rev.* **2021**, *40*, 201–214, doi:10.1002/mas.21633.
9. Buchberger, A.R.; DeLaney, K.; Johnson, J.; Li, L. Mass Spectrometry Imaging: A Review of Emerging Advancements and Future Insights. *Anal. Chem.* **2018**, *90*, 240–265, doi:10.1021/acs.analchem.7b04733.
10. UNODC. Global Synthetic Drugs Assessment 2020 **2020**.
11. UNODC. World Drug Report 2021: Booklet 2 - GLOBAL OVERVIEW: DRUG DEMAND AND DRUG SUPPLY **2021**.
12. Park, Y.M.; Meyer, M.R.; Müller, R.; Herrmann, J. Drug Administration Routes Impact the Metabolism of a Synthetic Cannabinoid in the Zebrafish Larvae Model. *Molecules* **2020**, *25*, doi:10.3390/molecules25194474.
13. Cassar, S.; Adatto, I.; Freeman, J.L.; Gamse, J.T.; Iturria, I.; Lawrence, C.; Muriana, A.; Peterson, R.T.; van Cruchten, S.; Zon, L.I. Use of Zebrafish in Drug Discovery Toxicology. *Chem. Res. Toxicol.* **2020**, *33*, 95–118, doi:10.1021/acs.chemrestox.9b00335.

14. Park, Y.M.; Dahlem, C.; Meyer, M.R.; Kiemer, A.K.; Müller, R.; Herrmann, J. Induction of Liver Size Reduction in Zebrafish Larvae by the Emerging Synthetic Cannabinoid 4F-MDMB-BINACA and Its Impact on Drug Metabolism. *Molecules* **2022**, *27*, 1290, doi:10.3390/molecules27041290.
15. Phillips, J.B.; Westerfield, M. Zebrafish as a Model to Understand Human Genetic Diseases. *The Zebrafish in Biomedical Research*; Elsevier, 2020; pp 619–626, ISBN 9780128124314.
16. Hoppstädter, J.; Valbuena Perez, J.V.; Linnenberger, R.; Dahlem, C.; Legroux, T.M.; Hecksteden, A.; Tse, W.K.F.; Flamini, S.; Andreas, A.; Herrmann, J.; et al. The glucocorticoid-induced leucine zipper mediates statin-induced muscle damage. *FASEB J.* **2020**, *34*, 4684–4701, doi:10.1096/fj.201902557RRR.
17. Bachmann, K. Drug Metabolism. In *Pharmacology*: *Principles and practice*; Hacker, M.P., Messer, W.S., Bachmann, K.A., Eds.; Elsevier: Amsterdam, 2009; pp 131–173, ISBN 9780123695215.
18. *Global Drug Discovery Market Survey 2022 With Top Countries Data {CAGR With 8}*: *Growth Rate: Top Manufacturers Profiles, Key Stakeholders, Growth Opportunities and Sales Channels Analysis*, 2022AM.
19. Mordor Intelligence. *Drug Discovery Market- Growth, Trends, COVID-19 Impact, and Forecasts (2022 - 2027)*, 2022. Available online: https://www.mordorintelligence.com/industry-reports/drug-discovery-market.
20. Data Bridge Market Research Private Ltd. *Global ADME Toxicology Testing Market – Industry Trends and Forecast to 2027;* Data Bridge Market Research Private Ltd.
21. Meyer, M.R. New psychoactive substances: an overview on recent publications on their toxicodynamics and toxicokinetics. *Arch. Toxicol.* **2016**, *90*, 2421–2444, doi:10.1007/s00204-016-1812-x.
22. Wagmann, L.; Gampfer, T.M.; Meyer, M.R. Recent trends in drugs of abuse metabolism studies for mass spectrometry-based analytical screening procedures. *Anal. Bioanal. Chem.* **2021**, *413*, 5551–5559, doi:10.1007/s00216-021-03311-w.
23. Wagmann, L.; Maurer, H.H. Bioanalytical Methods for New Psychoactive Substances. *Handb. Exp. Pharmacol.* **2018**, *252*, 413–439, doi:10.1007/164_2017_83.
24. Souza Anselmo, C. de; Sardela, V.F.; Matias, B.F.; Carvalho, A.R. de; Sousa, V.P. de; Pereira, H.M.G.; Aquino Neto, F.R. de. Is zebrafish (Danio rerio) a tool for human-like metabolism study? *Drug Test. Anal.* **2017**, *9*, 1685–1694, doi:10.1002/dta.2318.
25. Rennekamp, A.J.; Peterson, R.T. 15 years of zebrafish chemical screening. *Curr. Opin. Chem. Biol.* **2015**, *24*, 58–70, doi:10.1016/j.cbpa.2014.10.025.
26. Zhang, Q.; Ji, C.; Yan, L.; Lu, M.; Lu, C.; Zhao, M. The identification of the metabolites of chlorothalonil in zebrafish (Danio rerio) and their embryo toxicity and endocrine effects at environmentally relevant levels. *Environ. Pollut.* **2016**, *218*, 8–15, doi:10.1016/j.envpol.2016.08.026.
27. Gierten, J.; Pylatiuk, C.; Hammouda, O.T.; Schock, C.; Stegmaier, J.; Wittbrodt, J.; Gehrig, J.; Loosli, F. Automated high-throughput heartbeat quantification in medaka and

zebrafish embryos under physiological conditions. *Sci. Rep.* **2020**, *10*, 2046, doi:10.1038/s41598-020-58563-w.

28. Zhao, Y.; Sun, H.; Sha, X.; Gu, L.; Zhan, Z.; Li, W.J. A Review of Automated Microinjection of Zebrafish Embryos. *Micromachines (Basel)* **2018**, *10*, doi:10.3390/mi10010007.
29. Chow, Y.T.; Chen, S.; Liu, C.; Liu, C.; Li, L.; Kong, C.W.M.; Cheng, S.H.; Li, R.A.; Sun, D. A High-Throughput Automated Microinjection System for Human Cells With Small Size. *IEEE/ASME Trans. Mechatron.* **2016**, *21*, 838–850, doi:10.1109/TMECH.2015.2476362.
30. Chi, Z.; Xu, Q.; Zhu, L. A Review of Recent Advances in Robotic Cell Microinjection. *IEEE Access* **2020**, *8*, 8520–8532, doi:10.1109/ACCESS.2020.2964305.
31. Cocchiaro, J.L.; Rawls, J.F. Microgavage of zebrafish larvae. *J. Vis. Exp.* **2013**, e4434, doi:10.3791/4434.
32. He, J.; Mo, D.; Chen, J.; Luo, L. Combined whole-mount fluorescence in situ hybridization and antibody staining in zebrafish embryos and larvae. *Nat. Protoc.* **2020**, *15*, 3361–3379, doi:10.1038/s41596-020-0376-7.
33. Schubert, S.; Keddig, N.; Hanel, R.; Kammann, U. Microinjection into zebrafish embryos (Danio rerio) - a useful tool in aquatic toxicity testing? *Environ Sci Eur* **2014**, *26*, 1, doi:10.1186/s12302-014-0032-3.
34. Stainier, D.Y.R.; Raz, E.; Lawson, N.D.; Ekker, S.C.; Burdine, R.D.; Eisen, J.S.; Ingham, P.W.; Schulte-Merker, S.; Yelon, D.; Weinstein, B.M.; et al. Guidelines for morpholino use in zebrafish. *PLoS Genet.* **2017**, *13*, e1007000, doi:10.1371/journal.pgen.1007000.
35. Moulton, J.D.; Yan, Y.-L. Using Morpholinos to control gene expression. *Curr. Protoc. Mol. Biol.* **2008**, *Chapter 26*, Unit 26.8, doi:10.1002/0471142727.mb2608s83.
36. Liu, L.Y.; Alexa, K.; Cortes, M.; Schatzman-Bone, S.; Kim, A.J.; Mukhopadhyay, B.; Cinar, R.; Kunos, G.; North, T.E.; Goessling, W. Cannabinoid receptor signaling regulates liver development and metabolism. *Development* **2016**, *143*, 609–622, doi:10.1242/dev.121731.
37. Jimenez, D. How technology could transform drug research in 2022: Pharmaceutical Technology takes a look at some of the tech innovations set to impact drug discovery and development in 2022. [Online], December 14, 2021. Available online: https://www.pharmaceutical-technology.com/analysis/how-technology-could-transform-drug-research-in-2022/.
38. Dara, S.; Dhamercherla, S.; Jadav, S.S.; Babu, C.M.; Ahsan, M.J. Machine Learning in Drug Discovery: A Review. *Artif. Intell. Rev.* **2021**, 1–53, doi:10.1007/s10462-021-10058-4.
39. Bender, A.; Cortés-Ciriano, I. Artificial intelligence in drug discovery: what is realistic, what are illusions? Part 1: Ways to make an impact, and why we are not there yet. *Drug Discov. Today* **2021**, *26*, 511–524, doi:10.1016/j.drudis.2020.12.009.
40. Zhavoronkov, A.; Ivanenkov, Y.A.; Aliper, A.; Veselov, M.S.; Aladinskiy, V.A.; Aladinskaya, A.V.; Terentiev, V.A.; Polykovskiy, D.A.; Kuznetsov, M.D.; Asadulaev, A.; et

al. Deep learning enables rapid identification of potent DDR1 kinase inhibitors. *Nat. Biotechnol.* **2019**, *37*, 1038–1040, doi:10.1038/s41587-019-0224-x.

41. Deep Knowledge Analytics. AI for Drug Discovery, Biomarker Development and Advanced R&D Landscape Overview 2019 / Q3 **2019**, 145.
42. Bai, Q.; Liu, S.; Tian, Y.; Xu, T.; Banegas-Luna, A.J.; Pérez-Sánchez, H.; Huang, J.; Liu, H.; Yao, X. Application advances of deep learning methods for de novo drug design and molecular dynamics simulation. *WIREs Comput Mol Sci* **2021**, doi:10.1002/wcms.1581.
43. Parkins, K.; Hillman, A. 2022 forecast: decentralised trials to reach new heights with 28% jump: eConsent and web-based questionnaires have largest growth, but telemedicine and mobile-based elements remain as pillars. [Online], December 14, 2021. Available online: https://www.clinicaltrialsarena.com/analysis/2022-forecast-decentralised-trials-to-reach-new-heights-with-28-jump/?utm_source=newsletter&utm_medium=email&utm_campaign=cta_1712.
44. Reynald Castañeda. Pharma developments in 2022: what you need to know: A look at healthcare trends that will likely impact pharma's efforts to research and develop therapeutics in 2022. *Pharmaceutical Technology [Online]*, January 5, 2022. Available online: https://www.pharmaceutical-technology.com/analysis/pharma-developments-in-2022-what-you-need-to-know/.
45. Kennedy, T. Managing the drug discovery/development interface **1997**, *2*, 436–444.
46. Kassel, D.B. Applications of high-throughput ADME in drug discovery. *Curr. Opin. Chem. Biol.* **2004**, *8*, 339–345, doi:10.1016/j.cbpa.2004.04.015.
47. Ott, C.E.; Perez-Estebanez, M.; Hernandez, S.; Kelly, K.; Dalzell, K.A.; Arcos-Martinez, M.J.; Heras, A.; Colina, A.; Arroyo, L.E. Forensic Identification of Fentanyl and its Analogs by Electrochemical-Surface Enhanced Raman Spectroscopy (EC-SERS) for the Screening of Seized Drugs of Abuse. *Front. Anal. Sci.* **2022**, *2*, 5460, doi:10.3389/frans.2022.834820.
48. Wagmann, L.; Meyer, M.R. Reviewing toxicokinetics with a focus on metabolism of new psychoactive substances in the zebrafish (larvae) model. *WIREs Forensic Science* **2022**, doi:10.1002/wfs2.1454.
49. EMCDDA. European drug report 2021: trends and developments.
50. Pagnotta, G.; Kalia, S.; Di Lisa, L.; Cicero, A.F.G.; Borghi, C.; Focarete, M.L. Progress towards 3D bioprinting of tissue models for advanced drug screening: In vitro evaluation of drug toxicity and drug metabolism. *Bioprinting* **2022**, *27*, e00218, doi:10.1016/j.bprint.2022.e00218.
51. Gao, G.; Ahn, M.; Cho, W.-W.; Kim, B.-S.; Cho, D.-W. 3D Printing of Pharmaceutical Application: Drug Screening and Drug Delivery. *Pharmaceutics* **2021**, *13*, doi:10.3390/pharmaceutics13091373.
52. Xiang, Y.; Miller, K.; Guan, J.; Kiratitanaporn, W.; Tang, M.; Chen, S. 3D bioprinting of complex tissues in vitro: state-of-the-art and future perspectives. *Arch. Toxicol.* **2022**, *96*, 691–710, doi:10.1007/s00204-021-03212-y.

53. Serras, A.S.; Rodrigues, J.S.; Cipriano, M.; Rodrigues, A.V.; Oliveira, N.G.; Miranda, J.P. A Critical Perspective on 3D Liver Models for Drug Metabolism and Toxicology Studies. *Front. Cell Dev. Biol.* **2021**, *9*, 626805, doi:10.3389/fcell.2021.626805.
54. Souza, I.R. de; Di Canavez, A.P.M.; Schuck, D.C.; Gagosian, V.S.C.; Souza, I.R. de; Vicari, T.; da Silva Trindade, E.; Cestari, M.M.; Lorencini, M.; Leme, D.M. Development of 3D cultures of zebrafish liver and embryo cell lines: a comparison of different spheroid formation methods. *Ecotoxicology* **2021**, *30*, 1893–1909, doi:10.1007/s10646-021-02459-6.
55. Bruzzone, M.; Chiarello, E.; Albanesi, M.; Miletto Petrazzini, M.E.; Megighian, A.; Lodovichi, C.; Dal Maschio, M. Whole brain functional recordings at cellular resolution in zebrafish larvae with 3D scanning multiphoton microscopy. *Sci. Rep.* **2021**, *11*, 11048, doi:10.1038/s41598-021-90335-y.
56. Paul, C.D.; Bishop, K.; Devine, A.; Paine, E.L.; Staunton, J.R.; Thomas, S.M.; Thomas, J.R.; Doyle, A.D.; Miller Jenkins, L.M.; Morgan, N.Y.; et al. Tissue Architectural Cues Drive Organ Targeting of Tumor Cells in Zebrafish. *Cell Syst.* **2019**, *9*, 187-206.e16, doi:10.1016/j.cels.2019.07.005.
57. Tutty, M.A.; Movia, D.; Prina-Mello, A. Three-dimensional (3D) liver cell models - a tool for bridging the gap between animal studies and clinical trials when screening liver accumulation and toxicity of nanobiomaterials. *Drug Deliv. Transl. Res.* **2022**, doi:10.1007/s13346-022-01147-0.
58. Atanasov, A.G.; Zotchev, S.B.; Dirsch, V.M.; Supuran, C.T. Natural products in drug discovery: advances and opportunities. *Nat. Rev. Drug Discov.* **2021**, *20*, 200–216, doi:10.1038/s41573-020-00114-z.
59. Wolfender, J.-L.; Marti, G.; Thomas, A.; Bertrand, S. Current approaches and challenges for the metabolite profiling of complex natural extracts. *J. Chromatogr. A* **2015**, *1382*, 136–164, doi:10.1016/j.chroma.2014.10.091.
60. Letertre, M.P.M.; Dervilly, G.; Giraudeau, P. Combined Nuclear Magnetic Resonance Spectroscopy and Mass Spectrometry Approaches for Metabolomics. *Anal. Chem.* **2021**, *93*, 500–518, doi:10.1021/acs.analchem.0c04371.
61. Sisco, E.; Forbes, T.P. Forensic applications of DART-MS: A review of recent literature. *Forensic Chemistry* **2021**, *22*, 100294, doi:10.1016/j.forc.2020.100294.
62. Nagae, M.; Igarashi, T.; Mizukoshi, K.; Kuniyoshi, K.; Oshiro, N.; Yasumoto, T. Development and Validation of an LC-MS/MS Method for the Ultra-Trace Analysis of Pacific Ciguatoxins in Fish. *J. AOAC Int.* **2021**, *104*, 1272–1281, doi:10.1093/jaoacint/qsab052.
63. Wagmann, L.; Frankenfeld, F.; Park, Y.M.; Herrmann, J.; Fischmann, S.; Westphal, F.; Müller, R.; Flockerzi, V.; Meyer, M.R. How to Study the Metabolism of New Psychoactive Substances for the Purpose of Toxicological Screenings-A Follow-Up Study Comparing Pooled Human Liver S9, HepaRG Cells, and Zebrafish Larvae. *Front. Chem.* **2020**, *8*, 539, doi:10.3389/fchem.2020.00539.
64. Richter, L.H.J.; Herrmann, J.; Andreas, A.; Park, Y.M.; Wagmann, L.; Flockerzi, V.; Müller, R.; Meyer, M.R. Tools for studying the metabolism of new psychoactive substances

for toxicological screening purposes - A comparative study using pooled human liver S9, HepaRG cells, and zebrafish larvae. *Toxicol. Lett.* **2019**, *305*, 73–80, doi:10.1016/j.toxlet.2019.01.010.

65. Schulz, S.; Becker, M.; Groseclose, M.R.; Schadt, S.; Hopf, C. Advanced MALDI mass spectrometry imaging in pharmaceutical research and drug development. *Curr. Opin. Biotechnol.* **2019**, *55*, 51–59, doi:10.1016/j.copbio.2018.08.003.
66. Balluff, B.; Hopf, C.; Porta Siegel, T.; Grabsch, H.I.; Heeren, R.M.A. Batch Effects in MALDI Mass Spectrometry Imaging. *J. Am. Soc. Mass Spectrom.* **2021**, *32*, 628–635, doi:10.1021/jasms.0c00393.
67. Vaysse, P.-M.; Heeren, R.M.A.; Porta, T.; Balluff, B. Mass spectrometry imaging for clinical research - latest developments, applications, and current limitations. *Analyst* **2017**, *142*, 2690–2712, doi:10.1039/c7an00565b.
68. Kooijman, P.C.; Nagornov, K.O.; Kozhinov, A.N.; Kilgour, D.P.A.; Tsybin, Y.O.; Heeren, R.M.A.; Ellis, S.R. Increased throughput and ultra-high mass resolution in DESI FT-ICR MS imaging through new-generation external data acquisition system and advanced data processing approaches. *Sci. Rep.* **2019**, *9*, 8, doi:10.1038/s41598-018-36957-1.
69. Taylor, A.J.; Dexter, A.; Bunch, J. Exploring Ion Suppression in Mass Spectrometry Imaging of a Heterogeneous Tissue. *Anal. Chem.* **2018**, *90*, 5637–5645, doi:10.1021/acs.analchem.7b05005.
70. Hansen, H.T.; Janfelt, C. Aspects of Quantitation in Mass Spectrometry Imaging Investigated on Cryo-Sections of Spiked Tissue Homogenates. *Anal. Chem.* **2016**, *88*, 11513–11520, doi:10.1021/acs.analchem.6b02711.
71. Heeren, R.M.A.; Smith, D.F.; Stauber, J.; Kükrer-Kaletas, B.; MacAleese, L. Imaging mass spectrometry: Hype or hope? *J. Am. Soc. Mass Spectrom.* **2009**, *20*, 1006–1014, doi:10.1016/j.jasms.2009.01.011.
72. Cole, L.M.; Clench, M.R. Mass spectrometry imaging for the proteomic study of clinical tissue. *Proteomics Clin. Appl.* **2015**, *9*, 335–341, doi:10.1002/prca.201400103.
73. Barry, J.A.; Groseclose, M.R.; Castellino, S. Quantification and assessment of detection capability in imaging mass spectrometry using a revised mimetic tissue model. *Bioanalysis* **2019**, *11*, 1099–1116, doi:10.4155/bio-2019-0035.
74. Dueñas, M.E.; Essner, J.J.; Lee, Y.J. 3D MALDI Mass Spectrometry Imaging of a Single Cell: Spatial Mapping of Lipids in the Embryonic Development of Zebrafish. *Sci. Rep.* **2017**, *7*, 14946, doi:10.1038/s41598-017-14949-x.
75. Huizing, L.R.S.; McDuffie, J.; Cuyckens, F.; van Heerden, M.; Koudriakova, T.; Heeren, R.M.A.; Vreeken, R.J. Quantitative Mass Spectrometry Imaging to Study Drug Distribution in the Intestine Following Oral Dosing. *Anal. Chem.* **2021**, *93*, 2144–2151, doi:10.1021/acs.analchem.0c03956.
76. Jove, M.; Spencer, J.; Clench, M.; Loadman, P.M.; Twelves, C. Precision pharmacology: Mass spectrometry imaging and pharmacokinetic drug resistance. *Crit. Rev. Oncol. Hematol.* **2019**, *141*, 153–162, doi:10.1016/j.critrevonc.2019.06.008.

77. Eiersbrock, F.B.; Orthen, J.M.; Soltwisch, J. Validation of MALDI-MS imaging data of selected membrane lipids in murine brain with and without laser postionization by quantitative nano-HPLC-MS using laser microdissection. *Anal Bioanal Chem* **2020**, *412*, 6875–6886, doi:10.1007/s00216-020-02818-y.
78. Wen, B.; Zhu, M. Applications of mass spectrometry in drug metabolism: 50 years of progress. *Drug Metab. Rev.* **2015**, *47*, 71–87, doi:10.3109/03602532.2014.1001029.
79. Cuyckens, F. Mass spectrometry in drug metabolism and pharmacokinetics: Current trends and future perspectives. *Rapid Commun. Mass Spectrom.* **2019**, *33 Suppl 3*, 90–95, doi:10.1002/rcm.8235.
80. Fung, E.N.; Jemal, M.; Aubry, A.-F. High-resolution MS in regulated bioanalysis: where are we now and where do we go from here? *Bioanalysis* **2013**, *5*, 1277–1284, doi:10.4155/bio.13.81.
81. de Vries R.; J. Vreeken R. J.; Cuyckens F. High-throughput analysis of drugsand metabolites in biological fluids using Quan-Qual approaches. *LCGC Eur.* **2016**, *29*, 26–30.
82. Korfmacher, W. High-resolution mass spectrometry will dramatically change our drug-discovery bioanalysis procedures. *Bioanalysis* **2011**, *3*, 1169–1171, doi:10.4155/bio.11.98.
83. Guilbault, G.G.; Hjelm, M. Nomenclature for automated and mechanised analysis (Recommendations 1989). *Pure and Applied Chemistry* **1989**, *61*, 1657–1664, doi:10.1351/pac198961091657.
84. Li, G.; Cao, Q.; Liu, Y.; DeLaney, K.; Tian, Z.; Moskovets, E.; Li, L. Characterizing and alleviating ion suppression effects in atmospheric pressure matrix-assisted laser desorption/ionization. *Rapid Commun. Mass Spectrom.* **2019**, *33*, 327–335, doi:10.1002/rcm.8358.
85. Hamm, G.; Bonnel, D.; Legouffe, R.; Pamelard, F.; Delbos, J.-M.; Bouzom, F.; Stauber, J. Quantitative mass spectrometry imaging of propranolol and olanzapine using tissue extinction calculation as normalization factor. *J. Proteomics* **2012**, *75*, 4952–4961, doi:10.1016/j.jprot.2012.07.035.
86. Dilmetz, B.A.; Lee, Y.-R.; Condina, M.R.; Briggs, M.; Young, C.; Desire, C.T.; Klingler-Hoffmann, M.; Hoffmann, P. Novel technical developments in mass spectrometry imaging in 2020: A mini review. *Analytical Science Advances* **2021**, *2*, 225–237, doi:10.1002/ansa.202000176.
87. Sun, C.; Li, Z.; Ma, C.; Zang, Q.; Li, J.; Liu, W.; Zhao, H.; Wang, X. Acetone immersion enhanced MALDI-MS imaging of small molecule metabolites in biological tissues. *J. Pharm. Biomed. Anal.* **2019**, *176*, 112797, doi:10.1016/j.jpba.2019.112797.
88. Harris, A.; Roseborough, A.; Mor, R.; Yeung, K.K.-C.; Whitehead, S.N. Ganglioside Detection from Formalin-Fixed Human Brain Tissue Utilizing MALDI Imaging Mass Spectrometry. *J. Am. Soc. Mass Spectrom.* **2020**, *31*, 479–487, doi:10.1021/jasms.9b00110.
89. Lanekoff, I.; Stevens, S.L.; Stenzel-Poore, M.P.; Laskin, J. Matrix effects in biological mass spectrometry imaging: identification and compensation. *Analyst* **2014**, *139*, 3528–3532, doi:10.1039/c4an00504j.

90. Janda, M.; Seah, B.K.B.; Jakob, D.; Beckmann, J.; Geier, B.; Liebeke, M. Determination of Abundant Metabolite Matrix Adducts Illuminates the Dark Metabolome of MALDI-Mass Spectrometry Imaging Datasets. *Anal. Chem.* **2021**, *93*, 8399–8407, doi:10.1021/acs.analchem.0c04720.
91. Race, A.M.; Palmer, A.D.; Dexter, A.; Steven, R.T.; Styles, I.B.; Bunch, J. SpectralAnalysis: Software for the Masses. *Anal. Chem.* **2016**, *88*, 9451–9458, doi:10.1021/acs.analchem.6b01643.
92. Deininger, S.-O.; Cornett, D.S.; Paape, R.; Becker, M.; Pineau, C.; Rauser, S.; Walch, A.; Wolski, E. Normalization in MALDI-TOF imaging datasets of proteins: practical considerations. *Anal. Bioanal. Chem.* **2011**, *401*, 167–181, doi:10.1007/s00216-011-4929-z.
93. Griffiths, R.L.; Randall, E.C.; Race, A.M.; Bunch, J.; Cooper, H.J. Raster-Mode Continuous-Flow Liquid Microjunction Mass Spectrometry Imaging of Proteins in Thin Tissue Sections. *Anal. Chem.* **2017**, *89*, 5683–5687, doi:10.1021/acs.analchem.7b00977.
94. Addie, R.D.; Balluff, B.; Bovée, J.V.M.G.; Morreau, H.; McDonnell, L.A. Current State and Future Challenges of Mass Spectrometry Imaging for Clinical Research. *Anal. Chem.* **2015**, *87*, 6426–6433, doi:10.1021/acs.analchem.5b00416.
95. Lee, C.; Lu, I.-C.; Hsu, H.C.; Lin, H.-Y.; Liang, S.-P.; Lee, Y.-T.; Ni, C.-K. Formation of Metal-Related Ions in Matrix-Assisted Laser Desorption Ionization. *J. Am. Soc. Mass Spectrom.* **2016**, *27*, 1491–1498, doi:10.1007/s13361-016-1424-y.
96. Škrášková, K.; Claude, E.; Jones, E.A.; Towers, M.; Ellis, S.R.; Heeren, R.M.A. Enhanced capabilities for imaging gangliosides in murine brain with matrix-assisted laser desorption/ionization and desorption electrospray ionization mass spectrometry coupled to ion mobility separation. *Methods* **2016**, *104*, 69–78, doi:10.1016/j.ymeth.2016.02.014.
97. Janowczyk, A.; Zuo, R.; Gilmore, H.; Feldman, M.; Madabhushi, A. HistoQC: An Open-Source Quality Control Tool for Digital Pathology Slides. *JCO Clinical Cancer Informatics* **2019**, 1–7, doi:10.1200/CCI.18.00157.
98. Goh, W.W.B.; Wang, W.; Wong, L. Why Batch Effects Matter in Omics Data, and How to Avoid Them. *Trends Biotechnol.* **2017**, *35*, 498–507, doi:10.1016/j.tibtech.2017.02.012.
99. Lamont, L.; Hadavi, D.; Viehmann, B.; Flinders, B.; Heeren, R.M.A.; Vreeken, R.J.; Porta Siegel, T. Quantitative mass spectrometry imaging of drugs and metabolites: a multi-platform comparison. *Anal. Bioanal. Chem.* **2021**, *413*, 2779–2791, doi:10.1007/s00216-021-03210-0.
100. Källback, P.; Shariatgorji, M.; Nilsson, A.; Andrén, P.E. Novel mass spectrometry imaging software assisting labeled normalization and quantitation of drugs and neuropeptides directly in tissue sections. *J. Proteomics* **2012**, *75*, 4941–4951, doi:10.1016/j.jprot.2012.07.034.
101. Treu, A.; Römpp, A. Matrix ions as internal standard for high mass accuracy matrix-assisted laser desorption/ionization mass spectrometry imaging. *Rapid Commun. Mass Spectrom.* **2021**, *35*, e9110, doi:10.1002/rcm.9110.

102. Ly, A.; Longuespée, R.; Casadonte, R.; Wandernoth, P.; Schwamborn, K.; Bollwein, C.; Marsching, C.; Kriegsmann, K.; Hopf, C.; Weichert, W.; et al. Site-to-Site Reproducibility and Spatial Resolution in MALDI-MSI of Peptides from Formalin-Fixed Paraffin-Embedded Samples. *Proteomics Clin. Appl.* **2019**, *13*, e1800029, doi:10.1002/prca.201800029.
103. Fonville, J.M.; Carter, C.; Cloarec, O.; Nicholson, J.K.; Lindon, J.C.; Bunch, J.; Holmes, E. Robust data processing and normalization strategy for MALDI mass spectrometric imaging. *Anal. Chem.* **2012**, *84*, 1310–1319, doi:10.1021/ac201767g.